Ph.D. Thesis

The final result of $\mu^+ \to e^+\gamma$ search with the MEG experiment

（MEG実験による$\mu^+ \to e^+\gamma$ 探索の最終結果）

by

Daisuke Kaneko

Department of Physics, Graduate School of Science,
The University of Tokyo

July 2016

Abstract

The charged lepton flavor violating decay, which has never been observed, is an evidence of physics beyond the Standard Model, if it is discovered. The MEG experiment has been searching for one of the charged lepton flavor violating decays $\mu^+ \to e^+\gamma$ with sensitivity in branching ratio of order 10^{-13}. The MEG experiment is conducted at the πE5 beam line in the Paul Scherrer Institute where the world's most intense positive muon beam is available.

The data taking of the MEG experiment started in 2008 and finished in 2013. The analysis to search for $\mu^+ \to e^+\gamma$ with the full dataset of the MEG experiment is presented, which is doubled compared to the previous result. The total number of muon stopped on the target is 7.5×10^{14}.

In this analysis, a deformation of the target was found, and countermeasures against the issue are applied. In addition, several improvements in analysis algorithm are also introduced. The sensitivity with all data in MEG experiment found to be 5.3×10^{-13}.

No significant excess of the signal events compared to the expected background events is found. The most stringent branching ratio upper limit of 4.2×10^{-13} (90% C.L.) has been established, which is tighter by factor of 30 than the previous experiment.

Contents

Chapter 1

Introduction

The Standard Model (SM) of the particle physics have been surviving many experimental trials, although it is thought not to be the "ultimate" theory but an effective theory at low energy. The SM contains quarks and leptons and both have three generations. But it cannot answer why three generations exist, and how flavors are mixed to each other. The question about the generation and flavor is one of the greatest themes of particle physics. Theories beyond SM which give the answer for this question is longed for, and many experiments have been searching for the hints for the new theories.

In year 2012, the last SM particle Higgs was found at 125 GeV by ATLAS [1] and CMS [2] collaborations at the CERN Large Hadron Collider, while no evidence beyond SM has been discovered. The existence of the mass and the flavor mixing of neutrino is one of the few discrepancies between experiments and the SM [3]. The mixing of the neutrino flavor can be described by Pontecorvo-Maki-Nakagawa-Sakata (PMNS) matrix [4]. Also in year 2012, reactor and accelerator neutrino experiments revealed the last mixing angle: θ_{13} to be relatively large (9°) [5] [6] [7].

However, the mixing in the charged lepton sector has never been observed since the discovery of the muon in year 1937 [8].

The MEG experiment has searched for $\mu \to e\gamma$ with unprecedentedly high sensitivity.

1.1 Physics motivations

When the neutrino mixing is considered, charged lepton flavor violating (CLFV) process (e.g. $\mu \to e\gamma$) occurs as shown in a diagram in Fig. 1.1. The probability of this decay mode is given by Eq. (1.1). This is too small to be measured experimentally, in other words, the discovery of the $\mu \to e\gamma$ will be an unwavering evidence of new physics.

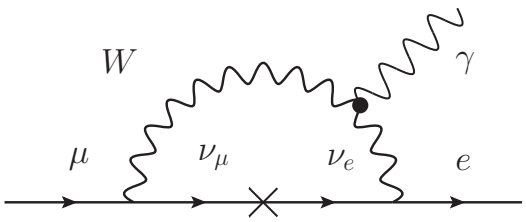

Figure 1.1: $\mu \to e\gamma$ decay via neutrino mixing, the probability amplitude is extremely small.

$$\mathcal{B}(\mu \to \mathrm{e}\gamma) = \frac{3\alpha}{32\pi}\left|\sum_{i=2,3} U^*_{\mu i}U_{ei}\frac{\Delta m^2_{i1}}{M^2_W}\right|^2 \sim 10^{-55}, \tag{1.1}$$

where U_{ij} is i-jth element of the PMNS matrix. The absolute value of this formula is extremely suppressed by the fourth power of the mass difference between W boson and neutrinos.

1.1.1 $\mu \to \mathrm{e}\gamma$ by theories beyond the standard model

A model-independent Lagrangian for the $\mu^+ \to \mathrm{e}^+\gamma$ process can be written as Eq. (1.2) [9].

$$\mathcal{L}_{\mu\to\mathrm{e}\gamma} = -\frac{4G_F}{\sqrt{2}}\left[m_\mu A_R \bar{\mu}_R \sigma^{\mu\nu} e_L F_{\mu\nu} + m_\mu A_L \bar{\mu}_L \sigma^{\mu\nu} e_R F_{\mu\nu} + (\mathrm{h.c.})\right], \tag{1.2}$$

where G_F is Fermi coupling constant, and A_R and A_L are coupling constants corresponds to $\mu^+ \to \mathrm{e_R}^+\gamma$ and $\mu^+ \to \mathrm{e_L}^+\gamma$, respectively, and are expressed as,

$$\begin{aligned} A_R &= -\frac{\sqrt{2}e}{8G_F^2 m_\mu^2}(f^*_{E1}(0) + f^*_{M1}(0)), \\ A_L &= \frac{\sqrt{2}e}{8G_F^2 m_\mu^2}(f^*_{E1}(0) - f^*_{M1}(0)). \end{aligned} \tag{1.3}$$

f_{E1} and f_{M1} are electro-magnetic form factors when the general transition amplitude of vertex of muon (4-momentum p_μ), electron (p_e) and photon ($q = p_\mu - p_\mathrm{e}$) is written as,

$$\begin{aligned} \mathcal{M} = -eA^*_\mu(q)\bar{u}_\mathrm{e}\Big[&(f_{E0}(q^2) + \gamma_5 f_{M0}(q^2))\gamma_\nu(g^{\mu\nu} - \frac{q^\mu q^\nu}{q^2}) \\ &+(f_{M1}(q^2) + \gamma_5 f_{E1}(q^2))\frac{i\sigma_{\mu\nu}}{m_\mu}\Big]u_\mu(p_\mu). \end{aligned} \tag{1.4}$$

The differential angular distribution is given by Eq. (1.5).

$$\frac{dB(\mu^+ \to \mathrm{e}^+\gamma)}{d\cos\theta_e} = 192\pi^2\left(|A_R|^2(1 - P_\mu\cos\theta_e) + |A_L|^2(1 + P_\mu\cos\theta_e)\right), \tag{1.5}$$

where θ_e is the angle between the muon polarization and the positron momentum in the muon rest frame, and P_μ is the magnitude of the muon polarization. A_R and A_L depend on the model, so the measurement of positron emission angle with respect to polarized muon gives another information to restrict models.

The introduction of the supersymmetry (SUSY) [10] is one of the most prevailing extensions of the standard model. It helps the SM from the ultraviolet divergence of Higgs boson mass due to the higher order quantum effect. Even in the minimum SUSY extension of the standard model (MSSM), there are huge degrees of freedom in the parameter space. Hence, the MSSM is often considered within the constraints to meet the phenomenological observations (pMSSM). In the MSSM scheme, a muon can decay into a positron and a photon as in Fig. 1.2 [11].

In this example, the decay occurs via a loop of neutralino and slepton. The slepton is spin-0 SUSY partner of lepton, and neutralino is spin-1/2 particle which is made by mixing of SUSY partners of electro-weak boson and Higgs boson. The decay of Fig. 1.2 is possible if the

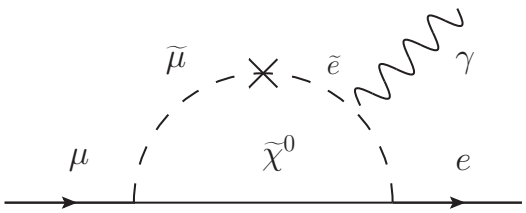

Figure 1.2: An example of $\mu \to e\gamma$ decay in the SUSY model.

theory has non-diagonal element (mixing) in slepton mass matrix. However some mechanism which suppresses the matrix to be almost diagonal is thought to exist, otherwise the probability of the decay was much higher than experimental observation. Two kinds of sources of the non-vanishing off-diagonal element are proposed in the pMSSM scheme.

seesaw mechanism with SUSY Heavy right-handed neutrino with seesaw model is a well-motivated candidate of the new physics. Since it can naturally explain the small neutrino mass by introducing a right handed neutrino with a heavy Majorana mass. As the Yukawa coupling matrix for electron and neutrino are independent, off-diagonal elements appear in left-handed slepton mass matrix as,

$$(m^2_{\tilde{l}L})_{ij} \approx -\frac{1}{8\pi^2}(y_\nu)^*_{ki}(y_\nu)_{kj}m_0^2(3+|A_0|^2)\ln(\frac{M_P}{M_R}), \tag{1.6}$$

where y_ν is the Yukawa coupling matrix for neutrino, m_0 is the universal scalar mass, A_0 is the universal trilinear coupling, M_P and M_R are the Planck mass and mass of the right handed neutrino. The effect from right-handed neutrino contributes only A_R, in other words, only $\mu^+ \to e^+_R\gamma$ occurs and thus the angular dependence will be a form of $(1 - P_\mu \cos\theta_e)$. Figure 1.3 shows the prediction of branching ratio of $\mu \to e\gamma$ and $\tau \to \mu\gamma$ by MSSM with seesaw model [12]. Since θ_{13} is already found to be $\sim 9°$, purple region is remaining.

SUSY GUT A combination of the MSSM and Grand Unification Theory (GUT) is a candidate for the origin of the slepton flavor mixing. The GUT is a theory to explain the electroweak and the strong interactions using a larger gauge group which includes the gauge groups both $SU(2)_L \times U(1)_Y$ and $SU(3)_C$. The quarks and leptons are summed up into one multiplet and newly introduced bosons causes a new kind of the interaction that transforms quarks to leptons vice versa. The SUSY GUT is a favoured theory, because coupling constants of electromagnetic, weak and strong interactions converge to one value as the energy scale goes up to $\sim 10^{15}$ GeV (GUT scale). The smallest group which satisfies the requirement is $SU(5)$, while $SO(10)$ or larger groups are also the candidate of the extended theory of the SM.

The GUT as a source of LFV is suggested in [11]. This is an independent LFV source of the see-saw mechanism, since it originates from off-diagonal element in up-type quarks. In the case of $SU(5)$, LFV appears in the right-handed slepton sector (negligibly small in the left-handed side). In this model, the higher branching ratio is expected with the larger $\tan\beta$, where $\beta = \langle h_2\rangle/\langle h_1\rangle$ is the ratio of the expectation values of two Higgs fields. (h_1 for down-type quark and lepton, h_2 for up-type quark.) Figure 1.4 shows the calculation with $SU(5)$ model [16]. In the case of $SO(10)$, both A_R and A_L have non-vanishing values [17].

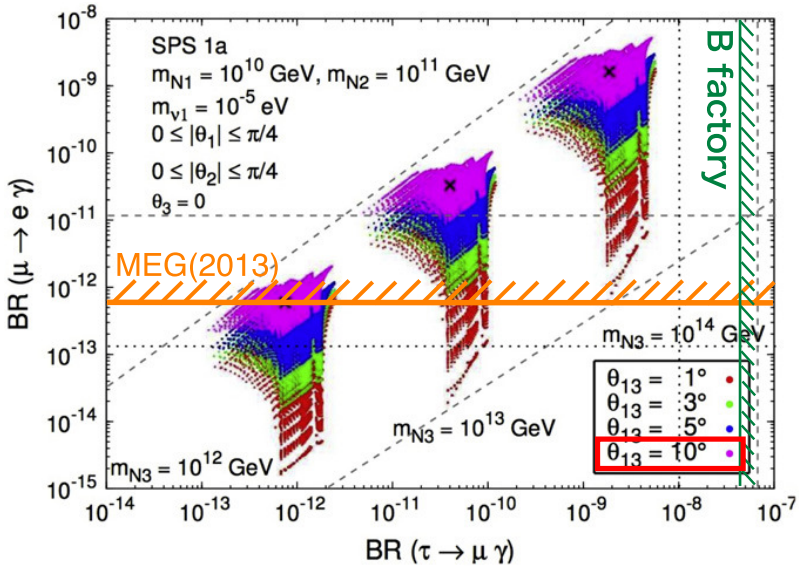

Figure 1.3: Branching ratio of $\mu \to e\gamma$ and $\tau \to \mu\gamma$, expected by MSSM with seesaw mechanism [12] depending on neutrino mixing angle θ_{13} and mass of right handed neutrino. The lines showing the experimental bounds [13] [14] [15] are added to the original figure.

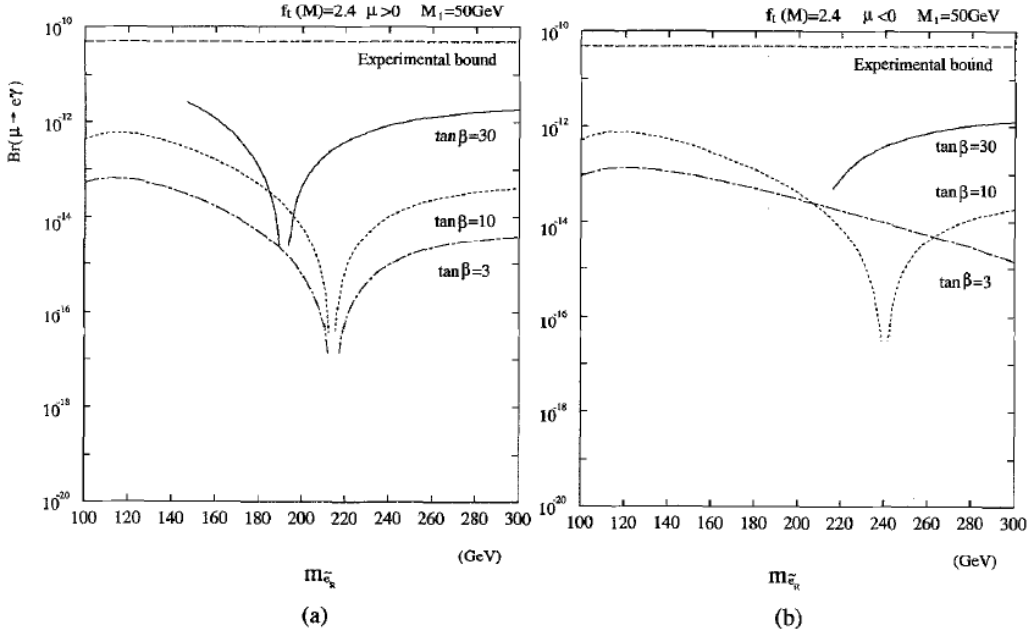

Figure 1.4: $\mu \to e\gamma$ branching ratio calculated in SUSY $SU(5)$ model [16]. The horizontal axis is mass of the right-handed selectron. The top Yukawa coupling at the Planck scale ($f_t(M)$) is fixed to be 2.4, and the bino mass (M_1) is fixed to be 50 GeV. (a) and (b) show the cases with positive and negative sign of the higgsino mass parameter (μ), respectively.

other models Not only theories mentioned above, many theories such as, SUSY with R-parity violation [18], SM with 4-th generation [19], littlest Higgs model with T-parity [20], Randall-Sundrum model [21], etc. predict sizable rates of the LFV process.

Therefore, the search for the $\mu \to e\gamma$ is a good probe for the new physics beyond the SM,

and the precise measurement of the branching ratio gives a information to restrict theories. The branching ratio in $O(10^{-13})$ is a region where many theories predict and it is meaningful to search for $\mu \to e\gamma$ in the sensitivity.

1.2 $\mu \to e\gamma$ search

1.2.1 Past experiments

The search for $\mu \to e\gamma$ has a long history since the first result in year 1947 using cosmic ray [22]. From the result that a muon doesn't directly change to an electron, it turned out that a muon is not a excited state of an electron. Then in 50s, the upper limit of the branching ratio was improved in the experiments using accelerators, such as 2×10^{-5} in year 1954 [23], 7×10^{-7} in 1959 [24]. These results are inconsistent with the theoretical calculation under an assumption of one "meson" [25]. The existence of the "lepton flavor" was established from these measurements results, where it is considered that electron and muon are different particles, and there are different types of neutrino to interact.

In the following decade, the search for $\mu \to e\gamma$ was not so active, but in late 70s, intense muon sources were becoming available, for example at Swiss Institute for Nuclear research (SIN[1]), TRIUMF in Canada, and Los Alamos National Laboratory Meson Physics Facility (LAMPF). In 1982, LAMPF group reached to the branching ratio sensitivity of 1.7×10^{-10} [26]. The world record of the branching ratio limit was overwritten with Crystal Box [27] and then MEGA [28]. 1.2×10^{-11} set by MEGA experiment was the most stringent upper limit before the MEG experiment was started. The history of the branching ratio improvement in the LFV search is summarized in Fig. 1.5 [29]. Table 1.1 shows the world records of the muon LFV search [30].

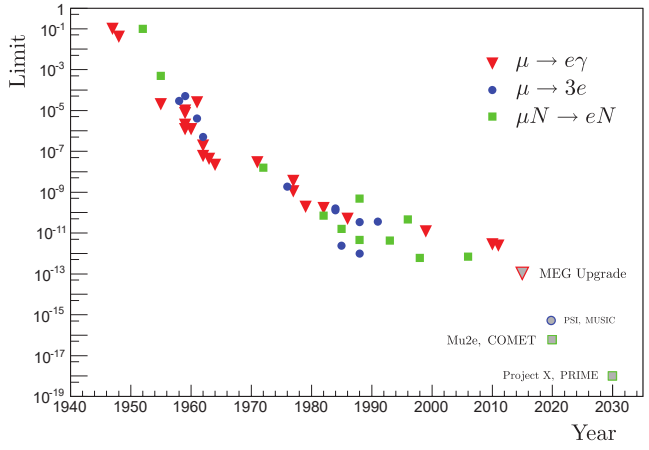

Figure 1.5: History of the result of CLFV search experiments [29].

Table 1.1: Current limits of muon decays from Particle Data Group [30].

Mode	Branching ratio	C.L.
$e^-\bar{\nu}_e\nu_\mu$	$\approx 100\%$	
$e^-\bar{\nu}_e\nu_\mu\gamma$	$1.4 \pm 0.4\%$	
$e^-\bar{\nu}_e\nu_\mu e^+e^-$	$3.4 \pm 0.4 \times 10^{-5}$	
$e^-\nu_e\bar{\nu}_\mu$	$< 1.2\%$	90%
$e^+\gamma$	$< 5.7 \times 10^{-13}$	90%
$e^-e^+e^-$	$< 1.0 \times 10^{-12}$	90%
$e^-2\gamma$	$< 7.2 \times 10^{-11}$	90%

[1] former organization of Paul Scherrer Institute (PSI)

1.2.2 Signal and background

The $\mu^+ \to e^+\gamma$ signal has a very simple kinematics. When the initial state is a stopped muon, the directions of γ-ray and positron are back-to-back and simultaneously emitted from a point, and the energies are well approximated to be the half of the rest mass of muon. Therefore, the measurement of the emission angle, timing and energy of γ-ray and positron is important in order to separate signal from background.

There are two kinds of backgrounds (BG): One is called "prompt" background or Radiative Muon Decay (RMD), and the other is "accidental" background (ACC). As for RMD, the muon decays as $\mu^+ \to e^+\nu_e\bar{\nu}_\mu\gamma$ and when the energy carried by the neutrinos is small, the event looks like a signal. The "accidental" (the dominant in our case) is a coincidence of positron from normal muon decay and γ-ray from other sources. The probabilities of RMD and accidental background are estimated below.

radiative muon decay An approximative decay width of the radiative muon decay is given in [31]. (Its exact calculation is demonstrated in [32] [33].)

$$dB(\mu^+ \to e^+\nu_e\bar{\nu}_\mu\gamma) = \frac{\alpha}{16\pi}\left[J_1(1 - P_\mu\cos\theta_e) + J_2(1 + P_\mu\cos\theta_e)\right]. \tag{1.7}$$

When γ-ray energy, positron energy and angle resolutions of an experiment are taken into account, the J_1 and J_2 in Eq. (1.7) are expressed by

$$J_1 = \frac{8}{3}(\delta x)^3(\delta y)(\frac{\delta z}{2})^2 - 2(\delta x)^2(\frac{\delta z}{2})^4 + \frac{1}{3}(\frac{1}{\delta y})^2(\frac{\delta z}{2})^8, \tag{1.8}$$

$$J_2 = 8(\delta x)^2(\delta y)^2(\frac{\delta z}{2})^2 - 8(\delta x)(\delta y)(\frac{\delta z}{2})^4 + \frac{8}{3}(\frac{\delta z}{2})^6, \tag{1.9}$$

where $\delta x = 2\delta E_e/m_\mu$, $\delta y = 2\delta E_\gamma/m_\mu$ and $\delta z = \delta\theta_{e\gamma}$. The δE_e, δE_γ and $\delta\theta_{e\gamma}$ show the half width of the analysis region of the γ-ray energy, positron energy and angle, respectively.

accidental background The accidental background makes majority of all background event. The branching ratio by the accidental can be estimated with a formula of Eq. (1.10) [9].

$$\mathcal{B}(\mathrm{ACC}) = R_\mu \cdot {f_e}^0 \cdot {f_\gamma}^0 \cdot \frac{\Omega_{e\gamma}}{4\pi} \cdot 2\delta t, \tag{1.10}$$

where R_μ is beam rate, ${f_e}^0$ and ${f_\gamma}^0$ are fraction of positron and gamma ray whose energy is within the signal region, respectively, $\Omega_{e\gamma}$ is range of solid angle of angle resolution, if it is square shape, $\Omega_{e\gamma}/4\pi = (\delta z)^2/4$ and δt is half width of the time window.

Since E_e spectrum from Michel decay shows flat distribution near $m_\mu/2$, and a sharp edge at higher energy side, ${f_e}^0$ can be approximated as ${f_e}^0 \sim 2\delta x$. The gamma background from RMD rapidly drops as the energy approach to the signal energy, after integration over energy around signal and the polarization,

$${f_\gamma}^0 \approx \frac{\alpha}{2\pi}(\delta y)^2\left[\ln(\delta y) + 7.33\right] \tag{1.11}$$

By summarizing all above, we get the approximation of the number of the background,

$$\mathcal{B}(\mathrm{ACC}) \approx R_\mu \cdot (2\delta x) \cdot \left[\frac{\alpha}{2\pi}(\delta y)^2(\ln(\delta y) + 7.33)\right] \cdot \left(\frac{\delta\theta^2}{4} \cdot (2\delta t)\right). \tag{1.12}$$

In Eq. (1.12), only γ-ray from RMD is taken into account, and other sources of the BG γ-ray depend on the apparatus of the experiment. For the situation of MEG experiment, another major BG source is annihilation-in-flight (AIF) of positron. The AIF mainly occurs in the muon stopping target and the drift chamber (positron tracker). The amount is comparable to that of RMD, and has larger fraction near the signal energy.

Figure 1.6 shows the effective branching ratios for (a) accidental background and (b) RMD, as functions of lower edge of the energy window, which is defined by $E_{\mathrm{e,min}} < E_{\mathrm{e}} < 53.5$ MeV, $E_{\gamma,\mathrm{min}} < E_{\gamma} < 53.5$ MeV, $|t_{\mathrm{e}\gamma}| < 0.24$ ns and $|\Theta_{\mathrm{e}\gamma}| < 28$ mrad. With the given window, the background of the accidental is about one order of magnitude more.

Therefore, the continuous muon beam is required, instead of the pulsed beam to minimise the accidental background. There is an optimal beam rate to achieve best sensitivity, since the branching ratio of accidental background increases in proportion to beam rate as shown in Eq. (1.12), while that of the signal do not depends on beam rate. The timing resolution is also important to reject accidental background.

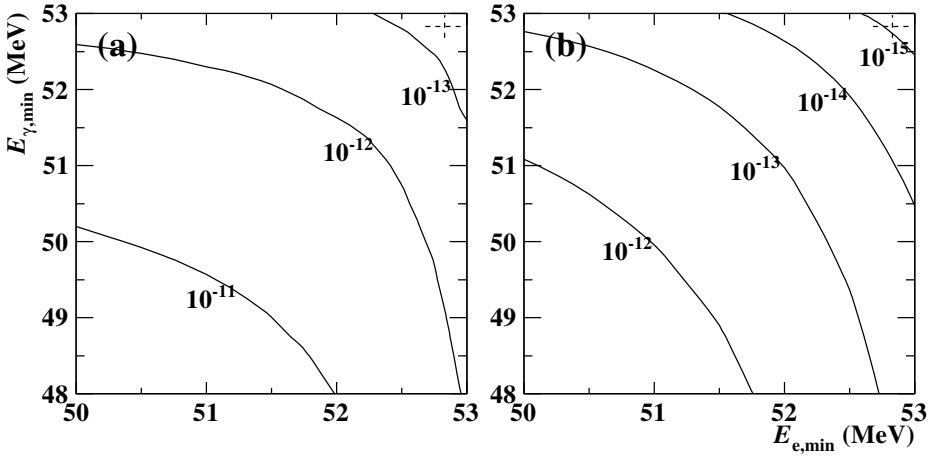

Figure 1.6: Effective branching ratio of (a) accidental background and (b) RMD. The plot for accidental background is made from observed number in the MEG experiment. The branching ratio of RMD is calculated from formula and the detector performance.

1.3 Relation with other experimental searches

1.3.1 $\mu - \mathrm{e}$ conversion

When negative muon stops inside of the matter, the muon can be captured by an atom to form a muonic atom. In the standard model, the muon decays as $\mu^- \to \mathrm{e}^- \bar{\nu}_{\mathrm{e}} \nu_{\mu}$ (decay in orbit), or is captured by the nucleus of the atom in a process as $\mu^- + N(A, Z) \to \nu_{\mu} + N(A, Z-1)$ where $N(A, Z)$ is a nucleus of the atom whose mass number is A and atomic number is Z.

The $\mu - \mathrm{e}$ conversion is a phenomenon which is expressed as Eq. (1.13).

$$\mu^- + N(A, Z) \to \mathrm{e}^- + N(A, Z) \tag{1.13}$$

The decay is forbidden within SM but predicted in the theories beyond the SM.

The effective Lagrangian for this process can be written as [34],

$$\mathcal{L} = \frac{m_\mu}{(\kappa+1)\Lambda^2}\bar{\mu}_R\sigma_{\mu\nu}\mathrm{e}_L F^{\mu\nu} + \frac{\kappa}{(\kappa+1)\Lambda^2}\bar{\mu}_L\gamma_\mu\mathrm{e}_L(\bar{f}_L\gamma^\mu f_L) \tag{1.14}$$

where Λ is a parameter of mass 1-dimension which represents the effective mass scale of the new physics, κ is a 0-dimension parameter which shows the relative size of first and second term. f is the ferimionic fields: quarks in a nuclei in this case.

The first term in Eq. (1.14) corresponds to a interaction via electro-magnetic coupling (shown in Fig. 1.7(a)), and is dominant when $\kappa \ll 1$. It has a common term in Eq. (1.2) of the case of $\mu \to \mathrm{e}\gamma$ decay. However the diagram of a μ-e conversion includes one more vertex comparing with that of $\mu \to \mathrm{e}\gamma$, the probability of the conversion is more suppressed by several hundred times than $\mu \to \mathrm{e}\gamma$ decay. The second term originates from four fermion coupling (tree interaction), and is dominant when $\kappa \gg 1$. There is no corresponding term in Eq. (1.2), hence the $\mu-$e conversion search is complimentary to $\mu \to \mathrm{e}\gamma$ search.

The signal is characterized by only one electron whose energy around 105 MeV, which slightly depends on the different binding energy of muon in 1S orbit by different nuclide. A major background against this reaction is called Decay in Orbit (DIO) where the muon decays in normal way. The energy of the decayed electron has edge at the half of the muon mass, however the spectrum has a long tail and sharply drops at the signal energy due to the interaction with nucleus [35]. Another background for the $\mu-$e conversion experiment is contamination in the muon beam (especially π). Therefore pulsed beam is better, and beam system to remove the contamination is important.

As of year 2016, the best experimental upper limit is achieved by SINDRUM-II experiment [36], and several experiments are being prepared, DeeMe experiment [37], COMET experiment [38] at J-PARC in Japan and Mu2e experiment at Fermilab in USA [39].

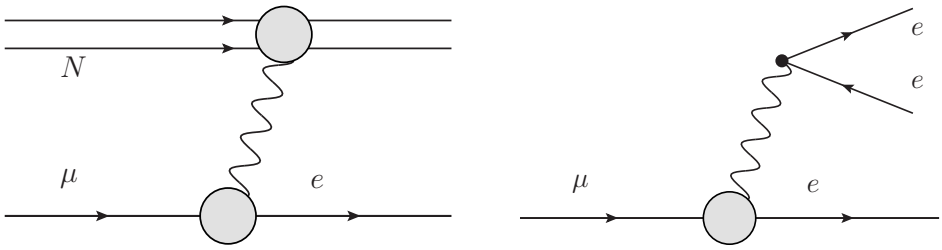

Figure 1.7: A diagram of μ-e conversion (left) and $\mu \to$ eee decay (right). Intermediate particle is not limited for photon in these cases.

1.3.2 $\mu \to$ eee decay

A decay process: $\mu \to$ eee is also a CLFV decay which is forbidden within the SM. Figure 1.7(b) shows an example of the diagram for $\mu \to$ eee decay, the intermediate particle is not necessarily photon as well as $\mu-$e conversion. From the theoretical point of view, the search for this decay is similar to $\mu-$e conversion, because the model-independent Lagrangian for this decay can be written as the same as that in Eq. (1.14), the coupling fermion is, however, not quarks but an electron in this channel.

Many well-motivated theories predict $\kappa \ll 1$, but some theories such as supersymmetric models with trilinear R-parity violation or theories which include leptoquarks predict $\kappa \gg 1$. In the case of $\kappa \ll 1$, the $\mu \to e\gamma$ search have an advantage, and opposite in the case of $\kappa \gg 1$. In Fig. 1.8, the sensitivities of experiments are shown as functions of κ value.

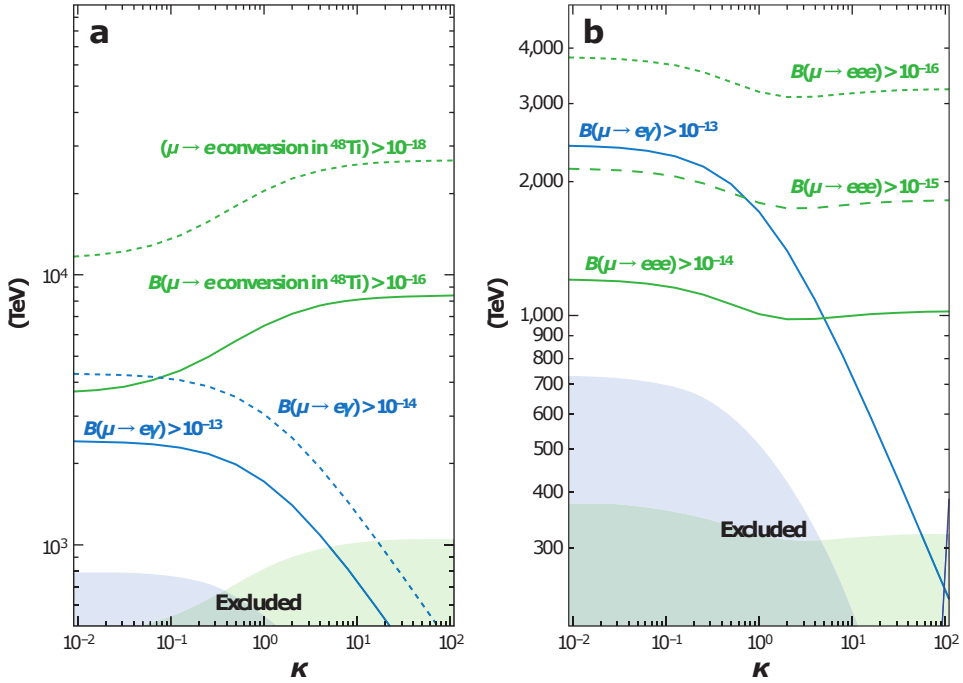

Figure 1.8: Sensitivities of the experiments, as functions of the κ parameter. (left) experimental sensitivity of $\mu \to e\gamma$ and $\mu -$ e conversion (normalized to a case of ^{48}Ti), (right) and that of $\mu \to e\gamma$ and $\mu \to eee$. Λ is the scale of new physics as seen in Eq. (1.14) [34].

An experiment to search for $\mu \to eee$ is planned in PSI (Mu3e) [40].

1.3.3 Muon anomalous magnetic moment

There is a well known relation $\boldsymbol{M}_\mu = g \cdot e\boldsymbol{s}/2m_\mu$, where $\boldsymbol{M}_\mu$ is magnetic moment by muon spin and $\boldsymbol{s}$ is spin angular momentum. g is a factor to connect magnitudes of magnetic momentum and spin, and is exactly 2 when only tree-level process is considered, but deviates from 2 with higher order processes. Recent both theoretical [41] and experimental [42] progresses found a non-negligible discrepancy between the SM prediction and the experimental observation Δa_μ at the order of $O(10^{-9})$.

If it is true, the deviation comes from a contribution of loop diagrams with new particles. One of the diagrams contains SUSY particles like in Fig. 1.9. This diagram is topologically the same as that in Fig. 1.2 except for the flavor violation. In a SUSY model discussed in [43] (Fig. 1.10), the $\mu \to e\gamma$ branching ratio and Δa_μ are related to each other as,

$$\mathcal{B}(\mu \to e\gamma) \approx 10^{-4} \left(\frac{\Delta a_m u}{200 \times 10^{-11}} \right)^2 |\delta^{12}_{LL}|^2. \tag{1.15}$$

$|\delta^{12}_{LL}|$ is a factor coming from CLFV coupling and assumed to be 10^{-4}.

Experiments of next generation Δa_μ measurements, E989 experiment at Fermilab in USA, and J-PARC g-2/EDM experiment in Japan, are in preparation.

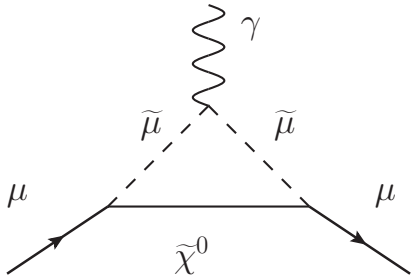

Figure 1.9: An example of contribution to vertex function of μ in the SUSY model.

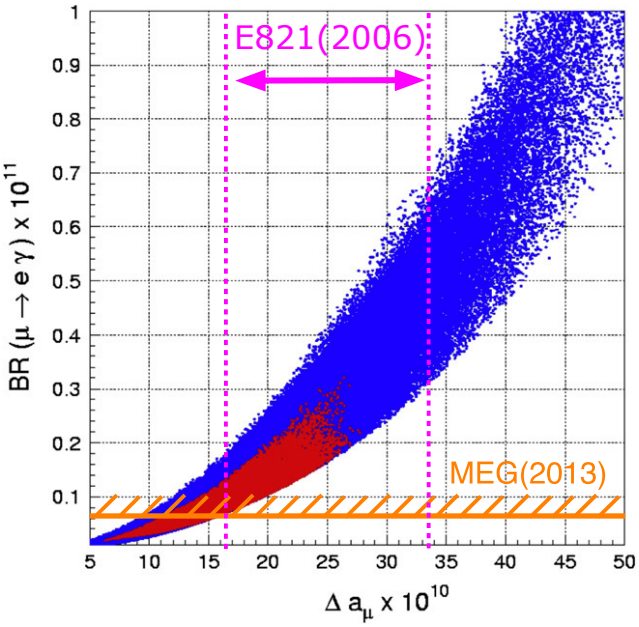

Figure 1.10: Expected relation between branching ratio of $\mu \to e\gamma$ and muon anomalous magnetic moment [43]. The lines to show the experimental bounds of $\mu \to e\gamma$ [13] and δa_μ [44] are added to the original figure. Large area is already excluded by measurements.

1.3.4 LFV search with τ decay

LFV searches via τ particle decay are undertaken by B-factory experiments such as Belle, BaBar and LHCb. A lot of LFV decays are possible for τ, since τ has a mass of 1.777 GeV and is larger than that of μ and lightest baryons and mesons. Those collaborations are searching for the LFV decay with a data of $\sim$ 1 ab^{-1} in each possible channel, however no evidence for the LFV has been found. The results are summarized in Fig. 1.11.

A decay channel $\tau \to \mu\gamma$ has the same topology as $\mu \to e\gamma$, and correlation is pointed out in some model of new physics. Figure 1.3 shows a prediction by MSSM with seesaw model [12]. According to the plot, $\mu \to e\gamma$ search is more advantageous than $\tau \to \mu\gamma$, and being considered the $\theta_{13} \approx 9°$, the experiment starts covering the predicted area.

In year 2016, LHCb is still taking data, and Belle is updating results of $\tau \to l\gamma$ channels. SuperKEKB/Belle II in Japan is in construction. A τ and charm factory is also being considered in Russia.

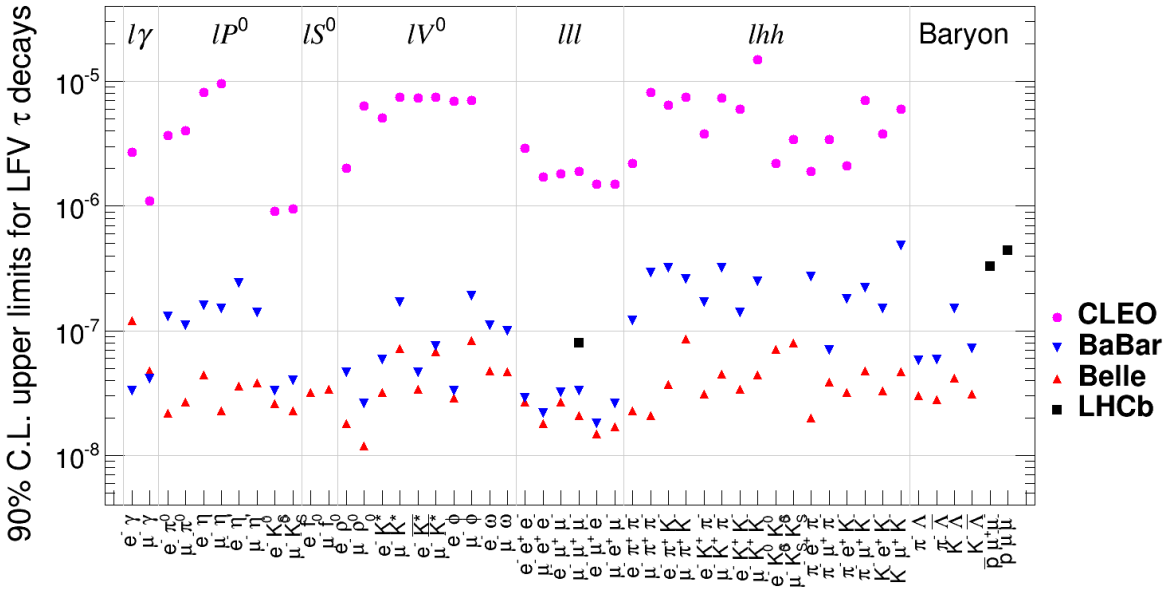

Figure 1.11: Upper limits of LFV search in τ decay [45].

Chapter 2

MEG experiment setup

The MEG experiment is performed at a national laboratory of Switzerland, Paul Scherrer Institute (PSI). An overview image of the experiment setup is shown in Fig. 2.1.

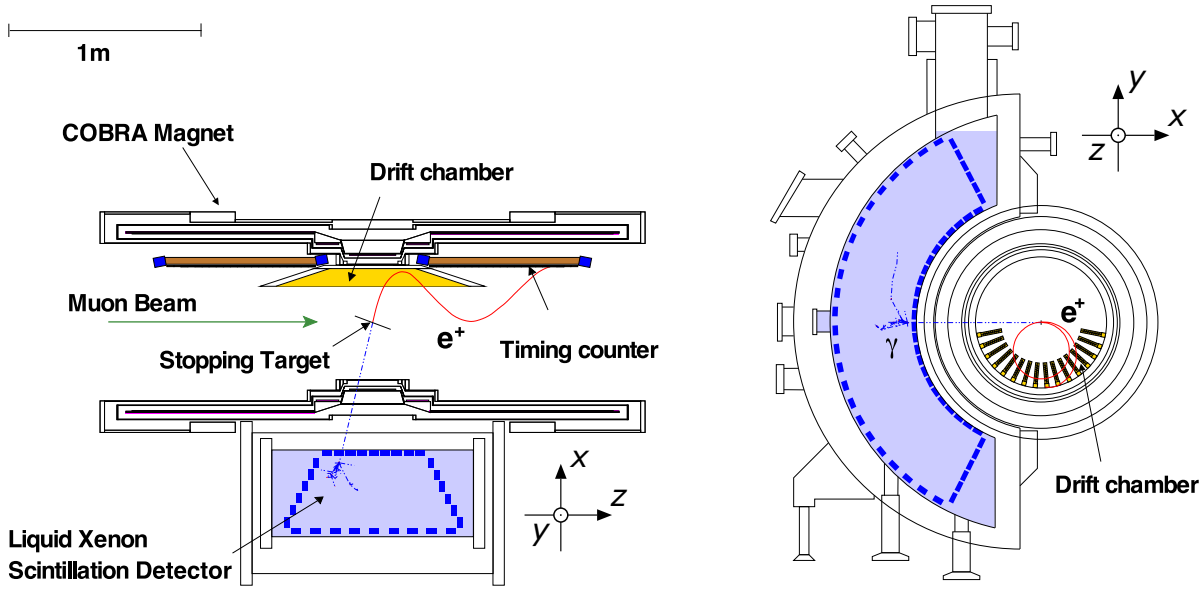

Figure 2.1: Overview of the MEG setup

The MEG experiment uses positive muon beam, because negative muons can be captured by atomic nuclei and form muonic atom. The positive muons from the beamline are stopped on the target at a center. The liquid xenon detector (Sec. 2.3) detects γ-ray, and the positrons are measured in a magnetic field by COBRA magnet (Sec. 2.4.1) via the drift chamber (Sec. 2.4.2) as a tracking detector, then hit the timing counter (Sec. 2.4.3).

The coordinate system is defined as follows. The origin is set at the center of the COBRA magnet. The z axis is parallel with muon beam, the y axis is set vertical upward, and the x is defined as such (x, y, z) to be a right-handed-system, i.e. the liquid xenon detector locates negative side of x coordinate. In addition, the cylindrical coordinates, $r = \sqrt{x^2 + y^2}$, $\theta = \tan^{-1}(z/r)$ and $\phi = \tan^{-1}(y/x)$ are also used.

The details of the detector design are described in [46].

2.1 Beam

In order to achieve a high sensitivity in the MEG, there are two important requirements on beam. One is the intensity in order to gain data statistics. The other one is the property of Direct Current (DC), to minimize the accidental pile-up. The MEG experiment is being conducted in the πE5 beamline where the most intense DC μ^+ beam up to 10^8 /s is available. The beam bunch interval is $\sim$ 20 ns (repetition rate 50.6 MHz), and is well shorter than the mean life of muon at rest state: 2.2 μs. Therefore, the beam can be considered as DC beam. Requirements for beam property are the small transverse size, small momentum spread and small beam contamination.

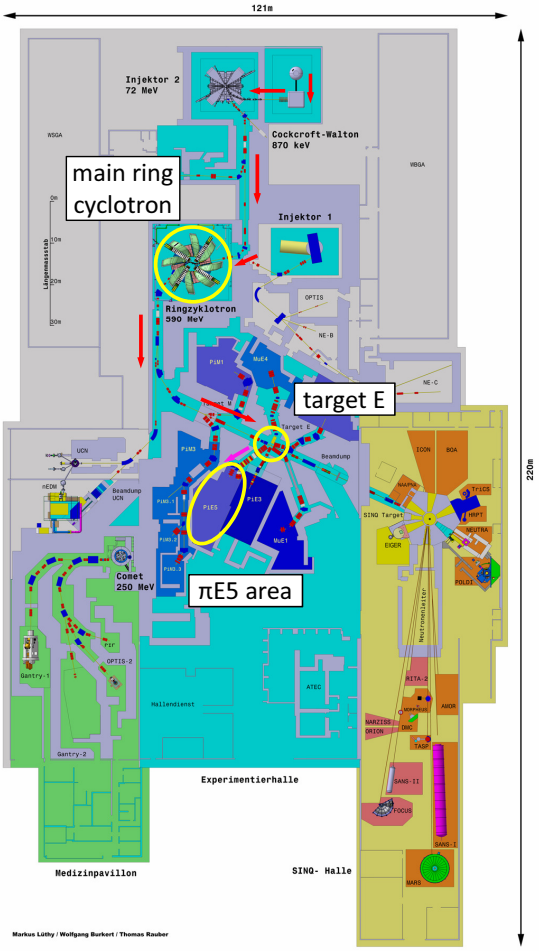

Figure 2.2: Top view of beam facility in PSI main experimental hall. The beam path is shown in arrows.

2.1.1 PSI accelerator facility

In Figure 2.2, a map of PSI main experimental hall is shown. PSI provides μ^+ beam with High Intensity Proton Accelerators (HIPA) [47]. HIPA consists of three accelerators, Cockcroft-Walton accelerator, Injector 2 cyclotron and main ring cyclotron (Fig. 2.3(a))[1]. The energy of

[1] In operation since 1974.

proton is 590 MeV and the nominal beam current at the year 2013 was 2.2 mA.

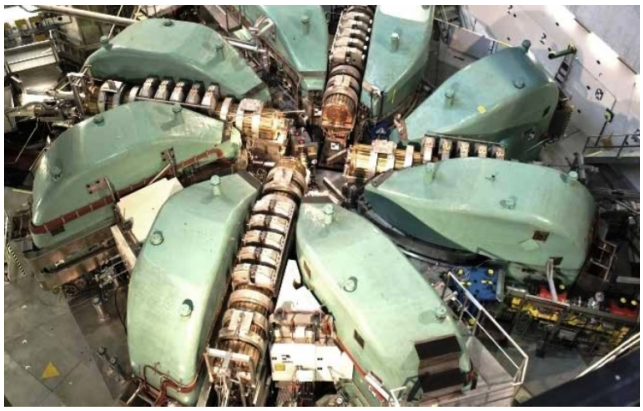

(a) PSI proton main ring cyclotron

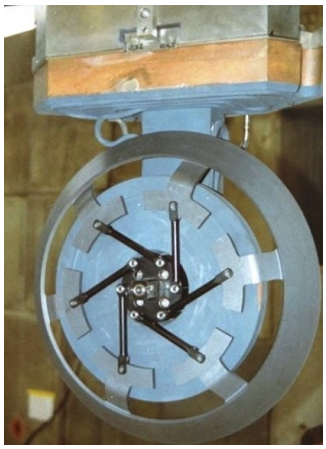

(b) Target E. The outermost part is graphite target.

Figure 2.3

The proton beam is lead to a production target made of carbon graphite with 4 cm length along beam axis. The target is shown in Fig. 2.3(b), the wheel keeps on rotating during the operation for cooling. The surface muon is produced from decay of positive pion ($\pi^+ \to \mu^+\nu_\mu$) which stopped near surface of the target. The energy of μ^+s is uniform (since the pion is stopped) and spin is completely polarized. The surface muon beam is contaminated with positron, which is needed to be removed before it reaches the MEG detector. The πE5 beam line is located at 166° from the original beam, where surface muons [48] from the target are extracted with an array of magnets. The main specification of the beam is summarized in Table 2.1.

Table 2.1: Specs of πE5 beam line

Item	Value
momentum center	28 MeV/c
momentum spread (FWHM)	5-7%
solid angle	150 msr
spot size (FWHM)	15 mm horizontal
	20 mm vertical
angular divergence (FWHM)	450 mrad horizontal
	120 mrad vertical

2.1.2 Beam transport system

Figure 2.4 shows the layout in the πE5 area. The secondary beam runs through the control magnets which consist of a chain of bending, quadrupole and sextupole magnets. An Wien filter is equipped between two quadrupole triplets, in order to separate μ^+ from the other particles (mainly positron). In the Wien filter, horizontal 133 Gauss magnetic field and vertical 195 kV electric field in 19 cm gap of electrodes are applied to the beam. The separation power for muon from positron is as high as 8.1 σ. The muon beam is then injected into Beam Transport

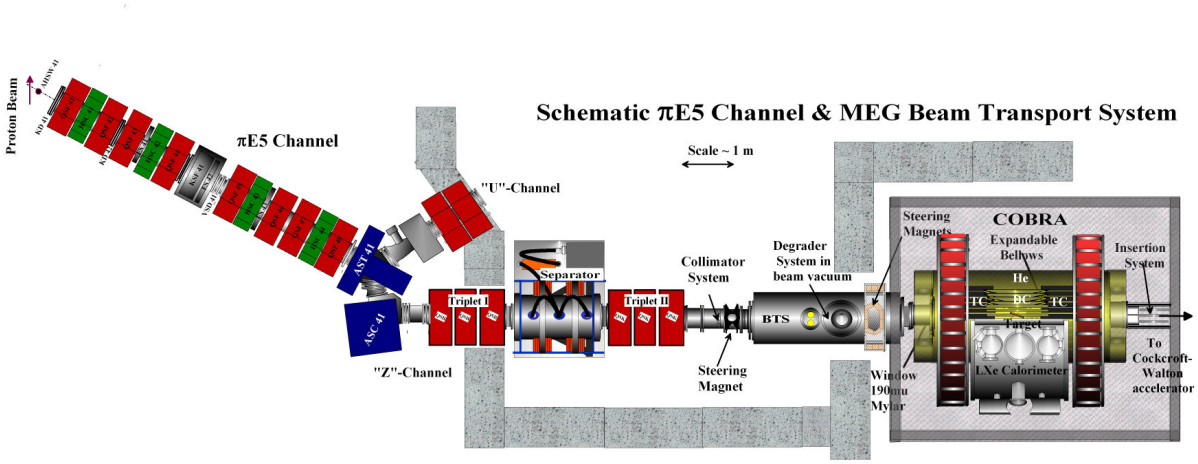

Figure 2.4: Layout in πE5, MEG experiment area

Solenoid (BTS, picture in Fig. 2.5). The main component of the BTS is liquid helium cooled superconducting[2] solenoid with 380 mm bore diameter and 2.63 m length. The nominal current is 199 A and the field strength is 0.36 T. The purposes of BTS are to conduct and focus muon at target, and to make beam spot smaller with collimator. A degrader of thin Mylar film is placed at the center of BTS to maximize the stopping efficiency at the target. The thickness of the film is 300 μm.

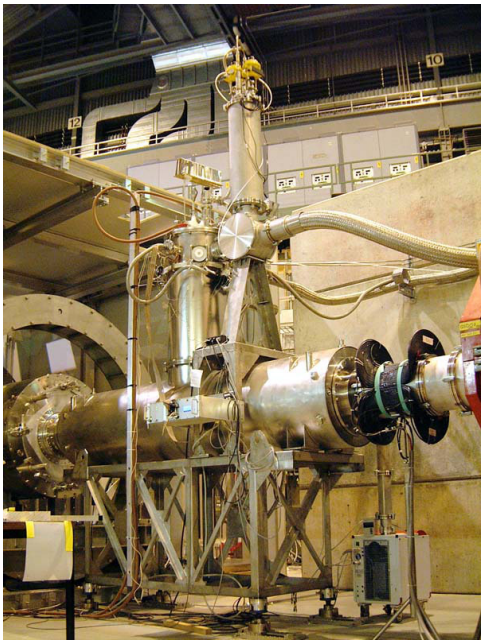

Figure 2.5: Beam Transport Solenoid

The BTS and the spectrometer magnet are connected with an end-cap with thin beam window. While all the beam pipes are evacuated, the spectrometer volume is filled with helium[3] gas for drift chamber (Sec. 2.4.2.1).

[2] Nb/Ti superconductor

[3] Synthetic air is slightly mixed for measure against discharge.

At the stopping target, the beam has round Gaussian profile of $\sigma_{x,y} \approx 10$ mm, and the polarization of muon is measured to be $P_\mu = -0.86 \pm 0.02(\text{stat.})^{+0.05}_{-0.06}(\text{syst.})$ and is consistent with the expectation [49].

2.2 Stopping target

The purpose of the stopping target is to stop muon on it. Therefore, a certain thickness of material is required. On the other hand, the target material on the trajectory of the decayed positron should be minimized for two reasons. The electromagnetic multiple scattering worsens angular resolution, and positron can annihilate with electrons in target. γ-ray which is emitted by annihilation is one of the sources of γ-ray background.

The muon stopping target is shown in Fig. 2.6. It is made of a layered films of polyethylene and polyester with a total thickness of 205 μm and is assembled in a flame, which is made of light but rigid material: Rohacell[4]. The target is laid with a slant angle of 20.5° with respect to the beam direction. The angle was optimized considering muon stopping power (stopping efficiency $\sim 80\%$) and multiple scattering. The target has elliptical shape of 20 cm and 8 cm respectively in major and minor axes and has six holes (10 mm in diameter) and seven cross markers, which are used for the alignment of the target (Sec. 4.4).

The target can be moved remotely for when another target is inserted from the downstream side for the LXe γ-detector calibration.

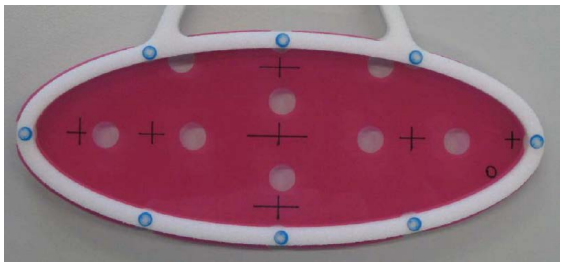

Figure 2.6: MEG stopping target, 6 holes and 7 cross markers are seen.

2.3 Gamma detector

The gamma detector plays a key role in a $\mu \to e\gamma$ search, because background γ energy spectrum rapidly falls around the endpoint, and the energy resolution is important to reject backgrounds. Therefore, also the past experiments [27] [50] paid special attention on gamma detection. The MEG experiment adopted liquid xenon (LXe) scintillation detector. The details will be discussed in next sections.

The design of LXe gamma detector [51] is shown in Fig. 2.7. The concept of the detector is viewing many fast scintillation photons from single active volume with high performance sensors. Because we need to detect ~ 175 nm wavelength photon in environment of liquid xenon, we developed a special PMT for LXe detector. The development of the MEG LXe detector can be found in [52].

[4] By EVONIC, foamed polymethacrylimide (PMI)

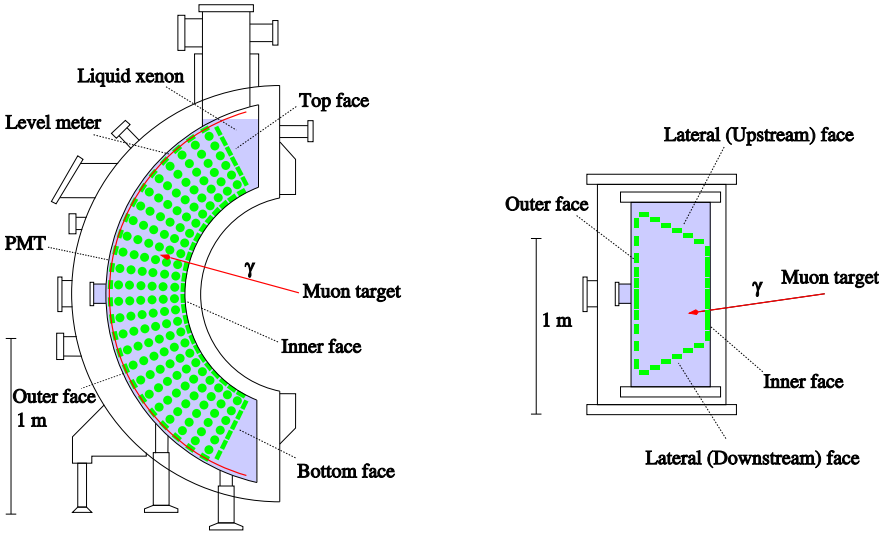

Figure 2.7: Schematic view of gamma detector

2.3.1 Liquid xenon

Liquid xenon is nowadays widely used in experimental physics [53], dark-matter search experiment such as XENON [54] and XMASS [55], or neutrino-less double beta decay experiment EXO [56] etc. Not only for experiment, but also applications are developed for medical use. Excellent characteristics of LXe are as follows.

- High light yield
- High density
- Fast response
- Uniformity as fluid
- No self-absorption of scintillation photon

These properties enable high rate, high precision γ-ray measurement. The LXe also has properties of the ionization and phonon which are available for many applications for particle detection such as timing projection chambers, but we utilize only scintillation light for the simplicity of the detector.

On the other hand there are some difficulties to deal with liquid xenon. As shown in Fig. 2.8, the pressure of triple point is near normal pressure. The range to be in liquid state is therefore narrow at operation pressure. This means the stable temperature and pressure control is required. The wavelength is also a difficulty with LXe scintillation detector. The wavelength of LXe is measured to be $174.8 \pm 0.1(\text{stat.}) \pm 0.1(\text{syst.})$ nm [57]. The wavelength is in a range which is called Vacuum Ultra-Violet (VUV) light, where special treatment for detection is needed (See Sec. 2.3.3 and 2.3.5.3). Basic physical properties of xenon is listed in Table 2.2.

2.3.2 Scintillation

When a gamma-ray is injected into material, generally 3 types of reactions are possible, photoelectric absorption, Compton scattering and pair creation. Figure 2.9 shows the probability of the reactions in liquid xenon. Around the energy of the γ-ray from the $\mu \to e\gamma$, Compton

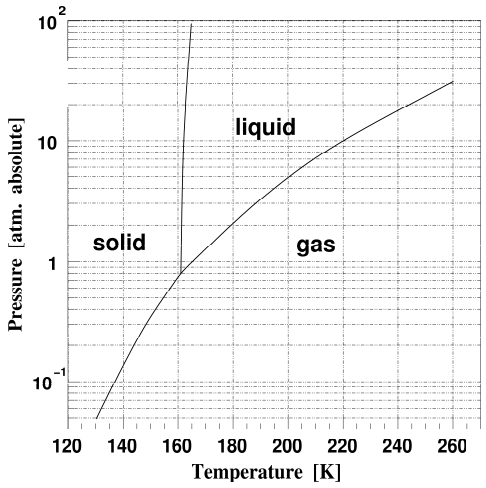

Figure 2.8: Phase diagram of xenon

Table 2.2: Basic properties of xenon

Item	Value
Atomic Number (Z)	54
Atomic Weight	131.293
Density	2.978 g/cm^3
Triple point temperature	161.405 K
Triple point pressure	0.0816 MPa
Radiation length	2.872 cm
Moliere radius	5.224 cm
Scintillation Wavelength	175 nm
Decay constant (fast)	4.2 ns
Decay constant (slow)	22 ns
Decay constant (recomb.)	45 ns
W (for α)	17.9 eV
W (for electron, γ)	21.6 eV

scattering and pair creation are dominant. Therefore the gamma-ray around the signal energy makes electromagnetic shower starting from the first conversion by scattering or creation.

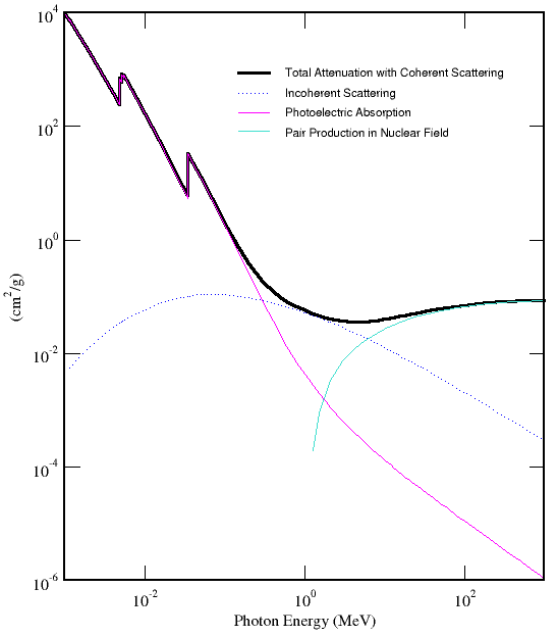

Figure 2.9: Photon interaction in LXe as a function of photon energy [58].

Some part of the deposited energy in the liquid xenon is used to emit scintillation photon. The scintillation photons are generated from two reaction paths [53]. The first path is excitation as follows,

$$Xe^* + Xe \rightarrow Xe_2^* \tag{2.1}$$
$$Xe_2^* \rightarrow 2Xe + h\nu \tag{2.2}$$

where Xe_2^* is called excimer: excited state of diatomic molecule of xenon and $h\nu$ corresponds photon. The second path is called recombination,

$$Xe^+ + Xe \rightarrow Xe_2^+ \tag{2.3}$$
$$Xe_2^+ + e^- \rightarrow Xe^{**} + Xe \tag{2.4}$$
$$Xe^{**} \rightarrow Xe^* \tag{2.5}$$
$$Xe^* + Xe \rightarrow Xe_2^* \tag{2.6}$$
$$Xe_2^* \rightarrow 2Xe + h\nu \tag{2.7}$$

Since the excited state of Xe in Eq. (2.5) is the same state as that in Eq. (2.1), the rest part of the process is the same as the first. The fraction of excitation and recombination depends on the species of the incident particle. In the case of the gamma, the recombination part is more. The recombination step of Eq. (2.4) has the time constant of 45 ns. The time constant of excitation path consist of fast and slow components, which are determined by the step Eq. (2.2). Due to two different spin state of the excimer $^1\Sigma_u^+$ and $^3\Sigma_u^+$, there are two time constants 4.2 and 22 ns [59].

2.3.3 PMT

Scintillation photons are detected by photo-multiplier tube (PMT). For our application for MEG LXe detector, the difficulties are (1) detection of VUV light whose central wavelength is 175 nm and (2) operation in liquid xenon at 165 K. We developed a VUV-sensitive PMT for the LXe detector in collaboration with Hamamatsu Photonics [60]. In order to detect VUV light, photo-cathode of VUV sensitive material[5] and VUV-transparent quartz window is adopted. Aluminum strips (seen in Fig. 2.10(a)) is introduced to stabilize performance in cold environment. For our design, PMTs are located between target and LXe volume, hence a compact design is required. The metal channel dynode is employed for the PMT for that reason.

2.3.4 Design

The schematic view of the LXe gamma detector is illustrated in the Fig. 2.7. It has "C"-shaped structure fitting the outer radius of COBRA. The detector is assembled inside of a vacuum-insulated cryostat. In order to reduce heat inflow, a multi-layered superinsulator installed in the vacuum-insulation. The total volume of liquid xenon is 900 l (2.7 t).

LXe volume covers 11% solid angle viewed from center of the target. The radial depth of LXe of 38.5 cm was determined to completely absorb signal γ of 52.8 MeV. It corresponds to $14X_0$. The LXe detector local coordinates (u, v and w) are used to indicate position inside of detector. u shows the direction parallel to the beam axis, v is curved axis along inner face, and w is the depth from the inner face. The definition is also illustrated in Fig. 2.11(a).

[5] K-Cs-Sb

(a) Outer view of Hamamatsu R9869

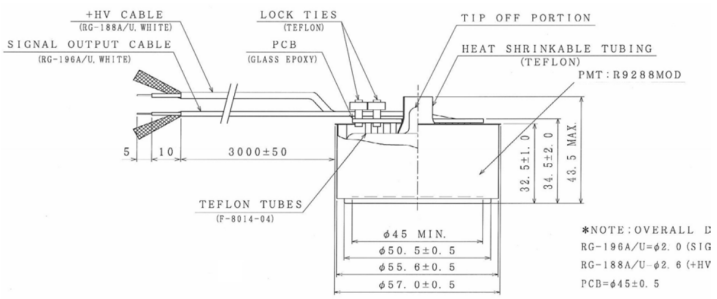

(b) Drawing of PMT

Figure 2.10: PMT for the LXe detector

The PMTs are inserted in PMT holders, and the PMT holders are arrayed on the six faces. As shown in Fig. 2.11(b), the six faces are named inner, outer, up-stream, down-stream, top and bottom. 216 PMTs are installed on inner face with an array of 9 columns along u direction and 24 rows along v. In w direction, there are 6 levels of PMTs from inner to outer. Outer face has the same number of PMTs as inner face basically, but PMTs are arrayed denser in a small region at the center. The total number of the PMTs is 846.

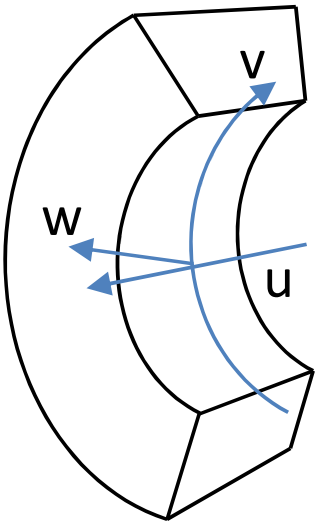

(a) Definition of local coordinates.

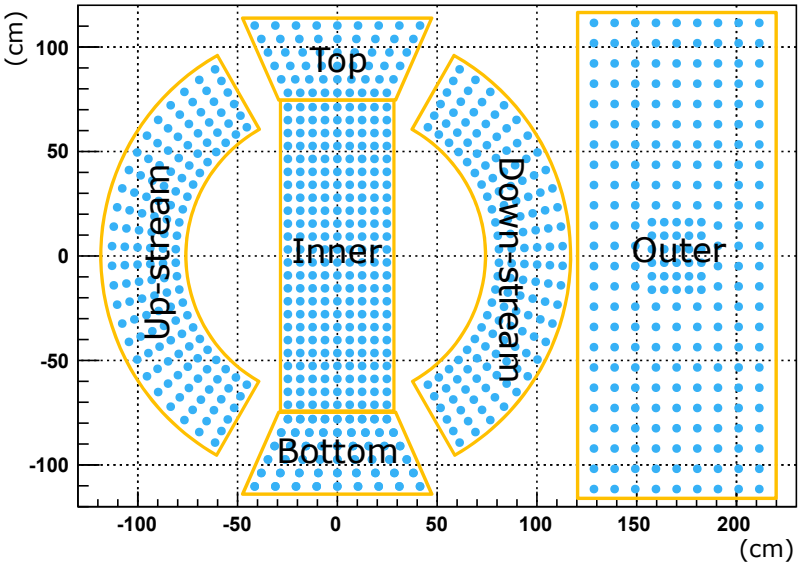

(b) PMT arrangement in developed figure

Figure 2.11

The γ-ray from the target must traverse the inside and outside vessel walls. It is desirable to have less material at inner wall to reduce the interaction of γ-ray before reaching the LXe volume. However the mechanical strength is also required to bear the pressure difference of xenon–vacuum layer–air. This issue is solved by installing an aluminum honeycomb panel covered with carbon fiber sheet for the entrance in the inner vessel (Fig. 2.12). The honeycomb material is Aluminum 5052 with the cell thickness of 0.0254 mm, and the cell size is 4.76 mm. The averaged material amount in the window region corresponds to $0.075X_0$ [61].

Figure 2.12: Honeycomb panel is attached on the entrance window of inner vessel. The panel has a dimension of $1315 \times 611\text{mm}^2$ along curved inside face.

2.3.5 Xenon handling system

2.3.5.1 Pulse tube refrigerator

(a) Pulse tube refrigerator for LXe detector

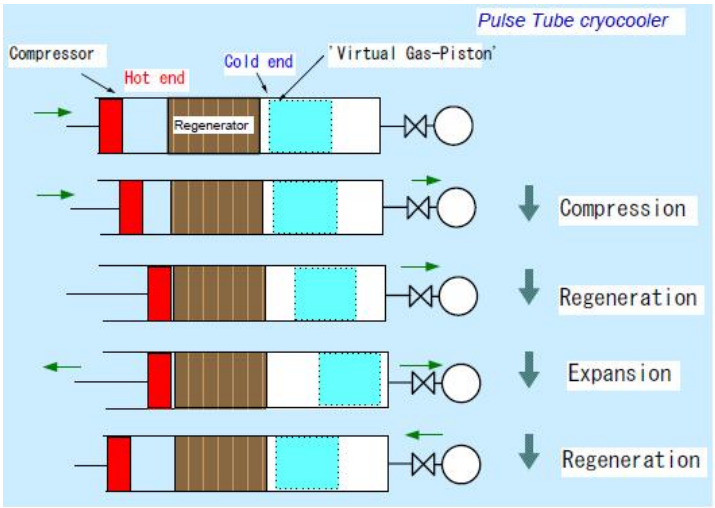

(b) Operation principle of pulse tube refrigerator

Figure 2.13: Pulse tube refrigerator

As explained in Sec. 2.3.1, liquid xenon has narrow liquid state range at the operation pressure. Powerful and stable refrigeration is required for LXe detector. A 200 W pulse tube refrigerator (Fig. 2.13(a)) is mounted at the top of the cryostat. The refrigerator was developed for the MEG LXe detector [62]. The pulse tube refrigerator does not cause mechanical vibration nor electric noise thanks to the operation principle as shown in Fig. 2.13(b). It contributes stable operation and low-noise measurement. During xenon liquefaction and a situation when cooling power is insufficient, liquid nitrogen is used supplementarily. The piping for liquid nitrogen is

attached on outside of the inner cryostat.

2.3.5.2 Storage system

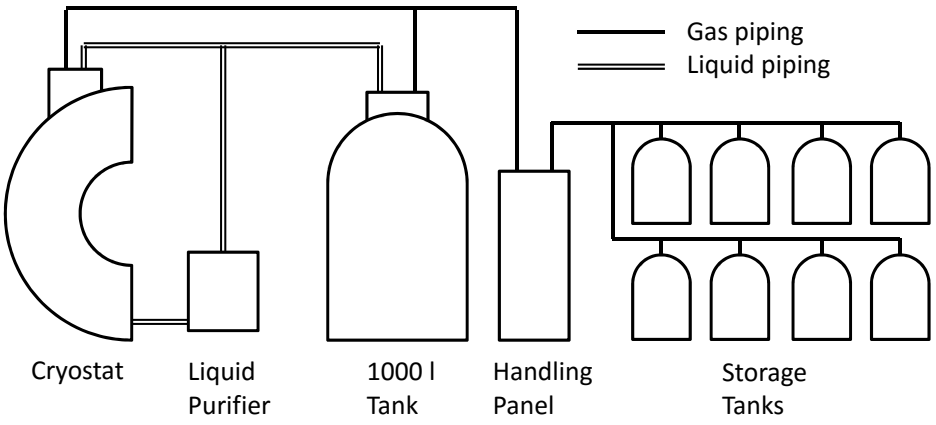

Figure 2.14: Connection of xenon control system

Besides the xenon detector cryostat, auxiliary components are connected to control the xenon flow for the purpose of storage and purification of the xenon. Figure 2.14 shows a diagram of the xenon handling system.

Two types of xenon storage are prepared in the auxiliary system. One is the 1000 l tank which can hold all LXe. It has an independent liquid nitrogen cooling system. It is used to store LXe during the short-term maintenance of the detector. The other one is high pressure gas storage. The storage consists of 8 tanks of the same design. Each tank has 250 l capacity and is tolerable to 8 MPa pressure. Xenon is transferred to the high pressure tanks for long-term detector maintenance.

2.3.5.3 Purification system

The scintillation light yield is very sensitive to impurities in LXe such as Oxygen, Nitrogen, water [63]. The impurities affect scintillation in two ways. (a) The electronegative molecules trap ionized electron in recombination process. (b) The molecules such as water absorbs scintillation photon. The contaminations must be suppressed in ppb order. Therefore the purification system and monitoring of light yield are mandatory.

In order to remove contaminations from xenon, 2 types of purifiers are connected to the system. One is a gaseous state purifier which is installed in the handling panel in Fig. 2.14. The purifier is based on a metal-heated getter which can absorb most of kinds of molecules except rare gas. Xenon goes through the getter when it is sent from storage to detector. Purification by gas state circulation is also available. But the purification speed was limited by the evaporation of gas xenon (0.6 l/hour). The liquid phase purification is introduced to improve the speed of the purification. The liquid purifier is connected to liquid circulation path. It has molecular sieves to adsorb water. A centrifugal pump is used and the circulation speed is ~70 l/hour [64].

2.4 Positron Spectrometer

The positron detector has to treat very high rate positrons. Firstly the all muons eventually decay into positrons, secondly the ratio of positron with energy around signal region is high. (See Fig. 2.15). The normal (positive) muon decay in SM is given by Eq. (2.8) [9].

$$\frac{d^2\Gamma}{dx d\cos\theta_{\rm e}} = \frac{m_\mu}{4\pi^3} W_{e\mu}^4 G_F^2 \sqrt{x^2 - x_0^2} \left(F(x) + P_\mu \cos\theta_{\rm e} G(x) \right) \tag{2.8}$$
$$F(x) = x(1-x) + \frac{2}{9}\rho(4x^2 - 3x - x_0^2) + \eta x_0 (1-x)$$
$$G(x) = \frac{1}{3}\xi\sqrt{x^2 - x_0^2} \left\{ 1 - x + \frac{2}{3}\delta[4x - 3(\sqrt{1 - x_0^2} - 1)] \right\},$$

where $W_{e\mu} = (m_\mu^2 + m_e^2)/(2/m_\mu)$, $x = E_e/W_{\rm e\mu}$, and $x_0 = m_{\rm e}/W_{e\mu}$. The parameters ρ, η, ξ and δ are called Michel parameters, and given as $\frac{3}{4}$, 0, 1 and $\frac{3}{4}$ in the SM. The energy distribution as a function of x is shown in Fig. 2.15, the probability is at maximum around $x = 1$. It means positron cannot be vastly reduced just by a precise energy measurement like in the case of gamma-ray. However, it is important to reduce low energy positron to suppress the total hit rate in the detector.

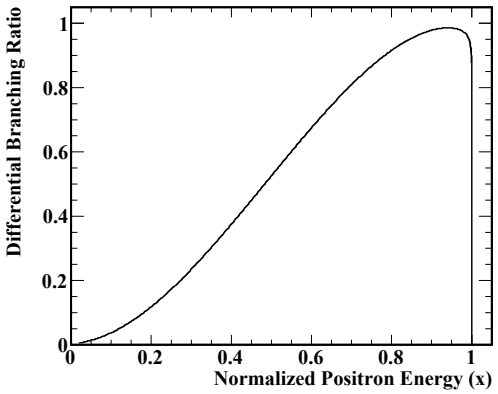

Figure 2.15: Spectrum of positron from rest muon. The spin of the final state positron is averaged. The radiative correction is considered here.

The mass of the detector must be small, because the original information of positron can easily be deteriorated by the effect of electro-magnetic multiple scattering in the detector, around the signal momentum of 52.8 MeV/c. Low material detector also has an advantage for reducing generation of gamma-ray background.

To meet all the requirements above, we designed a positron spectrometer system, in a special gradient magnetic field with the spectrometer magnet COBRA. The tracking of positron is done by ultra low mass drift chambers and a plastic scintillator hodoscope for timing measurement.

2.4.1 COBRA magnet

2.4.1.1 Gradient field

The name "COBRA" is an abbreviation of COnstant Bending RAdius. The COBRA magnet was specially developed for the MEG experiment and is characterized by the gradient field [65]. The magnetic field varies from 1.27 T (center) to 0.49 T (both ends) along the z-axis (See Fig. 2.16).

There are two advantages on the gradient field, as shown in Fig. 2.17. (1) Positron trajectories of the same momentum have the constant bending radius not depending on the emission angle. This is the origin of the name "COBRA". This characteristics enables to easily separate positions by their radius. (2) A positron which emit on perpendicular to the direction of solenoid axis is rapidly swept out. With constant B-field, such a positron hits chambers many times, causing pile-up.

Due to the advantage of (1), positrons whose energies are much lower than signal energy can be isolated, by putting detectors in region of larger radius.

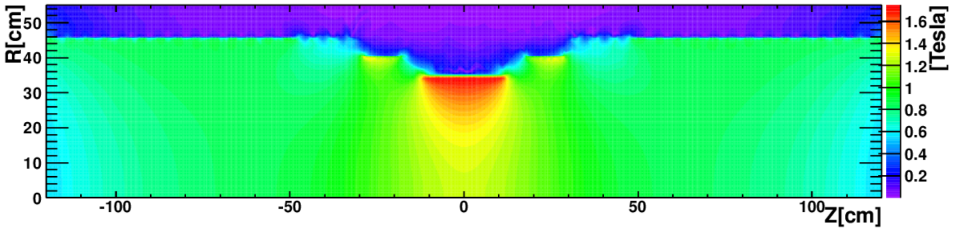

Figure 2.16: Magnetic field by COBRA magnet

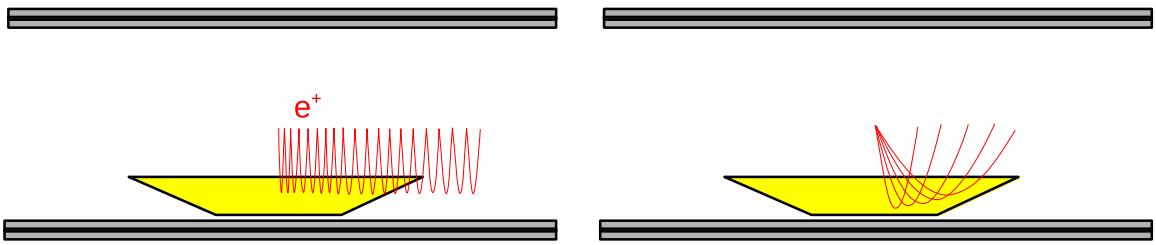

(a) The case of the uniform magnetic field. Positron of $\theta \sim 90°$ turns many times before leaving drift chamber (left). The radius of the trajectory depends on the θ angle (right).

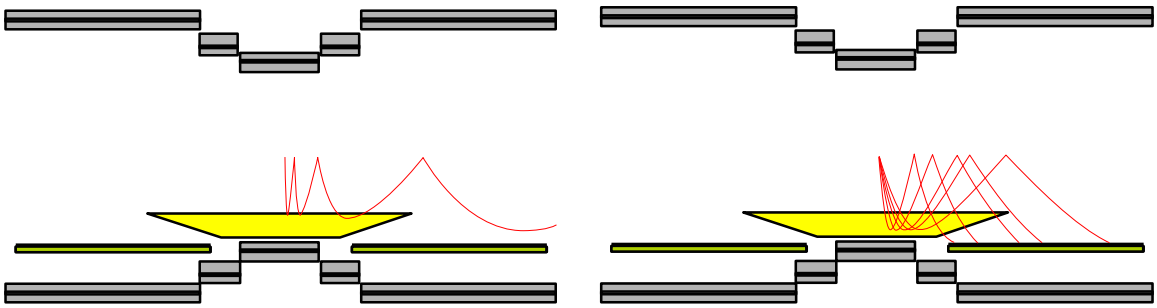

(b) The case of the gradient magnetic field. The number of turns is suppressed (left). Radius is independent of the emission angle (right).

Figure 2.17: Comparison of uniform and gradient field.

2.4.1.2 Design

The COBRA magnet is needed to have low mass structure for gamma ray to minimize the interaction of the γ-ray before reacting the gamma detector which is located outside of the COBRA. The requirement was achieved by thin superconducting (NbTi/Cu) coil with high-strength aluminum stabilizer. The superconducting coil is cooled with two GM refrigerators. The thickness of the magnet (including all support structure) is 3.83 g/cm^2 ($\sim 0.2X_0$). The concept of the gradient field is realized by the array of 7 solenoids which have common axis and have three different coil diameters (700, 810, 920 mm in inner diameters, Fig. 2.18(a)).

Two compensation magnets are installed in the COBRA. They are ring-shaped normal conducting magnets in common axis with COBRA. The purpose of the compensation magnets is to reduce the stray magnetic field at the PMTs in the xenon detector down to $< 5 \times 10^{-3}$ T. The arrangement of magnet is seen in Fig. 2.18(b).

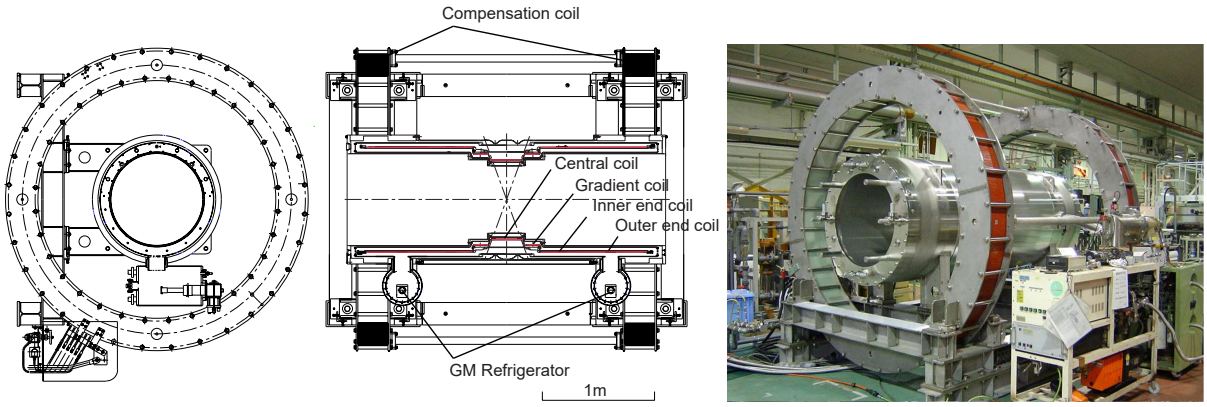

(a) Cross-sectional image of the COBRA magnet (b) Assembled COBRA magnet

Figure 2.18: COBRA magnet

2.4.1.3 Magnetic field

The magnetic field of COBRA is measured with a specially developed field measuring machine with 3-axis Hall probes, scanning the range of $|z| < 110$ cm, $0 < r < 29$ cm and $0° < \phi < 360°$. The probes are orthogonal to each other to individually measure B_z, B_r and B_ϕ. Because the strength of the field along z axis is much larger than the other ($B_\phi = 0$ in ideal case), B_z contaminate the measurement of B_r and B_ϕ if the probe is misaligned. In order to reduce uncertainty, we use magnetic field based on measured B_z and measurement on reference plane $z = z_0$ [66]. z_0 is considered to be the center in magnetic field where the measured B_r is minimized. B_r and B_ϕ are calculated from following formulas,

$$B_r(z, r, \phi) = B_r(z_0, r, \phi) + \int_{z_0}^{z} \frac{\partial B_z(z', r, \phi)}{\partial r} dz', \tag{2.9}$$

$$B_\phi(z, r, \phi) = B_\phi(z_0, r, \phi) + \frac{1}{r} \int_{z_0}^{z} \frac{\partial B_z(z', r, \phi)}{\partial \phi} dz'. \tag{2.10}$$

The formulas are derived from the Maxwell's equations. The magnetic field map to be used in the track reconstruction is obtained by interpolating the measuring points with B-spline

prescription [67]. Figure 2.16 shows the magnetic field inside of the COBRA magnet. The magnetic field around the LXe detector is illustrated in Fig. 2.19. Thanks to the compensation magnets, the strength of the field is suppressed to be $\sim 5 \times 10^{-3}$ T.

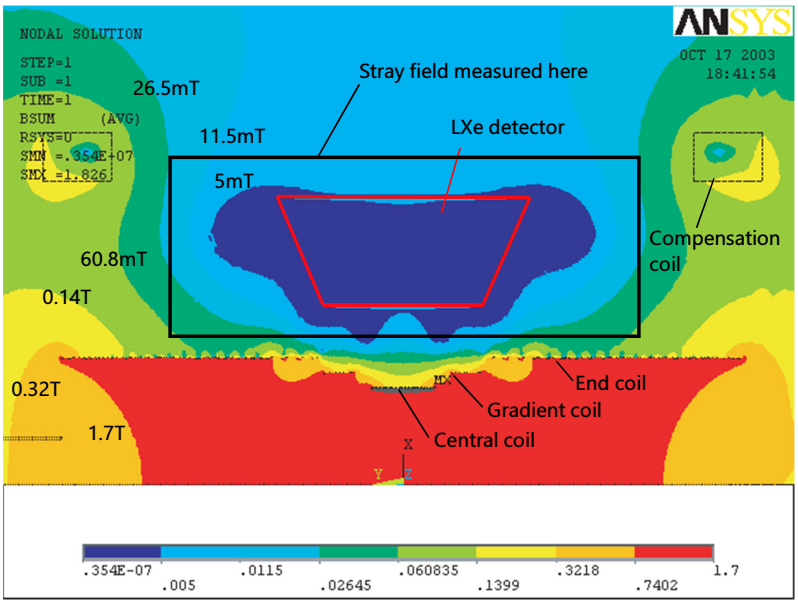

Figure 2.19: Magnetic field around the LXe detector. PMTs of LXe detector are placed along the trapezoidal line.

2.4.2 Drift chamber

Drift CHamber (DCH) is adopted for the positron tracker [68]. It detects the ionization charge by the positron, then the positron trajectory is reconstructed, and finally the emission angle and the vertex position are reconstructed. The DCH is assembled inside of the COBRA magnet. As the momentum of positron is roughly separated by track radius, positron of near signal energy can be selected by simple detector geometry. In other words, if the detector is installed at a large radius r, positrons with lower momentum go away without hitting drift chamber.

In order to reduce multiple scattering and background γ-ray generation, an ultra low mass drift chamber has been developed for the MEG experiment. The DCH consists of identical 16 modules arrayed radially in ϕ direction with an interval of 10.5°. The DCH modules cover azimuthal (ϕ) region from 191.25° to 348.75° and radial (r) region from 19.3 cm to 27.9 cm. The assembled DCH is seen in Figure 2.20. The detail of the R&D of the drift chamber can be found in [69].

2.4.2.1 Drift chamber module

DCH module has a frame structure of a trapezoidal shape whose base lengths of 40 cm and 104 cm, as illustrated in Fig. 2.21. The frame is made of carbon fiber reinforced plastic. The structure is characterized by the open frame geometry which is designed to reduce material on positron trajectories. In other words, a module doesn't have rigid frame on longer base side which is assembled in inner side.

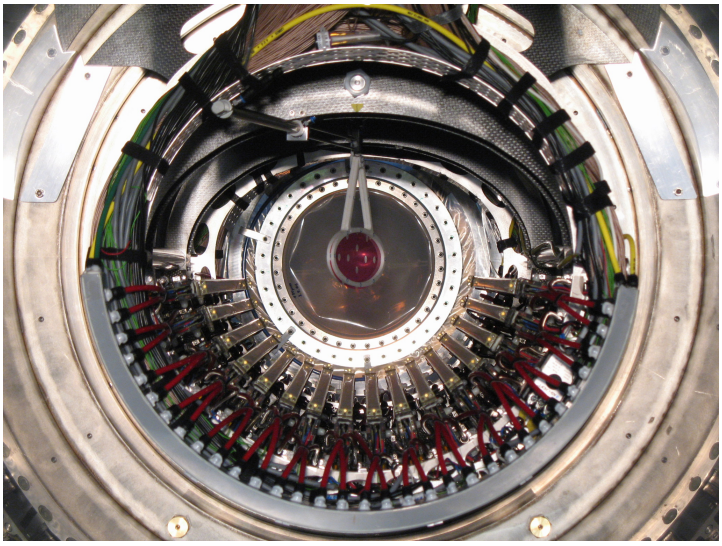

Figure 2.20: Assembled drift chamber. The DCH modules are radially arranged at the bottom half of the COBRA volume. A red elliptical object at the center is stopping target whose dimension is 8×20 cm^2.

Anode and field wires are stretched parallel to z-axis, with a 9.0 mm anode-anode interval. The length of the longest (inner most) wire is 82.8 cm, and the shortest is 37.6 cm. The configuration in $r - \phi$ plane is shown in Fig. 2.22(a). One DCH module has two independent layers sharing gas, the gap between layers is 3.0 mm. Each layer has 9 drift cells and r positions of cells are shifted by half of the width of the cell in 2 layers. The staggered structure is designed to remove left-right ambiguity.

Cathode consists of thin aluminum-deposited polyimide[6] film of 12.5 μm thickness. The distance between films is 7.0 mm, and thus the distance anode and cathode is 3.5 mm. The cathode pattern is separated into 9 cells, and each cell is further separated into two, by zig-zag shaped gap as seen in Fig. 2.22(b). This is called vernier pattern, it will be explained in Sec. 3.2.1. The inner end of the chamber is covered with a hood film.

The chamber is filled with counting gas of 50%:50% mixture of He and C_2H_6. It is adopted to reduce the multiple scattering and the energy loss of the positrons. Another advantage is fast drift velocity, which is important for the operation in the high-rate environment. At the nominal voltage (1800 V), the velocity is ~ 4 cm/μs. The field map and electron drift is simulated using GARFIELD program. Figure 2.23 shows the result of the simulation.

The pressure is carefully controlled, because only a slight change of the pressure causes deformation of the thin cathode film and thus results in the disturbance of electric field. The fluctuation of the pressure difference to outside of chamber (He volume inside of COBRA) is suppressed to be less than 0.005 Pa.

The design information is summarized in the Table 2.3. The average amount of the material per a module is $2.6 \times 10^{-4} X_0$, and total amount in a positron track is $2.0 \times 10^{-3} X_0$ on average.

[6] UPILEX®

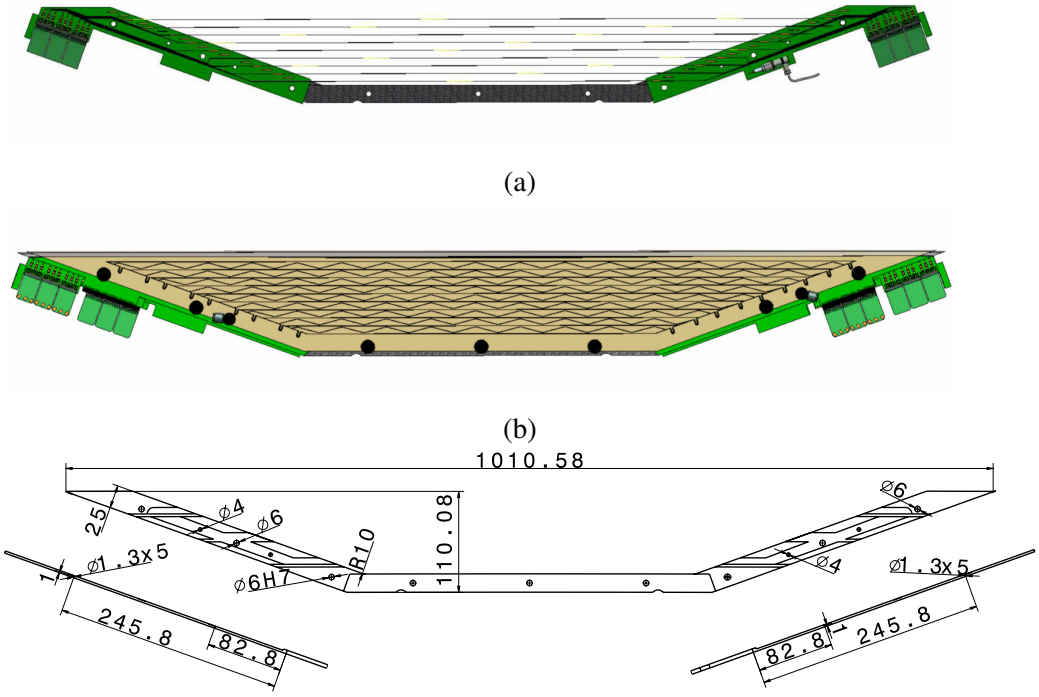

(a)

(b)

(c)

Figure 2.21: Drawing of a drift chamber module. (a) anode and field wire (b) cathode foil

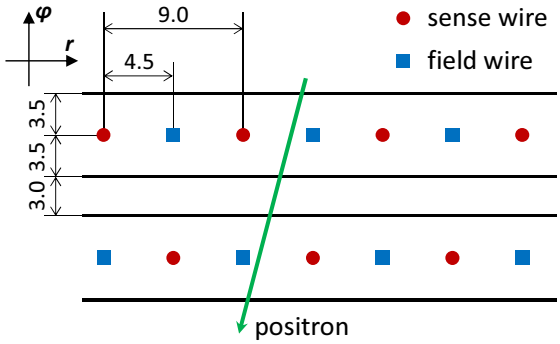

(a) Intersectional view of DCH module (unit in mm). Thanks to the staggered structure, left-right ambiguity (in which side of the wire a positron passed) can be solved.

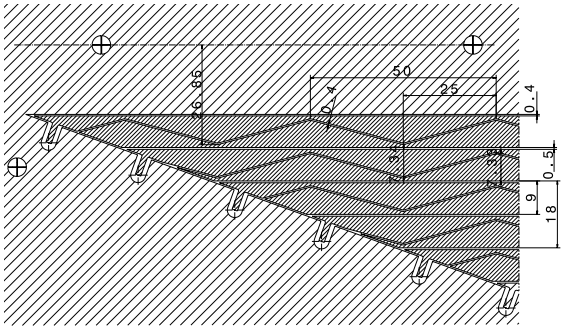

(b) The vernier pattern on cathode film. This is introduced to improve position resolution along z-axis.

Figure 2.22: Features of DCH module design

2.4.2.2 Readout of drift chamber

One drift chamber module has 2 planes × 9 cells. Each cell consists of an anode wire and two cathode pads. The anode and cathodes are read out by pre-amplifier at the both end of the module. The anode signal is coupled with condenser to cut HV. The pre-amplifier is designed to meet DCH requirement, the gain is ∼ 50, and band width is 190 and 140 MHz for anode and cathode respectively. The outputs of all channels are sent to DCH patch panel via coaxial cables. At the patch panel, anode signal is split into two by a fraction of 1:9. The larger part is

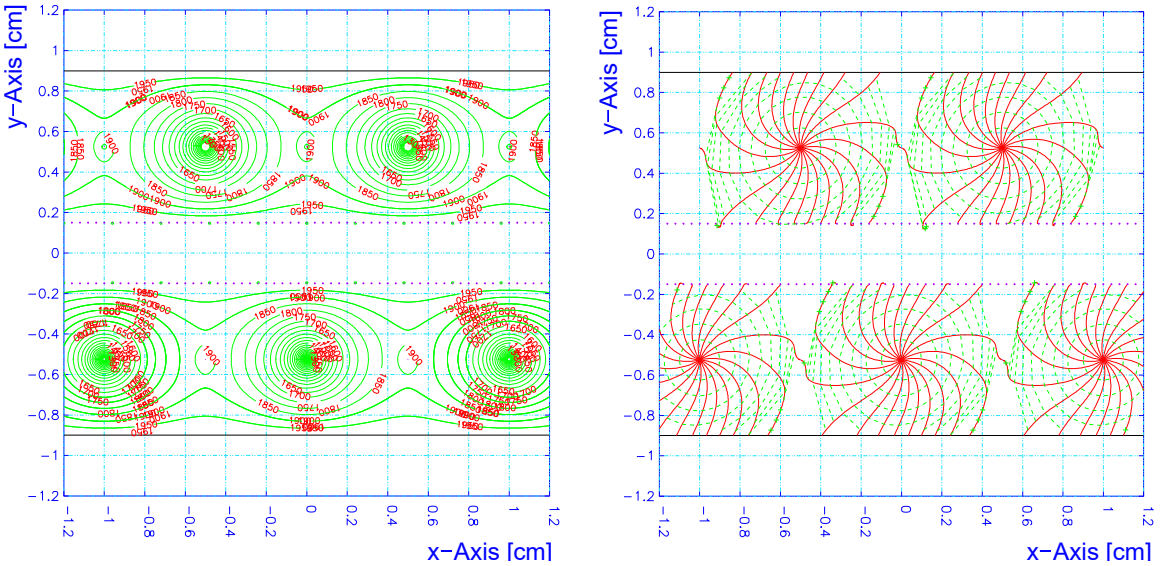

(a) Contour plot of electric potential.

(b) Isochron (green) and drift line (red).

Figure 2.23: Result of GARFIELD simulation

Table 2.3: Details of drift chamber design

Part	Item	Description
Sense wire	material	Ni Cr (80:20)
	diameter	25 μm
	tension	50 gf
Field wire	material	Be Cu (2:98)
	diameter	50 μm
	tension	120 gf
Cathode	foil	12.5 μm polyimide
	pad	250 nm aluminum deposition
Gas	mixture	He C_2H_6 (50:50)
	pressure	~ 1 atm
HV	anode	+1800 V (nominal)
	cathode	ground

sent to Domino Ring Sampler (DRS, a kind of waveform digitizer) and the smaller is used for the trigger.

2.4.3 Timing counter

Timing counter (TIC) [70] [71] is placed at the both end side of the spectrometer to measure the timing of the positron (Fig. 2.1 and 2.24(a)). It also has a role to generate the trigger information for the positron. The TIC is composed of two independent detectors; however, z counter (Sec. 2.4.3) was not used.

ϕ counter One is called ϕ-counter (TICP). One TICP is an array of 15 plastic scintillator bars of $4.0 \times 4.0 \times 79.6$ cm^3. We adopted BC404 scintillator, for the fast rise time constant and large light yield. The bars are set with the interval of 10.5° along ϕ-axis (the same pitch of the DCH modules), they lie at $r > 32$ cm and from 29 cm to 109 cm in z-axis. The bars are read out by PMT (Hamamatsu R5294) at the both ends. The PMT has a fine-mesh dynode structure and attached to bar with slanted angle (Fig. 2.24(b)), in order to reduce the effect of the magnetic field. The TIC is covered with plastic bag (made of 0.5 mm thick EVAL) in order for PMT to prevent from being exposed to helium gas. The volume inside of the bag is continuously flushed with nitrogen gas.

z counter The other part is z-counter (TICZ), which is an array of 128 arch-shaped scintillation fibers. It is designed to detect z position of positron. The fiber material is 6×6 mm^2 SAINT-GOBAIN BCF-20. The fibers are separated at the center, and each side is read out by Hamamatsu S8664 avalanche photo diodes (APD).

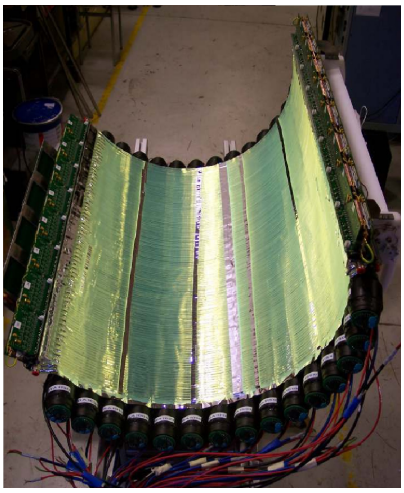

(a) The assembled TIC module of one side.

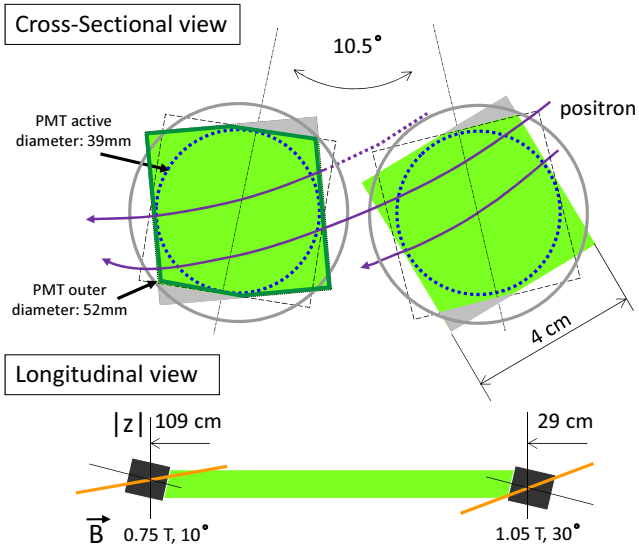

(b) The schematic image of the TICP counter.

Figure 2.24: MEG Timing counter

readout The signal from PMT is first sent to passive splitter and split into two in a ratio of 80%:20%. The larger part is then sent to Double Threshold Discriminator (DTD). DTD has two thresholds one for trigger and the other is veto for small signal. The output of DTD is digital NIM level signal, and is recorded with DRS. The smaller fraction is sent to an active splitter and then sent to the trigger and the DRS. The scheme is adopted for minimizing the time-walk effect. The method to reconstruct hit timing is described in Sec. 3.3.

2.5 Electronics

The MEG experiment adopts MIDAS system [72] which was developed in PSI and TRIUMF for general data acquisition and slow control framework. It gives a front-end readout in many

platforms such as CAMAC, VME, etc. The users can control start/stop DAQ and access slow control via dedicated HTTP server.

2.5.1 DAQ scheme

A schematic image of MEG DAQ is shown in Fig. 2.25. The signals from all (except APD of TICZ) detectors are recorded with waveform digitizer "DRS" (details in Sec. 2.5.2.1), and the signal waveforms are sent to trigger system in parallel. In order to split the signals into two, active splitters with high-bandwidth amplifier are used. These electronics are all implemented on VME boards. For each triggered event, the digitized signal is processed by online computers. Then, waveforms are recorded with MIDAS support data format (".mid") and are compressed. The data size of raw data is 2.4 MB/event in typical runs, and compressed to be 0.9 MB/event using bzip2 algorithm. The data can be monitored in display simultaneously. The data quality can be checked after offline data processing. The result of the offline process is output in ".root" format.

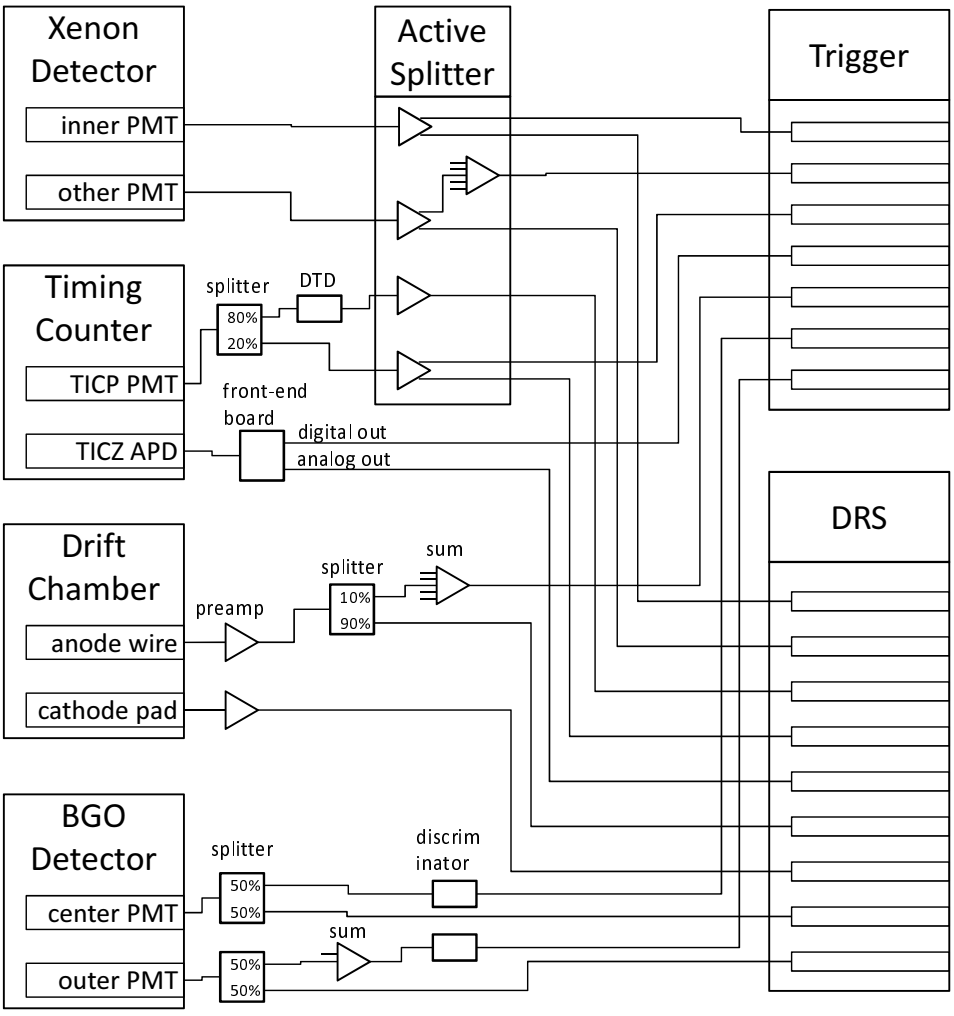

Figure 2.25: Schematic diagram of signal from detectors.

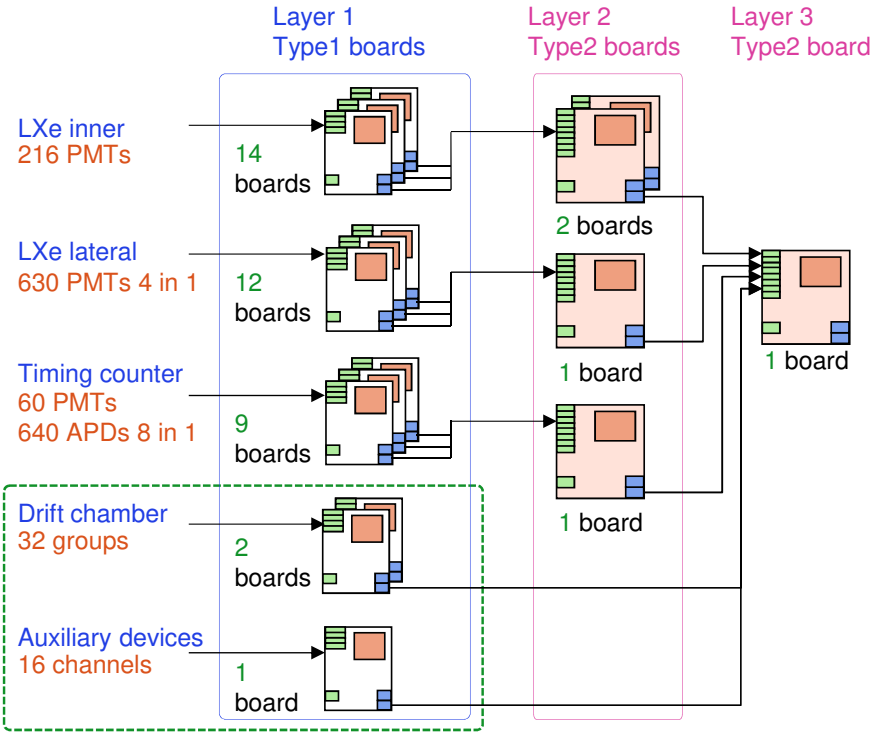

Figure 2.26: Schematic diagram of trigger structure

2.5.2 Trigger

The trigger system [73] is based on flash analog to digital converters (FADC)[7] for 10-bit, 100 MHz waveform sampling, and field programmable gate array (FPGA)[8] for data processing. There are two types of trigger board: (1) Type1 board, which is implemented on 6U VME board with 16 input channels, (2) type2 board on 9U VME board, which integrates information from type1 boards.

The trigger system has three layers as shown in Fig. 2.26. The first layer is composed of type1 boards. This layer receives the waveform from each sensor. The second layer combines the outputs of the first layer for each sub-system. The third layer is composed of one type2 board, and makes final decision of the trigger.

The γ-ray and positron are reconstructed [74], independently of the data taken with DRS. The energy is estimated by summing up the photons from all PMTs in LXe detector. The timing is calculated from the sampled waveform. The position (angle) of γ-ray is given as the position of the inner PMT which detected the largest number of photons. The positron reconstruction is done for first-hit TIC bar. The timing is calculated from the sampled waveform with two PMTs in the bar. The position in z direction is reconstructed from the ratio of the light yield of PMTs in both ends.

The MEG trigger is determined according to (1) energy of γ-ray (2) timing between γ-ray and positron, and (3) direction matching of γ-ray and positron. Not only the trigger for $\mu^+ \to e^+\gamma$, there are several kinds of triggers for calibration. The trigger types are listed in Table 2.4.

A pre-scaling factor is a factor to adjust the number of the taken data. For the trigger with a

[7] Analog Devices, AD9218
[8] Xilinx Virtex-IIpro XC2VP20

Table 2.4: List of trigger types, pre-scaling factor (Presc.) and conditions

Id	name	Presc.	Condition
0	MEG	1	(Q_{LXe}High) $\wedge$ (ΔTNarrow) $\wedge$ (DMNarrow)
1	MEG lowQ	200	(Q_{LXe}Low) $\wedge$ (ΔTNarrow) $\wedge$ (DMNarrow)
2	MEG Wide Angle	550	(Q_{LXe}Low) $\wedge$ (ΔTNarrow) $\wedge$ (DMWide)
3	MEG Wide Time	250	(Q_{LXe}Low) $\wedge$ (ΔTWide) $\wedge$ (DMNarrow)
4	RMD Narrow Time	1100	(Q_{LXe}Low) $\wedge$ (ΔTNarrow)
5	RMD Wide Time		(Q_{LXe}Low) $\wedge$ (ΔTWide)
6	Pi0		(Q_{LXe}High) $\wedge$ preshower counter coincidence
7	Pi0 w/o PrSh		(Q_{LXe}High) $\wedge$ BGO detector coincidence
8	BGO		BGO detector alone
9	LXe HighQ	20000	(Q_{LXe}High)
10	LXe LowQ		(Q_{LXe}Low)
12	Alpha	22000	(Q_{LXe}Alpha) $\wedge$ A/Qratio
14	LED	6	LED pulser
15	Neutron Ni		Neutron generator
16	Michel	1.5×10^7	DCH $\wedge$ TIC
18	DC Track		DCH alone
22	TC	1×10^7	TIC alone
31	Pedestal	20000	Random trigger

pre-scaling factor of n, the data is taken once in every n time trigger requests.

2.5.2.1 Waveform digitizer

In the MEG experiment, all waveforms from the detectors are recorded in order to enable analysis such as removing pile-up etc, which cannot be done with conventional DAQ with ADC/TDC. Domino Ring Sampler (DRS) [75] is originally developed at PSI, and adopted for the MEG waveform digitizer. The DRS is based on switched capacitor arrays (1024 cells) with a high speed and a high accuracy. Figure 2.27(a) shows the schematic diagram of the DRS sampling. The sampling speed of DRS is adjustable from 0.7 to 6 GSPS[9]. An actual sampling speed is 1.4 GSPS except DCH waveform (0.7 GSPS). DRS version 2 was used for all detectors at the first run of MEG in year 2007. All of them were replaced with DRS version 4 by the run in 2009.

One DRS chip can read 4 channels plus a synchronizing clock signal at the same time. Four DRS chips are mounted on a "mezzanine" board and the mezzanine is mounted on a VME board. (16 channels per module, see Fig. 2.27(b)). All of the DRS boards are in operation with a synchronization signal, in order to adjust timing among the boards. 19.44 MHz common clock signal from low-jitter clock generator is transferred to each mezzanine board.

2.5.3 Online computers

The MEG online computer consists of 9 front-end computers ("megon01"-"megon09") and 1 backend computer ("megon00"). The trigger (DAQ) boards are mounted in 4 (5) VME crates, and each crate is connected with one front-end computer with optical fibers. The nine online

[9] giga samples per second

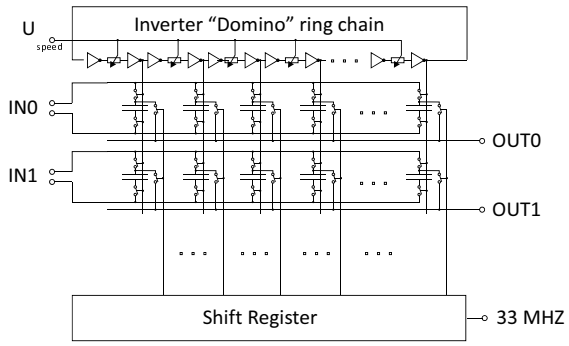

(a) A simplified diagram of DRS.

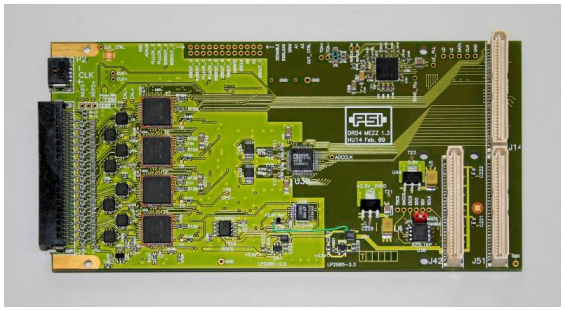

(b) DRS mezzanine board. 4 square shaped chips on left side are DRS4 chips.

Figure 2.27: Domino Ring Sampler

computers and the backend computer are connected via a Gigabit Ethernet switch. On the back-end computer, a process to associate data from each frontend is running, and the processed data is written in online storage in the computer, then the data is transferred to offline cluster (named "lcmeg").

2.5.4 Slow control

The slow control manages the control and monitoring of the experimental apparatus, such as temperature, pressure and etc., as their change is slow (> ms) comparing with the signal (~ ns). We adopt a system called Midas Slow Control Bus (MSCB) which is a part of the MIDAS. The feature of the MSCB is the ability to handle via Ethernet. In order to connect the end-devices (sensor, voltage source, etc.) to the Ethernet, a device developed at PSI: "SCS" is commonly utilized in the MEG experiment. In an SCS module, daughter cards can be mounted, and the cards work as ADC and etc.

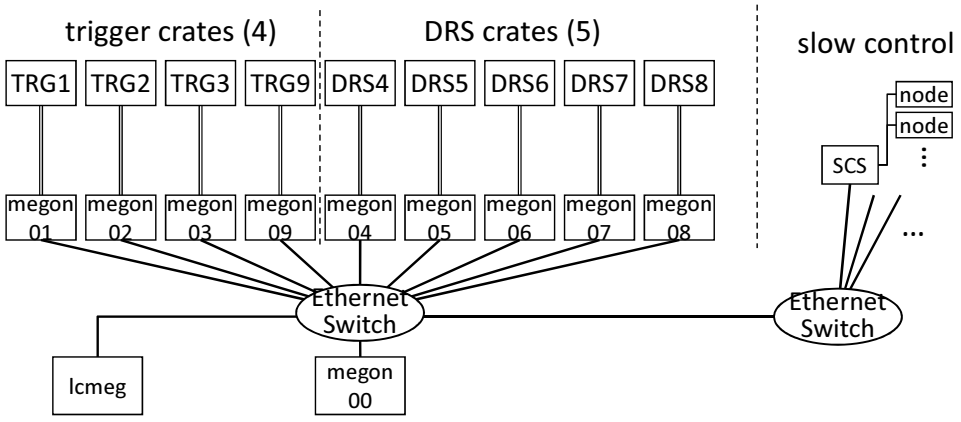

Figure 2.28: Schematic diagram of online computers

Chapter 3

Event reconstruction

In this chapter, the way to reconstruct event is discussed. A simplified diagram of the data flow is summarized in Fig. 3.1.

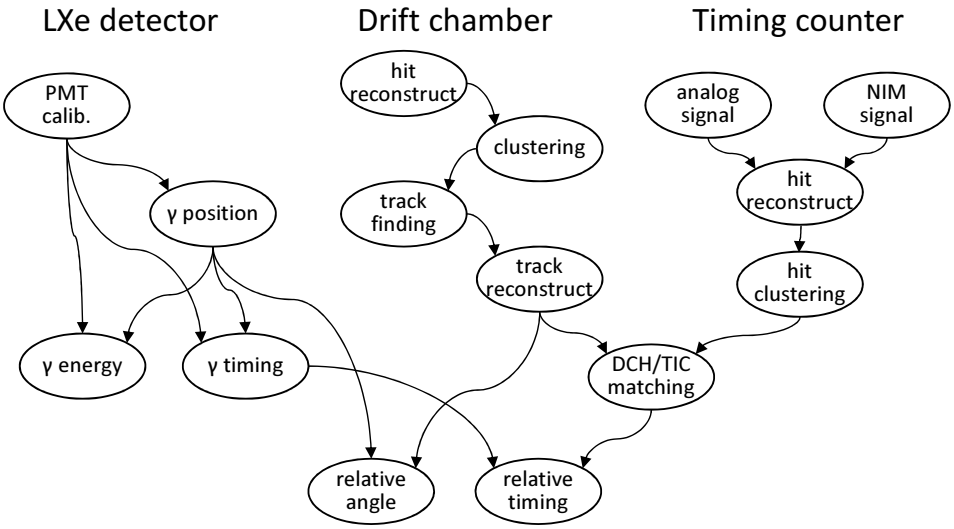

Figure 3.1: Flowchart of the MEG event reconstruction

3.1 γ reconstruction

Reconstruction of the γ-ray is done from information of 846 PMTs in the liquid xenon detector. First, hits are defined for each PMT, and then the γ-ray observables are reconstructed with the processed PMT hits.

3.1.1 Waveform analysis for each PMT

The waveform is integrated to obtain charge (Q) and thus the number of photo-electrons. Before the integration, the waveform is processed with software filtering. A high-pass filter based on moving-average method is adopted, since we found low frequency ($\sim$ 1MHz) noise. The

filtering is written as,

$$y[i] = x[i] - \frac{1}{M}\sum_{j=1}^{M} x[i - M + j], \tag{3.1}$$

where $x[i]$ and $y[i]$ is original and filtered waveform, M is a number of averaged bins: 125. It corresponds to a cut frequency of 11 MHz. The integration width is 67 ns. Figure 3.2 shows raw and filtered waveform.

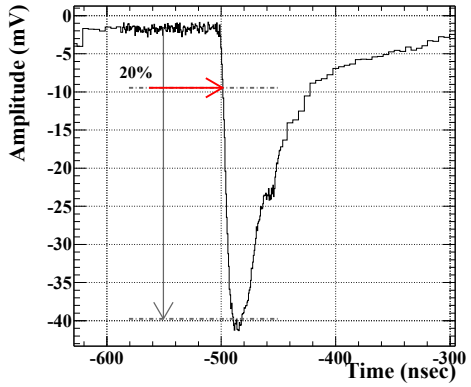

(a) Raw waveform. The horizontal line shows the threshold for timing reconstruction.

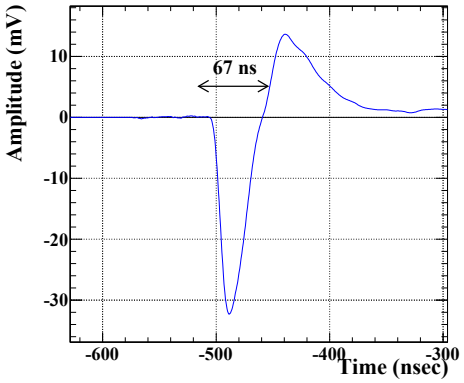

(b) Waveform after high-pass filtering. The charge is obtained by integration of the waveform.

Figure 3.2: Typical waveform of PMT

Sometimes the PMT waveform exceeds the dynamic range of the digitizer. If the photon interacts within 1 cm from a PMT (This happens in 15% of all the triggered event.), mostly the closest PMT saturates like Fig. 3.3. In the saturated cases, the charge integration is done with another method: Time-over-Threshold (ToT). The ToT is defined as the duration time that the pulse is higher than a threshold (150 mV). The charge is calculated with a conversion function from the ToT.

The number of photo-electron (N_{phe}) and the number of photon (N_{pho}) are calculated from the charge for each PMT as formula Eq. (3.2) and (3.3). G_i and QE_i are the gain and quantum efficiency of i-th PMT respectively. The quantum efficiency used in this paper includes the collection efficiency of photo-electron to dynodes unless otherwise remarked. The methods to obtain these values are discussed in Sec. 4.1.

$$N_{\mathrm{phe}i} = Q_i/(e \times G_i) \tag{3.2}$$
$$N_{\mathrm{pho}i} = N_{\mathrm{phe}i}/QE_i \tag{3.3}$$

The timing is calculated with the technique of constant fraction: The time walk due to the difference of absolute pulse size can be suppressed by this technique. In order not to lose the timing information, non-filtered waveform is used for timing reconstruction. The time when the waveform cross the line of 20% of height is defined as the timing of a PMT ($t_{\mathrm{hit},i}$). Here, "height" is not a direct height but estimation from the charge.

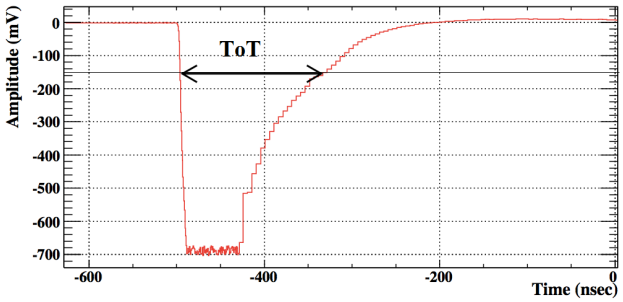

Figure 3.3: Saturated waveform of PMT

3.1.2 γ position reconstruction

The position of the γ-ray conversion is computed from the photon distribution measured by 216 PMTs on the inner face. The first estimation of position is a weighted mean of the amplitudes, on PMTs around the PMT of the maximum signal. Then, a fitting is performed to minimize the function χ^2_{position} which is defined as Eq. (3.4). The function is based on an assumption that the scintillation photons are isotropically emitted from one point.

$$\chi^2_{\text{position}}(u,v,w) = \sum_i^{\text{PMT}} \left(\frac{N_{\text{pho}i} - c \times \Omega_i(u,v,w)}{\sigma_i(N_{\text{pho}i})} \right)^2 \tag{3.4}$$

$$\sigma_i(N_{\text{pho}i}) = \sigma(N_{\text{phe}i}/QE_i) = \sqrt{N_{\text{pho}i}/QE_i} \tag{3.5}$$

In the Eq. (3.5), error of the QE estimation is ignored for simplicity. $\Omega_i(u,v,w)$ is the solid angle of PMT active area seen from the point (u,v,w). The PMTs used for the fitting is within 3.5 times of PMT interval from maximum N_{pho} PMT (about 45 PMTs). If w (depth from inner face) is fitted less than 12 cm, the second fit is performed with a reduced number of PMTs whose 2D (u,v) distance from fitted peak is less than 2 times of PMT interval (about 15 PMTs).

The fitted u and w include biases, because the electro-magnetic shower by γ-ray has a finite size, and the shower spreads larger in the direction of momentum of gamma ray. It results $|u|$ and w fitted larger than the first conversion point. The bias is corrected by a correction function made from Monte Carlo simulation. The reason of the bias is the slant incident angle of γ-ray. That is why v is not biased because γ-ray is always perpendicular to the inner face in $x-y$ plane.

3.1.3 γ timing reconstruction

The time of gamma-ray conversion in liquid xenon (t_{LXe}) is calculated from the estimated hit time by each PMT (t_{hit}).

$$t_{\text{hit}} = t_{\text{PMT}} - t_{\text{delay}} - t_{\text{offset}}, \tag{3.6}$$

where t_{PMT} is timing for each PMT calculated in Sec. 3.1.1. The second term is the time from the photon emission to the detection. The flight time of the photon is calculated with the position of γ-ray conversion and effective speed of light in LXe (≈ 8 cm/ns), which is measured in the calibration using two γ-rays in $\pi^0 \to \gamma\gamma$ (Sec. 4.1.2.3). The shadowing effect of the cylindrical chamber shape, reflection and scattering effect and the time walk effect of PMT are also considered in second term. The third term is constant for each readout channel due to hardware effects such as the cable length.

The combined timing of γ-ray is calculated by the fitting, such that t_{LXe} minimizes the function χ^2_{time} as defined in Eq. (3.7).

$$\chi^2_{\mathrm{time}} = \sum_{i}^{\mathrm{PMT}} \left(\frac{(t_{\mathrm{hit},i} - t_{\mathrm{LXe}})}{\sigma_{t,i}(N_{\mathrm{phe}i})} \right)^2 \tag{3.7}$$

The sum is done over PMTs which detect > 50 photo-electrons, typically about 150 PMTs are involved and typical number of used photo-electrons is ~ 70000 in a signal event. $\sigma_{t,i}$, the time resolution of PMT, is a function of the number of photo-electron (approximately proportional to $1/\sqrt{N_{\mathrm{phe}}}$). The fitting is iterated, rejecting PMTs which contribute to largely increase the χ^2_{time} value. Those PMTs are affected by the γ-ray pile-up.

3.1.4 γ energy reconstruction

The γ-ray energy is reconstructed based on an assumption that the total number of the scintillation photon is proportional to the γ-ray energy, since the γ-ray deposits its all energy in the liquid xenon volume.

The γ-ray energy is determined by integrating the summed waveform with 67 ns window. The summed waveform is made by superposing filtered waveforms from all PMT with the weight of F_i where the timing is shifted considering the time of flight of the scintillation photon. The variable defined as Eq. (3.8) is calculated from the result of the PMT calibration, position and timing reconstruction.

$$F_i = \frac{A_i \cdot W_i(\boldsymbol{r}_\gamma)}{eG_i(t) \cdot QE_i(t)} \cdot \Omega(\boldsymbol{r}_\gamma) \cdot U(\boldsymbol{r}_\gamma) \cdot H(t) \cdot S, \tag{3.8}$$

where A_i is a factor to correct for the position-dependent PMT coverage, $W_i(\boldsymbol{r}_\gamma)$ is a factor to optimize energy resolution. It depends on the reconstructed position and is common for each 6 faces of the detector. The value is determined from the π^0 calibration. $\Omega(\boldsymbol{r}_\gamma)$ shows a solid-angle correction, which is a correction by the solid angle of PMT sensitive region seen from the conversion point, because when γ-ray conversion happens at very close point to the inner PMT, the scintillation photon collection largely depends on the relative location of conversion point and PMT array. This correction is applied for events of $w < 3$ cm. $U(\boldsymbol{r}_\gamma)$ is a correction by non-uniformity factor in order to correct remaining position dependence. It will be explained in Sec. 4.1. $H(t)$ represents the time-dependent transition of light yield. Finally the factor is converted to the absolute energy scale with the factor S that is determined from 55 MeV γ-ray in a π^0 calibration.

3.1.5 Pile-up identification

More than one gamma ray hits xenon detector in 15% of the event at $3 \times 10^7 \mu$/s beam rate. In such an event, the γ-ray observables reconstruction can be failed due to the pile-up γ-ray. There are two methods to identify pile-up, one by spacial distribution on the PMT outputs, and the other utilizes the summed waveform [76]. The former method searches for peaks in inner and outer faces. If the second (the smaller) peak is found, the distribution is fitted except for the pile-up region. Then the PMT output in pile-up region is replaced with the estimation from fitting and calibration data. Finally the energy of main γ-ray is reconstructed. The later method

is based on the summed waveform which is made in Sec. 3.1.4, considering the reconstructed position and timing and pile-up (if found in the former method). In case a pulse is found in the sum waveform, and if the pulse is judged to be pile-up, the pulse is subtracted using a template waveform, and the energy is calculated again with the summed waveform. An example of unfolding of pulses is shown in Fig. 3.4.

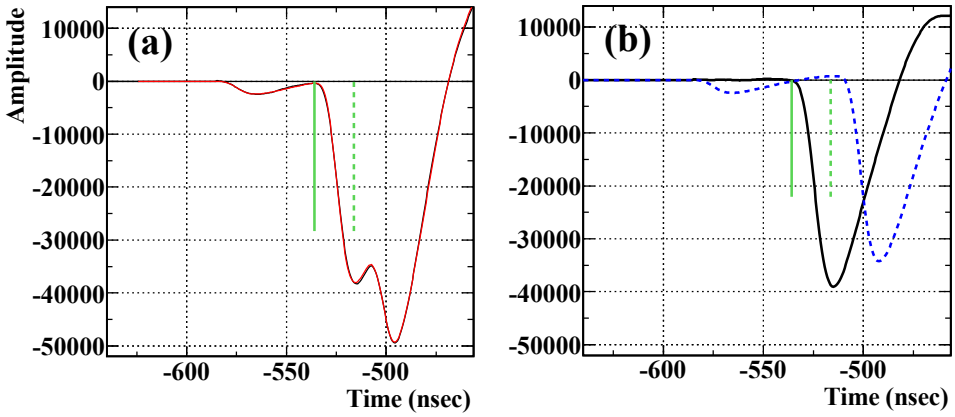

Figure 3.4: (a) Black line shows the summed waveform after high-pass filtering; the fitted waveform is also shown in red line (Two lines are almost overlapping). (b) Waveform after pile-up unfolding is shown with black solid line. The start time of integration is changed from green dashed line to solid line.

3.1.6 Cosmic ray rejection

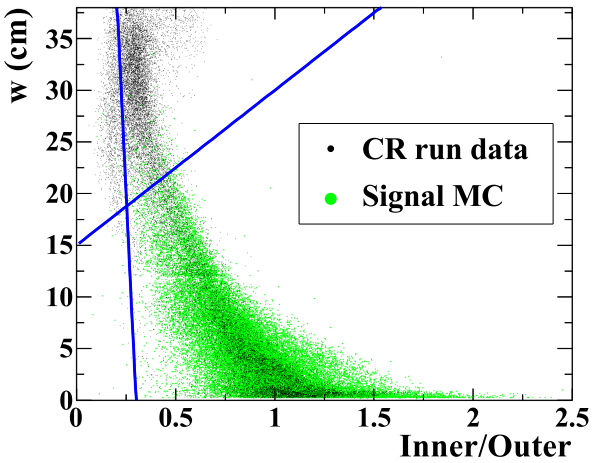

Figure 3.5: The cut criteria are shown with blue lines in (charge ratio)-w plane. The green dots show signal by Monte Carlo. The black dots are the events collected in the dedicated CR runs.

The cosmic ray (CR) is a source of the background. The cosmic ray is efficiently rejected using topological cuts. The cosmic ray events are characterized by the position in the detector, because most of the cosmic rays enter LXe volume from the outer side of the detector. We

defined CR cut focusing on two parameters: the charge ratio collected by inner and outer PMT, and reconstructed depth w. The cosmic ray rejection is demonstrated in Fig. 3.5. The cut criteria are selected to optimise rejection power keeping signal efficiency in 99%. The removable CR event is 56% of all CR, and combined signal efficiency of pile-up identification in Sec. 3.1.5 and CR rejections is 97%.

3.2 Positron track

The charge induced by positron is detected with the anode wires and the cathode pads in the drift chamber. The positron momentum, the position at the target and the emission angle are reconstructed from those hits. The information about the trajectory by DCH and the reconstructed hit position at TIC are sent to the DCH/TIC matching reconstruction described in Sec. 3.3.2.

3.2.1 Hit reconstruction

3.2.1.1 Waveform analysis

We record six waveforms per single drift cell, two sides of an anode wire and two sides of two series of cathode pads as shown in Fig. 3.6. In order to suppress known noise components, a filtering based on FFT[1] is applied on the raw waveform [77]. The pulse larger than threshold (5 mV) from the baseline is considered as a hit. The threshold is set to be 3 times larger than the baseline noise σ_{B}. The charge of the hit is obtained by an charge integration from −24ns to 56ns around the peak excepting region where waveform exceeds $-2\sigma_{\mathrm{B}}$.

3.2.1.2 Hit position

The rough position on z axis is given by the ratio (ϵ_{a}) of the charge on two sides of the anode.

$$\epsilon_{\mathrm{a}} = \frac{Q_{\mathrm{U}} - Q_{\mathrm{D}}}{Q_{\mathrm{U}} + Q_{\mathrm{D}}} \tag{3.9}$$

$$z = \left(\frac{L}{2} + \frac{Z}{\rho}\right) \cdot \epsilon_{\mathrm{a}} \tag{3.10}$$

where L is the length of the anode wire, Z is the input impedance and ρ is the resistivity of the anode wire. The estimation will be improved by the vernier method. As explained in Sec. 2.4.2.1, the cathode foil is divided into two series by zig-zag pattern, and the fraction of detected charges on the cathode depends on the z position. The charge-fractions of two channels (ϵ_1 and ϵ_2) makes pattern as Fig. 3.7. The final z estimator with the vernier information is defined as,

$$z = l \cdot \left(\frac{\alpha}{2\pi} + i\right), \tag{3.11}$$

where l is the period of the pattern (5 cm), $\alpha = \tan^{-1}(\epsilon_2/\epsilon_1)$ is the azimuthal angle and i shows in which period the hit is belonging (count from DS side). There was a mistake in treatment of the case with faulty pad readout, previously. Therefore, all data are processed again with corrected algorithm.

[1] Fast Fourier Transform

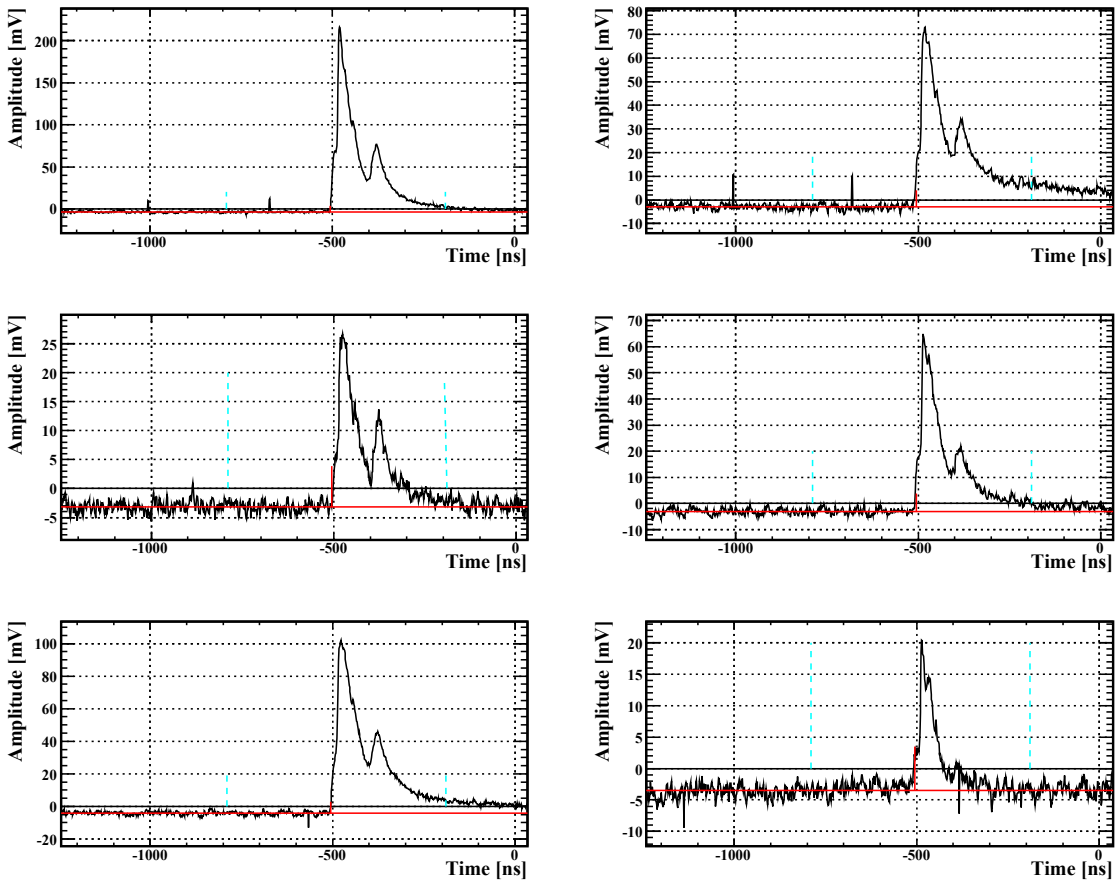

Figure 3.6: Example waveform of DCH. Top low from anode wire, and central and bottom lows from cathode pads. Recognized hit timing is shown in red vertical line [77].

The drift distance, which gives the detailed information of the positron position in a drift cell, is calculated from the time of the detected pulse and the estimated time of the track where the information of the timing counter is also considered. Since the drift time from the initial ionization to the detection by wire depends on the strength of the magnetic field and the incident angle, the drift distance is calculated with a function which is generated from a simulation using GARFIELD. The drift time is shown in a function of the incident angle and distance in Fig. 3.8.

3.2.2 Clustering and track finding

The hits in one DCH module are combined into a cluster, to remove many accidental hits which are not related to the real positron track. If hits in a chamber lie in near cells and z position the hits are associated to one hit cluster, especially hits in the neighbouring period in the vernier pattern are taken into account for the case of misreconstruction to the next period.

The next step is to find the seed of the positron track. Starting from the largest r cluster, neighboring clusters are connected to make a candidate of the positron track. In searching for clusters on the trajectory, an adiabatic invariant p_{T}^2/B_z is used (p_{T} is the positron transverse momentum), because the axial component of magnetic field slowly varies The left/right ambiguity can be solved during track seed finding in most of cases. Then, the track seed (connected clusters) is fitted by circle in the $x-y$ plane. With the more precise x, y hit position by fitting,

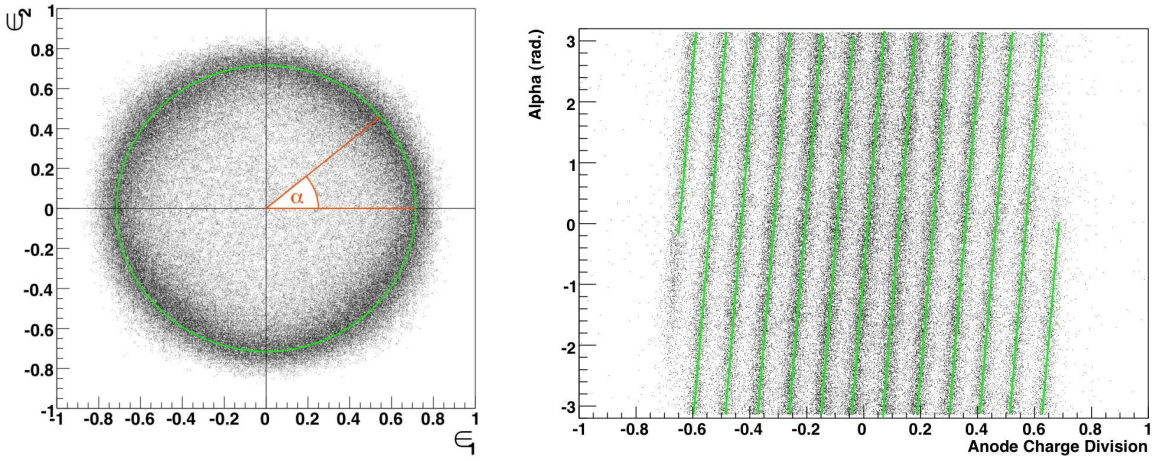

(a) The circle pattern, a turn correspond one period of the pattern.

(b) α angle vs ϵ_a. vernier gives better z resolution. A period is the length of pattern, 5 cm.

Figure 3.7: z hit reconstruction by vernier pattern.

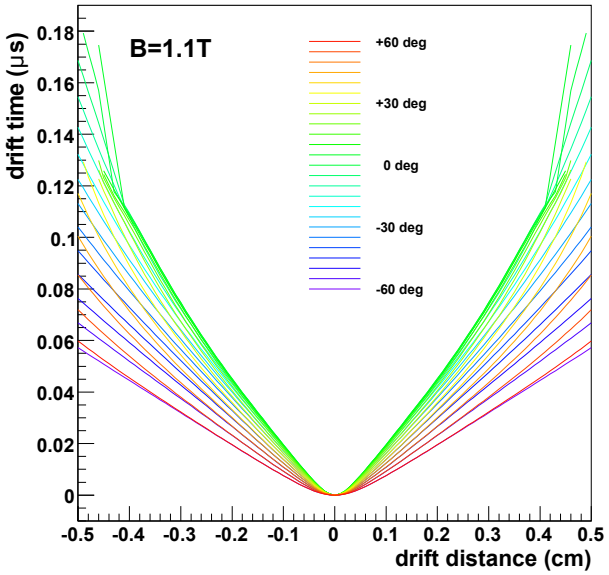

Figure 3.8: Drift time simulation with GARFIELD. The result with $B = 1.1$ T is shown as a function of the distance and angle.

the track timing can be estimated by using track time-distance dependence in Fig. 3.8, a solution for left/right ambiguity is also improved.

3.2.3 Track fitting

We adopted the technique of Kalman filter [78] [79] for the track reconstruction. The Kalman filter is an algorithm to estimate the status from the given information of state which is discrete in time, and it has wide application in technological and engineering field. Since it can handle the existence of an unexpected disturbance, and can include it as the error of the estimation, the method of Kalman filter is suitable for tracking of positron that is affected by multiple

scatterings. The GEANE software [80] is also used.

The state vector of the positron is successively estimated from hit to hit. Finally the track is propagated to the muon stopping target to retain the initial state vector of the positron on target. The hits used in the track fit are updated by the fitting result in the track reconstruction: hits not included in the candidate are added if appropriate and hits are removed if they are inconsistent.

The positron track fitting method was revised in our previous physics analysis. Details of the revised method can be found in [81] and [77].

3.2.4 Per-event error

The method of Kalman algorithm enables us to calculate the error propagation in the track fitting. It also provides information of the error matrix which includes the correlation between variables. Since the calculation is done event-by-event, it is called "per-error". It will be used to compose event-by-event PDF in the physics analysis.

The errors of following variables are represented with the per-error of Eq. (3.12),

- E_{e} : initial energy of positron,
- ϕ_{e} : ϕ emission angle on target,
- θ_{e} : θ emission angle on target,
- y_{e} : y position on target plane,
- z_{e} : z position on target plane,

$$\boldsymbol{\sigma}' = (\sigma'_{E_{\mathrm{e}}}, \sigma'_{\phi_{\mathrm{e}}}, \sigma'_{\theta_{\mathrm{e}}}, \sigma'_{y_{\mathrm{e}}}, \sigma'_{z_{\mathrm{e}}}) \tag{3.12}$$

where σ' is per-error, and σ'_x represents the uncertainty of the parameter "x".

3.2.5 Missing turn recovery

Since the MEG drift chamber covers only bottom-half region in ϕ, a positron trajectory is separated when the positron turns more than one time. The separated turns are connected to each other in the normal case of the track fitting algorithm. If the connection fails, there is fear about reconstructing those tracks to be different positrons. It is dangerous especially when the first turn is missed, because the decay vertex is reconstructed at a wrong position, and then the timing is also wrongly reconstructed. In the current analysis, an algorithm to identify and recover the missing turn is newly implemented.

The algorithm works as follows. For all found tracks, hits are searched for in the expected z range and modules. When potential missing turn hits are found, the vertex state vector is propagated toward each potential hit, and the hit is discarded if the position is far from propagation. If the remaining number of the hits is more than threshold, the track fit algorithm as in Sec. 3.2.3 is applied for the track candidate. The track fitting is further propagated to the stopping target, and if the crossing point is found in the target, the recovered vertex and momentum of the positron is calculated. In Fig. 3.9, a recovered missing track is illustrated.

profit of missing turn recovery The improvement in overall positron detection efficiency by the missing turn recovery is defined as, the ratio of total number of the recovered Michel positron to the total number of reconstructed Michel positrons. The improvement in the efficiency is

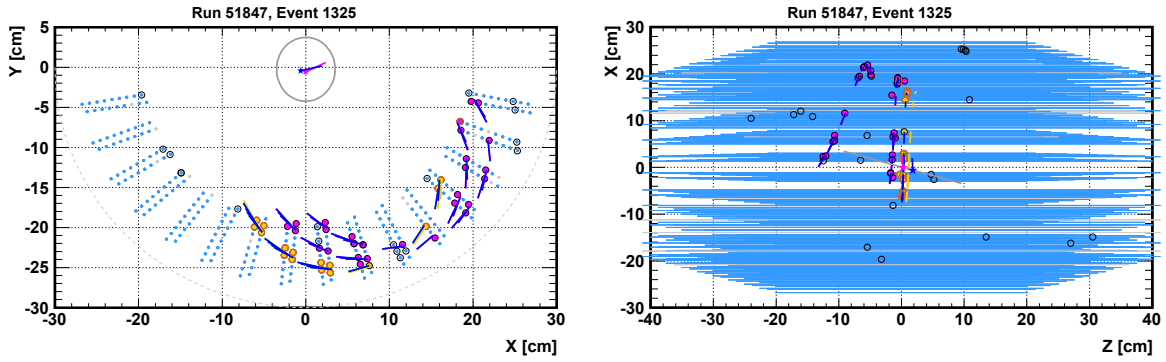

(a) (b)

Figure 3.9: An example of the recovered missing first turn. Originally reconstructed track hits are shown in magenta, the brown hits are identified to be a part of track. The original and recovered vertex are shown with magenta and blue star.

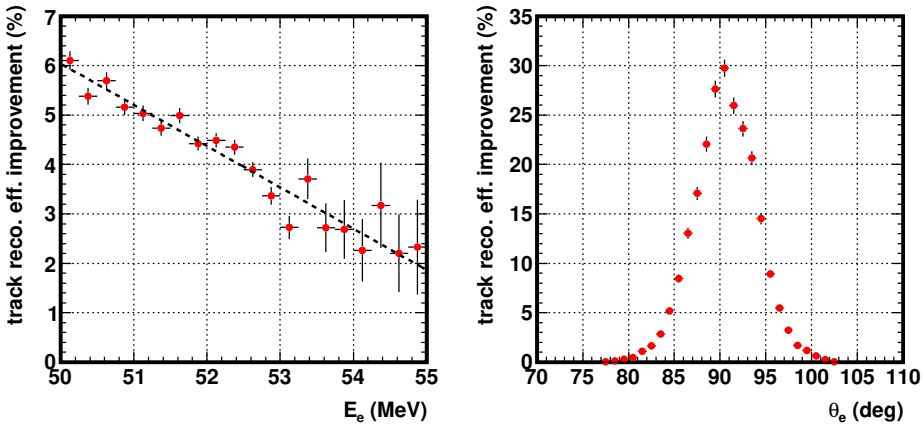

Figure 3.10: Improvement in overall positron detection efficiency due to missing turn recovery, as a function of E_e and θ_e.

evaluated using data and shown in Fig. 3.10. The averaged improvement is $\approx$ 4%. The improvement decreases as increasing the E_e, it is due to more efficient positron reconstruction at high E_e. The efficiency improvement is maximal around $\theta_e = 90°$, because the positron which emitted around the angle are likely to make multiple turns in the drift chamber.

3.3 Positron timing

The timing of the positron is measured by 15×2 TIC ϕ counters (Sec. 2.4.3). The timing measured by TIC (t_{TIC}) is combined with the track information, then the timing of positron emission on target (t_e) will be obtained.

3.3.1 Timing calculation by TICP

The PMT signals are divided into two with a ratio of 8:2. The larger fraction is converted to digital pulse (NIM signal) by DTD and is recorded by DRS. The leading edge of the NIM pulse

is fitted with a template waveform to get the timing. The smaller fraction is directly used in DRS and trigger. The time walk effect in the NIM pulse is corrected by using the direct DRS waveform with a formula.

$$w(x) = A + B\sqrt{x} + C\log(x), \tag{3.13}$$

where x is the ratio of the DTD low level threshold to the pulse height. The parameters A, B and C are determined for each PMT, by fitting a template waveform made from calibration data. The optimal DTD threshold is determined to get the best timing resolution. Two PMTs (IN: near target side, OUT: far target side) read one scintillator bars, so the timing and z position can be calculated from the two timing,

$$t_{\mathrm{TIC}} = \frac{t_{\mathrm{IN}} + t_{\mathrm{OUT}}}{2} - \frac{b_{\mathrm{IN}} + b_{\mathrm{OUT}}}{2} - \frac{w_{\mathrm{IN}} + w_{\mathrm{OUT}}}{2} - \frac{L}{2v}, \tag{3.14}$$

$$z_{\mathrm{TIC}} = \frac{v}{2}\left\{(t_{\mathrm{IN}} - t_{\mathrm{OUT}}) - (b_{\mathrm{IN}} - b_{\mathrm{OUT}}) - (w_{\mathrm{IN}} - w_{\mathrm{OUT}})\right\}, \tag{3.15}$$

where L is the length of scintillator bar, v is the effective speed of light in the scintillator, and $b_{\mathrm{IN,OUT}}$ are offsets peculiar to channel and $w_{\mathrm{IN,OUT}}$ are time walks in Eq. (3.13). When there are more than two bars hit by one positron, hits are combined to TIC cluster. The fastest hit represents the cluster.

3.3.2 DCH-TIC interconnection

In order to get the time of the positron emission, the time-of-flight (t_{TOF}) is needed to be considered. We compute it from the length of track between the decay vertex and the hit point at TIC. Due to the drift chamber support structure between the DCH sensitive region and TIC, the positron can be scattered during flight. The effect of the scattering is evaluated by matching quality of DCH and TIC. The fitted track from the drift chamber is propagated to the surface of timing counter. The event is classified by the matching quality of estimation from track and TIC hit.

- (MQ 0) The track is propagated to the hit bar, and $\Delta z < 12$ cm.
- (MQ 1) The track is propagated to the extended region of the bar, and $\Delta z < 12$ cm.
- (MQ 2) The track do not cross the extended region, but $\Delta r < 5$ cm.
- Otherwise, matching is judged to be failed.

Δz is distance between z_{TIC} and z of propagated point and Δr is the distance in r coordinate from the TIC surface to the closest point of track to TIC bar. Then, the Kalman filter algorithm is applied to back-propagate to target, in order to get the best estimation of the emission timing of positron on target (t_{e}).

3.4 Combination of γ and positron

In this section, the variable of relative angle and timing between γ-ray and positron are defined. The reconstructed position of γ-ray and positron vertex at the target are written as ($\boldsymbol{r}_\gamma$) and ($\boldsymbol{r}_{\mathrm{e}}$), respectively. The normal vector of the γ-ray momentum ($\boldsymbol{n}_\gamma$) and positron momentum on target ($\boldsymbol{n}_\gamma$) are also used.

The emission angle of γ-ray is defined as the vector from the reconstructed vertex to the reconstructed position of the γ-ray, because LXe detector cannot reconstruct the direction of γ-ray.

$$\boldsymbol{n}_\gamma = \frac{\boldsymbol{r}_\gamma - \boldsymbol{r}_\mathrm{e}}{|\boldsymbol{r}_\gamma - \boldsymbol{r}_\mathrm{e}|}, \tag{3.16}$$

The relative angle of γ-ray and positron ($\Theta_{\mathrm{e}\gamma}$) is given by

$$\Theta_{\mathrm{e}\gamma} = \cos^{-1}(\boldsymbol{n}_\mathrm{e} \cdot \boldsymbol{n}_\gamma). \tag{3.17}$$

The relative angle is separated to two directions, $\theta_{\mathrm{e}\gamma}$ and $\phi_{\mathrm{e}\gamma}$.

$$\theta_{\mathrm{e}\gamma} = (\pi - \theta_\mathrm{e}) - \theta_\gamma \tag{3.18}$$

$$\phi_{\mathrm{e}\gamma} = (\pi + \phi_\mathrm{e}) - \phi_\gamma \tag{3.19}$$

The relative time of γ-ray and positron is given by the difference between the time of γ-ray and positron. The timing of γ-ray is defined by the timing of γ-ray emission from the vertex. The time is calculated by using time of flight of γ-ray from the target to where it is detected.

$$t_{\mathrm{e}\gamma} = t_\gamma - t_e = (t_\mathrm{LXe} - t_\mathrm{tof}) - t_e \tag{3.20}$$

$$t_\mathrm{tof} = \frac{|\boldsymbol{r}_\gamma - \boldsymbol{r}_\mathrm{e}|}{c} \tag{3.21}$$

3.5 Reconstruction of AIF

Annihilation In Flight (AIF) of positron is one of the sources of γ-ray background in LXe detector. The γ-ray background mainly consists of RMD and AIF, and in the signal energy region the AIF is dominant. Figure 3.11 shows background spectrum where the horizontal axis is shown in $y = 2E_\gamma/m_\mu$. If we can tag the γ-rays which come from AIF, the $\mu \to \mathrm{e}\gamma$ search sensitivity can be improved by removing the tagged accidental background. The AIF which occurred inside of the DCH can be tagged, because the positron leaves a track before the annihilation.

We newly developed a method to find AIF that happens in the drift chamber. The method is done in two steps. The first step is to look for a positron track which disappears in the drift chamber. It is called an AIF track. The second step is to compare the AIF track and the γ-ray detected by the LXe detector.

3.5.1 Candidate finding

In order to find the AIF candidate track, we use the hit and cluster data independent of normal positron reconstruction explained in Sec. 3.2.2. The method starts from connecting positron clusters. The series of the cluster is called AIF seed. The clusters which can be considered as a part of a track are added to the seed. Following criteria are required for the seed: (a) contain no hit in the last plane of DCH and (b) the last hit must not be the inner most cell. Otherwise a normal track can be recognised as an AIF seed.

A circle fit is applied for all AIF seed. Along the fitted circle, the number of the empty DCH plane is counted, and AIF candidate must have more than 2 empty planes after the last cluster. The (x, y) position of the AIF is given by the intersection point of the fitted circle and the DCH

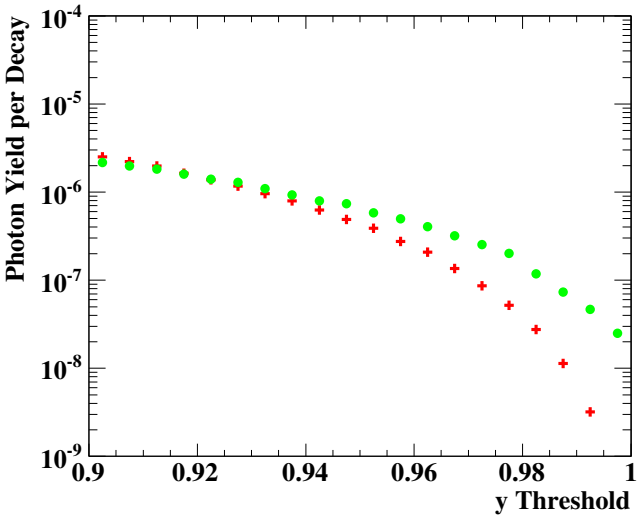

Figure 3.11: Integrated E_γ spectra of RMD (red) and AIF (green) by MC for the MEG detector, γ-ray whose energy is more than y is integrated.

cathode plane, DCH support or COBRA wall which appears just after the last cluster. The z coordinate is calculated by the extrapolation of xz-vector of last two clusters. The direction of AIF is also calculated from the tangent of the fit circle and the xz-vector. Time of AIF is also reconstructed from the timing information of DCH hit. If the last cluster includes hit in plane-A (down-stream side), then the candidate is categorised into type-A, else the candidate is categorised into type-B.

An example of the AIF candidate is shown in Fig. 3.12.

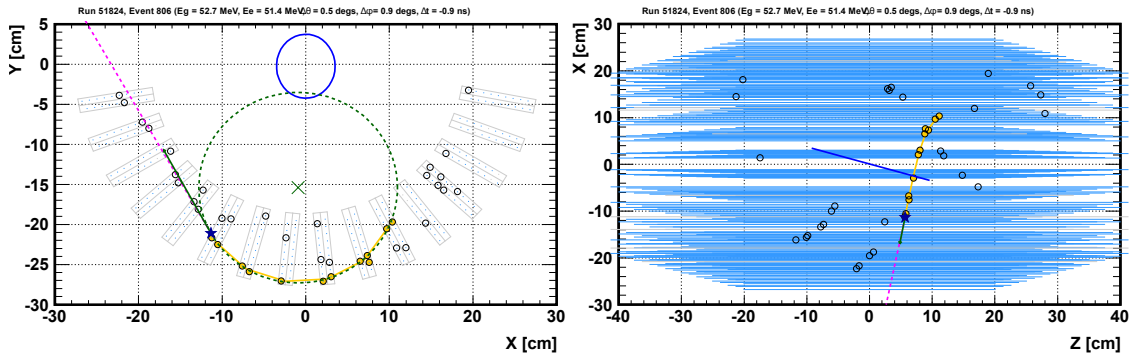

(a) (b)

Figure 3.12: An example of the AIF candidate in 2009 data. The AIF candidate is plotted in yellow circle, the result of circle fit is shown in green dashed line, the AIF position is blue star and the direction is drawn in green arrow. The vector to observed γ-ray is shown in dashed magenta line.

3.5.2 Matching DCH and LXe

According to the AIF candidate information and the γ-ray, AIF observables are calculated.

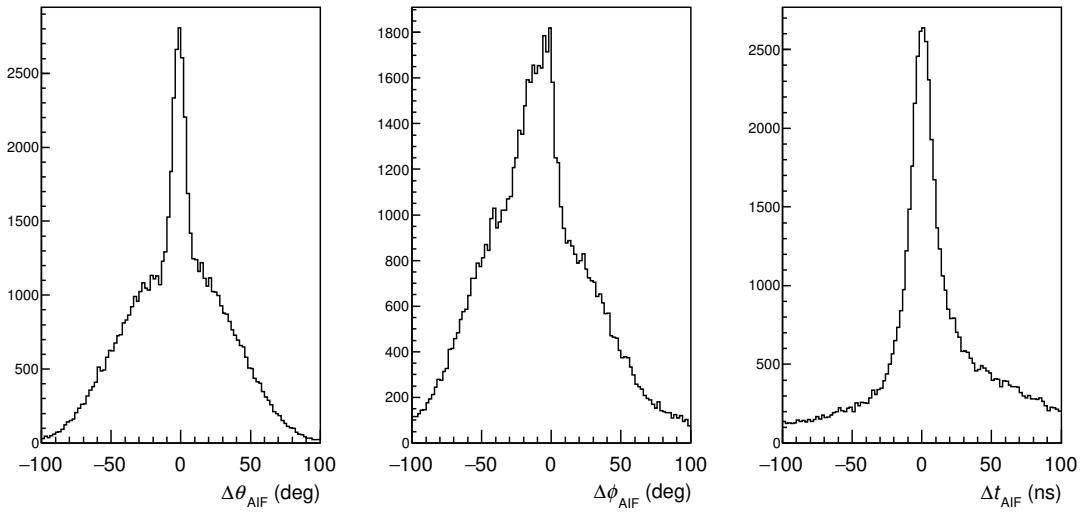

Figure 3.13: AIF observables $\Delta\theta_{\mathrm{AIF}}$ (left), $\Delta\phi_{\mathrm{AIF}}$ (center) and Δt_{AIF} (right) found in calibration data, in year 2009.

$$\Delta\theta_{\mathrm{AIF}} = \theta_{\mathrm{AIF}} - \theta_{\gamma-\mathrm{AIF}}, \tag{3.22}$$

$$\Delta\phi_{\mathrm{AIF}} = \phi_{\mathrm{AIF}} - \phi_{\gamma-\mathrm{AIF}}, \tag{3.23}$$

$$\Delta t_{\mathrm{AIF}} = t_{\gamma} - t_{\mathrm{AIF}}, \tag{3.24}$$

where θ_{AIF} and ϕ_{AIF} are θ and ϕ component of the AIF vector and t_{AIF} is the reconstructed timing of the AIF, and $\theta_{\gamma-\mathrm{AIF}}$ and $\phi_{\gamma-\mathrm{AIF}}$ are θ and ϕ component of the vector from AIF point to reconstructed point of γ-ray.

When there are multiple AIF candidates in an event, those candidates are selected by following variable,

$$\chi^2_{\mathrm{AIF}} = \frac{\Delta\theta^2_{\mathrm{AIF}}}{w^2_{\theta}} + \frac{(\Delta\phi_{\mathrm{AIF}} - \phi_{\mathrm{offset}})^2}{w^2_{\phi}} + \frac{\Delta t^2_{\mathrm{AIF}}}{w^2_{t}}, \tag{3.25}$$

where $w_{\theta} = 4.5^{\circ}(3.5^{\circ})$, $w_{\phi} = 10^{\circ}(4.5^{\circ})$, $\phi_{\mathrm{offset}} = -10^{\circ}(0^{\circ})$ and $w^2_t = 10$ ns for type-A (B) candidate. The candidate of the least χ^2_{AIF} is selected, as it is most likely to be a true pair with observed γ-ray.

Figure 3.13 shows the result of the AIF reconstruction in $\Delta\theta_{\mathrm{AIF}}$ and $\Delta\phi_{\mathrm{AIF}}$, the peak around 0 comes from events truly correlated in the track and γ-ray. The peak around -10° in $\Delta\phi_{\mathrm{AIF}}$ is due to events where the positron annihilates at the first plane of the next module after leaving the last hit in plane-A.

Chapter 4

Calibration

The calibration is an indispensable operation in physics experiments. The calibrations are performed to measure the performance of the detector, to monitor the detector status or to check our understanding about the detectors. In this chapter, the calibration methods will be described for each. The main calibration sources are summarized in Table 4.2.

4.1 LXe detector

4.1.1 PMT calibration

4.1.1.1 Gain calibration

The PMT gain calibration is mandatory in order to convert the charge into the number of photo-electron. For this calibration, blue-light LEDs are mounted on the up-stream and down-stream sides of the inside wall of the detector. The positions of the LEDs are shown in Fig. 4.1. The data of all PMTs are taken with a trigger which is synchronized to a LED pulser.

gain calculation We calculate the gain under an assumption that the number of photo-electrons observed with each PMT follows the Poisson distribution.

$$\sigma^2_{N_{\mathrm{phe}}} = \mu_{N_{\mathrm{phe}}} + \sigma_0^2 \tag{4.1}$$

$\sigma_{N_{\mathrm{phe}}}$ and $\mu_{N_{\mathrm{phe}}}$ are the standard deviation and mean of the number of observed photo-electrons, respectively, and σ_0 is additional fluctuation such as noise from electronics. Using the PMT gain G, we can transform Eq. (4.1) as follows,

$$\sigma_Q^2 = G \times \left(\mu_Q + G\sigma_0^2\right) \tag{4.2}$$

where $Q = G \times N_{\mathrm{phe}}$ is charge observed by the PMT, σ_Q and μ_Q are the standard deviation and mean of the charge, respectively.

In one set of gain calibration runs, the LEDs are driven with different 9 intensities. For each intensity, σ_Q and μ_Q is calculated by fitting the Q distribution with a Gaussian function. The gain is obtained from a linear fit on $\sigma_Q^2 - \mu_Q$ plot. Figure 4.2 is an example of the result.

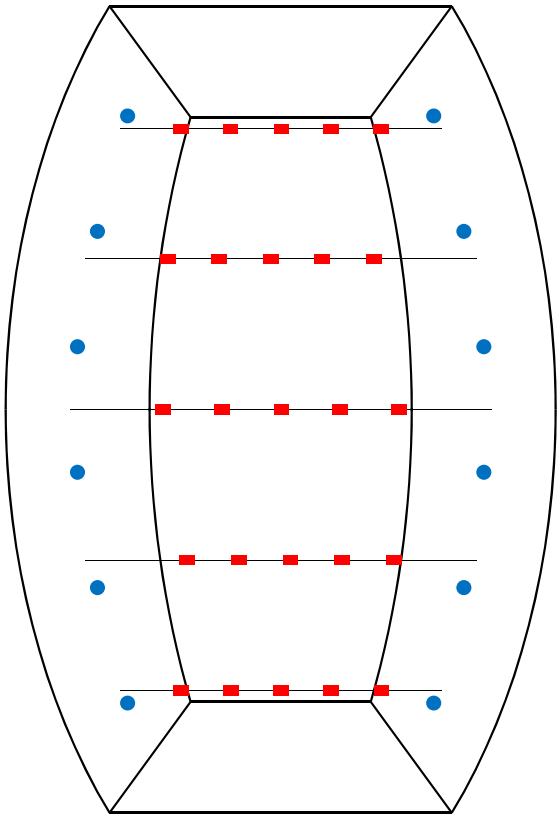

(a) Location of the calibration sources

(b) LED for the gain calibration. Three LEDs of different intensities are bundled.

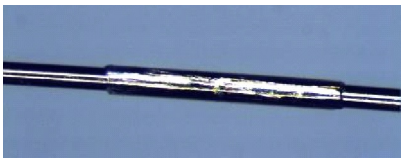

(c) α-source rolled on a wire.

Figure 4.1: Calibration sources inside of the LXe detector. (a) is view from outside of the detector. A set of LEDs is shown with blue circle, and an ^{241}Am alpha source is shown with a red rectangle.

gain shift by beam It is known that the PMT gain shifts by the light irradiation. It results in the dependence on the beam condition. When we take the calibration data, beam blocker is closed, and it is opened before the physics data taking. The change of the gain is corrected by the LED light events during the operation of the beam blocker. The gain shift is about 2-3% in average, but depends on individual PMT. Figure 4.3 shows gain shift of PMT which is the most sensitive to the beam condition.

gain adjustment The gain is normally set to 1.8×10^6 for all the PMTs by adjusting HV to match the dynamic range of the electronics. The gain G is proportional to V^{nk}, where V is voltage bias, n is number of stages of the dynodes and k is a factor determined by the PMT design. For LXe PMT, the gain voltage dependence is more complex due to Zener diodes to regulate voltage between the last dynodes, but is approximately proportional to V^{10} around the nominal operation voltage.

The PMT gain tends to decrease during run, and the speed is individually different. So the PMTs are needed to be adjusted periodically. We adjusted HV before the physics run in each year. Some PMTs need more frequent adjustment for the fast gain decrease. Averaged PMT gain in year 2012 is shown as a function of date in Fig. 4.4. The leftmost marker shows the result just after the gain adjustment. The gain decrease is an issue for the trigger, because the energy

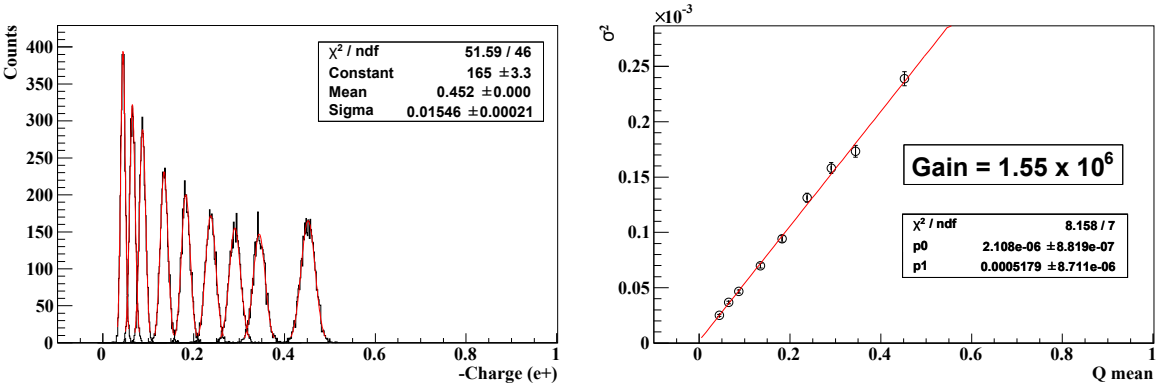

(a) Charge distributions with different LED intensities.

(b) 2D plot of σ_Q^2 vs μ_Q. The gain is calculated from fitted slope.

Figure 4.2: PMT gain calibration with LED.

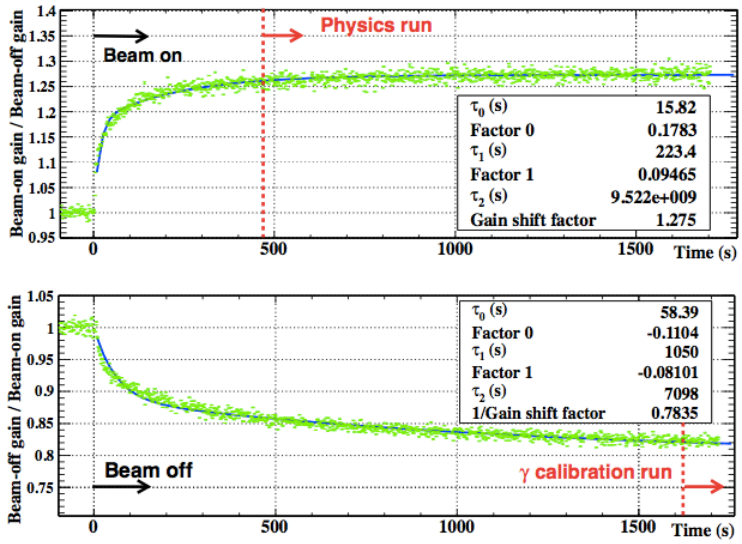

Figure 4.3: PMT gain shift when the beam blocker is opened (top) and closed (bottom) [82].

threshold for the LXe detector in the trigger condition is changed if the PMT gain decreases. The trigger parameter is adjusted by the PMT gain calibration, otherwise trigger efficiency would be decreased.

4.1.1.2 QE calibration

The calibration of the quantum efficiency (QE) of a PMT is performed with α-sources which are attached on gold plated tungsten wires with 100 μm diameter [83]. Five sources are attached on each of five wires, therefore 25 sources in total are mounted. The wires are stretched inside the xenon volume along z-axis. The locations of the α-sources are shown in Fig. 4.1. The nuclide of the source is ^{241}Am. It emits α of 5.485 MeV (84.5%) and 5.443 MeV (13.0%), and its half-life is 432.2 years. The strength of the source is $\sim$ 1 kBq each.

We calculate the PMT QE by comparing observation and MC simulation. The position of the source, number of emitted photons, and photon propagation (scattering, absorption and

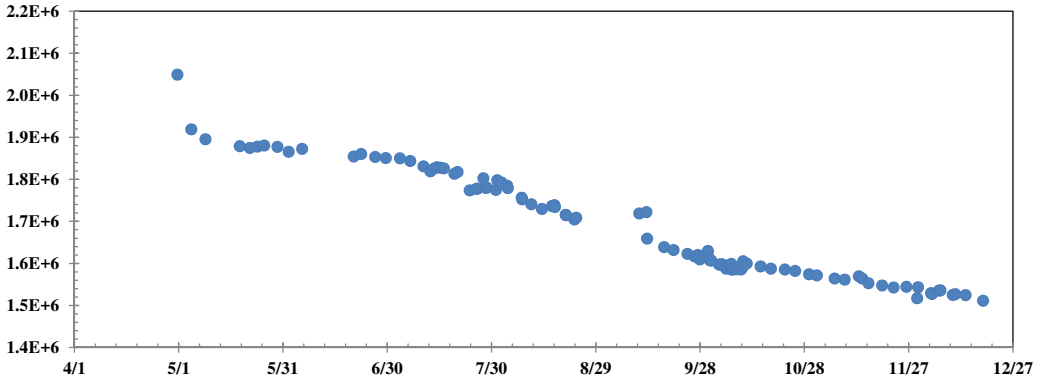

Figure 4.4: Average PMT gain obtained from LED calibration. An interval from August to September is a period for π^0 calibration. A small gain recovery is seen after the interval which is due to non operational period of the detector modification for the calibration.

reflection) in the liquid xenon are simulated in the MC, under a constant known QE. The number of photo-electrons in data and MC are compared for each α source. The QE of the PMT is obtained by combining the ratio, $N_{\mathrm{phe}}^{\mathrm{data}}/N_{\mathrm{phe}}^{\mathrm{MC}}$. Figure 4.5 illustrates a result of QE calibration.

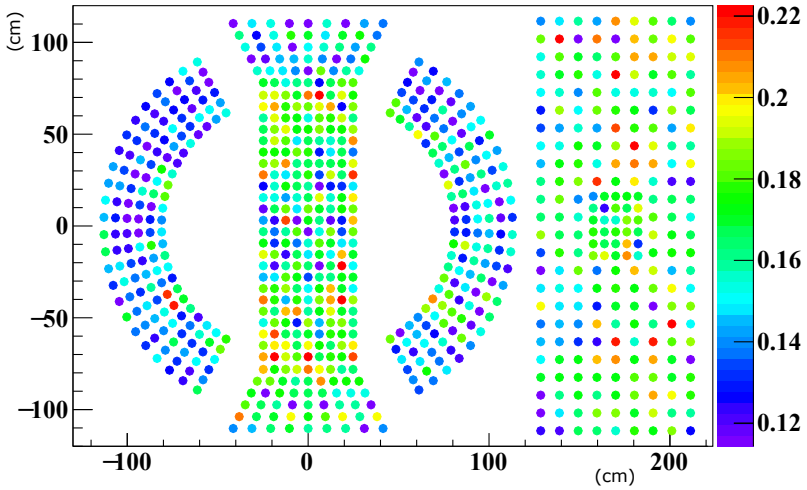

Figure 4.5: QE of PMTs in LXe detector. The plot shows an averaged result of some calibration runs.

4.1.2 Gamma calibration

4.1.2.1 CW accelerator calibration

We perform calibrations with Cockcroft-Walton (CW) proton accelerator[1] to monitor the light yield of the LXe, and the data is also used to estimate the position dependence of the γ-ray response.

reaction A target made of lithium tetra-borate ($Li_2B_4O_7$) is adopted in this calibration. This allows us to utilize both Li and B reactions simultaneously. The nuclear reaction ${}^{7}_{3}\mathrm{Li}(p,\gamma){}^{8}_{4}\mathrm{Be}$

[1] High Voltage Engineering Europe

produces 14.8 MeV and 17.6 MeV γ-ray. The reaction ${}^{11}_{5}\mathrm{B}(p,\gamma){}^{12}_{6}\mathrm{C}$ produces some energies of gamma, 4.4 MeV γ-ray from deexcitation of ${}^{12}_{6}\mathrm{C}^{*}$ is used for calibration for the sharp peak. Figure 4.6 is an observed spectrum with the Li reaction.

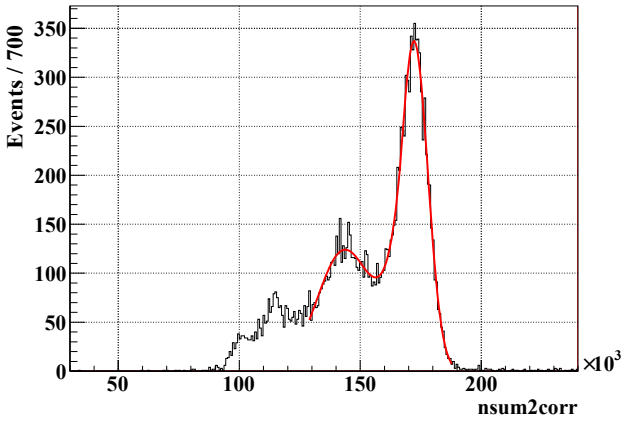

Figure 4.6: An example of the spectrum with ${}^{7}_{3}\mathrm{Li}(p,\gamma){}^{8}_{4}\mathrm{Be}$ reaction. The right most peak is the peak from 17.6 MeV γ-ray.

setup The CW is installed at the down-stream side of the MEG detectors as illustrated in Fig. 4.7. Before the CW calibration, the normal target for muon is remotely removed by a pneumatic drive system with compressed He gas, and a movable beam pipe is inserted to the COBRA volume. The airtightness is kept by extendable bellows system with a stroke of $\sim$ 2 m. It takes as short about 20 minutes to replace the targets.

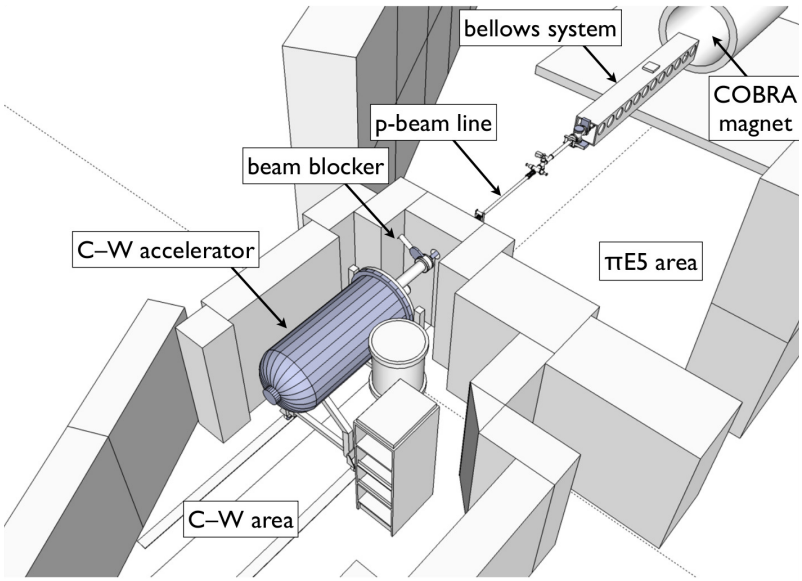

Figure 4.7: Location of the CW accelerator in the experimental area. The accelerator and beam pipe are settled at the opposite side of muon beam line.

4.1.2.2 Neutron generator

γ-ray from the neutron capture reaction of nickel, $^{58}_{28}\mathrm{Ni}(n,\gamma)^{59}_{28}\mathrm{Ni}$ is used for calibration. A neutron generator[2] and nickel plates are set as shown in Fig. 4.8, and the setup is put on the opposite side of the LXe detector against the COBRA magnet. (γ-ray transits COBRA from the neutron generator to the LXe detector.) An advantage of this calibration is the availability in beam time. By using a trigger which is synchronized with neutron generator, the data with the neutron generator can be taken even during the normal data taking with the beam. This enables a direct comparison between beam on/off.

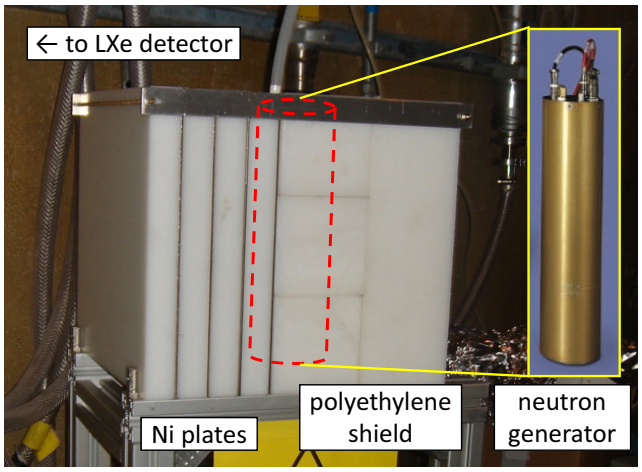

Figure 4.8: Setup of the neutron generator. The generator and target are surrounded by polyethylene shield.

4.1.2.3 π^0 calibration

π^0 calibration is one of the most important calibrations of the LXe detector, because it provides γ-ray near the signal energy. We determine the absolute scale, i.e. the factor to convert the number of the detected photo-electrons to the energy of γ-ray according to this calibration. It requires a special target and another γ-ray detector, so it was operated once or twice per year.

principle We use π^- beam in this calibration, and the target is proton. The Charge EXchenge reaction (CEX) occurs and then π^0 immediately decays to two γ-rays, namely

$$\pi^- + p \to \pi^0 + n \to \gamma + \gamma + n. \tag{4.3}$$

The momentum of the π^- beam is optimized to be 70.5 MeV/c . π^0 particle has a momentum $\sim$ 28 MeV/c in the laboratory frame, and the γ-rays are emitted back-to-back in π^0's rest frame. In the laboratory frame, γ-rays are boosted by π^0 momentum.

$$E_\gamma = \frac{m_{\pi^0}}{2}\gamma(1 \pm \beta\cos\theta_{\mathrm{CM}}), \tag{4.4}$$

where β is the velocity, γ is the Lorentz factor and θ_{CM} is the angle between direction of π^0 momentum and γ-ray in the rest frame.

[2] ThermoFisher

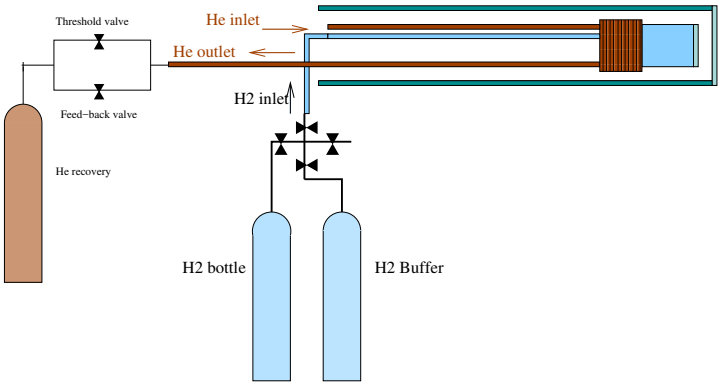

Figure 4.9: Scheme to hold liquid hydrogen in LH2 target for π^0 calibration.

The energy spectrum of the γ-ray shows flat distribution between 54.9 and 82.9 MeV. The energies of two γ-rays have correlation with the opening angle between two directions of gamma. If gammas with opening angle $> 175°$ ($> 170°$) are selected, their energies are sharply defined with a width narrower than $\sigma/E_\gamma < 0.2\%$ (1.0%). Besides the CEX reaction, there are reactions where the final particle is one γ-ray and neutron (radiative capture: Eq. (4.5)) and neutral pion decay into γ-ray and electron-positron pair (Dalitz decay: Eq. (4.6)).

$$\pi^- + p \to \gamma + n \tag{4.5}$$

$$\pi^- + p \to \pi^0 + n \to \gamma + e^+ + e^- + n \tag{4.6}$$

liquid hydrogen target In the π^0 calibration, the normal target is removed together with the CW beam line. A liquid hydrogen target is installed instead. The target has a cylindrical shape and the volume (where liquid hydrogen is liquefied) is $\sim$ 150 cm^3. It has a vacuum window (warm side) and LH_2 window (cold side) as the beam entrance. Both windows are made of 135 μm thickness Mylar. The cooling is done by liquid helium from a Dewar tank. During the operation, the temperature and pressure are controlled at 20 K and 0.12 MPa (Fig. 4.9).

tagging detector The LXe detector covers only $\sim 120°$ in ϕ axis, therefore another detector is mandatory to detect γ-ray at 180° opposite side.

We use a smaller, but movable γ-ray detector and move it to scan the LXe detector. From year 2008 to 2010, a detector of 3×3 arrayed NaI(Tl) crystals ($62.5 \times 62.5 \times 305$ mm^3) read out with APDs was used [84], and it was replaced with a one with 4×4 arrayed Bismuth Germanium Oxide (BGO)[3] crystals ($46.0 \times 46.0 \times 200$ mm^3) read out with PMTs from year 2011 to 2013. (See Fig. 4.10(a).) In order to avoid event where a large fraction of the shower escapes from the crystals, the trigger is set to require a hit only at the central NaI crystal. It was widened to central 2×2 crystals of the BGO detector. The trigger efficiency is improved by this modification, and resulted in the more efficient calibration. The energy and position resolutions are also improved. The detail about the BGO detector is described in Appendix. A.

The detector is mounted on a detector mover (Fig. 4.10(b)). It can be controlled remotely without interrupting beam. The mover has motors to move the detector in ϕ (vertical), z

[3] $Bi_4Ge_3O_{12}$

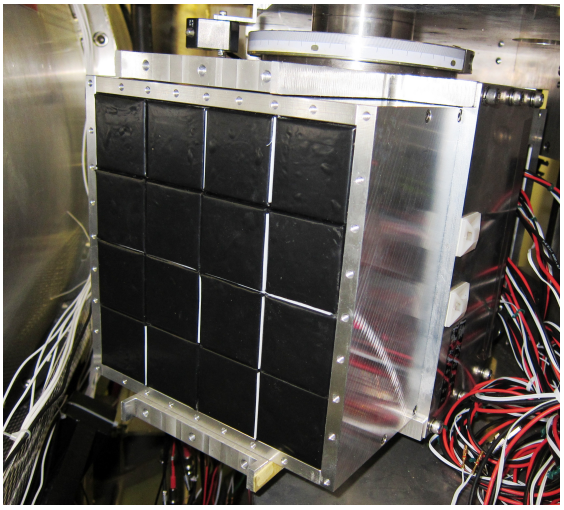

(a) Tagging detector with BGO crystal is installed in detector mover. A cover in front of the crystals is not attached.

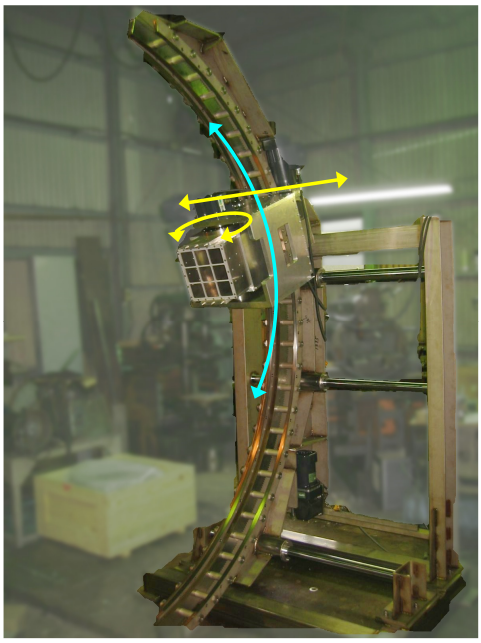

(b) Detector mover, NaI detector is mounted on it. The degree of freedom is shown with arrows.

Figure 4.10: Apparatus for π^0 calibration

(horizontal) direction, and to rotate detector in order to face the detector perpendicular to LH_2 target.

The energy reconstruction is done by summing light yield in each crystal, and γ-ray position in NaI detector was reconstructed to the center of the detector, while position in BGO detector was reconstructed by weighted mean of the light yield.

In addition to NaI (BGO), there is small counter to detect the timing of γ-ray. It consists of two plastic scintillator plate and a 5 mm thick lead plate as a photon converter, the scintillators are read out by fine mesh PMTs on top and bottom side via light-guides.

operation The acceptance of the LXe detector is divided into 3×8 patches as shown in Fig. 4.11(a), and each has an area corresponding to 3×3 array of inner PMTs. We scan LXe detector by moving the tagging detector at the opposite side of the patch with respect to LH2 target. For the π^0 calibration, a dedicated trigger which requires a coincidence of (a) LXe detector, (b) pre-shower counter hit and (c) energy deposit in tagging detector. Figure 4.11(b) shows measured energy with the LXe and BGO detectors in the calibration.

analysis The energy resolution is evaluated with the CEX γ-ray, and the face factor and non-uniformity of scale ($W_i(\boldsymbol{r}_\gamma)$ and $U(\boldsymbol{r}_\gamma)$ in Sec. 3.1.4) dependent on the position position in the detector are evaluated at the same time.

The LXe E_γ is corrected in order to remove correlation of Eq. (4.4) with opening angle between two γ-rays, then corrected γ-ray energy distribution is fitted with a dedicated function. The function is composed starting from a normal response function which is a combination of Gaussian at higher region and exponential at lower region. It is then convolved with γ-ray

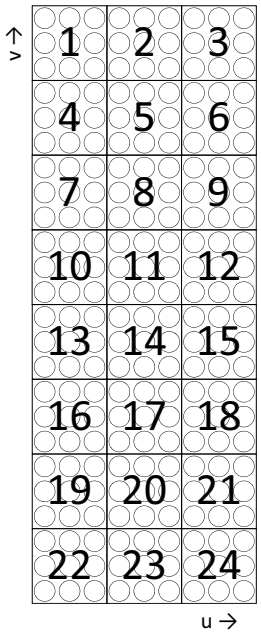

(a) 24 patches for π^0 calibration. LXe area is divided into 3×8. Calibration data is taken for each, the tagging detector located at the opposite position.

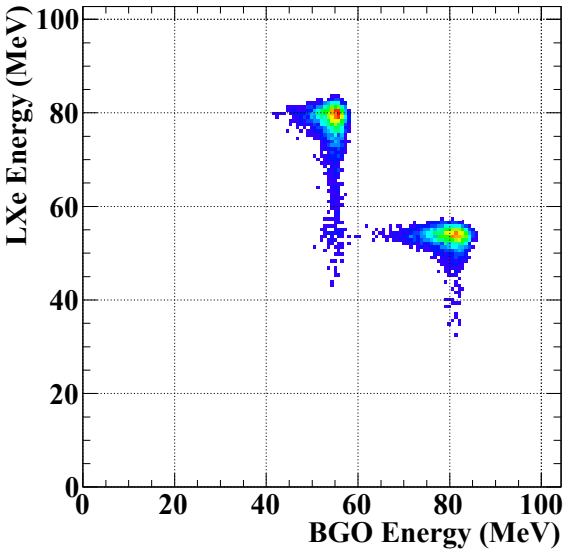

(b) The energies in LXe and BGO detectors in π^0 calibration. The two bunches of events 54.9 MeV in LXe and 84.9 MeV in BGO and the reversed pattern are seen.

Figure 4.11: π^0 calibration.

energy spread and extra pedestal fluctuation due to different beam condition. Figure 4.12 shows an example of fit in a region.

4.1.3 Energy scale stability

The long-term stability of the LXe detector is monitored with various calibrations (Sec. 4.1). Figure 4.13 illustrates the relative light yield by measuring several types of calibrations as a function of date. The absolute scale is adjusted with π^0 calibration for each year, and relative scale is determined by interpolating different light yield calibrations.

4.1.4 LXe detector alignment

We performed 3D alignment of the LXe detector with laser scanner. According to the result of the 3D measurement, we correct the position of the reconstructed γ-ray.

result of the measurement We measured the positions of the 24×2 holes on arch structure which is used to fix PMT holders at both (US and DS) end of the detector, and the surface of the inner window where the PMT holders are installed. The measured misalignment of the vector from DS hole to US hole from that in the drawing is displayed in Fig. 4.14. The surface points array on the window are fitted with a cylinder, and error from cylinder is negligible, but slant and displacement is also found (Table 4.1).

The following vectors are calculated from the measurement, $\boldsymbol{h}_i$: a direction vector which shows the direction of PMT holder, and $\boldsymbol{d}_i$: a normal vector which is perpendicular to the surface

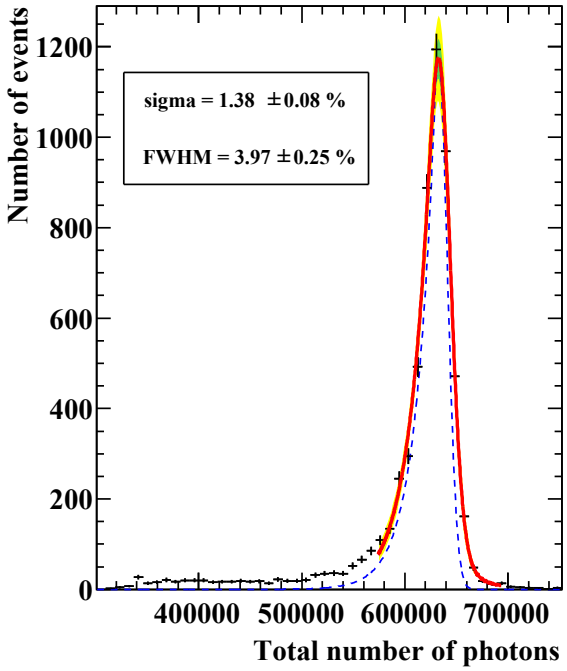

Figure 4.12: Fit on the π^0 calibration data (cross with error). Red line shows the fit result, and blue dashed line shows the detector response function before convolution.

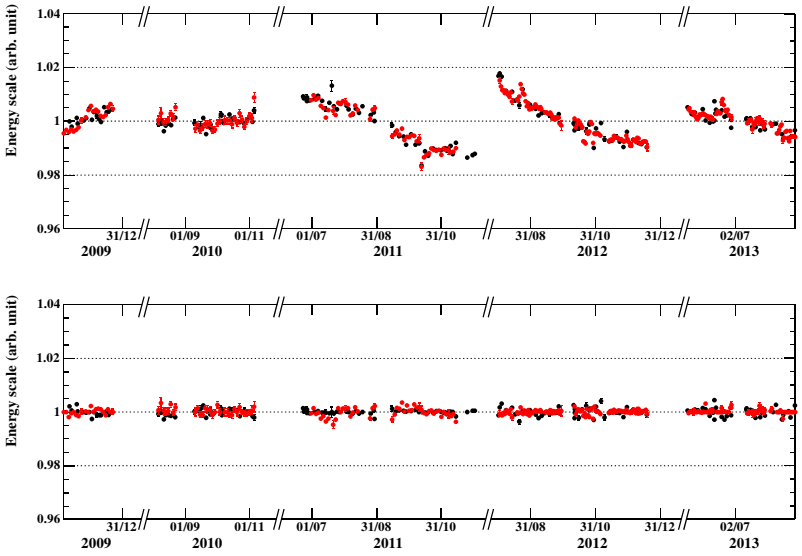

Figure 4.13: History of light yield by calibration before (top) and after (bottom) scale adjustment. Black marker is by CW calibration, red marker is from background spectrum.

of the inner window at the center of the holder. An index i shows the value of i-th PMT holder from top. These are used in correction of the γ-ray position.

method to correct position Since the position of the γ-ray is reconstructed in internal coordinate (u, v, w), we previously used dimensions of drawing which is expressed by a simple coordinate transformation,

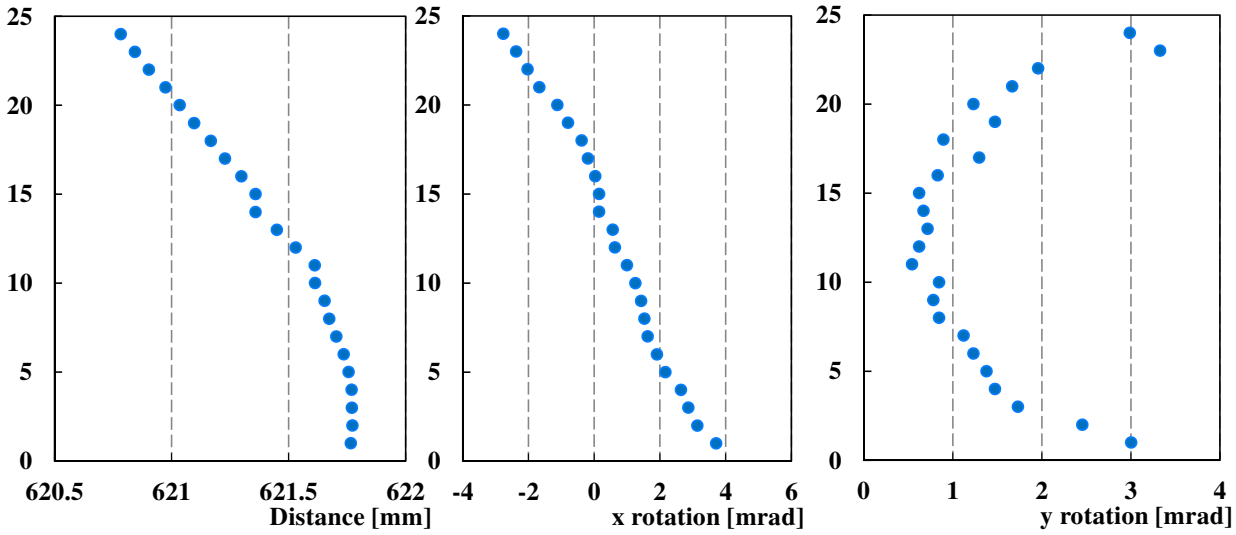

(a) (b) (c)

Figure 4.14: Measured distance and tilt angle of DS→US vector. The designed distance is 622 mm and angle 0. y-axis just shows the id number of the holes which is enumerated from top (1) to bottom (24).

Table 4.1: Fitted parameters of inner window

Item	Unit	Measured	Design
Radius	mm	681.0	678.5
X shift	mm	3.24	0
Y shift	mm	-0.14	0
X slant	mrad	-3.4	0
Y slant	mrad	5.5	0

$$x = -(w + R_{\mathrm{IN}}) + \cos(\frac{v}{R_{\mathrm{IN}}}) + x_0, \tag{4.7}$$

$$y = (w + R_{\mathrm{IN}}) + \sin(\frac{v}{R_{\mathrm{IN}}}) + y_0, \tag{4.8}$$

$$z = u + z_0, \tag{4.9}$$

where R_{IN} is radius of the inner face of the LXe detector, and (x_0, y_0, z_0) is parallel shift of LXe detector from drawing. They were determined from cosmic ray data, where the cosmic rays penetrate the LXe detector and the drift chamber. x_0 and y_0 are found to be consistent with zero, while z_0 is shifted by 6.2 mm in 2009, 2010 data, and 4.2 mm in 2011-2013 data.

According to the distortion which was measured with 3D scanner, we introduced a position correction which is based on how the PMTs are settled in the LXe detector.

- For 24 PMT holders, unit vectors of the longitudinal direction of the holder $\boldsymbol{h}_i$, and normal vectors of the holder $\boldsymbol{d}_i$ are calculated.
- The LXe acceptance is divided into 25 sections by v coordinate. A section-i ranges between centers of i-th and i + 1-th PMT holders, the section 0 and 24 are top-end and bottom-end part.

- The index of a section (i) and a coordinate in the section (s) are calculated according to the v position where γ-ray is reconstructed.
- The vectors $\boldsymbol{h}_\gamma$ and $\boldsymbol{d}_\gamma$ are calculated by interpolating i-th and i + 1-th $\boldsymbol{h}$ and $\boldsymbol{d}$ according to s for the case where γ-ray is in section 1-23. In section 0 or 24, 0-th or 24-th vectors are used.
- The point P is calculated by interpolating points of i-th and i + 1-th hole on the US-side arch. The ratio of the interpolation is calculated from s.
- The point Q is calculated by adding a vector to the point P, the vector is parallel to $\boldsymbol{h}_\gamma$ and the length of the vector is calculated from the u position of the γ-ray.
- The point Q is projected onto the surface of the inner window with respect to the axis of the fitted cylinder face; the point is named point R.
- The vector $w \cdot \boldsymbol{d}_\gamma$ is added to the point R. The point is the corrected reconstructed position of the γ-ray.

In the procedure of position correction, thermal expansions of the detector parts are considered. The main structure of the detector cryostat is made of stainless steel, SUS316L ($\alpha \sim 16 \times 10^{-6}$/K), and PMT holders are made of PEEK[4] resin ($\alpha \sim 50 \times 10^{-6}$/K).

effect of the correction Average shift of γ-ray position over acceptance is (-0.6, -1.9, 2.1) (mm) in (x, y, z). The shift is LXe detector shift with respect to the COBRA frame. Additional z shift to connect the COBRA frame to drift chamber frame is determined from measurements which use both LXe detector and drift chamber, alignment run by cosmic ray and AIF, result is +2.0 ± 0.4 mm for shift in z coordinate.

Figure 4.15 shows the effect by the correction. Shift toward negative y is consistent with thermal shrink, but also consistent with the zero shift with other measurement within uncertainty. The effect of thermal shrink of PMT holder was not considered in previous analysis but is included in the correction, although the thermal effect cannot be confirmed in any calibration. Average difference in stereo angle is $\sim$ 4 mrad, it is not negligible compared with the angular resolution of γ-ray.

4.2 Drift chamber

4.2.1 z-coordinate

Since the reconstruction of z (longitudinal direction of wire) is based on the charges measured at both ends Eq. (3.10), the calibration is done via the calibration of relative gain of the preamplifiers.

Figure 4.16 is an example of the calibration for the anode wire for the Michel positron data. The gains of the amplifiers at the both ends are calibrated so the fitted curve to pass the origin of the plane. For the cathode the relative charge in both end of two series were compared like in the anode, but more precise z_{track} which is obtained from the track fitting is used instead of z_{anode}. The uncertainty in z is estimated to be 70 μm from the comparison of z_{anode} and z_{track}.

[4] polyetheretherketone

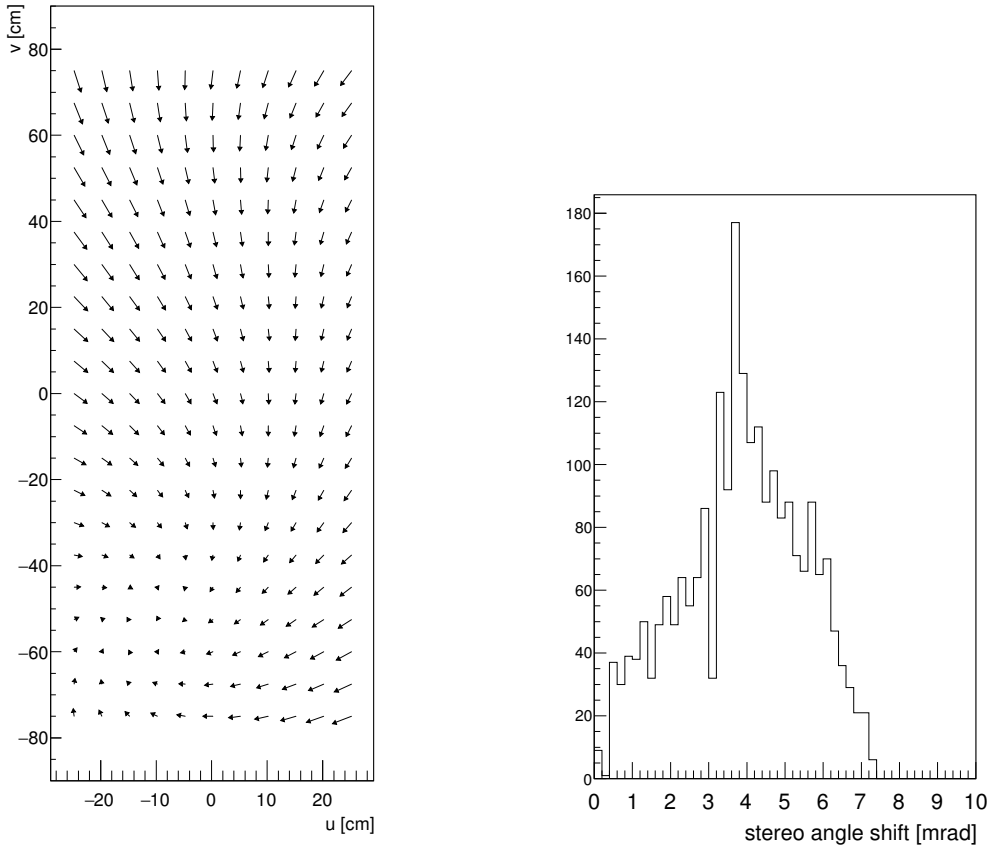

(a) Shift in u and v coordinate, w is fixed at 1 cm. The arrow shows the direction and distance of correction at the position. The length is magnified by factor 10.

(b) Difference of reconstructed points with previous and current methods in stereo angle.

Figure 4.15: Result of the LXe detector alignment

4.2.2 Time calibration

The timing offset between channels is caused by the difference of the amplifier characteristics, cable length and electronics at down-stream. The time offset information is extracted from the Michael and cosmic ray data. The leading edge timings after z coordinate correction and the track timing fitting are plotted, and the timing for the channel is found by fitting the leading edge timing distribution.

4.2.3 Alignment

The relative position of each DCH module is quite important as a high precision tracker. We have two methods to measure the alignment of the drift chamber modules, an optical survey with laser-tracker, and a method by reconstruction of the tracks.

4.2.3.1 Optical method

For the optical survey, a drift chamber module is equipped with cross-hair markers and corner cubes at both ends of the module, as shown in Fig. 4.17. The position of the wire and cathode against the DCH module is measured when it was produced. The position is related to a

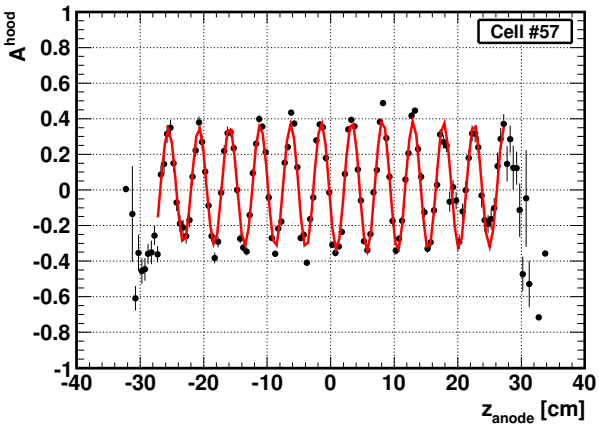

Figure 4.16: z_{anode} versus asymmetry found in cathode. The wave length of the sinusoidal curve is 5 cm of the cathode pattern.

alignment pin, which is also measured in survey. In each year before data taking, measurement with theodolite[5] is performed for cross-hairs and pins, target markers are also surveyed (Sec. 4.4). The accuracy is expected to be 0.2-0.3 mm in x and y and 1.5/2.5 mm in z for DS/US side of the modules. The difference in US and DS is because the theodolite is located in DS side of the detectors. From year 2011, the optical survey is updated with corner cube and laser tracker[6]. The accuracy of the method is determined from the uncertainty of the alignment of the corner cube and expected to be 0.15-0.25 mm in x, y and z, although the spacial resolution of the tracker is 0.015 mm for each axis.

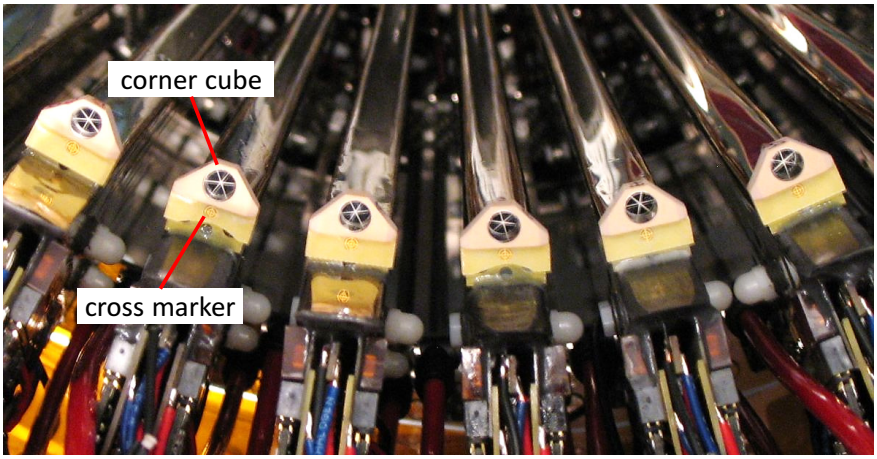

Figure 4.17: View from down-stream side of drift chambers. Corner cubes and cross-hair markers are seen.

[5] Leica Geosystems Total Station TC2002
[6] Leica Absolute Tracker AT901

4.2.3.2 Software method

The relative positions of the modules were also measured with two independent methods of cosmic ray and Michel positrons.

The cosmic ray counter (CRC) was installed for this calibration, to trigger events in which the cosmic rays pass through the DCH modules. The CRC consists of 10 plastic scintillator bars with PMT read out, and are mounted on the outer surface of COBRA magnet as illustrated in Fig. 4.18. The magnet is turned off during the cosmic ray dedicated runs. We processed the cosmic ray data by the algorithm called "Millipede" [85]. It is a kind of linear fitting with a lot of free parameters in a matrix of a large number of laws and columns. The optimal displacement vector for each module is calculated with the algorithm, by minimizing the residuals with respect to straight track of cosmic rays. The parameters are determined within 150 μm accuracy by the method.

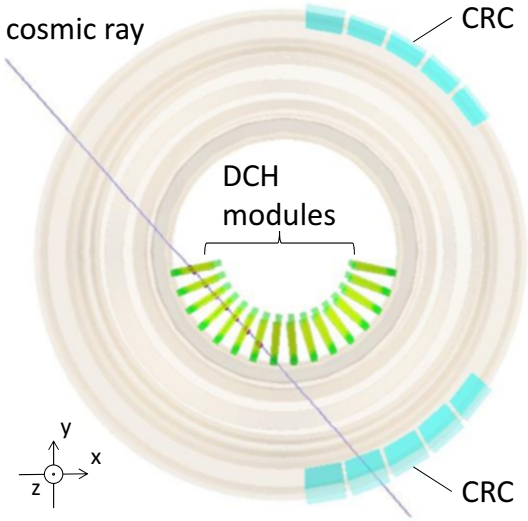

Figure 4.18: CRC mounted on the COBRA magnet. The figure is shown in cross-sectional view of a plane perpendicular to the beam axis.

The other method is an iterative algorithm to optimize radial and longitudinal displacement of each module using Michel positron tracks. This method is conducted by minimizing the residual of radial and longitudinal directions between the reconstructed track and hits in each module. The process repeated iteratively, updating positron tracks with corrected modules position. This method is confirmed by checking consistency with Mott calibration data (Sec. 4.2.4).

4.2.4 Mott calibration

Mott scattering Mott calibration [86] takes a use of Mott scattering, which is elastic scattering of a relativistic Dirac particle by point like nucleus. We make a use of Mott data to evaluate the positron track resolution, and alignment of chamber.

When the nucleus satisfy $Z \ll 137$, the scattering cross section is approximated as [87],

$$\frac{d\sigma}{d\Omega} = \left(\frac{Ze^2}{2E}\right)^2 \frac{\cos^2(\theta/2)}{\sin^4(\theta/2)} \tag{4.10}$$

where E is the initial energy of the particle (positron). The energy of the positron after scattering is given as,

$$E' = E\left(1 - \frac{E}{Mc^2}\frac{1-\cos\theta}{1+(E/Mc^2)(1-\cos\theta)}\right). \tag{4.11}$$

operation In operation, we select positron beam of momentum 53 MeV/c (rejecting pulse-correlated particles with RF signal from accelerator). The positrons with uniform energy hits target and undergo Mott scatting, a noticeable point is that in our setting, energy of scattered positron can be regarded approximately monochromatic (Fig. 4.19). The energy spread of measured positrons are 620 keV in σ.

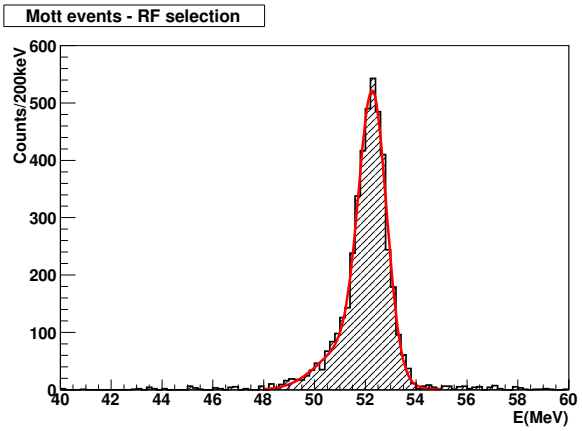

Figure 4.19: Spectrum of Mott scattered positron

4.3 Timing counter

4.3.1 PMT gain adjustment

As the TICP is placed at off-centered in z, the PMTs at both ends are subject to the magnetic field of different strength and direction. The gains of the PMTs are needed to be equalized, and a rough equalization is done with cosmic-ray events. When the cosmic-ray passes through the TICP bar, the hit rate and energy deposit is uniform throughout the bar. The PMT bias voltages are adjusted to equalize the fitted peak of the charge distribution by cosmic ray events. The fine tuning is done in software, by finding a weight to get uniform trigger rate.

4.3.2 z calibration

Since we reconstruct z-coordination from the time difference of two PMTs at the end of bar, the z calibration is equivalent to the timing offset calibration. The extended track from DCH is used for reference in each bar calibration. The time offset is determined so $z_{\mathrm{DCH-TIC}}$ to be zero. In Fig. 4.20, the z coordinate calibration is demonstrated.

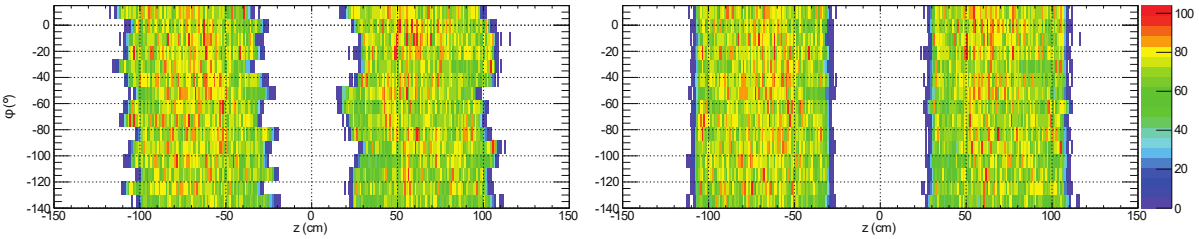

Figure 4.20: TICP cosmic ray hit map before (left) and after (right) z calibration.

4.3.3 Relative calibration

Timing offset between bars is calibrated with CW-B reaction ${}^{11}_{5}\mathrm{B}(p,\gamma,\gamma){}^{12}_{6}\mathrm{C}$. In this reaction, gammas of energy 4.4 MeV and 11.6 MeV are always simultaneous. We calibrate TIC timing with 11.6 MeV, while monitoring 4.4 MeV γ in LXe detector.

This method can be also used for the crosscheck of LXe-TIC relative timing adjustment. For the same purpose, we use timing information of RMD, where gamma ray and positron are always coincident.

4.4 Target alignment

Information about the target position is an important issue for the high precision measurement. Since we reconstruct the initial position and direction by the propagation of the measured track to the target plane, the position of the target along z_t (direction that perpendicular to target plane) is especially important. For example, $\sim$ 1 mm of z_t error causes 10 mrad error in ϕ_e: positron emission angle in ϕ direction (Fig. 4.21(a)). The shift of ϕ_e by target displacement Δz can be expressed as,

$$\Delta\phi_\mathrm{e}(\Delta z) = -\frac{\Delta z \sin\theta_\mathrm{e}}{R\cos\phi_\mathrm{e}\sin(\theta_\mathrm{e}+\theta_\mathrm{tar})}, \tag{4.12}$$

where R is the radius of curvature at the decay point, and $\theta_\mathrm{tar} = 20.5°$ is the slant angle of the target.

4.4.1 Conventional alignment methods

The position of the target is confirmed by an optical survey with theodolite in every year. The estimated accuracy of this survey is $\pm(0.5, 0.5, 1.5)$ mm in the (x, y, z) directions. A plane fit of the measured point of 7 cross-marks are adopted for target–drift chamber alignment in the previous analysis. For crosschecking with optical alignment, we observe the reconstructed position of hole on the target. Target holes can be seen in mapping of reconstructed vertex positron on target like Fig. 4.22. If assumed position of the target is wrong by Δp, the position of hole depends on the incident angle of positrons, and ideally y_hole is proportional to Δp and $\tan\phi_\mathrm{e}$ (Fig. 4.21(b)). By checking all six holes, position and inclination of the target can be observed.

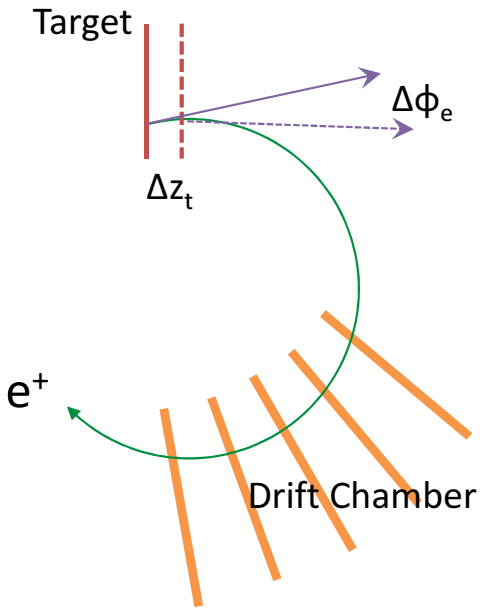

(a) Schematic image of the target and positron track shown in projection to $x - y$ plane. Error of the assumed target position causes error in ϕ_e.

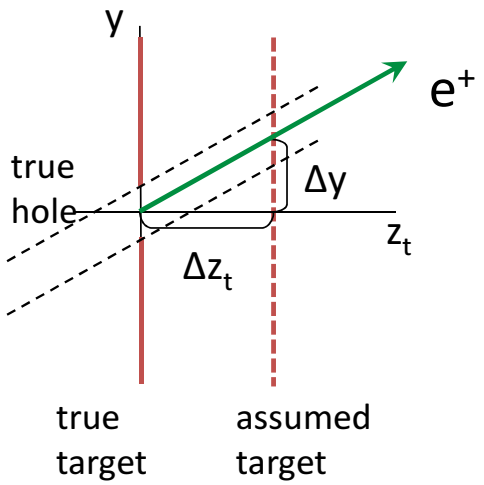

(b) Relation of ϕ_e and y_{hole}, when target is assumed at wrong position. The horizontal axis is z_t: an axis perpendicular to target face, and vertical axis is y.

Figure 4.21: Relation between target shift and error in ϕ_e.

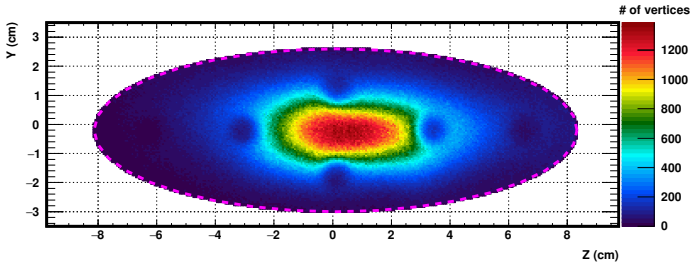

Figure 4.22: Vertex distribution on target in $y - z$ projection. Beam spot is around the center of target. The holes are seen as the deficit of vertexes.

4.4.2 Target deformation and countermeasure

The both results of the hole position and the optical survey indicate that the target was gradually getting deformed. The target deformation is obvious in year 2012 and 2013. On the other hand in 2009 and 2010, the target was consistent with a plane shape.

Further investigation into the shape was performed with the 3D laser scanner[7] at the end of year 2013. The result of 3D scan is displayed in Fig. 4.23(b) and also supports the bending of the target. The reference target plane for reconstruction of positron track is changed from conventional plane to paraboloid which is parametrized as

$$z_t = c_x(x_t - x_0)^2 + c_y(y_t - y_0)^2 + z_0, \tag{4.13}$$

where (x_t, y_t, z_t) are target local coordinate which x_t and y_t are semi-major and -minor axis of target and (x_0, y_0, z_0) are vertex of paraboloid (in target frame). The parameters are determined by

[7] FARO portable coordinate measuring machines

fitting on the result of theodolite measurement. The result of year 2013 is shown in Fig. 4.23(a). The two results largely differ especially in outer region, but considering the vertex distribution in Fig. 4.22, the agreement around the beam spot is good.

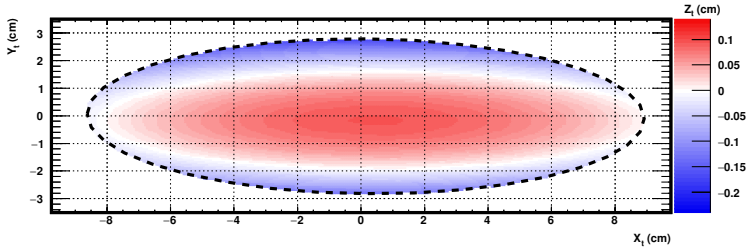

(a) Paraboloid fit on year 2013 optical survey data.

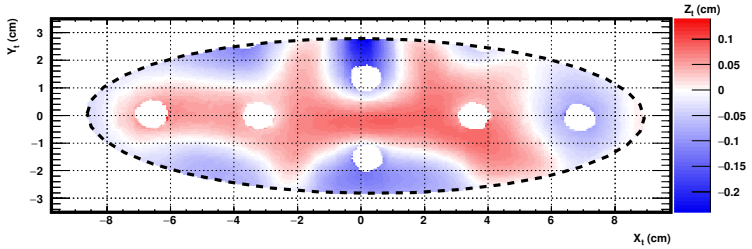

(b) Target deformation found with 3D laser scanner.

Figure 4.23: Results of the target measurements.

The track fitting is improved by the reconstructed paraboloid, not a plane as the previous analysis. The uncertainty of the target z_0 is determined by comparing the z_t with central four holes. Systematic uncertainties are estimated as $\sigma_{z_0} = 0.3$ mm for year 2009-2012 data, and $\sigma_{z_0} = 0.5$ mm for year 2013. The uncertainty due to the deformation from paraboloid shape of target is taken into account, using the difference between paraboloid and 3D scan.

4.5 DRS calibration

4.5.1 Voltage calibration

Each cell in the DRS chip has different characteristics. Since the DRS boards have calibration voltage source, the voltage calibration can be performed online. The response curve for each cell is stored, and recorded waveform is already corrected. Measured RMS after voltage calibration is 0.3 mV.

4.5.2 Timing calibration

Since the sampling speed is controlled by switching pulse inside the chip, it can be varied by each cell. The difference between DRS boards must be adjusted.

We used sinusoidal test wave to calibrate cell-by-cell speed. By taking events with random trigger, the time period of zero-crossing are compared. The adjustment is repeated until the all zero-crossing period to become that of input wave. In order to synchronize the boards, a dedicated clock signal of 19.44 MHz is distributed to all the boards. The accuracy to synchronize different boards improved in 2010, after DRSs were upgraded to version 4.

Table 4.2: Summary of calibration tools in MEG experiment

Category	Process	Source	Main Purpose	Frequency
Cosmic ray	atmospheric showers	Wide spectrum $\mu^{\pm}$ O(GeV)	LXe-DCH relative position	annually
			DCH alignment	
			TC energy and time offset calibration	
			LXe purity	on demand
CEX	$\pi^- \mathrm{p} \to \pi^0 \mathrm{n}$ $\pi^0 \to \gamma\gamma$	55, 83, 129 MeVγ	LXe energy scale/resolution	annually
RMD	$\mu^+ \to \mathrm{e}^+ \nu_e \bar{\nu}_\mu \gamma$	$\gamma > 40$ MeV	LXe-TC relative timing	continuously
		$\mathrm{e}^+ > 45$ MeV	Normalisation	
Michel decay	$\mu^+ \to \mathrm{e}^+ \nu_e \bar{\nu}_\mu$	52.83 MeV end-point e^+	DCH energy scale/resolution	continuously
			DCH and target alignment	
			Normalisation	
Mott	$\mathrm{e}^+ N \to \mathrm{e}^+ N$	≈ 50 MeVe^+	DCH energy scale/resolution	annually
			DCH alignment	
CW accelerator	${}^{7}_{3}\mathrm{Li}(p,\gamma)^{8}_{4}\mathrm{Be}$	14.8, 17.6 MeV γ	LXe uniformity/purity	weekly
	${}^{11}_{5}\mathrm{B}(p,\gamma)^{12}_{6}\mathrm{C}$	4.4, 11.6, 16.1 MeV γ	TC inter bar/ LXe–TC timing	weekly
Neutron generator	${}^{58}\mathrm{Ni}(n,\gamma)^{59}\mathrm{Ni}$	9 MeV γ	LXe energy scale	weekly
Am source	${}^{241}\mathrm{Am}(\alpha,\gamma)^{237}\mathrm{Np}$	5.5 MeV α	LXe PMT QE/purity	weekly
AmBe source	${}^{9}\mathrm{Be}(\alpha_{{}^{241}\mathrm{Am}},n)^{12}\mathrm{C}^{\star}$ ${}^{12}\mathrm{C}^{*}(\gamma)^{12}\mathrm{C}$	4.4 MeV γ	LXe energy scale	on demand
LED			LXe PMT calibration	continuously

Chapter 5

Performance

The methods to estimate detector performance and the typical results are shown in this chapter.

5.1 Timing

The timing resolution which is finally used in the physics analysis is given by the RMD calibration which contains all the same elements: γ-ray, positron and the trigger as for the signal events. We also calculate breakdown of each to crosscheck of our understanding for the detectors.

5.1.1 γ timing

The timing resolution of LXe detector is evaluated with two ways. The data with 54.9 MeV γ-ray in π^0 calibration is used.

One is called intrinsic resolution, all PMT are divided into two groups alternatively in arrangement. Timing is reconstructed independently with two groups (call them t_{even} and t_{odd}) The intrinsic resolution is defined from the distribution of a half of the difference, $(t_{\mathrm{even}} - t_{\mathrm{odd}})/2$. It is found to be $\sigma_\gamma^{\mathrm{int}} \approx 36$ ps. The resolution with other energies revealed that the resolution follows $1/\sqrt{E_\gamma}$ curve, and it implies the intrinsic resolution is dominated by statistic uncertainty.

The other way is more practical so it is normally called as the resolution of LXe detector. That is evaluated with time difference of two γ-rays from π^0 decay, the 54.9 MeV onw seen by the LXe detector and the 82.9 MeV onw seen by pre-shower counter (Sec. 4.1.2.3). The resolution σ_{LXe} is calculated the from distribution of $t_{\mathrm{LXe}} - t_{\mathrm{psc}}$. The example in year 2013 is shown in Fig. 5.1. A Gaussian fit is applied on the distribution. As the resolution still includes the TOF uncertainty of γ-ray and the resolution of pre-shower counter, the contributions are quadratically subtracted to obtain σ_{LXe}. In year 2012 and 2013, resolutions are 64 ps and 66 ps, respectively.

5.1.2 Positron timing

The timing resolution of the timing counter is determined from positrons which hit neighbouring TIC bars. The hit timing is compared considering the difference of pass length. The timing resolution of the single timing counter bar is 65 ps. The timing resolution of the total positron spectrometer is composed of the resolution of the timing counter and the uncertainty of the track length from vertex to the TIC hit. The positron timing resolution is estimated to be $\sim$ 100 ps

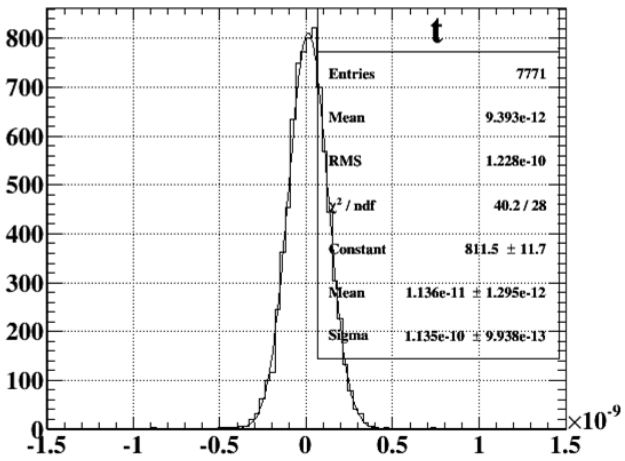

Figure 5.1: Distribution of $t_{\mathrm{LXe}}^{54.9} - t_{\mathrm{psc}}^{82.9}$ in 2013 CEX calibration. A fitted σ is calculated to be 113.5 ps.

5.1.3 Combined timing

The resolution of the time difference of γ-ray and positron is evaluated using the RMD data, which was taken by MEG trigger. For energy sideband (definition will appear in Sec. 7.2.2) data, the RMD event makes a peak on the top of the flat distribution by the accidental background. We fit the distribution with a double Gaussian plus constant function, and the result is shown in Fig. 5.2.

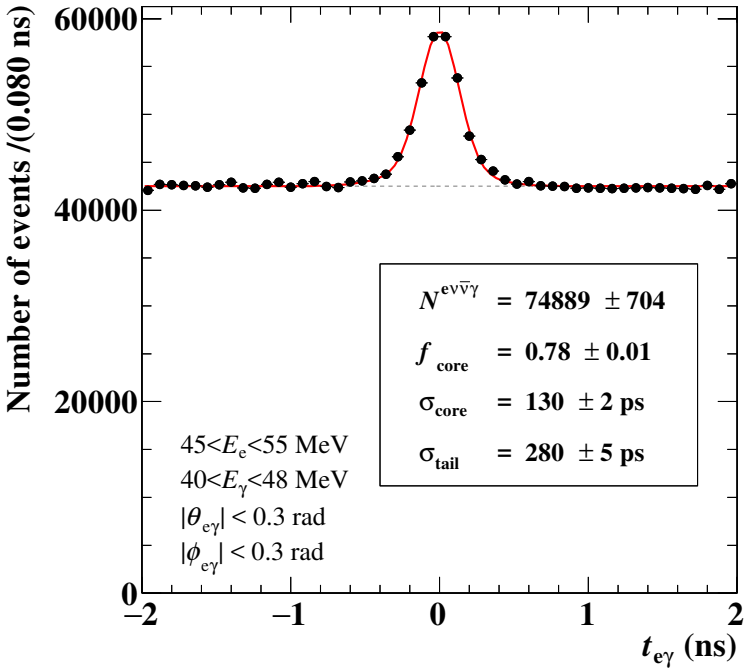

Figure 5.2: Fitting for $t_{e\gamma}$ distribution with RMD data, year 2009-2013 are combined.

5.2 Gamma energy

The energy resolution of γ-ray is evaluated with the method explained in Sec. 4.1.2.3. The energy resolution is worse in smaller w due to the fluctuation of photon collection efficiency which comes from the relative position of PMT and γ-ray. In other words, photon collection gets maximum when γ-ray converts just in front of PMT and minimum in an interval of PMTs. The difference in the width can be seen is the energy spectrum in Fig. 5.3. Figure 5.4 shows the energy resolution as a function of the position (u, v).

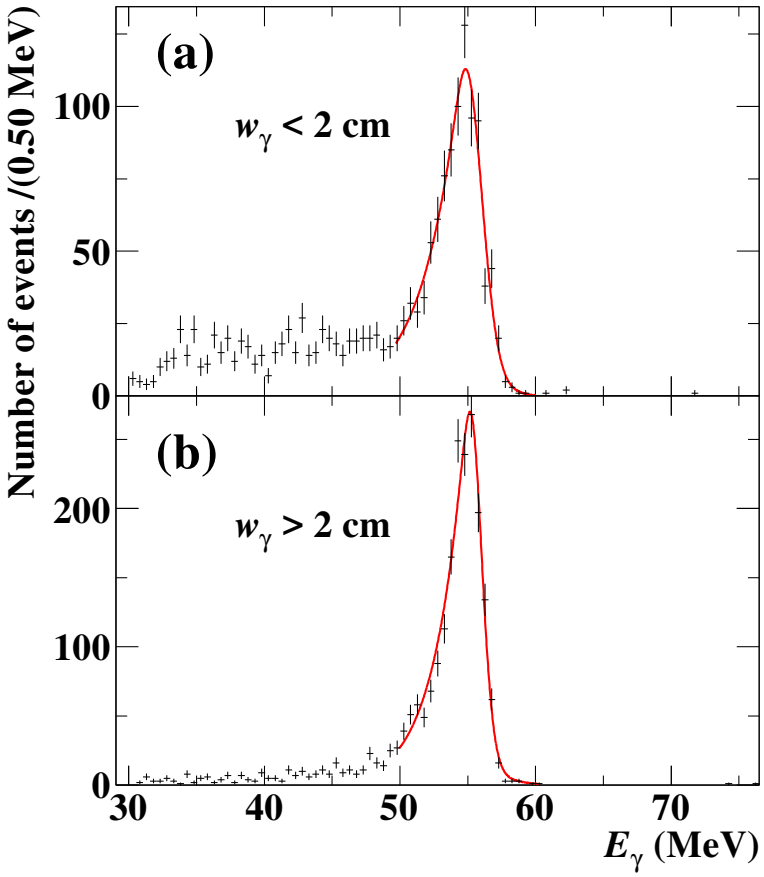

Figure 5.3: Response for 54.9 MeV γ in π^0 run. Top (bottom) figure is $w < 2$ ($w > 2$) area, the event fraction is 42% (58%).

The absolute scale factor S is determined from π^0 calibration run with the way explained in Sec. 4.1.2.3. Uncertainties in E_γ scale are estimated by combining various calibration data. The total uncertainty of γ-ray energy scale is 0.3%. The sources of the uncertainties are (1) the accuracy in estimation of peak energy in π^0 calibration (0.1%), (2) uncertainty between difference in conditions of π^0 calibration and normal muon beam (0.1%), (3) the accuracy of long term scale stability (0.2%), and (4) accuracy of the non-uniformity correction (0.2%).

5.3 Positron energy

The positron energy is evaluated in different two methods.

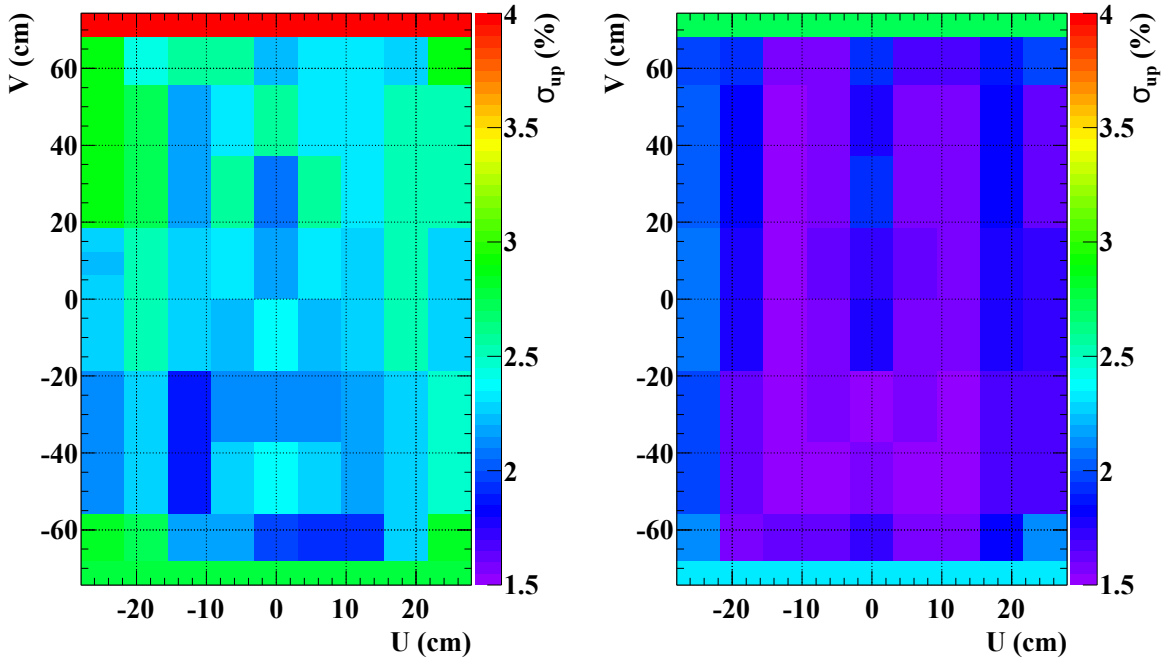

Figure 5.4: Energy resolutions measured in π^0 calibration of year 2012. Left and right figures show shallow ($0 < w < 2$ cm) and deep ($w > 2$ cm) event, respectively.

The first method uses the Michel spectrum. Since the Michel spectrum has a sharp edge at the energy $m_\mu/2$, the energy scale and resolution can be extracted by fitting. The fit function is composed of the theoretical Michel spectrum, the acceptance function, and the detector response. A result of the fit is shown in Fig. 5.5.

$$f(E_\mathrm{e}) = [(\mathrm{Michel}) \times (\mathrm{Acceptance})] * (\mathrm{Resolution}) \tag{5.1}$$

$$(\mathrm{Acceptance}) = \frac{1}{2}\left(1 + \mathrm{erf}\left(\frac{E_\mathrm{e} - \mu_\mathrm{Acc}}{\sqrt{2}\sigma_\mathrm{Acc}}\right)\right) \tag{5.2}$$

where μ_Acc and σ_Acc are parameters that model the acceptance of detector. They are extracted from the sideband data for each year and are $\mu_\mathrm{Acc} \sim 49$ MeV and $\sigma_\mathrm{Acc} \sim 2.5$ MeV through the period. The resolution factor in Eq. (5.1) is composed by double Gaussian functions,

Second method is called "double turn" and is described in Sec. 5.4.2. The positron energy resolutions measured in 2012 and 2013 are listed in Table 5.1.

5.4 Relative angle

5.4.1 Gamma position

The resolution of γ-ray position is evaluated with MC simulation and is confirmed by dedicated π^0 [84] and CW calibration [82] with lead collimators on the entrance window of the LXe detector. Figure 5.6 shows the result of the π^0 run with a collimator made of lead plate with a 10 mm width slit.

The evaluated resolution is 5 mm in u and v direction and 6 mm in w direction.

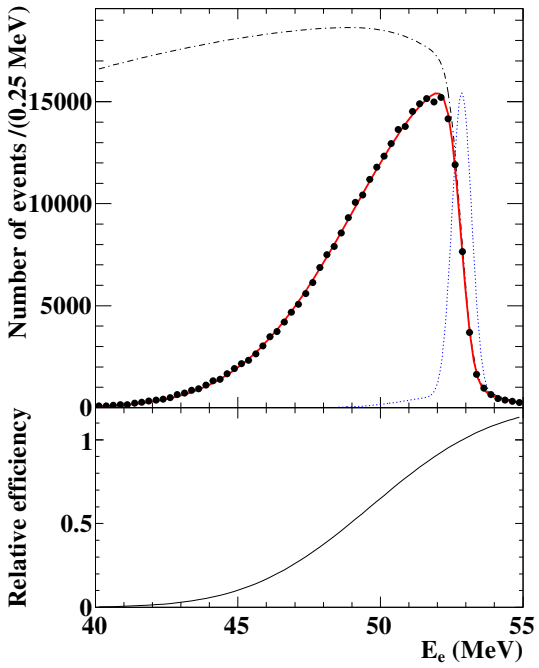

Figure 5.5: Fit on the Michel spectrum for all years averaged data. Dot-dashed line is the theoretical spectrum, blue dotted line is resolution function of the detector, and the acceptance function is drawn in bottom box.

Table 5.1: Energy resolution of positron. $\sigma_{\mathrm{core/tail}}$ means sigma of the core/tail part of the double Gaussian, and f_{core} shows fraction of the core part.

Value	2012	2013
σ_{core}	340 keV	325 keV
σ_{tail}	1.84 MeV	1.91 MeV
f_{core}	0.872	0.852

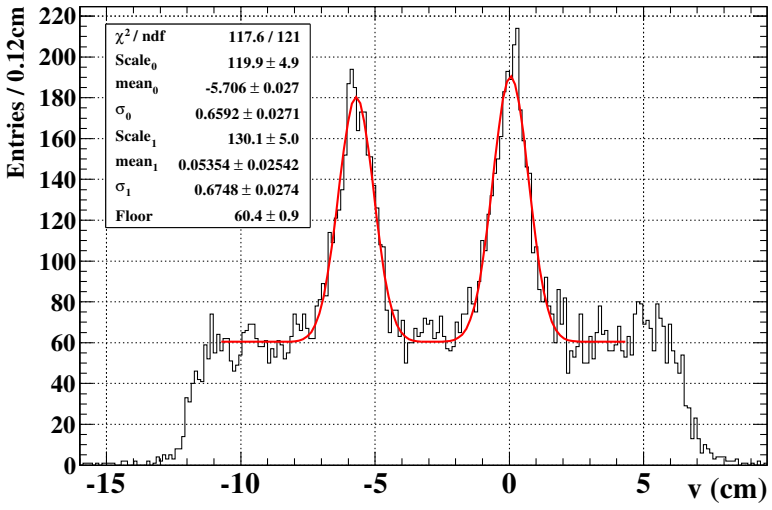

Figure 5.6: v projection of γ-ray reconstructed position. The slit lies along u direction [84].

5.4.2 Positron angle and vertex position

The positron energy, angle, vertex position are correlated to each other, so they are treated with per-error as introduced in Sec. 3.2.4. The parameters for resolutions and correlations are obtained from the double turn technique. It uses positrons which turn in drift chamber twice.

The first and second turns are not connected for this study and are propagated to imaginary target plane which locate between first and second turn. The intersection (imaginary vertex) and momentum on the plane should agree to each other if the turns come from the same positron track.

Figure 5.7 shows the result of double turn analysis which implies the averaged resolution. After dissolving the correlations, the averaged resolutions are found to be $\sigma_{\theta_e} = 9.4$ mrad, $\sigma_{\phi_e} = 8.4$ mrad, $\sigma_{y_e} = 1.1$ mm and $\sigma_{z_e} = 2.5$ mm. In the physics analysis, resolution are treated as in Sec. 7.4.

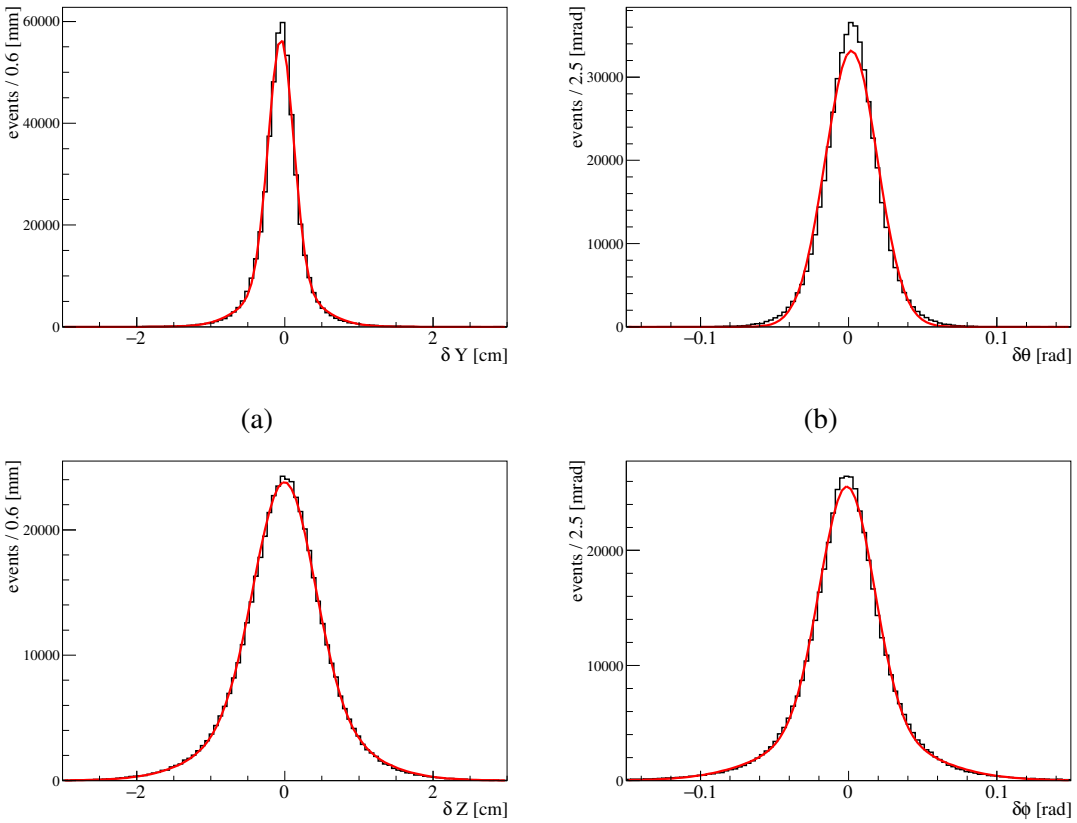

Figure 5.7: Differences in reconstructed observables from first and second turn. y_e, z_e, θ_e and ϕ_e, averaged data in year 2012.

5.4.3 Combined angle

The angle between γ-ray and positron, $\theta_{e\gamma}$ and $\phi_{e\gamma}$ are reconstructed by Eq. (3.18) and (3.19). The resolutions are evaluated from γ-ray postilion resolution, decay vertex resolution and positron angular resolution. The combined $\theta_{e\gamma}$ resolution after removing the correlations is 14.4 – 14.9 mrad depending on the year. The resolution of $\phi_{e\gamma}$ is 9.4 – 9.9 mrad after the correlations are resolved.

5.5 Detection efficiency

5.5.1 Gamma efficiency

We define a fiducial volume of the LXe detector as $|u| < 25\,\mathrm{cm} \wedge |v| < 71\,\mathrm{cm} \wedge 0 < w < 38.5\,\mathrm{cm}$. The signal γ-ray detection efficiency is evaluated with the MC simulation, taking into account the other observables distribution in signal. The loss is mainly coming from the material between the vertex and the LXe detector, the COBRA magnet (14%), the cryostat (7%), the PMT and the other materials (6%). Another kind of the inefficiency is the escape of shower from the entrance face (6%). The inefficiency, coming from pile-up rejection and cosmic ray rejection are taken into account. The estimated detection efficiency is $\epsilon_\gamma = 0.625 \pm 0.023$. The value is also confirmed by the π^0 calibration.

5.5.2 Positron efficiency

The absolute positron detection efficiency is difficult to measure; hence we do not use the absolute value in physics analysis but as in Sec. 7.7. We evaluated the efficiency for the signal positron with MC simulation, and the result is $\epsilon_\mathrm{e} \sim 0.48$. (for Michal positron, the efficiency is 0.37.)

5.5.3 Efficiency of DAQ system

The trigger efficiency consists of the efficiencies of (a) γ-ray trigger, (b) positron trigger and (c) direction matching of γ-ray and positron. The largest inefficiency is from the direction matching part.

At the beginning of the physics data taking, the bottleneck was the data transfer from VME board to the online disk, which took $t_\mathrm{ro} \approx 24$ ms while the dead time of DRS4 chip is 625 μs. It was overcome by upgrading to "multi buffer scheme", and our application has 3 buffers. The trigger is still active even when data is read out unless all three buffers are filled with unread data. With 3 buffers, the fraction of the livetime to total time is written as following formula,

$$f_\mathrm{LT} = \exp(-R_\mathrm{daq} \cdot t_\mathrm{ro})[1 + R_\mathrm{daq} \cdot t_\mathrm{ro} + (R_\mathrm{daq} \cdot t_\mathrm{ro})^2/2!]. \tag{5.3}$$

The livetime efficiency is $\geq 99\%$ for the event rate up to ~ 13 Hz, which is normal trigger rate after the improvement in year 2011, while it was ~ 7 Hz until year 2010. With the improved deadtime, an optimization in trigger rate and trigger efficiency (direction matching) was done as Fig. 5.8.

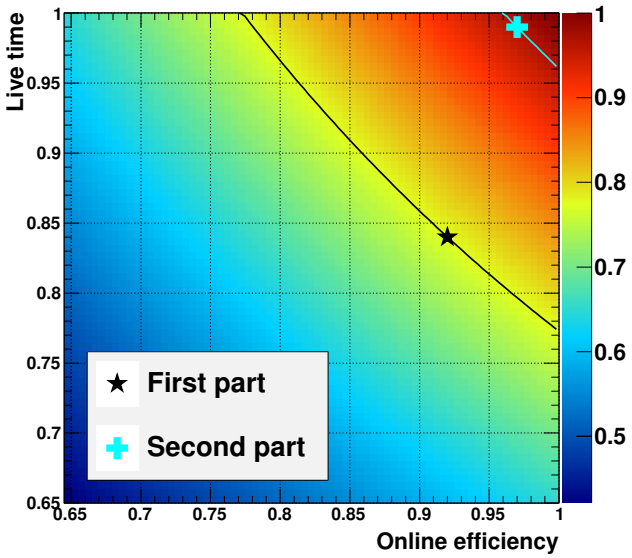

Figure 5.8: Trigger (online) efficiency and livetime ratio in previous scheme (black star) and current scheme (blue cross).

Chapter 6

Run

The status of the experiment is summarized in this chapter.

The PSI proton facility has a long maintenance period from the end of the year to late spring. The MEG physics data taking was also stopped and maintenances of the detector were performed during the period. There is scheduled shutdown in every two weeks, so the special calibrations which do not require beam, the repairment or modification works are performed in the shutdown.

The calibrations of the LXe detector were done twice per week basically. In the calibration, the PMT gain, QE light yield monitoring with γ-ray sources were performed. It also includes calibration with the CW accelerator which need the CW beam pipe operation is required. It took 3-4 hours to this calibration after we were trained to operate it.

6.1 Engineering run 2007

The assembly of instrument was finished in year 2007. We took data with muon beam in order to examine the normal operation of all instruments from October to December.

Some major problems were found in the engineering run. (1) Sparks happened at the HV feedthrough for the Xe PMT, hence we replaced connectors. The sparks damaged circuit elements at the input stage of readout electronics, also we must replace them. (2) Discharge happened at the DCH board. The He gas inside COBRA volume changed to contain small ratio of synthetic air. (3) The target misaligned due to the interference between DC support structure. The structure redesigned therefore.

These problems were fixed before the run 2008 were started.

6.2 Run2008

The data acquisition for the physics study started in this year. After the CEX calibration from the end of July to the end of August, the physics DAQ restarted in September. We published our first physics result with the data from September to December [88]. While the sensitivity of the search was 1.2×10^{-11}, the upper limit for the branching ratio was 2.8×10^{-11} (90% C.L.).

During the data taking, the drift chamber suffered from high-voltage discharge. It resulted in decrease in the number of operational modules and thus loss of positron detection efficiency

(finally the efficiency decreased about a third of that in beginning.), and poor angular resolution. The data of this year is not used for later analysis for this reason.

6.3 Run2009

In this year, the waveform digitizer, DRS was upgraded from ver.2 to ver.4, the final version. About the LXe detector, the light yield was improved by purifying the xenon. To take into account the condition of 6% air mixture inside of the COBRA volume, the degrader for muon beam was replaced from the one of 300 μm thick to 200 μm thick at the middle of DAQ period. The problem of the drift chamber discharge was solved by improving the design.

6.4 Run2010

Before physics data taking, we improved the timing accuracy by modifying the readout board. The effect for the timing resolution can be seen in Table 6.1. We started taking physics data in August and finished at beginning of November. The CEX calibration was performed between August and September. The finished date was earlier than the original plan due to a problem of helium leakage with the BTS magnet. However, the amount of taken data is about a double of that in run 2009. We published results by analysing data in year 2009 and 2010 to find the sensitivity of 1.6×10^{-12} and the upper limit of 2.4×10^{-12} in 90% C.L. [89].

6.5 Run2011

The noise condition of DCH was found to be bad. The problem was fixed by changing HV unit for DCH, and the software filtering process (Sec. 3.2.1) was also effective. As described in Sec. 5.5.3, the DAQ efficiency was improved by the modification of the data readout scheme in DAQ boards.

Many calibration techniques were developed in this year. (a) The BGO detector for CEX (Sec. 4.1.2.3). (b) A new γ source, neutron generator for LXe detector calibration (Sec. 4.1.2.2). (c) A spectrometer calibration with monochromatic energy which make use of Mott scattering (Sec. 4.2.4). (d) A drift chamber alignment with a laser tracker and corner cube.

We started data taking in July and ended in beginning of December due to a power failure in the experimental hall. The taken data amount in this year slightly exceeded the sum of those in 2009 and 2010. Our previous publication [13] based on the data up to this year.

6.6 Run2012 and 2013

A beam development was performed before the physics run in 2012, and thus the beam intensity was increased by ∼20% without deterioration of the beam profile. As we experienced run and calibration for more than 5 years, we did not have severe troubles in the operation of run 2012 and 2013. Data taken in these years are analyzed for the first time in this study. The statistical amount is about the same as that of accumulation of the previous years.

As mentioned in Sec. 4.4, it was found that the muon target in neither plane nor simple paraboloid. It seems to be deformed during long term operation. In order to treat this problem

as a systematic uncertainty, we introduced a new way of fitting in physics analysis. It will be discussed in Sec. 7.5.

6.7 Data summary

The statistical information of total data taken in MEG experiment is summarized in the Table 6.2 and Fig. 6.1. The total number of μ^+s which were stopped on target is 7.5×10^{14}. The length of a run is optimized to be $\sim$ 2000 MEG trigger event, considering a loss by accidents in DAQ and an overhead time for the start and stop of the run. The taken data amount is 94 TB in total. The performance of the detector after final calibration is also summarized in Table 6.1.

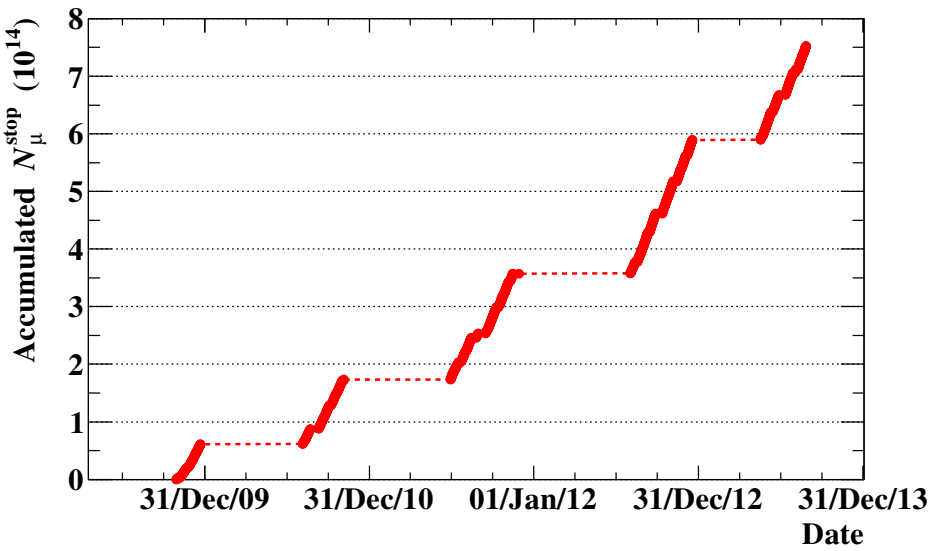

Figure 6.1: Accumulation of number of muons which stopped in the target. Flat regions between slopes correspond to the long maintenance periods.

Table 6.1: Summary of detector performance

Year	2009	2010	2011	2012	2013
γ-ray resolutions					
E_γ (w>2 cm) (%)	1.8	1.9	1.6	1.6	1.6
E_γ (w<2 cm) (%)	2.4	2.5	2.3	2.3	2.3
t_γ (ps)	96	67	67	64	66
u, v (cm)	5	5	5	5	5
w (cm)	6	6	6	6	6
Positron resolutions (core component)					
E_e (MeV)	0.31	0.31	0.30	0.34	0.33
θ_e (mrad)	9.2	10.3	10.4	10.9	11.2
ϕ_e (mrad)	8.5	9.5	9.4	10.1	10.4
y_e (mm)	1.2	1.2	1.3	1.3	1.4
z_e (mm)	2.3	2.9	3.0	3.2	3.3
Combined resolutions (core component)					
$t_{e\gamma}$ (ps)	143	126	117	119	111
$\theta_{e\gamma}$ (mrad)	14.5	14.4	14.5	14.8	14.9
$\phi_{e\gamma}$ (mrad)	9.5	9.8	9.5	9.5	9.9

Table 6.2: Summary of taken data amount

Year	(2008)	2009	2010	2011	2012	2013
DAQ time	48d 21h	37d 17h	56d 10h	81d 1h	90d 20h	63d 0h
Number of runs	10634	10343	12167	30852	43809	26985
μ^+ on target ($\times 10^{14}$)	0.9	0.6	1.1	1.8	2.3	1.6

Chapter 7

Physics analysis

In this chapter, the analysis methods of the search for $\mu \to e\gamma$ is discussed.

7.1 Analysis scheme

We adopt the maximum likelihood analysis to estimate the number of signal event ($N_{\rm sig}$). A likelihood function is composed of probability density functions (PDFs) of signal, radiative muon decay (RMD) and accidental background (ACC). The best fit value of $N_{\rm sig}$ is defined to maximize the likelihood function.

The normalization factor, which is used to convert $N_{\rm sig}$ to the branching ratio: $\mathcal{B}$, is calculated from the number of Michel decay and RMD. The confidence interval of $\mathcal{B}$ is obtained with the Feldman-Cousins approach, by processing many pseudo experiments considering systematic uncertainties.

7.2 Data sets

We analyzed data taken from year 2009 to year 2013. The data can be separated into two groups, (a) taken in year 2009-2011 or "Old" and (b) taken in year 2012-2013, or "New". We have already analysed the old data, however the analysis is revised in this study. The latter is first time to analyse for $\mu^+ \to e^+\gamma$ search. The data statistics of two groups are comparable (Sec. 6.7).

7.2.1 Pre-selection and blinding

In order to reduce the data size, "pre-selection" is applied before detailed calibrations. The definition of the pre-selection is as follows.

- -6.875 ns $< t_\gamma - t_{\rm TIC} < 4.375$ ns
- $|t_{\rm track} - t_{\rm TIC}| < 50$ ns

The window is determined so wide that we do not lose good event. The events which satisfy both criteria for at least one positron track remain in later analysis. As for the first condition, t_γ is a rough online estimation by trigger assuming the vertex at center of the target. The asymmetric range is set because $t_{\rm TIC}$ is not subtracted by the time of flight and the number of turns of positron before hit at the TIC cannot be known without track reconstruction.

When the event includes more than one positron, the likelihood analysis will be biased by correlations, i.e. not all the pairs of γ-ray and positron are independent in such a case. We apply a selection with a variable which indicates goodness of the track reconstruction.

$$P = -51\,\mathrm{rad}^{-1}\times\sigma'_{\phi_\mathrm{e}} - 185\,\mathrm{rad}^{-1}\times\sigma'_{\theta_\mathrm{e}} - 4.19\,\mathrm{MeV}^{-1}\times\sigma'_{E_\mathrm{e}} - 0.033\times\frac{\chi^2}{\mathrm{d.o.f.}} + 0.224\times N_\mathrm{hit}, \quad (7.1)$$

where χ^2 is fitting chi-square, and N_hit is the number of hits associated to the track.

The positrons are ranked with P, and the positron of highest P is selected. The selection eliminates ghosts which are additional track candidates reconstructed near a real positron track. The real signal positron is sometimes rejected by the accidental pile-up with higher P, but the probability of such a case is negligible.

We set a blind box in order to avoid human bias. Before the calibration and the analysis methods are finalized, we cannot access the data inside of the blind box. The 2009-2011 data which were already unblinded in the previous analysis. However, the data were blinded again after process with the renewed reconstruction algorithm. The blind box is defined by

- 48 MeV $< E_\gamma <$ 58 MeV,
- $|t_{\mathrm{e}\gamma}| <$ 1 ns,

and is also shown in Fig. 7.1.

7.2.2 Analysis region and side bands

We define the analysis region, where the likelihood fitting is applied, as follows.

- 48 MeV $< E_\gamma <$ 58 MeV
- 50 MeV $< E_\mathrm{e} <$ 56 MeV
- $|t_{\mathrm{e}\gamma}| <$ 0.7 ns
- $|\theta_{\mathrm{e}\gamma}| <$ 50 mrad
- $|\phi_{\mathrm{e}\gamma}| <$ 75 mrad

Figure 7.1 shows the projection of the analysis window to $(t_{\mathrm{e}\gamma} - E_\gamma)$ plane. The analysis region is not so called a signal region but is wide enough to include the background events, which is also estimated in the likelihood analysis. The size of the analysis window is determined by the resolution for each observable. The width of the region is set from 5 to 20 times of the resolutions, in order not to lose signal events, and not to contain so many background events. The width for $\phi_{\mathrm{e}\gamma}$ is widened in this analysis (previously 50 mrad [13]), for the reason of the target issue written in Sec. 7.5.

The region out of the blind box is called sideband. The sideband data is used to determine the parameters that are necessary for the physics analysis. The events with $t_{\mathrm{e}\gamma} < -1$ ns or $t_{\mathrm{e}\gamma} > 1$ ns are included in the negative or positive timing sideband. The timing sideband data with $E_\gamma > 40$ MeV is used for extract the accidental background. The selection of $|t_{\mathrm{e}\gamma} \pm 2\ \mathrm{ns}| < 0.7$ ns and the same criteria as the analysis window for the other observable are used to test the likelihood fit. The angle sideband is defined as the signal window except for the angle criteria $50 < |\theta_{\mathrm{e}\gamma}| < 150$ mrad or $75 < |\phi_{\mathrm{e}\gamma}| < 225$ mrad, which is used for consistency check.

The energy sideband of

- 40 MeV $< E_\gamma <$ 53 MeV
- 48 MeV $< E_e <$ 53 MeV
- $|\theta_{e\gamma}|, |\phi_{e\gamma}| <$ 300 mrad

is examined for the RMD dedicated study [90]. In the energy sideband, events from the RMD are clearly seen which is suppressed in the analysis region. The number of the RMD is used to determine the normalization. (Sec. 7.7)

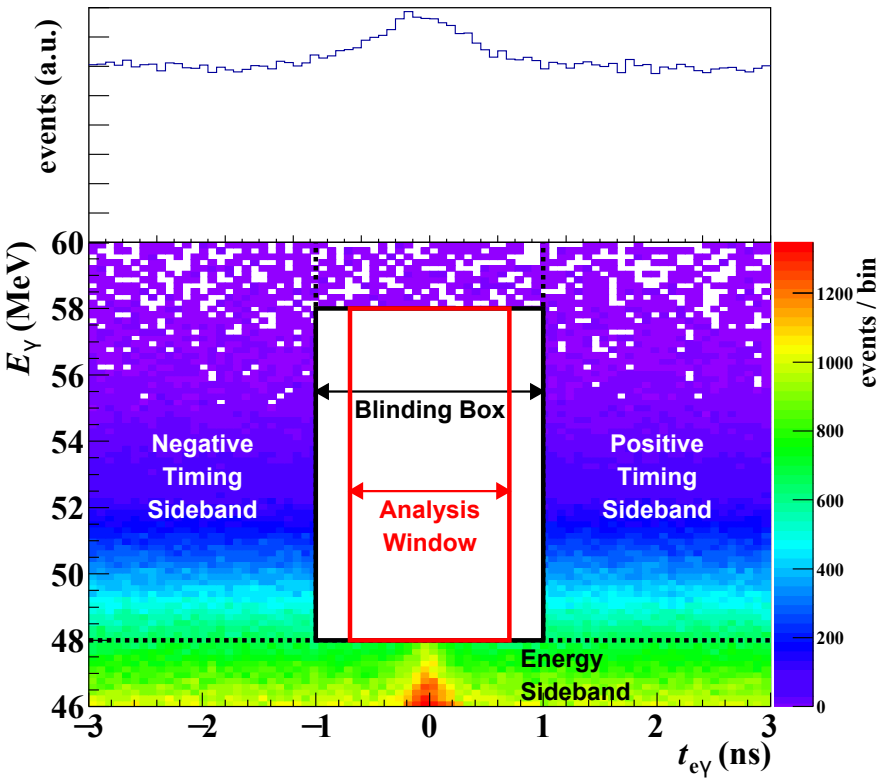

Figure 7.1: The analysis region and sideband in ($t_{e\gamma} - E_\gamma$)-plane. Top part is an 1D projection to $t_{e\gamma}$ axis.

7.3 Likelihood analysis

7.3.1 Likelihood function

The $\mu^+ \to e^+\gamma$ search analysis in the MEG experiment is performed using a likelihood fit. The basic likelihood function ($\mathcal{L}$) is defined when the total number of event N is fixed as

$$\mathcal{L}(X|\theta) = \prod_i^N p(\boldsymbol{x_i}|\theta), \tag{7.2}$$

where

- $\boldsymbol{x}_i$: a set of observables found in i-th event $\boldsymbol{x} = (t_{e\gamma}, E_e, E_\gamma, \theta_{e\gamma}, \phi_{e\gamma})$,
- $\boldsymbol{X}$: an array of all of N sets of the observables $(\boldsymbol{x}_1, \boldsymbol{x}_2, \cdots, \boldsymbol{x}_N)$,

- $\boldsymbol{\theta}$: a set of unknown parameters

and $p(\boldsymbol{x}_i|\boldsymbol{\theta})$ is a probability density function (PDF) which shows the probability to find $\boldsymbol{x}_i$ under a condition of $\boldsymbol{\theta}$. p is normalized as the integration over all possible region of $\boldsymbol{x}$ to be 1. The maximum-likelihood estimator, $\hat{\boldsymbol{\theta}}$ is defined such that maximizes the likelihood function with a given set of observations.

Although Eq. (7.2) is a basic definition of the likelihood function, we adopted the "extended likelihood function" [91] written as Eq. (7.3) for our $\mu^+ \to e^+\gamma$ search analysis. That is because in the MEG experiment, the number of signal events itself is one parameters to be estimated.

$$\mathcal{L}(\boldsymbol{X}|\boldsymbol{\theta}) = \frac{N^{N_{\rm obs}} e^{-N}}{N_{\rm obs}!} \prod_i^{N_{\rm obs}} p(\boldsymbol{x}_i|\boldsymbol{\theta}), \tag{7.3}$$

where $N_{\rm obs}$ is the number of events found in the analysis region. The statistical fluctuation of number of the signal in Poisson distribution is considered.

We set $\boldsymbol{\theta}$ for the number of events of the signal ($N_{\rm sig}$), the radiative muon decay ($N_{\rm RMD}$) and the accidental background ($N_{\rm ACC}$). In addition, we introduce nuisance parameters according to the study about the target deformation ($\boldsymbol{t}$), namely

$$\boldsymbol{\theta} = \left(N_{\rm sig}, N_{\rm RMD}, N_{\rm ACC}, \boldsymbol{t}\right). \tag{7.4}$$

The N in Eq. (7.3) and parameters in Eq. (7.4) have a relation of $N = N_{\rm sig} + N_{\rm RMD} + N_{\rm ACC}$. The PDF $p(\boldsymbol{x}_i|\boldsymbol{\theta})$ can be written as,

$$p(\boldsymbol{x}_i|\boldsymbol{\theta}) = \frac{N_{\rm sig}}{N} \cdot S(\boldsymbol{x}_i, \boldsymbol{t}) + \frac{N_{\rm RMD}}{N} \cdot R(\boldsymbol{x}_i) + \frac{N_{\rm ACC}}{N} \cdot A(\boldsymbol{x}_i), \tag{7.5}$$

where $S(\boldsymbol{x}_i, \boldsymbol{t})$, $R(\boldsymbol{x}_i)$ and $A(\boldsymbol{x}_i)$ are the PDF for signal, RMD and accidental background, respectively and are normalized for each. Then the likelihood function is described considering constraints for $N_{\rm RMD}$, $N_{\rm ACC}$ and $\boldsymbol{t}$ as,

$$\begin{aligned}
&\mathcal{L}(\boldsymbol{X}|N_{\rm sig}, N_{\rm RMD}, N_{\rm ACC}, \boldsymbol{t}) \qquad (7.6)\\
&= \frac{N^{N_{\rm obs}} e^{-N}}{N_{\rm obs}!} C(N_{\rm RMD}, N_{\rm ACC}, \boldsymbol{t}) \prod_i^{N_{\rm obs}} \left(\frac{N_{\rm sig}}{N} S(\boldsymbol{x}_i, \boldsymbol{t}) + \frac{N_{\rm RMD}}{N} R(\boldsymbol{x}_i) + \frac{N_{\rm ACC}}{N} A(\boldsymbol{x}_i) \right)\\
&= \frac{e^{-N}}{N_{\rm obs}!} C(N_{\rm RMD}, N_{\rm ACC}, \boldsymbol{t}) \prod_i^{N_{\rm obs}} \left(N_{\rm sig} S(\boldsymbol{x}_i, \boldsymbol{t}) + N_{\rm RMD} R(\boldsymbol{x}_i) + N_{\rm ACC} A(\boldsymbol{x}_i) \right)
\end{aligned}$$

The constrain function C has a form of Gaussian distribution

$$C(N_{\rm RMD}, N_{\rm ACC}, \boldsymbol{t}) = \exp\left(-\frac{(N_{\rm RMD} - \mu_{\rm RMD})^2}{2\sigma_{\rm RMD}^2} \right) \exp\left(-\frac{(N_{\rm ACC} - \mu_{\rm ACC})^2}{2\sigma_{\rm ACC}^2} \right) c(\boldsymbol{t}), \tag{7.7}$$

where $\mu_{\rm x}$ and $\sigma_{\rm x}$ (x = NRD or ACC) are respectively the average and error of the $N_{\rm RMD}$ or $N_{\rm ACC}$ estimated in the sidebands. The last term c is the constraint for the target parameter, whose detail is explained in Sec. 7.5.

7.3.2 Fitting and the confidence region

The best fit value for $\boldsymbol{\theta}$ is obtained by searching for $\hat{\boldsymbol{\theta}}$ which maximizes the likelihood function. The confidence interval is computed with the unified approach by Feldman and Cousins [92] with the profile-likelihood ordering [30]. The following test statistic is calculated on the data, as a function of N_{sig}.

$$q_{\mathrm{data}}(N_{\mathrm{sig}}) = -2 \ln \lambda(N_{\mathrm{sig}}) \tag{7.8}$$

$$\lambda(N_{\mathrm{sig}}) = \frac{\mathcal{L}(N_{\mathrm{sig}}, \hat{\hat{N}}_{\mathrm{RMD}}(N_{\mathrm{sig}}), \hat{\hat{N}}_{\mathrm{ACC}}(N_{\mathrm{sig}}), \hat{\hat{\boldsymbol{t}}}(N_{\mathrm{sig}}))}{\mathcal{L}(\hat{N}_{\mathrm{sig}}, \hat{N}_{\mathrm{RMD}}, \hat{N}_{\mathrm{ACC}}, \hat{\boldsymbol{t}})} \tag{7.9}$$

where $\hat{x}$ is the best estimate when all parameters are free, while $\hat{\hat{x}}(N_{\mathrm{sig}})$ are the best estimate under the condition of fixed N_{sig}.

Then, an ensemble of toy-MC is generated. It is not normal a Monte Carlo but is just to simulate observables considering the spectra, the detector response and the uncertainty, and the correlations between them are also considered. The number of events can fluctuate following Poisson distribution around the fixed N_{sig}, and expected number of N_{RMD} and N_{ACC}. For every event, one set of observables is randomly selected from the PDF of corresponding type of event.

In order to consider the systematic uncertainty, a set of uncertainty is randomly selected according to the list at the beginning of toy-MC (one set of value is common in one toy), and the uncertainties are included to observables. The considered uncertainties in the generation are, the target alignment parameter (position and shape), E_γ scale, E_{e} bias, the center of signal $t_{\mathrm{e}\gamma}$ PDF, the shape of PDF and the correlation between errors of positron observables. The impact of the systematic error on the result will be shown in Sec. 8.1.2.

For each toy-MC, $q_{\mathrm{MC}}(N_{\mathrm{sig}})$ are calculated in the same way as in Eq. (7.9), and $q_{\mathrm{data}}(N_{\mathrm{sig}})$ and the distribution $q_{\mathrm{MC}}(N_{\mathrm{sig}})$ are compared. If the N_{sig} where

$$q_{\mathrm{data}}(N_{\mathrm{sig}}) < q_{\mathrm{MC}}(N_{\mathrm{sig}}) \tag{7.10}$$

is satisfied in more than $(1 - X)\%$ of toy-MC were found, the upper or lower limit of $X\%$ confidence level can be set.

7.4 PDF

The formalism of the probability density function is explained in this section. As introduced in Sec. 7.3.1, there are three types of PDF: S, R and A which represents signal, radiative muon decay and accidental background, respectively.

7.4.1 Signal PDF

The signal PDF can be factorized into five factors, (1) Energy of γ-ray, (2) Energy of e^+ (3) Time difference of the e^+ and γ, (4) and (5) Angular difference between e^+ and γ in θ and ϕ. i.e.

$$
\begin{aligned}
S(E_\gamma, E_\mathrm{e}, t_{\mathrm{e}\gamma}, \theta_{\mathrm{e}\gamma}, \phi_{\mathrm{e}\gamma} | \boldsymbol{r}_\gamma, \boldsymbol{r}_\mathrm{e}, \sigma'_{E_\mathrm{e}}, \sigma'_{\theta_\mathrm{e}}, \sigma'_{\phi_\mathrm{e}}, \sigma'_{\boldsymbol{r}_\mathrm{e}}, \phi_\mathrm{e}, \boldsymbol{q}_\mathrm{e}, \boldsymbol{t}) = \\
& S_1(E_\gamma | \boldsymbol{r}_\gamma) \times \\
& S_2(t_{\mathrm{e}\gamma} | E_\gamma, E_\mathrm{e}, \sigma'_{E_\mathrm{e}}, \boldsymbol{q}_\mathrm{e}) \times \\
& S_3(E_\mathrm{e} | \sigma'_{E_\mathrm{e}}, \phi_e) \times \\
& S_4(\theta_{\mathrm{e}\gamma} | \boldsymbol{r}_\gamma, \boldsymbol{r}_\mathrm{e}, E_\mathrm{e}, \sigma'_{E_\mathrm{e}}, \sigma'_{\theta_\mathrm{e}}, \sigma'_{\boldsymbol{r}_\mathrm{e}}) \times \\
& S_5(\phi_{\mathrm{e}\gamma} | \boldsymbol{r}_\gamma, \boldsymbol{r}_\mathrm{e}, \theta_{\mathrm{e}\gamma}, E_\mathrm{e}, \sigma'_{E_\mathrm{e}}, \sigma'_{\theta_\mathrm{e}}, \sigma'_{\phi_\mathrm{e}}, \sigma'_{\boldsymbol{r}_\mathrm{e}}, \phi_\mathrm{e}, \boldsymbol{t}),
\end{aligned}
\tag{7.11}
$$

where $\boldsymbol{r}_\gamma$ is the first conversion point of the gamma-ray, $\boldsymbol{r}_\mathrm{e}$ is the decay point of muon, and $\boldsymbol{q}_\mathrm{e}$ is a set of the variable to indicate the quality of the positron tracking.

7.4.1.1 Signal E_γ PDF

The signal E_γ is defined by the detector response to signal γ-ray, where the dependence on the γ incident position is considered. The 54.9 MeV γ-ray in CEX calibration is used to evaluate the detector response. The extraction of PDF is as shown in Sec. 5.2. The position dependence is introduced by subdividing the acceptance as shown in Fig. 7.2, and each section has four regions for w (depth) direction. ($w < 0.8$ cm), ($0.8 < w < 3$ cm), ($3 < w < 8$ cm) and ($8 < w$ cm). The division is so determined that area of different response to be different region, keeping the required statistic per region. In the areas of the same color in Fig. 7.2, the data are combined because the response of the detector is similar.

7.4.1.2 Signal $t_{\mathrm{e}\gamma}$ PDF

The PDF for the relative timing of γ-ray and positron is evaluated with the radiative decay peak by fitting the distribution of the relative timing in E_γ sideband data with two Gaussian functions and a constant. The constant term is added to fit the accidental pile-up and is not included in the signal PDF. The PDF is categorized into 6 types by "Positron Category" (HQ, LQ) which represents the goodness of the positron trajectory estimation [77], and DCH-TIC matching quality which was explained in Sec. 3.3.2. The result of $t_{\mathrm{e}\gamma}$ fitting is shown in Fig. 7.3.

E_e correlation There is a correlation between $t_{\mathrm{e}\gamma}$ and E_e. As shown in Fig. 7.4, we extracted the correction parameter from signal Monte Carlo. The slope is 52.81 ± 1.6 ps/MeV.

E_γ correlation Since the LXe timing resolution depends on the number of the scintillation photons, the error of estimation of E_γ scale affects the $t_{\mathrm{e}\gamma}$ PDF. The effect is considered when including the systematic error.

7.4.1.3 Signal E_e PDF

The positron energy response is evaluated as described in Sec. 5.3. The signal E_e PDF is defined as resolution function corrected with window function. As we adopt the event-by-event PDF,

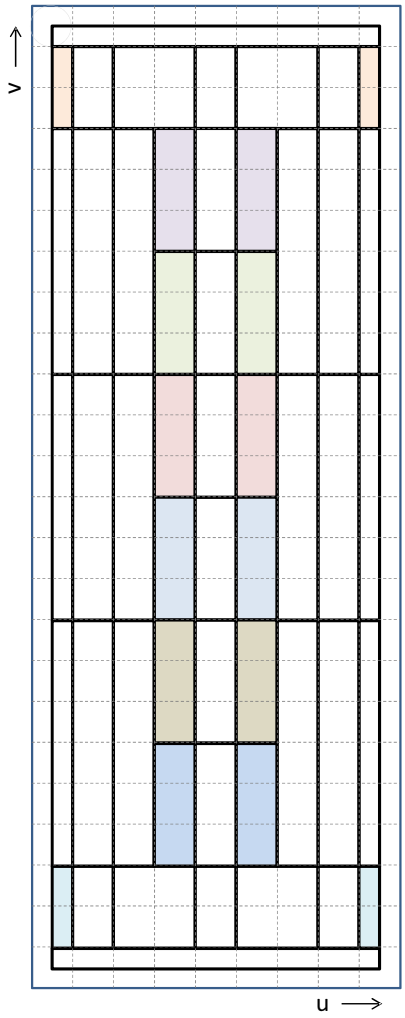

Figure 7.2: A map which shows the division of γ-ray acceptance in $u-v$ plane. Thin dashed lines show the border of the area corresponding to each PMT. The response for signal is calculated for each area in this map, the areas of the same color are combined.

the resolution is written by a product of sigma of pull (s, fixed value which is determined from calibration) and per-event error σ' (introduced in Eq. (3.12)).

$$(\text{Resolution})_i = f_{\text{core}} \cdot \mathcal{G}(\mu_{\text{core}}, s_{\text{core}}\sigma'_{E_e i}) + (1 - f_{\text{core}}) \cdot \mathcal{G}(\mu_{\text{tail}}, s_{\text{tail}}\sigma'_{E_e i}), \tag{7.12}$$

where $\mathcal{G}(a, b)$ means a Gaussian distribution whose mean is a and standard deviation is b.

Then the correlations of E_e with θ_e and ϕ_e are corrected. Finally, the corrected function is multiplied with the "window" function that simulates the effect due to the analytical region cut of $t_{e\gamma}$, $\theta_{e\gamma}$ and $\phi_{e\gamma}$. The window function is obtained by fitting E_e distribution of toy-MC with and without region cut for $t_{e\gamma}$, $\theta_{e\gamma}$ and $\phi_{e\gamma}$. An typical example of the window function is shown in Fig. 7.5.

The errors in the fitting are introduced as a covariance matrix. For the signal PDF, the correlation among f_{core}, μ_{tail} and σ_{tail} are taken into account.

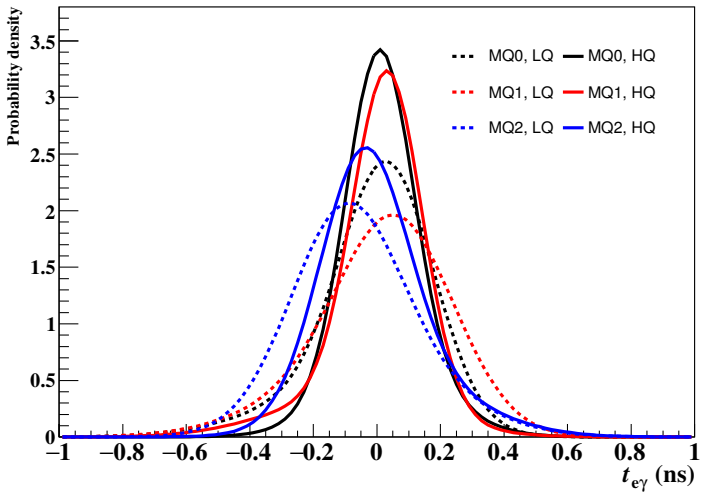

Figure 7.3: $t_{e\gamma}$ PDF of individual 6 categories for 2012 data. HQ and LQ show high and low quality of positron track fitting. MQ means matching quality between DCH and TIC, and (MQ0, MQ1, MQ2) means (good, middle, bad) matching.

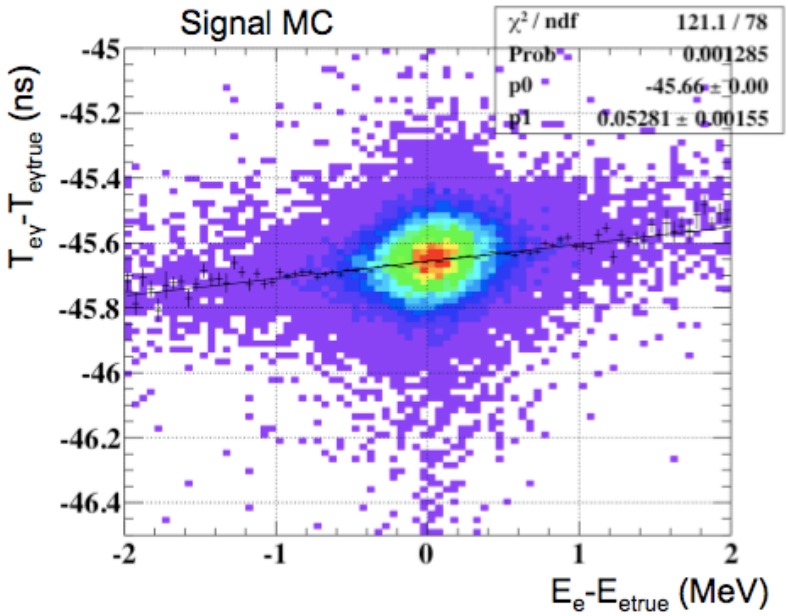

Figure 7.4: The correlation in E_e and $t_{e\gamma}$ for MC signal events. The correlation parameter is extracted by a linear fit on this distribution.

7.4.1.4 Signal $\theta_{e\gamma}$ PDF

The $\theta_{e\gamma}$ PDF is formed by per-event scheme. The detailed method to include the correlation in the per-event PDF can be found in [77]. The correlation between y coordinate of vertex and E_e is corrected with the following formula. We extract the correlation parameter $p_{y_e E_e}$ from the double-turn positrons.

$$\mu_{\delta y_e} = p_{y_e E_e} \delta E_e \tag{7.13}$$

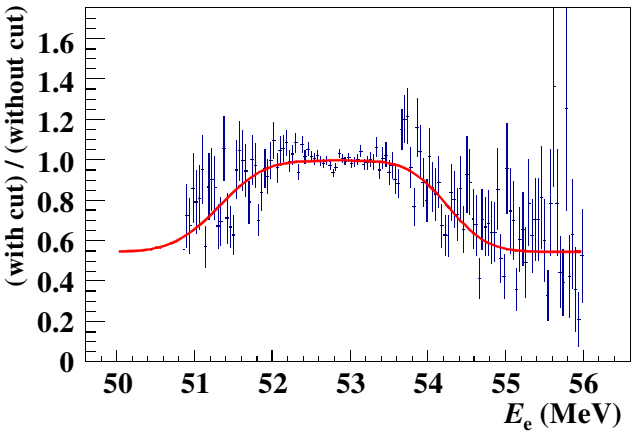

Figure 7.5: Event ratio of toy-MC with and without region cut is shown with line and statistic error. The window correction function for E_e PDF is shown with the red line (year 2009).

The correlation between z and θ_e is also introduced. However the correlation is not directly used to shift the center of peak, but to correct the positron resolution. The θ resolution for positron: σ_{θ_e} is then calculated as,

$$\sigma_{\theta_e} = \sqrt{\sigma^2_{\text{core}} + \sigma^2_{\theta_e} + 2\sigma_{\theta_e} C_{z\theta}}. \tag{7.14}$$

The resolution of $\theta_{e\gamma}$ is finally calculated by adding σ_{θ_γ} quadratically to the positron resolution. The σ_{θ_γ} is composed of core and tail part each u and w direction.

7.4.1.5 Signal $\phi_{e\gamma}$ PDF

The $\phi_{e\gamma}$ PDF depends on the parameters which are shown in Eq. (7.11).

σ_{ϕ_e} dependence on ϕ_e The resolution of ϕ_e depends on ϕ_e itself, the dependence is incorporated in the pull of σ_{ϕ_e} as,

$$s_{\phi_e \text{inner}} = s_{\phi_e \text{min}} \sqrt{\frac{1 - (c_\phi^2) - 2c_\phi k_\phi \tan(\phi_e)/\sigma_{\phi_e(0)}}{1 + \left(k_\phi \tan(\phi_e)/\sigma_{\phi_e(0)}\right)^2}}, \tag{7.15}$$

where $s_{\phi_e \text{min}}$ is the pull sigma where s_{ϕ_e} is minimum. $\sigma_{\phi_e(0)}$ and k_ϕ are extracted from the data, while c_ϕ is from MC.

ϕ_e and E_e correlation The ϕ_e center is shifted by the next formula.

$$p'_{E_e \phi_e} = \frac{c_\phi - k_\phi \tan(\phi_e)}{\sqrt{\sigma_{\phi_e(0)} + (k_\phi \tan(\phi_e))^2}} \tag{7.16}$$

$\phi_{e\gamma}$ and $\theta_e\gamma$ correlation The correlation between $\phi_{e\gamma}$ and $\theta_{e\gamma}$ are corrected with $p'_{\phi_{e\gamma}\theta_{e\gamma}}$ which is defined by a polynomial function as Eq. (7.17).

$$p'_{\phi_{e\gamma}\theta_{e\gamma}} = a + b\phi_e + c\phi_e^2 + d\phi_e^3 \tag{7.17}$$

In summary, the center of the mean of $\phi_{e\gamma}$ is shifted by the formula

$$\delta\mu_{\phi_{e\gamma}} = p'_{E_e\phi_e}\frac{\sigma'_{\phi_e}}{\sigma'_{E_e}}\delta E_e + p'_{p'_{\phi_{e\gamma}\theta_{e\gamma}}}\frac{\sigma'_{\phi_{e\gamma}}}{\sigma'_{\theta_{e\gamma}}}\theta_{e\gamma} + \mathcal{E}_\phi(p_{E_e y_e}\delta E_e). \tag{7.18}$$

$\mathcal{E}_\phi$ is a function to translate δy_e to $\delta\phi_{e\gamma}$.

The resolution of $\phi_{e\gamma}$ is finally composed by combining the resolutions of ϕ_e, contribution from the vertex position resolution and the ϕ resolution of LXe detector.

$$\sigma_{\phi_{e\gamma}} = \sqrt{s^2_{\phi_e\text{inner}}\sigma'^2_{\phi_e}\left(1-\rho'^2_{\theta_e\phi_e}\right)\left(1-\rho'^2_{z_e\phi_e}\right) + \mathcal{F}^2_\phi\left(s_{y_e,\text{inner}}\sigma'_{y_e}, s_{z_e}\sigma'_{z_e}\right) + \sigma^2_{\phi\text{XEC}}}, \tag{7.19}$$

where $\mathcal{F}$ is a function which convert the resolution of y_e and z_e to the resolution of $\phi_{e\gamma}$, and $\sigma_{\phi\text{XEC}}$ is the ϕ resolution of the LXe detector.

7.4.2 RMD PDF

The PDF for the RMD event is written as,

$$\begin{aligned} R(E_\gamma, E_e, t_{e\gamma}, \theta_{e\gamma}, \phi_{e\gamma}|\boldsymbol{r}_\gamma, \boldsymbol{r}_e, \sigma'_{E_e}, \sigma'_{\theta_e}, \sigma'_{\phi_e}, \sigma'_{\boldsymbol{r}_e}, \phi_e, \boldsymbol{q}_e) = & \\ R_1(t_{e\gamma}|E_\gamma, E_e, \boldsymbol{q}_e)\times & \\ R_2(E_\gamma, E_e, \phi_{e\gamma}, \theta_{e\gamma}|E_\gamma, E_e). & \end{aligned} \tag{7.20}$$

7.4.2.1 RMD $t_{e\gamma}$ PDF

The $t_{e\gamma}$ PDF is the same as the signal PDF except for the $t_{e\gamma} - E_e$ correlation. The correlation coefficient is measured from data and MC, but is found to be much smaller than that in signal. It is understood by the fact that E_e is not fixed in the RMD event.

7.4.2.2 Physically correlated part

In RMD events, all of the energy of the γ-ray, energy of positron, relative angle between them are correlated each other. The relation can be calculated using the standard model as,

$$\begin{aligned} d\mathcal{B}(\mu^+ \to e^+\nu_e\bar{\nu}_\mu\gamma) = & \\ \frac{\alpha}{64\pi^3}\beta dx\frac{dy}{y}d\Omega_e d\Omega_\gamma\left|F(x,y,d) - \beta\boldsymbol{p}_\mu\cdot\hat{\boldsymbol{p}}_e G(x,y,d) - \boldsymbol{p}_\mu\cdot\hat{\boldsymbol{p}}_\gamma H(x,y,d)\right|, & \end{aligned} \tag{7.21}$$

where $\boldsymbol{p}_\mu$ is polarization of initial muon, $\hat{\boldsymbol{p}}$ is the unit vector of the vector $\boldsymbol{p}$, $d = 1 - \beta\hat{\boldsymbol{p}}_e\cdot\hat{\boldsymbol{p}}_\gamma$, and the functions F, G, H are given in [9].

The theoretical spectrum is convoluted with the detector response function for each observable.

7.4.3 Accidental background PDF

The PDF for the accidental background is defined as,

$$A(E_\gamma, E_e, t_{e\gamma}, \theta_{e\gamma}, \phi_{e\gamma} | \boldsymbol{r}_\gamma, \sigma'_{E_e}, \phi_e) = \tag{7.22}$$
$$A_1(\theta_{e\gamma}|u_\gamma)\times$$
$$A_2(\phi_{e\gamma}|v_\gamma)\times$$
$$A_3(E_e|\sigma'_{E_e}, \phi_e)\times$$
$$A_4(E_\gamma|\boldsymbol{r}_\gamma).$$

The $t_{e\gamma}$ distribution in accidental background events should be flat and it is confirmed by sideband analysis. Therefore, the $t_{e\gamma}$ factor for the accidental background is constant.

7.4.3.1 Accidental $\theta_{e\gamma}$ and $\phi_{e\gamma}$ PDF

The PDF of the relative angle ($\theta_{e\gamma}$ and $\phi_{e\gamma}$) is made from the timing sideband. The angular selection is loosened to gain data amount, and to fit the angular distribution in wider range. The dependence on the position on the LXe detector is included by slicing data into 5(8) sections in v_γ (u_γ) for $\phi_{e\gamma}$ ($\theta_{e\gamma}$) and fit them with a polynomial function of degree 5.

7.4.3.2 Accidental E_e PDF

The E_e PDF is extracted from the timing sideband, by fitting the spectrum with a fit function which is a convolution of theoretical function, the acceptance function and the resolution function of double Gaussian. The correlation in the event-by-event error is considered in systematic error. The correlation matrix of each parameter is shown in Fig. 7.6.

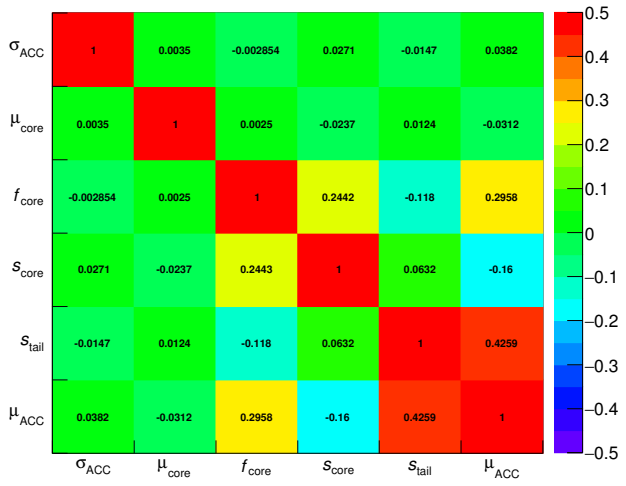

Figure 7.6: Correlation among E_e PDF parameters, which is included in the systematic error.

7.4.3.3 Accidental E_γ PDF

There are two dominant source of the accidental γ-ray, RMD and AIF. In addition, a part of the cosmic ray remains after CR cut as discussed in Sec. 3.1.6. Figure 3.11 shows the E_γ spectrum from RMD and AIF. A fraction of the RMD is 55% and the AIF is 45% when threshold is at $y = E_\gamma/E_{\rm signal} = 0.9$. In order to include the difference of the fraction of the source γ-ray and to include the position dependence of energy resolution, the accidental E_γ PDF is composed for each section which is shown in Fig. 7.7.

The accidental background E_γ PDF is based on the observed energy spectrum. The spectrum is fitted by E_γ template function which is composed by, (a) adding the RMD and AIF spectra, (b) smearing the spectrum to simulate pedestal, (c) convoluting a response function of Gaussian, (d) adding the CR spectrum, and (e) multiplying a function which simulates the trigger efficiency. One of the fit results is shown in Fig. 7.8.

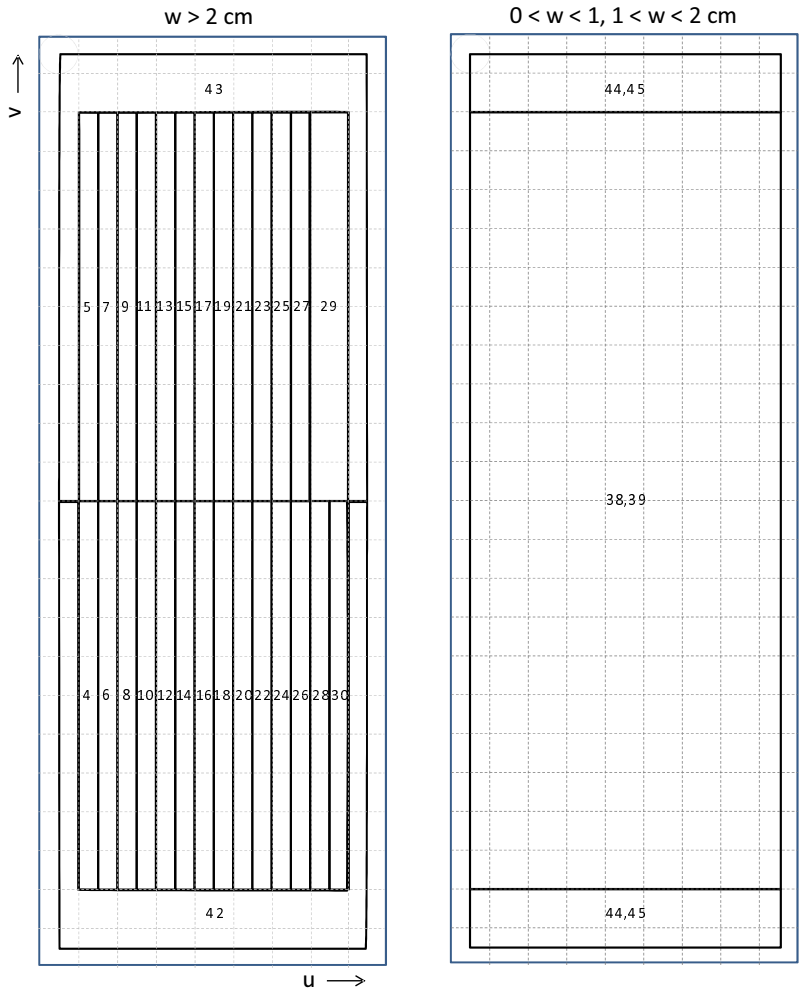

Figure 7.7: Division of the γ-ray acceptance in LXe detector for accidental background PDF.

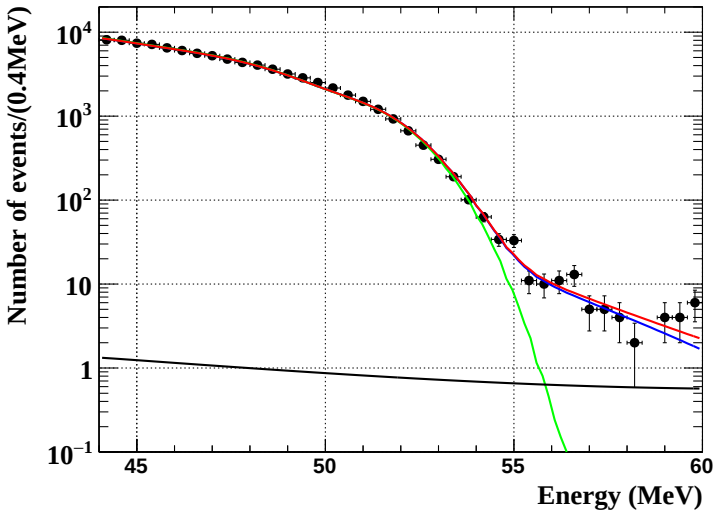

Figure 7.8: Example of E_γ fit on year 2012 data. The green line shows sum of RMD and AIF. The blue shows green convolved with pedestal pile-up. The black line is contribution from cosmic ray. The red line is total fitted function which is sum of blue and black.

7.5 Target Alignment

As concluded in Sec. 4.4, the target bowing is confirmed with the consistent results from three independent measurements. The positron momentum and vertex position are corrected by the method shown in the section.

The shift of the observable $\phi_{e\gamma}$ mainly comes from the shift of ϕ_e in Eq. (4.12). The shift of the decay point $(\Delta x_e, \Delta y_e, \Delta z_e)$ does not affect reconstruction of $\phi_{e\gamma}$ significantly, because we select almost back-to-back positron and γ-ray, hence the contribution from the shift of vertex cancels out. The effect by the shifts of the any observables on $\theta_{e\gamma}$ is not significant.

The target position uncertainty in z_t axis and local deformation which is seen with FARO scanner still remains as the source of the systematic uncertainty. The uncertainties are taken into account by profiling. We introduce two nuisance parameters for each year. The parameters are p_i and s_i to indicate the uncertainty of global shift and local shape respectively. (i indicates the year.) These parameters are used to shift the center of $\phi_{e\gamma}$ PDF. This shift is done after all corrections shown in Sec. 7.4.1.5.

$$\mu_\phi = \Delta_p \phi_{e\gamma}(p, \phi_e) + [\Delta_{\mathrm{FARO}} \phi_{e\gamma}(x_e, y_e) - \Delta_{\mathrm{para}} \phi_{e\gamma}(x_e, y_e)] \cdot s \tag{7.23}$$

Δ_{FARO} is scaled for each year according to the fitted curvature of paraboloid. When $s = 1$, the PDF follows the shape observed by FARO scanner. On contrary, the PDF follows paraboloid when $s = 0$.

Finally, the PDF for $\theta_{e\gamma}$ and $\phi_{e\gamma}$ including the nuisance parameters can be written as,

$$P(\theta_{e\gamma}, \phi_{e\gamma}) = \mathcal{G}(\theta_{e\gamma}; \mu_\theta(p, s), \sigma_\theta) \cdot \mathcal{G}(\phi_{e\gamma}; \mu_\phi(p, s), \sigma_\phi) \cdot P(p) \cdot P(s), \tag{7.24}$$

where $\mathcal{G}(x; \mu, \sigma)$ shows a Gaussian distribution, $P(p)$ and $P(s)$ are PDF for the nuisance parameters p and s to determine the region to be fitted and uncertainty. We assigned a Gaussian PDF for p with mean of 0 and year-dependent σ according to the accuracy of the reliability

of the target hole analysis. For the shape parameter s, constant distributions are assigned, and the range of the distribution is 0 to 1 for year 2013 data, while a narrower range is assigned for 2009-2012 data, as the deformation is not visible for 2009 and 2010 data, and the deformation is thought to gradually progressed. The parameters for the $P(p)$ and $P(s)$ are shown in Table 7.1.

Table 7.1: PDF parameters for p global shift and s the parameter for shape

Year	p σ (mm)	Range of s
2009	0.3	[0, 0.1]
2010	0.3	[0, 0.1]
2011	0.3	[0, 0.4]
2012	0.3	[0, 0.5]
2013	0.5	[0, 1.0]

7.6 AIF reduction

The AIF which was described in Sec. 3.5 is newly introduced in physics analysis. For the events where AIF candidates are found, the "distance" is calculated. If the distance is smaller than the certain threshold, the event is discarded from the likelihood analysis.

7.6.1 Definition of the distance

There is structure with two peaks in $\Delta\theta_{\mathrm{AIF}} - \Delta\phi_{\mathrm{AIF}}$ distribution, and the size and shape of the peak differ from year to year. In order to treat the nearness in common scale, we defined the distance in the AIF analysis, based on Mahalabinos distance (a distance considering the correlation in multi-dimensional space).

$$D = \mathrm{Min}(D_1, D_2) \tag{7.25}$$

$$D_i = \left[(\boldsymbol{x} - \boldsymbol{c}_i)^T S_i^{-1} (\boldsymbol{x} - \boldsymbol{c}_i) \right]^{\frac{1}{2}}, \tag{7.26}$$

where $i = 1, 2$ indicate peaks of type-A and B events, $\boldsymbol{x} = (\Delta\theta_{\mathrm{AIF}}, \Delta\phi_{\mathrm{AIF}})$, and $\boldsymbol{c}$ shows the positron of the peak, and S is a matrix which shows spread of the distribution. The Mahalabinos distance is normalized with the width of the distribution. If the distribution has no correlation and Gaussian shape for each axis, $D = 1$ means the distance of σ from the peak. The parameters $\boldsymbol{c}_i$ and S are determined by fitting the data in the timing sideband. The fitting is performed for the data with

- 48 MeV $< E_\gamma <$ 58 MeV,
- 50 MeV $< E_{\mathrm{e}} <$ 56 MeV,
- $|\theta_{\mathrm{e}\gamma}|, |\phi_{\mathrm{e}\gamma}| <$ 200 mrad,
- $|\Delta t_{\mathrm{AIF}}| <$ 50 ns.

The angular cut is loosened in order to collect more data. It is known that, when the $\phi_{\mathrm{e}\gamma}$ cut is loosened, the shape of $\Delta\phi_{\mathrm{AIF}}$ distribution changes.

However, this fit is used just to parameterize the shape of the distribution and define the cut threshold, so an excellent agreement between the fitting function and the data distribution is not necessary. It is found that in the range of 200 mrad, the distribution still shows the similar shape to that for the final analysis range of 75 mrad. The fitting function is defined as,

$$
\begin{aligned}
F(\Delta\theta_{\mathrm{AIF}}, \Delta\phi_{\mathrm{AIF}}) &= \sum_{i=1}^{3} a_i \mathcal{G}_i^{(2)} \\
&= \sum_{i=1}^{3} a_i \frac{1}{2\pi\sqrt{|S_i|}} \exp\left(-\frac{1}{2}(\boldsymbol{x}-\boldsymbol{c}_i)^T S_i^{-1}(\boldsymbol{x}-\boldsymbol{c}_i)\right),
\end{aligned}
\tag{7.27}
$$

where $i = 1, 2, 3$ show components of type-A, B peaks and base and $\mathcal{G}^{(2)}$ is Gaussian distribution with correlation in 2D space (is defined in the second line). There are 3 components times 6 parameters, i.e.

$$
a, \quad \boldsymbol{c} = (\theta^0, \phi^0)^T, \quad S = \begin{pmatrix} \alpha & \gamma \\ \gamma & \beta \end{pmatrix}. \tag{7.28}
$$

$\sqrt{\alpha}^{-1}$ and $\sqrt{\beta}^{-1}$ corresponds σ in $\Delta\theta_{\mathrm{AIF}}$ and $\Delta\phi_{\mathrm{AIF}}$ axis.

7.6.2 Fit parameters

Figure 7.9 and 7.10 shows the result of the fit for each year. The fraction of the type-A, B, base and the fraction not to find any AIF candidate is summarized in Table 7.2.

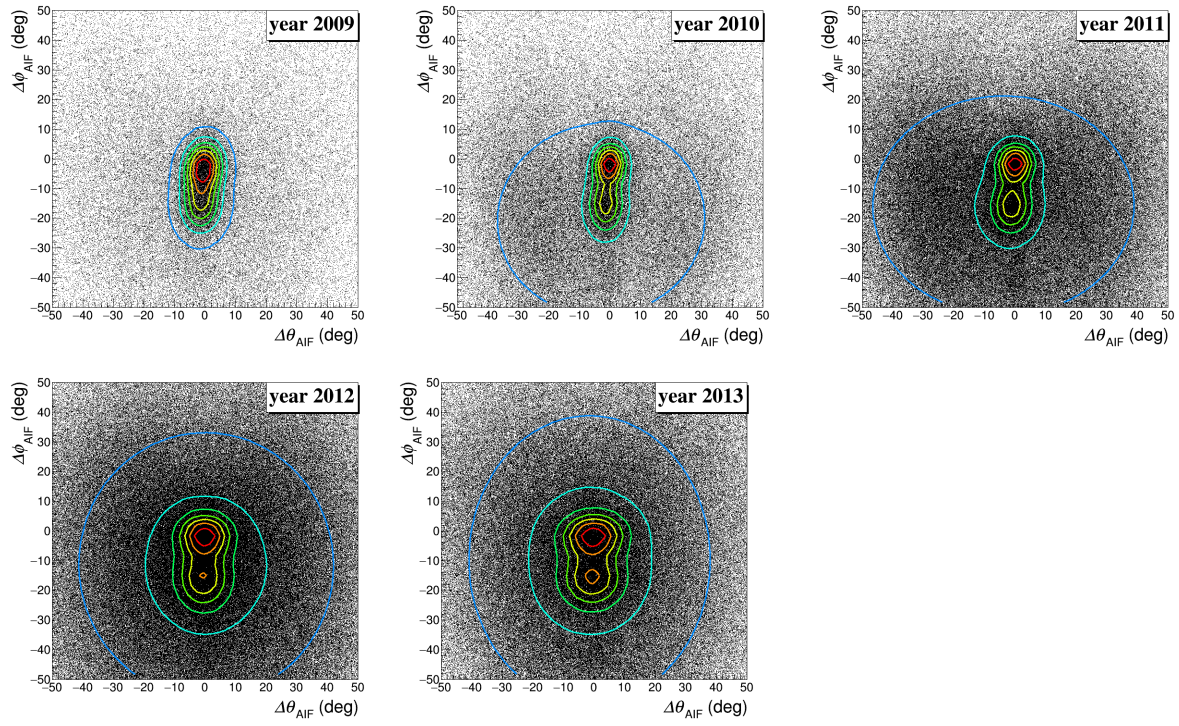

Figure 7.9: Fit result on sideband data of each year. The fitted function is shown with contour.

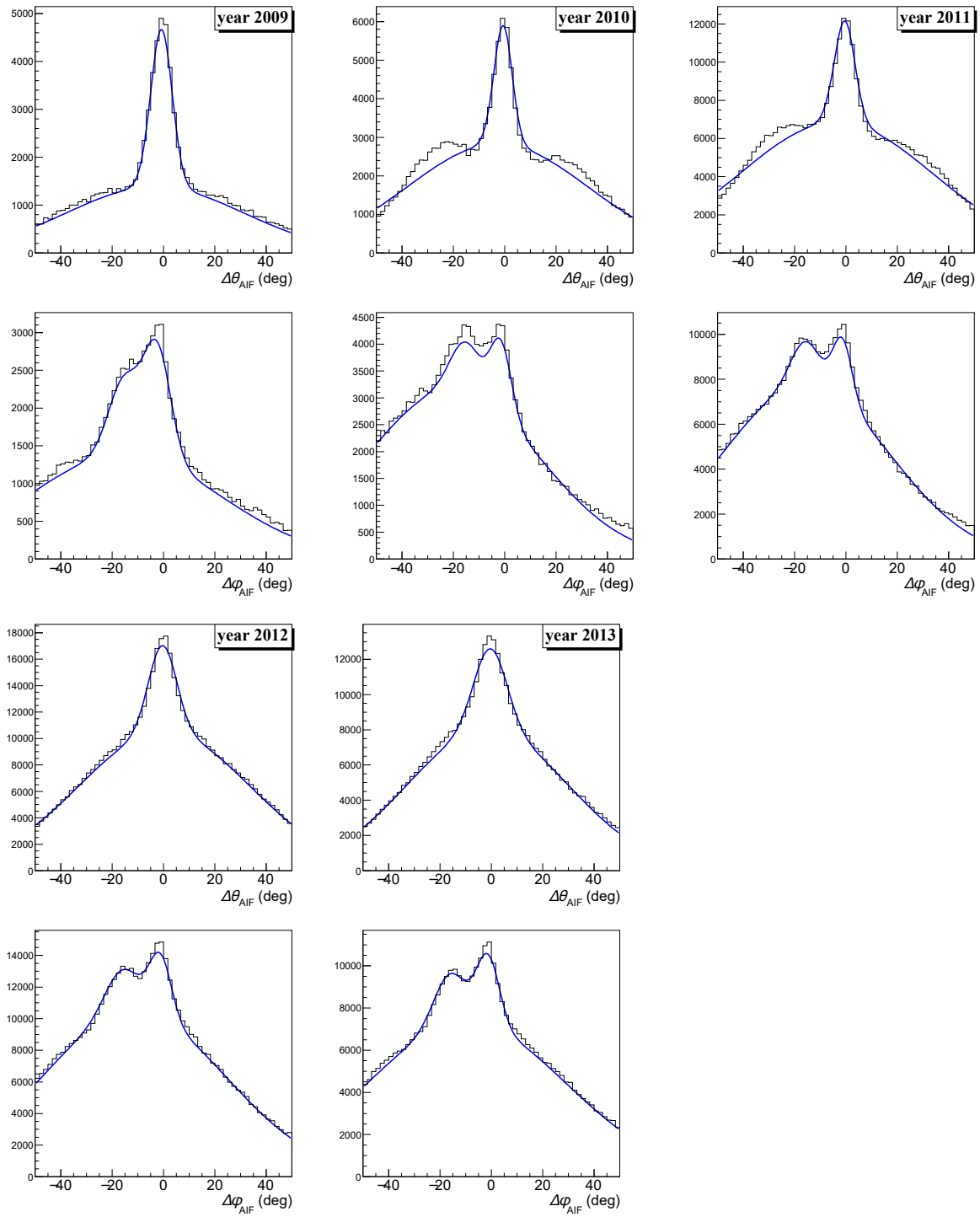

Figure 7.10: Projection of 2D fit to $\Delta\theta_{\mathrm{AIF}}$ and $\Delta\phi_{\mathrm{AIF}}$ for each year. The data and fitted function are shown with black and blue lines, respectively.

Table 7.2: Fraction of the fitted peak and events out of the selection. f_1, f_2, f_{base}, f_{out} and f_{noAIF} means the fraction of type-A, type-B, base, out of the boundary and no AIF events, respectively. The numbers are shown in percentage.

Year	f_1	f_2	f_{base}	f_{out}	f_{noAIF}
2009	4.1 ± 0.1	3.1 ± 0.1	32.0 ± 0.3	44.5 ± 0.4	16.3 ± 2.4
2010	1.5 ± 0.03	1.5 ± 0.03	33.6 ± 0.2	46.4 ± 0.3	17.0 ± 1.9
2011	1.2 ± 0.02	1.3 ± 0.02	36.2 ± 0.1	43.3 ± 0.2	18.0 ± 2.1
2012	1.4 ± 0.02	1.5 ± 0.03	35.3 ± 0.1	46.3 ± 0.2	15.4 ± 2.1
2013	1.7 ± 0.03	1.8 ± 0.03	38.3 ± 0.2	45.6 ± 0.2	12.6 ± 2.0

Since the timing sideband only includes accidental background, the fitted result is what actually expected for the accidental background in the analysis window. The information of the timing is different, but it is not used in calculation of the distance. Figure 7.11 shows the efficiency to reject accidental background and acceptance of the signal. The efficiencies of each year are shown in Table 7.3. The way to estimate efficiency for signal is described in Appendix B. As the signal inefficiency of more than 1%, which is the same as that for CR cut in LXe, is not acceptable, and the BG/signal ratio is relatively flat there, the cut threshold is set to be 0.7σ (blue circle in Fig. 7.11).

The sensitivity was examined with and without the AIF cut, and it is shown that the cut does not significantly improve the sensitivity. However, the AIF event possibly lie in the signal region accidentally. The cut is applied for just to avoid such an outlier event.

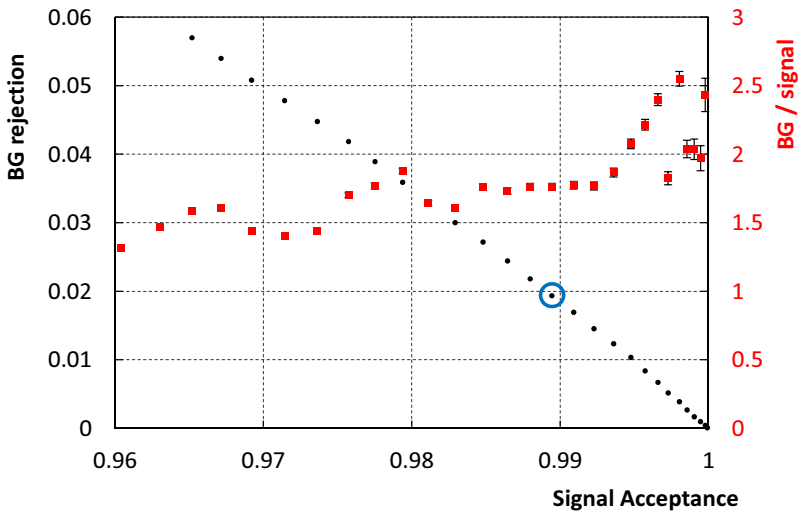

Figure 7.11: Black marker shows relation of the signal acceptance and BG rejection with various cut thresholds. The cut at the blue circle is adopted. Red marker shows the ratio of BG against signal as a function of signal efficiency. Data of the all years are summed.

7.7 Normalization

Since the result of the likelihood fitting provides the number of the signal event, we need to convert it to the branching ratio of the $\mu^+ \to e^+\gamma$ decay. We defined the normalization factor k

Table 7.3: Selection inefficiency by the AIF cut. The numbers show fraction in percentage.

Year	ACC	signal/RMD
2009	1.00 ± 0.03	3.00 ± 0.20
2010	0.64 ± 0.02	1.33 ± 0.09
2011	0.61 ± 0.01	1.34 ± 0.10
2012	1.46 ± 0.02	2.23 ± 0.11
2013	1.30 ± 0.02	2.22 ± 0.11
Old	0.68 ± 0.01	1.57 ± 0.06
New	1.39 ± 0.02	2.23 ± 0.08
Full	1.05 ± 0.01	1.94 ± 0.05

as follows,

$$\mathcal{B}(\mu^+ \to e^+\gamma) = \frac{\Gamma(\mu^+ \to e^+\gamma)}{\Gamma_{\text{total}}} = \frac{N_{\text{sig}}}{k} \tag{7.29}$$

The normalization factor is regarded to be the number of the muon multiplied by detector acceptance and efficiency, $k = N_\mu \times \Omega \times \varepsilon$. ($N_\mu$ is the number of all muons which stopped on MEG target.) The inverse of factor, k^{-1} is equivalent to a single event sensitivity in the box counting scheme (though we do not adopt that analysis scheme). We calculate the normalization factor from two independent samples and combine them to reduce the uncertainty.

7.7.1 Michel normalization

One method is to calculate the normalization from the number of Michel decay events with following formula.

$$k_{\text{Michel}} = \frac{N^{\text{Michel}}}{f_{E_e}^{\text{Michel}}} \times \frac{P^{\text{Michel}}}{\varepsilon_{\text{trg}}^{\text{Michel}}} \times \frac{\varepsilon_e^{e\gamma}}{\varepsilon_e^{\text{Michel}}} \times A_\gamma^{e\gamma} \times \varepsilon_\gamma^{e\gamma} \times \varepsilon_{\text{trg}}^{e\gamma} \times \varepsilon_{\text{sel}}^{e\gamma}, \tag{7.30}$$

- N_{Michel} : The number of observed event in analysis window, for data taken with Michel trigger, which requires only hits in TIC. $N_{\text{Michel}} = 245860$ is the number which are observed in the full data set.
- $f_{E_e}^{\text{Michel}}$: The fraction that the energy spectrum of the Michel positron within the analysis window.
- P^{Michel} : ($= 10^7$) The pre-scaling value of the Michel trigger. See Sec. 2.5.2.
- $\epsilon_e^{\text{Michel}}$: The correction factor to recover trigger live time, where paralyzable behavior of trigger is assumed.
- $\varepsilon_{\text{signal}}^e / \varepsilon_{\text{Michel}}^e$: The ratio of efficiencies of the positron spectrometer for signal and Michel events. It is obtained to be 1.149 ± 0.017, by fitting response function which is the theoretical Michel spectrum convoluted with the detector resolution and the acceptance functions.
- $A_\gamma^{e\gamma}$: ($= 0.985 \pm 0.005$) The geometrical acceptance for γ-ray when a signal positron is detected.
- $\varepsilon_\gamma^{e\gamma}$: γ-ray detection efficiency which is described in Sec. 5.5.1.
- $\varepsilon_{\text{trg}}^{e\gamma}$: The efficiency to trigger positron–γ-ray pair for signal events. It is calculated to be 0.91 ± 0.01 from 2009 to 2010 and 0.96 ± 0.01 after 2011. (Also see Sec. 5.5.3)

- $\varepsilon_{\rm sel}$: This term includes the selection efficiency calculated from (a) efficiency that signal event comes within the analysis window. It is evaluated with signal PDF. (b) miss-reconstructed positron track, missing turn. (Sec. 3.2.2) (c) signal inefficiency due to AIF rejection (Sec. 7.6 and Appendix. B). The efficiency is 0.943 ± 0.010 in total of (a)-(c).

In total, the uncertainty on $k_{\rm Michel}$ is 4.5%.

7.7.2 RMD normalization

The normalization factor from RMD is calculated as,

$$k_{\rm RMD} = \frac{N_{\rm RMD}}{\mathcal{B}^{\rm RMD}_{E_{\rm e}}} \times \frac{\varepsilon^{\rm signal}_{\rm e}}{\varepsilon^{\rm RMD}_{\rm e}} \times \frac{\varepsilon^{\rm signal}_{\gamma}}{\varepsilon^{\rm RMD}_{\gamma}} \times \frac{\varepsilon^{\rm signal}_{\rm trg}}{\varepsilon^{\rm RMD}_{\rm trg}} \times \frac{\varepsilon^{\rm signal}_{\rm sel}}{\varepsilon^{\rm RMD}_{\rm sel}}. \tag{7.31}$$

Since RMD contains also γ-ray, more terms can be written as the ratio between signal and RMD and it helps to reduce systematic uncertainty from normalization factor. The definition of the parameters are,

- $N^{\rm RMD}$: The number of observed RMD events, the trigger is the same for MEG signal, but analysis window is different (Sec. 7.2.2). The number is obtained by fitting on the $t_{\rm e\gamma}$ distribution.
- $\mathcal{B}^{\rm RMD}$: ($\sim 4.9 \times 10^{-9}$). The branching ratio of muon decays into RMD with the range of kinematics. It is calculated from the theoretical formula by standard model.
- positron efficiency : $E_{\rm e}$ dependent detection efficiency is extracted from the Michel spectrum, $E_{\rm e}$ dependence of the missing turn probability is considered in this factor.
- γ efficiency : Energy dependent γ detection efficiency is calculated from the data with different E_γ threshold. The effect by muon polarization, which makes asymmetric angular distribution, is taken into account here.
- other differences in efficiency : Inefficiency by direction matching for RMD is evaluated from accidental background. The window efficiency for the timing of RMD is the same as signal, so the difference in efficiency on angular window is taken into account. The inefficiency by the AIF rejection is thought to be equivalent to signal and to RMD, therefore no correction term is needed for that.

The number of muons is evaluated in 12 independent bins (3 bins for $E_{\rm e}$ and 4 bins for E_γ), and the best value was obtained with χ^2 fitting to be 29950 ± 527 in the full data set. Figure 7.12 shows the distribution of observed events in the energy sideband, projected on E_γ and $E_{\rm e}$, the expectation from the standard model is superposed. The measured number is consistent to the expectation within 5% error. The details are described in our another publication [90]. Total uncertainty for $k_{\rm RMD}$ is 5.5%.

7.7.3 Combination

The two methods of the normalization uses different data, hence the uncertainties of normalization can be reduced by combining them. The combination is done by averaging the values with weighting by errors. The result is shown in Fig. 7.13. The results from Michel and RMD are in good agreement, the breakdown for each year is summarized in Table 7.4, and the final normalization factor for 2009-2013 combined data is $k = (1.71 \pm 0.06) \times 10^{13}$.

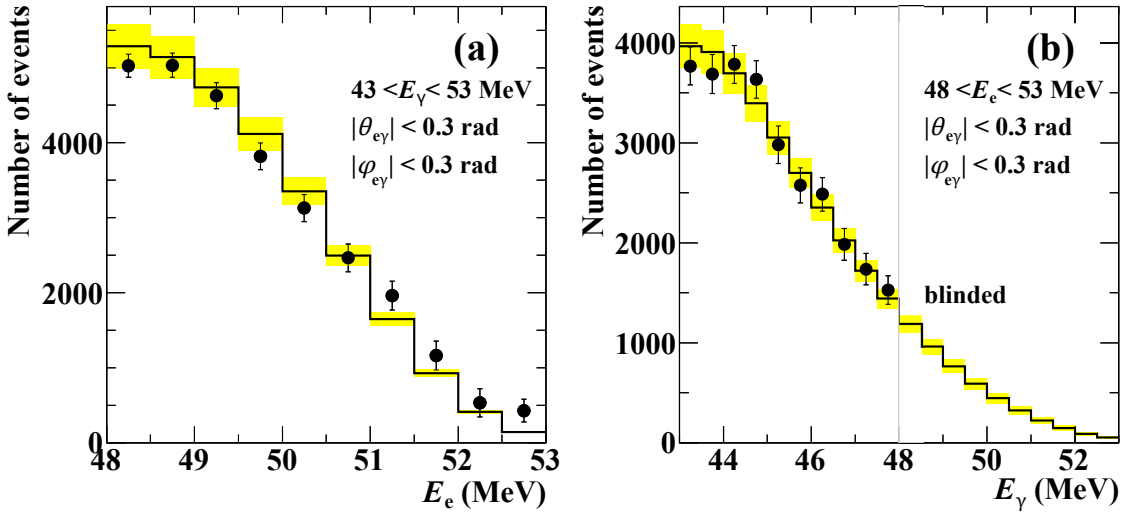

Figure 7.12: Number of observed RMD events in sideband year 2009-2013 projected on (a) E_e and (b) E_γ. The data is plotted with marker and error. Expectation with theoretical calculation of the lowest order SM with the detector response is shown in yellow band.

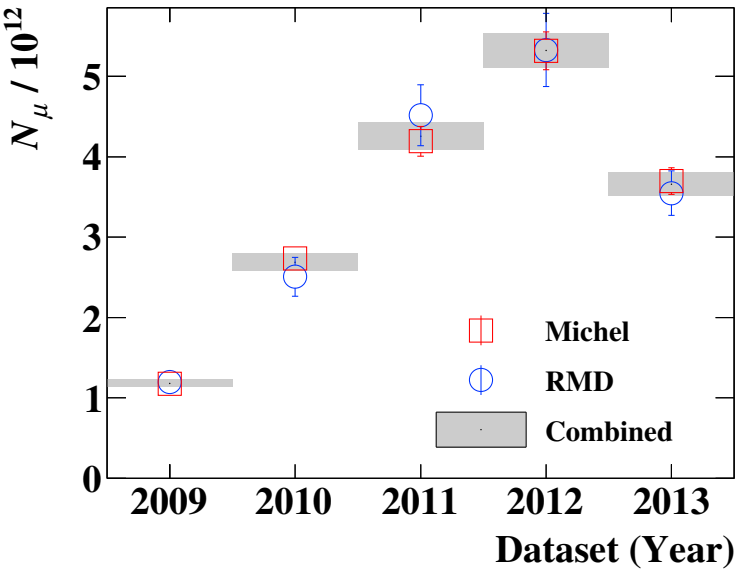

Figure 7.13: Calculated normalization factors from Michel (Red), RMD (Blue) and combined result (Black).

Table 7.4: Summary of normalization constant.

Year	k_{Michel} ($\times 10^{12}$)	k_{RMD} ($\times 10^{12}$)	k_{Combined} ($\times 10^{12}$)
2009	1.18 ± 0.05	1.20 ± 0.11	1.18 ± 0.05
2010	2.73 ± 0.12	2.53 ± 0.24	2.69 ± 0.11
2011	4.19 ± 0.19	4.52 ± 0.39	4.26 ± 0.17
2012	5.32 ± 0.24	5.33 ± 0.46	5.32 ± 0.21
2013	3.70 ± 0.17	3.55 ± 0.28	3.66 ± 0.14
Old	8.10 ± 0.36	8.27 ± 0.55	8.16 ± 0.30
New	9.02 ± 0.41	8.85 ± 0.53	8.96 ± 0.33
Full	17.12 ± 0.77	17.10 ± 0.94	17.11 ± 0.60

Chapter 8

Results

8.1 Sensitivity

The search sensitivity is given by the median of the 90% C.L. upper limits observed in the many pseudo experiments with a background-only hypothesis: in generation, N_{sig} is fixed to be zero, N_{ACC} and N_{RMD} are randomly fluctuated around the expectation value by Poisson distribution. The procedure to calculate the upper limit is as explained in Sec. 7.3.2. The systematic uncertainties (It will be discussed in Sec. 8.1.2) are included in the calculation of the upper limit.

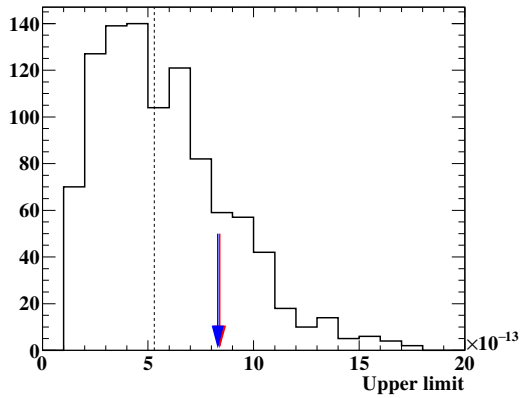

Figure 8.1: The distribution of the ULs of pseudo experiments. UL in N_{sig} is converted to that in branching ratio, with the normalization factor which was explained in Sec. 7.7. Vertical dashed line shows median which represents the sensitivity. Two arrows show the upper limits obtained from the timing sidebands.

Figure 8.1 shows the distribution of the upper limit (UL) for pseudo experiments for 2009-2013 combined, full dataset. The horizontal axis is shown in branching ratio. The sensitivity for the full, old and new data are 5.3×10^{-13}, 8.0×10^{-13} and 8.2×10^{-13}, respectively.

The sensitivity with new statistics has worse sensitivity despite more data amount. It is due to worse positron angle resolution, and the larger uncertainty of the target parameter. We already analysed 2009-2011 dataset in our last publication [13] with the sensitivity 7.7×10^{-13}. The sensitivity for 2009-2011 data presented here is slightly worse than that presented in the

previous publication even though the analysis method was improved. The main reason for this degradation is that more conservative uncertainty is assigned for the target alignment also for 2009-2011 data where an obvious target deformation was not observed.

8.1.1 Results in the sidebands

For the purpose of the sanity check of our likelihood analysis, a likelihood analysis on the timing sideband is performed. The timing sideband is defined as the same selection for analysis window except for the timing (Sec. 7.2.2). In the timing sideband, the data can essentially be regarded as pure accidental background. The likelihood function is modified for the timing sideband in two points. (a) The constraint term for the N_{RMD} is removed. (b) The definition of $t_{\mathrm{e}\gamma}$ in PDF is shifted.

The fit results are shown in Fig. 8.2 and Table 8.1. The projected PDF spectra agree to data spectra. The best fit N_{sig} and N_{RMD}, which are expected to be null, are zero consistent within the statistical error.

The confidence interval for the branching ratio is calculated. The upper limits for the negative (−2ns) and positive (+2ns) sidebands in the full combined datasets are 8.4×10^{-13} and 8.3×10^{-13}. They are consistent with the sensitivity as shown in Fig. 8.1.

Table 8.1: Best fit value and fit error in the timing sidebands.

	Data set	Full	Old	New
negative	N_{sig}	2.8 ± 5.8	7.3 ± 5.2	−3.7 ± 2.1
timing	N_{RMD}	39 ± 45	46 ± 32	−3.7 ± 32
(−2ns)	N_{ACC}	7756 ± 38	3475 ± 26	4281 ± 28
positive	N_{sig}	3.9 ± 4.6	1.0 ± 3.1	2.8 ± 3.6
timing	N_{RMD}	17 ± 45	21 ± 31	−3 ± 32
(+2ns)	N_{ACC}	7736 ± 38	3468 ± 26	4268 ± 28

8.1.2 Systematic error

The systematic uncertainties considered in the analysis are the alignment of γ-ray and positron detectors, the alignment of the muon stopping target, the γ-ray energy scale, the positron energy bias, the center of the $t_{\mathrm{e}\gamma}$ PDF, the shapes of signal and background PDFs, the correlations between the errors of the positron observables and the normalization factor.

The largest systematic uncertainty comes from the alignment of muon stopping target; it degrades the average sensitivity by 13%, while the effect from all the other systematics is less than 1%. The breakdown of the systematic errors is listed in Table 8.2.

8.2 Results in analysis window

8.2.1 Event distributions

Figure 8.3 shows the event distributions in the analysis window. In order to avoid the window is too much crowded, selections of $\cos\Theta_{\mathrm{e}\gamma} < -0.99963$ and $|t_{\mathrm{e}\gamma}| < 0.24$ ns are applied for

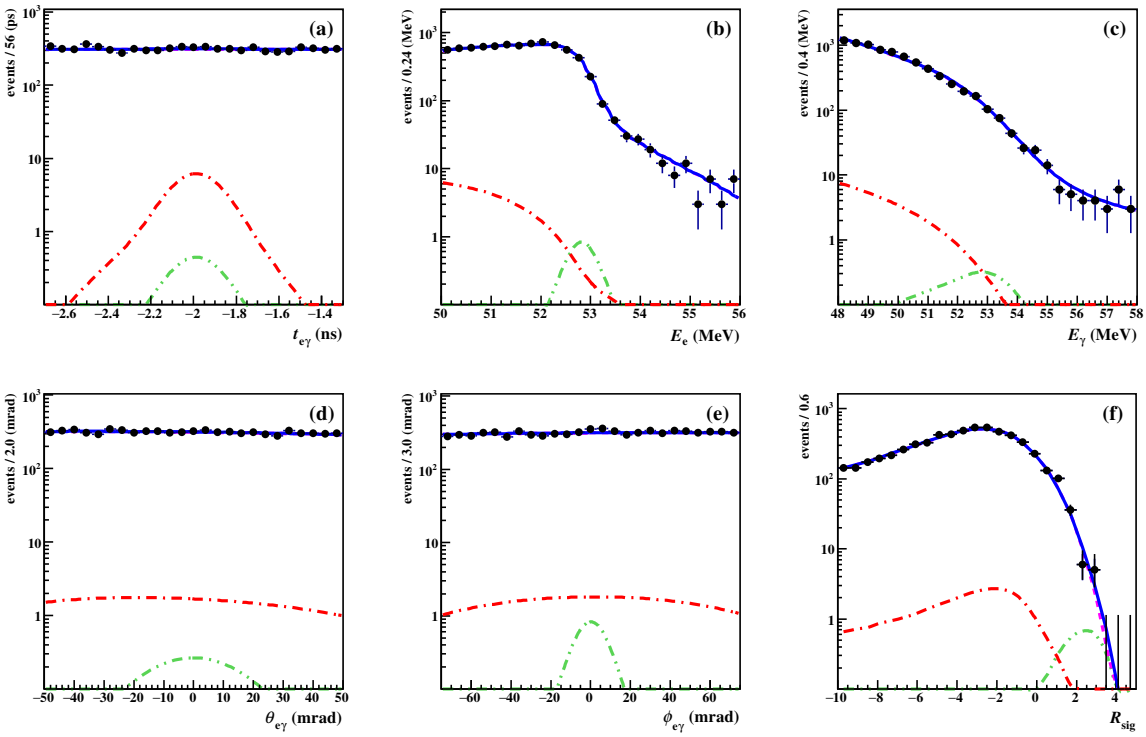

(a) Negative Timing Sideband ($-2.7 < t_{e\gamma} < -1.3$ns)

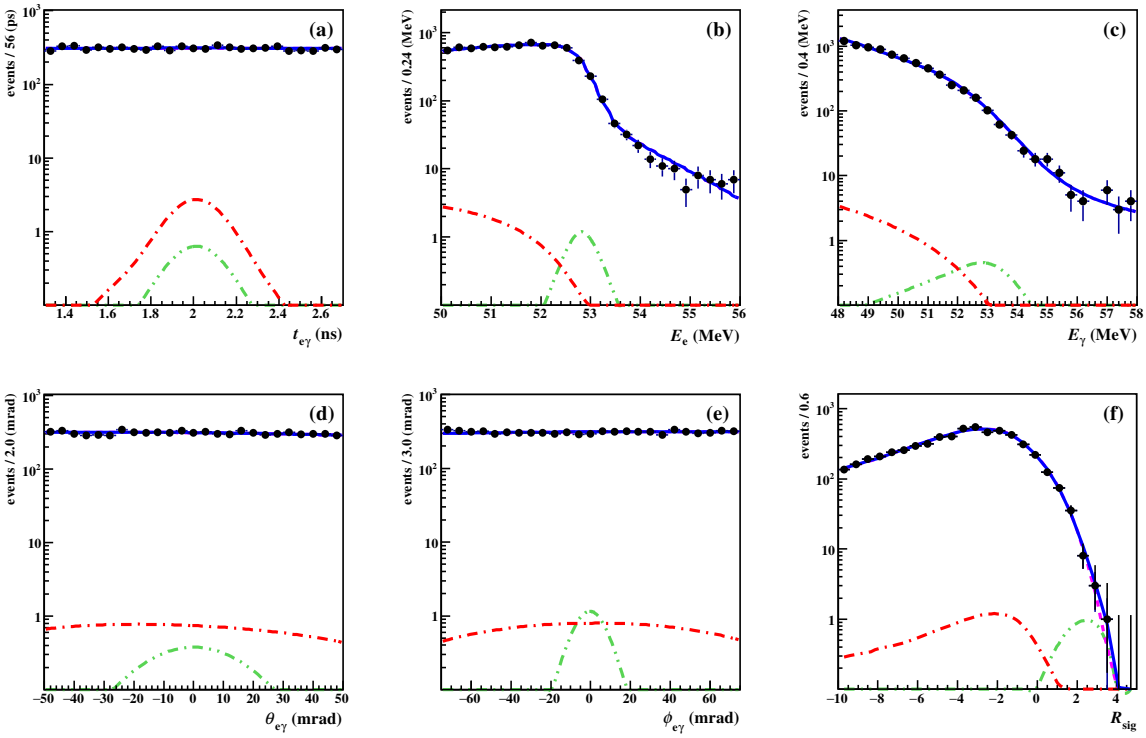

(b) Positive Timing Sideband ($1.3 < t_{e\gamma} < 2.7$ns)

Figure 8.2: Result of the fitting on the timing sidebands for the full dataset. The projection on the main observables and R_{sig} (Sec. 8.2.2). The parameters f_R and f_A are set to be 0 and 1, in calculation of the R_{sig}.

Table 8.2: The list of the considered systematic uncertainties. The impact of the target is dominant. The fractions of impacts of the other uncertainties are written in parentheses.

Element	Impact on sensitivity
Alignment of muon stopping target	13%
All the other	<1%
Alignment of LXe detector - tracker	(37%)
E_γ scale	(23%)
bias of center of $t_{e\gamma}$ PDF	(19%)
E_e bias	(11%)
Normalization	(7%)
errors in event-by-event PDF	(3%)

left figures both with 90% efficiency for signal, and $51.0 < E_\gamma < 55.5$ MeV and $52.4 < E_e < 55.0$ MeV are applied for right figures with 74% and 90% efficiency, respectively. The contours of the averaged signal PDFs are also shown. An obvious correlated excess of signal is not found in any datasets.

8.2.2 Highly ranked events

We rank the events in the order of the signal likelihood R_{sig} which is defined as

$$R_{sig} = \log_{10}\left(\frac{S(\boldsymbol{x}_i)}{f_R R(\boldsymbol{x}_i) + f_A A(\boldsymbol{x}_i)}\right), \tag{8.1}$$

where f_R and f_A are ratio of RMD and accidental background which are taken from the best fit values 0.07 and 0.93, respectively. The events with the highest R_{sig} are listed in Table 8.3.

Table 8.3: Highly ranked (signal like) events

Rank	Year	Run	Event	R_{sig}	$t_{e\gamma}$ (ps)	E_e (MeV)	E_γ (MeV)	$\theta_{e\gamma}$ (mrad)	$\phi_{e\gamma}$ (mrad)	$\cos\Theta_{e\gamma}$
1	2010	77431	1715	3.01	142	52.93	53.98	-25.2	-2.4	-0.99968
2	2012	195187	1856	2.70	-75	53.34	51.74	-0.1	-9.2	-0.99996
3	2012	189150	1089	2.41	-6	52.19	52.95	10.6	16.6	-0.99981
4	2012	160737	785	2.31	48	52.82	51.92	8.3	6.1	-0.99995
5	2009	56081	35	2.26	-22	52.52	52.81	-20.7	15.8	-0.99967
6	2012	167931	1076	2.25	415	53.18	53.78	-7.7	-23.6	-0.99969
7	2013	228740	1892	2.23	397	52.95	50.55	-0.8	-5.7	-0.99998
8	2011	123579	1318	2.23	-21	52.81	55.13	-33.6	13.0	-0.99936
9	2012	185612	1612	2.18	13	52.82	55.41	12.9	-29.8	-0.99948
10	2010	87743	1484	2.15	-81	52.91	52.28	-18.1	24.0	-0.99955

Figure. 8.4 shows the $(E_e - E_\gamma)$ and $(\cos\Theta_{e\gamma} - t_{e\gamma})$ plots for 10 events of highest signal-like. Some events which are not drawn in Fig. 8.3 appear, as the selection defined in Sec. 8.2.1 is not applied here. The contours show averaged signal PDF of 1σ, 1.64σ and 2σ, respectively.

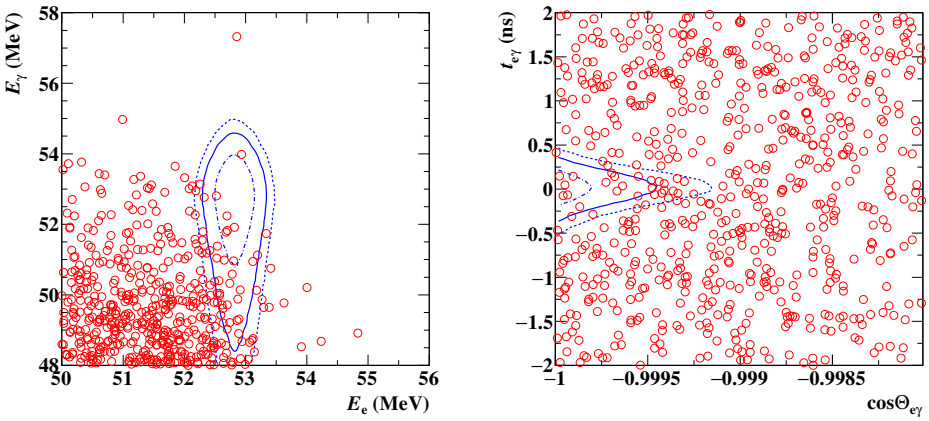

(a) 2009-2013 dataset

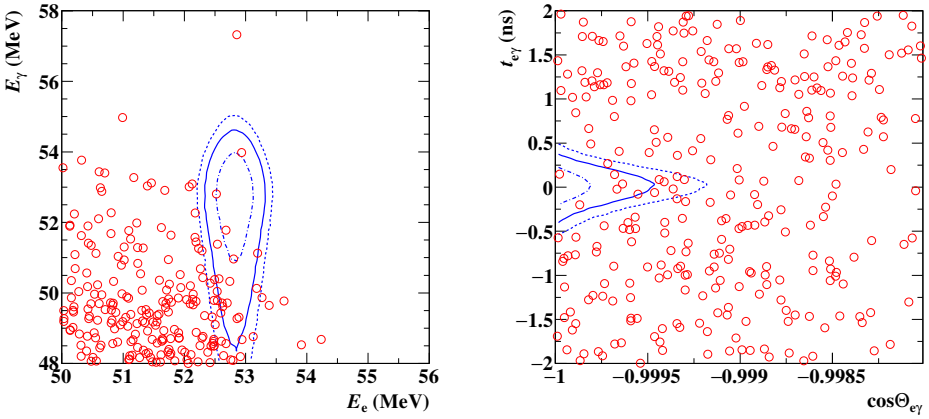

(b) 2009-2011 dataset

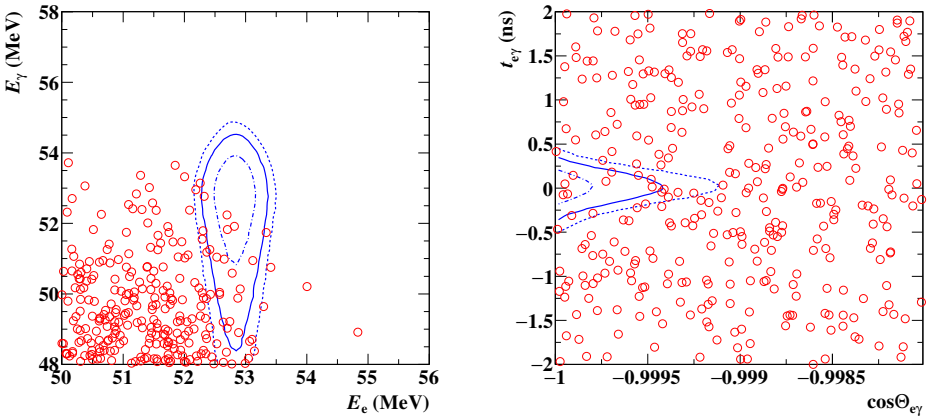

(c) 2012-2013 dataset

Figure 8.3: Event distributions observed in the analysis window. The signal PDFs are shown with contour (1σ, 1.64σ and 2σ).

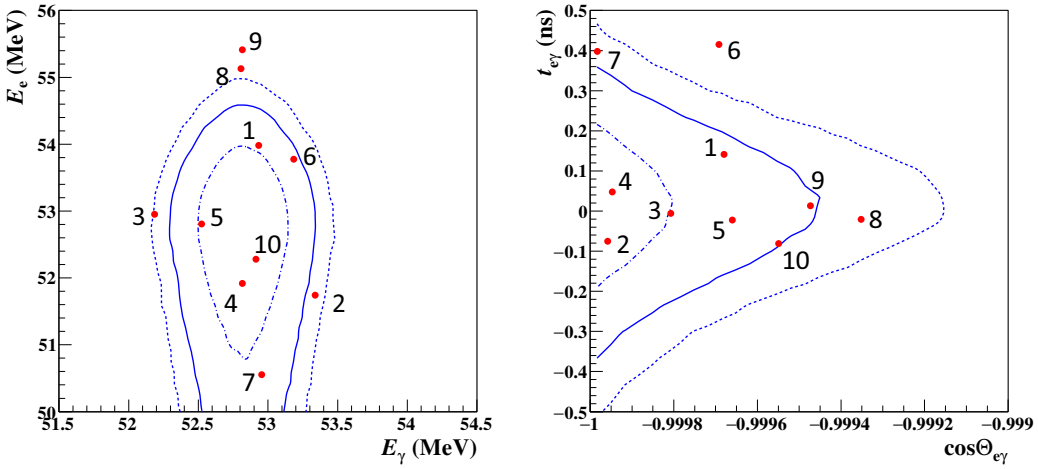

Figure 8.4: Top 10 highest signal-like events in $(E_e - E_\gamma)$- and $(\cos\Theta_{e\gamma} - t_{e\gamma})$-planes. Contours show averaged signal PDF of 1σ, 1.64σ and 2σ.

8.2.3 Fit results

The maximum likelihood fitting was performed on the data in the analysis window. The best fit value, $(\hat{N}_{sig}, \hat{N}_{RMD}, \hat{N}_{ACC})$ for the all combined dataset is $(-3.8\pm3.6, 624.6\pm28.4, 7739.1\pm37.7)$. The errors are the fit error with MINUIT. With this best fit $N_{\rm sig}$, the best fit branching ratio is $(-2.2 \pm 2.1) \times 10^{-13}$. The projections onto the 5 main observables are shown in (a)-(e) of Fig. 8.5.

The data and the fitted PDF shows good agreement. The agreement of fit is checked with the variable $R_{\rm sig}$. The comparison of data and the PDF on $R_{\rm sig}$ axis is shown in (f) of Fig. 8.5.

Table 8.4: Best fit value and fit error

Data set	Full	Old	New
$N_{\rm sig}$	7739.1 ± 37.7	3470.7 ± 25.2	4269.0 ± 27.6
$N_{\rm RMD}$	624.6 ± 28.4	284.6 ± 16.6	337.1 ± 17.8
$N_{\rm ACC}$	−3.8 ± 3.6	−1.0 ± 2.0	−4.9 ± 4.4
p_{09}	10 ± 297	6 ± 300	
p_{10}	−83 ± 321	−32 ± 300	
p_{11}	−1 ± 297	−1 ± 300	
p_{12}	8 ± 289		11 ± 300
p_{13}	−2 ± 499		−4 ± 500
s_{09}	0 ± 0.7	0 ± 0.1	
s_{10}	0 ± 0.5	0 ± 0.1	
s_{11}	1 ± 0.5	1 ± 0.1	
s_{12}	1 ± 1.0		1 ± 0.1
s_{13}	0 ± 0.5		0 ± 0.1

The results for the other datasets are shown in Fig. 8.6 and summarized in Table 8.4. The best fit value for target observables p and s are found by the fitting, but it does not imply the real shape of the target, because only the signal PDF has a peak in $\phi_{e\gamma}$ and the best fit $N_{\rm sig}$ is consistent with 0. No information for the true center of $\phi_{e\gamma}$ can be extracted from the observed

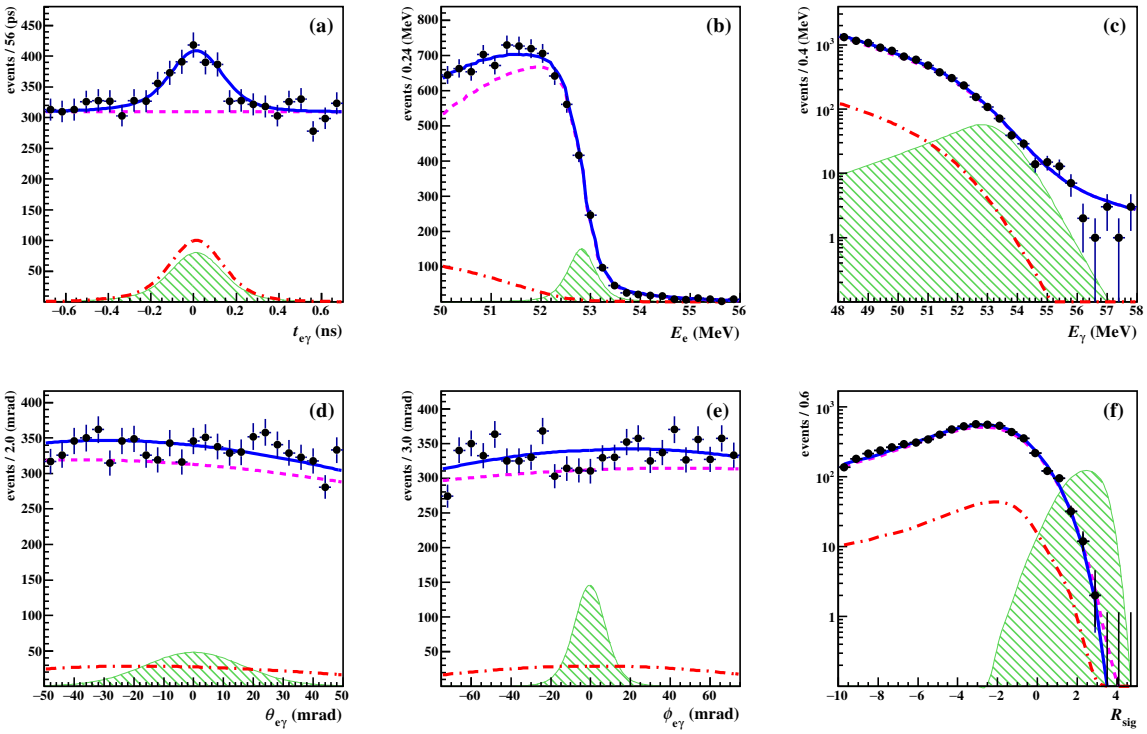

Figure 8.5: The 1D projections of the 2009-2013 combined data. The marker is data with statistic error. The solid blue lines are sum of the best fit PDFs. The dashed magenta and dot-dashed red lines are accidental background and RMD PDF which are normalized to best fit value of each component. The hatched green histograms show signal PDF scaled to 500 events.

data.

8.2.4 Upper limit for branching ratio

The confidence interval for the data is calculated with the procedure described in Sec. 7.3.2. Figure 8.7(a) shows the negative log likelihood Eq. (7.9) as a function of the branching ratio. The best fit value of the target parameter s shifts from one to another, when the branching ratio moves over zero. This is the reason for the bending of the curve around zero. The results for the all datasets are consistent with null-signal hypothesis, therefore only upper limits are defined. In Fig. 8.7(b), the fraction of the toy-MCs which satisfies Eq. (7.10) are shown as the function of the branching ratio. The 90% C.L. upper limits are obtained to be

- 4.2×10^{-13} with 2009-2013 (full) data set,
- 6.1×10^{-13} with 2009-2011 (old) data set and
- 7.9×10^{-13} with 2012-2013 (new) data set, respectively.

Our previous result with 2009-2011 data is 5.7×10^{-13} [13]. The previous limit is slightly more stringent but is consistent when differences of the analysis are considered. Firstly since the reconstructed observables were slightly changed because of the updates of the analysis, the observed upper limit can be changed due to the statistical effect. Secondly the sensitivity becomes worse as described in Sec. 8.1 due to the larger systematics.

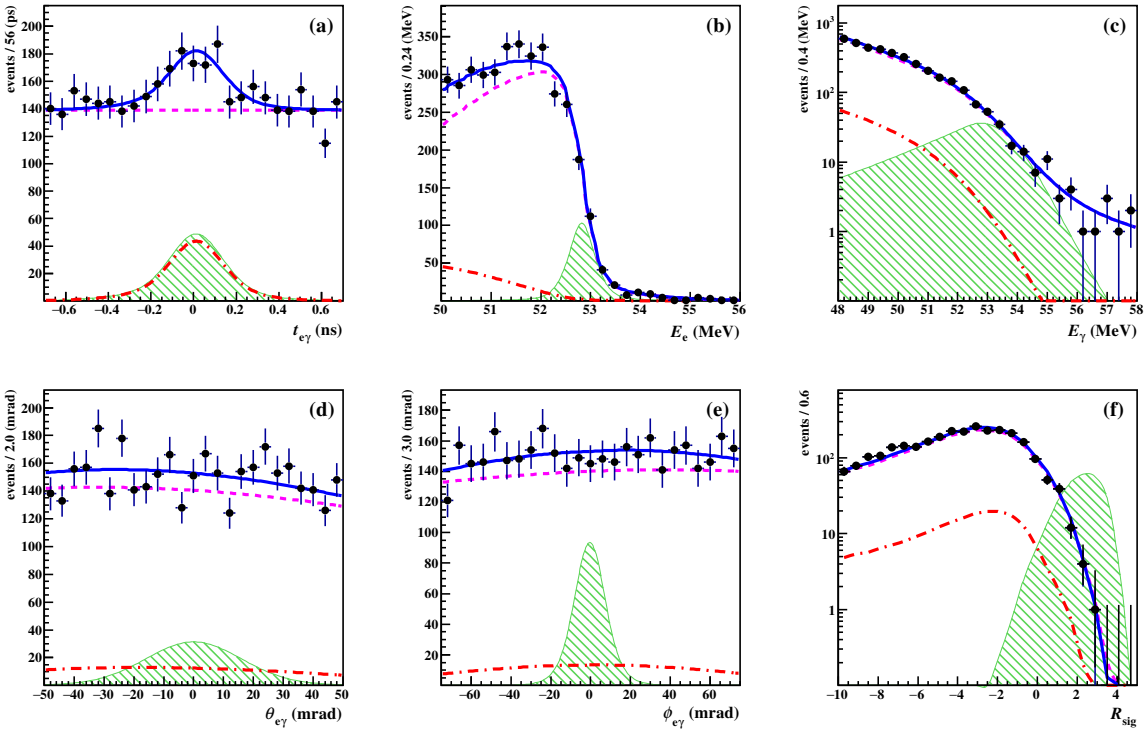

(a) 2009-2011 dataset

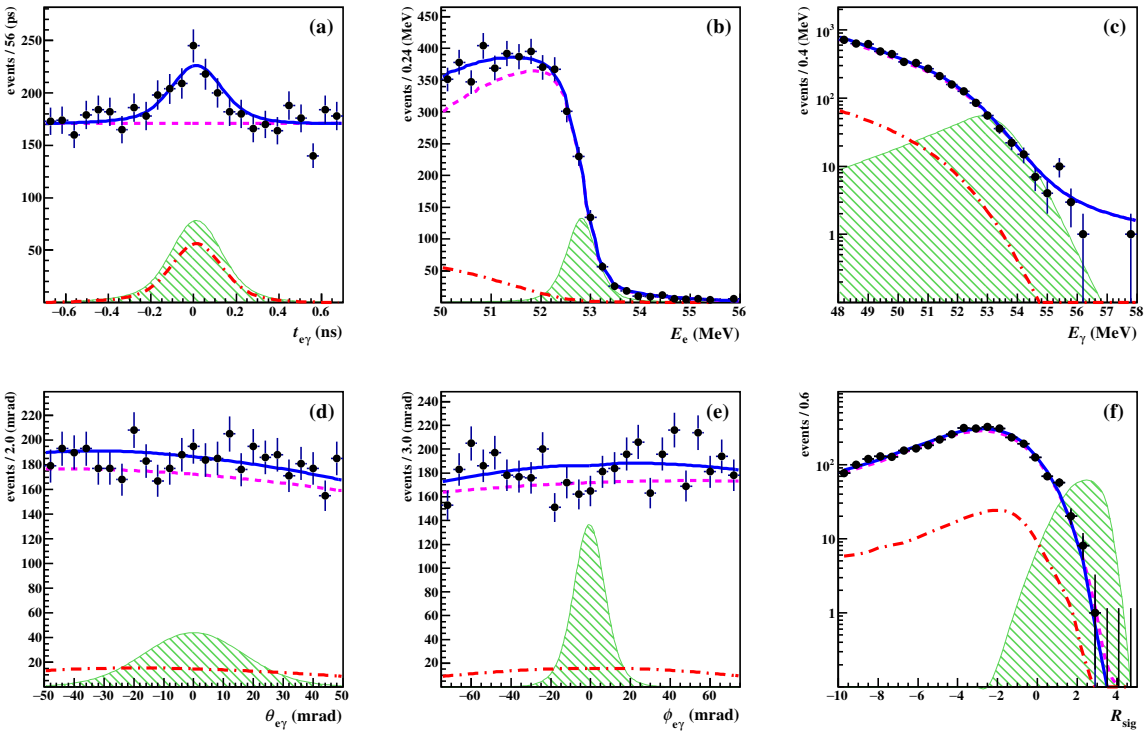

(b) 2012-2013 dataset

Figure 8.6: The 1D projections of (a) old and (b) new data. Notation follows Fig. 8.5. Normalization of the signal PDFs are 250 events for both (a) and (b).

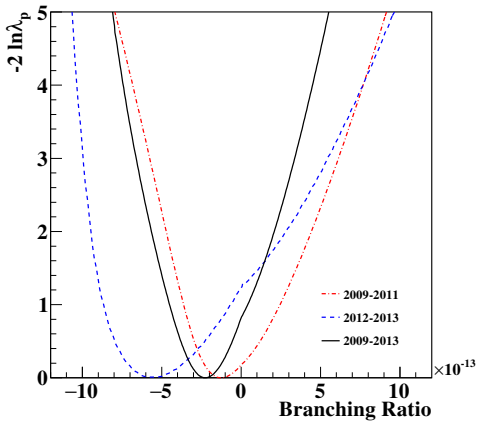

(a) The negative log likelihood as a function of the branching ratio. The point where $-2\ln(\lambda) = 0$ shows the best fit value.

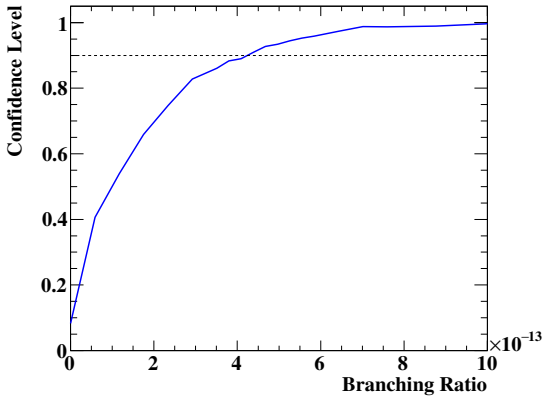

(b) The confidence level as a function of the branching ratio. 90% C.L. limit is defined by the crossing point of curve and 0.9 horizontal line.

Figure 8.7: Result of the limit calculation by maximum likelihood analysis.

The effect of the systematic uncertainty is studied with the observed data. The largest contribution is the effect from the target uncertainty. The deterioration in upper limit is calculated to be $\sim 5\%$ for the full dataset. The other systematics are also considered, however, the impact of all the other systematics is less than 1%.

8.3 Check for the analysis

8.3.1 Comparison with previous analysis

The difference of the result between this and the previous analysis was studied. We have changed the analysis method from the reconstruction level, so the main observables can move event-by-event. The changed item and affected observables are the followings.

- Drift chamber pad issue : There was a mistake in the treatment of the case of defective cathode pad (Sec. 3.2.1). The hit position in z axis is fixed in track reconstruction, for hits at defective channels. All of the positron observables are affected. For newer data, the size of the effect is larger.
- Target alignment : The affected observable is mostly $\phi_{e\gamma}$. The impact for the observable is almost negligible for 2009 and 2010 data.
- LXe detector alignment : γ-ray position is affected. $\theta_{e\gamma}$ and $\phi_{e\gamma}$ moves in all events.
- Missing turn : The fraction of the affected event is small. However if a missing turn is recovered, the event moves out or in the analysis window.
- AIF reduction : If the AIF distance is less than the threshold, the event disappears.

We compared the current 2009-2011 combined dataset with the previous one. Out of the events included in previous dataset, 14% go out from the analysis window, and 62% (of the number in the previous dataset) newly appeared in the analysis region. The reason of more

appearance than disappearance is the current analysis window is widened. Figure 8.8 and 8.9 shows the comparison of the observables for the events commonly selected in previous and current analysis.

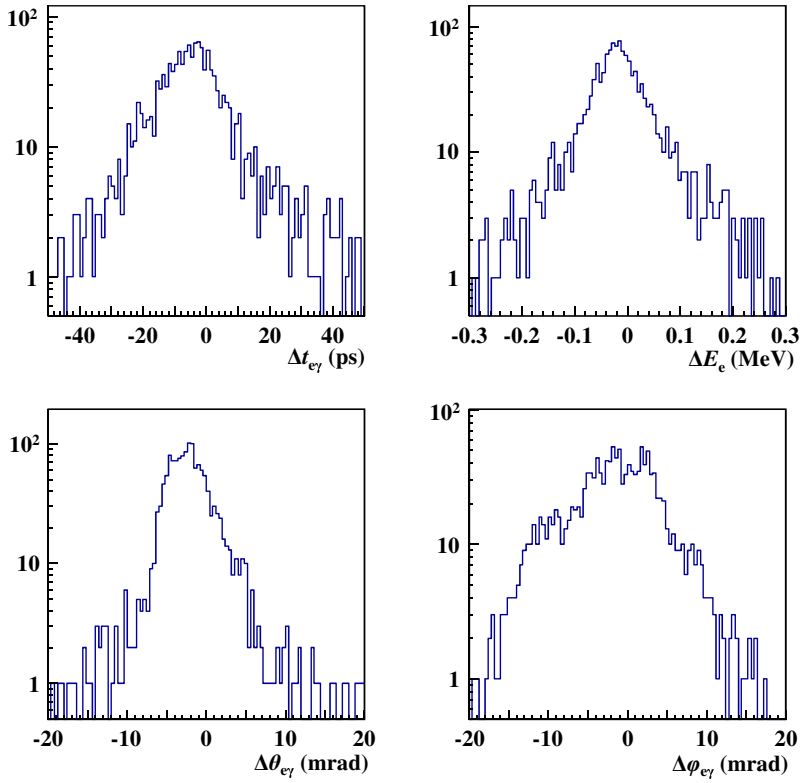

Figure 8.8: Change of the observables. (previous) - (current)

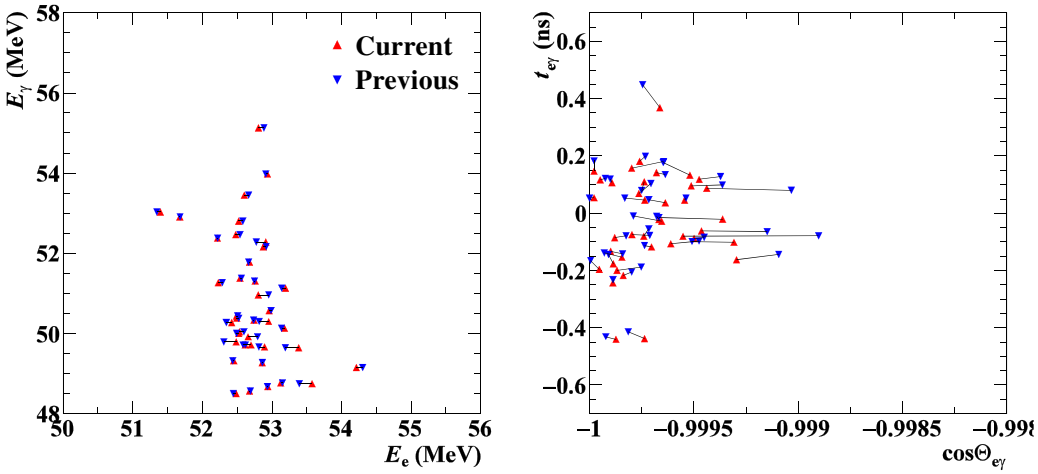

Figure 8.9: Move of the observables in ($E_e - E_\gamma$)- and ($\cos\Theta_{e\gamma} - t_{e\gamma}$)-planes. Only events of the higher signal-likelihood are plotted.

The bias and the RMS of $\Delta t_{e\gamma}$, ΔE_e, $\Delta\theta_{e\gamma}$ and $\Delta\phi_{e\gamma}$ are -4 ± 14 ps, -15 ± 79 keV, -2.1 ± 3.8 mrad and -1.6 ± 5.8 mrad. E_γ is unchanged.

We performed a simulation of the change in the upper limit by the change of the reconstruction with pseudo experiments which include both previous and current information. The difference

in the average branching ratio upper limit simulated for 2009-2011 dataset has a spread of 4.2×10^{-13} in RMS. The observed shift in the data 0.4×10^{-13} lies within the spread.

8.3.2 Fitting without constraints

The constraint function $C(N_{\mathrm{RMD}}, N_{\mathrm{ACC}}, \boldsymbol{t})$ is dropped from Eq. (7.6) of likelihood function. The other conditions are the same as the main likelihood analysis. This is another way to check the consistency of the analysis. The fit result is shown in Table 8.5. The fitted number agrees with the expected number within the statistical error.

Table 8.5: The expected and observed numbers of events in the analysis region.

Data set	Full	Old	New
N_{obs}	8344	3761	4583
$N_{\mathrm{ACC}}^{\mathrm{exp}}$	7744 ± 41	3469 ± 28	4274 ± 31
$N_{\mathrm{ACC}}^{\mathrm{fit}}$	7684 ± 103	3477 ± 70	4210 ± 75
$N_{\mathrm{RMD}}^{\mathrm{exp}}$	614 ± 34	284 ± 19	330 ± 20
$N_{\mathrm{RMD}}^{\mathrm{fit}}$	663 ± 59	285 ± 40	378 ± 43

8.3.3 Comparison with alternative analysis

We have prepared an alternative simplified analysis for cross check with the main event-by-event PDF. It is called constant PDF, and the PDF parameters do not change for every event but there are only several categories of the PDF parameters. The category is classified by the quality of the positron reconstruction and the first conversion point of the γ-ray. The angular observable $\Theta_{\mathrm{e}\gamma}$: stereo angle between momenta vector of positron and γ-ray (in degree) is used instead of $\theta_{\mathrm{e}\gamma}$ and $\phi_{\mathrm{e}\gamma}$. A angular selection criteria for the analysis window is defined differently as $\Theta_{\mathrm{e}\gamma} > 176^{\circ}$. Figure 8.10 shows the data and the best fit PDF projected on observables E_γ, E_{e}, $\Theta_{\mathrm{e}\gamma}$ and $t_{\mathrm{e}\gamma}$.

The consistency between the main and alternative PDF is tested with common pseudo experiments. The upper limits with the ensemble of the toy MCs under null signal hypothesis are plotted in red dots in Fig. 8.11. The upper limits by two analyses show clear correlation, and the sensitivity is found to be better in event-by-event PDF by $\sim 20\%$.

The best fit branching ratio by the maximum likelihood fitting with the constant PDF is -2.5×10^{-13}, and 90% C.L. upper limit is 4.3×10^{-13}. They show good agreement and it is consistent with the correlation observed with the common pseudo experiments as seen in Fig. 8.11. The best fit values of N_{ACC} and N_{RMD} are 630 ± 66 and 7927 ± 148, while expectation from sidebands are 683 ± 115 and 7915 ± 96. Considering the difference in selection criteria, the result is consistent with that with event-by-event PDF.

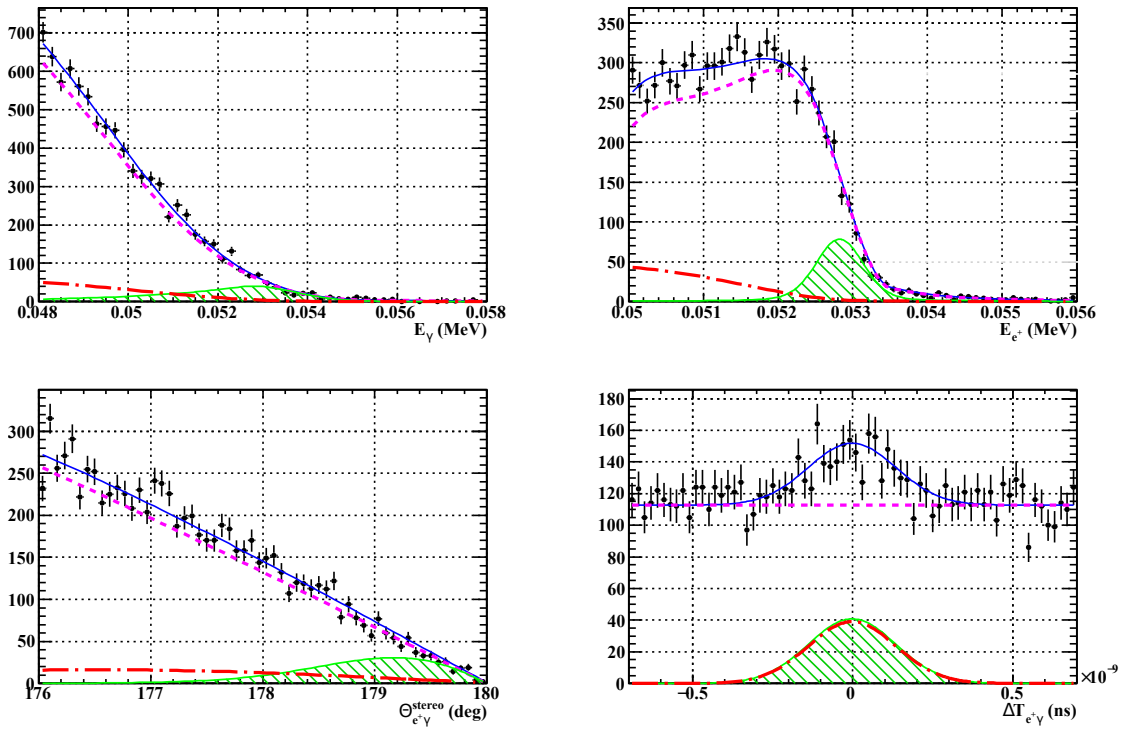

Figure 8.10: Likelihood fit result with the constant PDF. The notations are the same as with Fig. 8.5 as well as the scaling of the signal PDF.

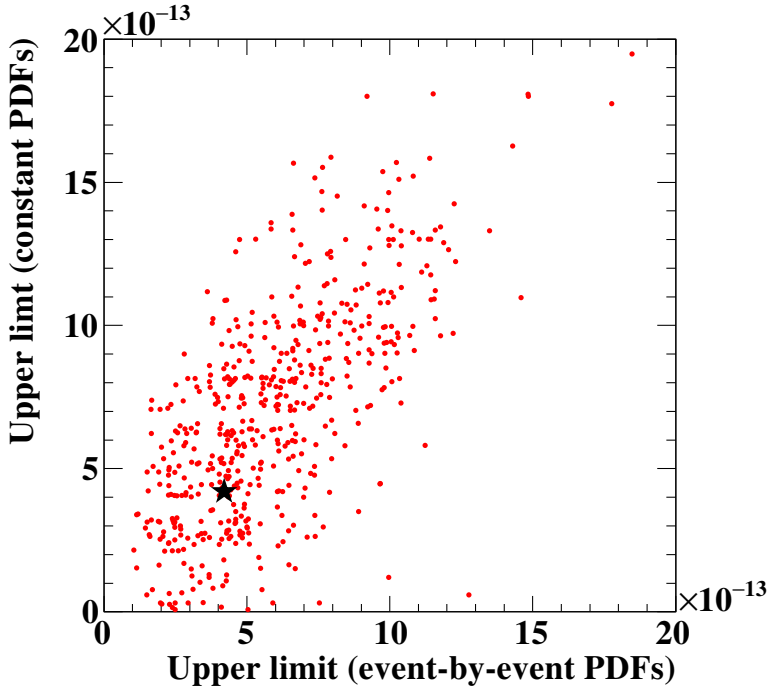

Figure 8.11: Red dots show 90% upper limits of common toy MCs with event-by-event PDF (horizontal axis) and with constant PDF (vertical axis). The data is plotted with black star marker, and it lays around center of the distribution.

Chapter 9

Prospects

We took data for 5 years, but the speed of the sensitivity improvement is slowing down. It is because the expected number of background is becoming non-negligible. When the experiment is background-free, the sensitivity improves in proportional to the data amount, while when the average number of background is large, the sensitivity is proportional to the square root of the data amount.

In order to achieve higher sensitivity efficiently, the increase of data statistics per unit time or the improvement of rejection power of background are mandatory.

9.1 MEG II experiment

The MEG II experiment is an upgrade of the MEG experiment, aiming at one order of magnitude higher sensitivity. The upgrade takes over the basic concept of MEG experiment, while almost all major detectors are upgraded. Our upgrade proposal was approved in year 2013, and we are in a construction stage. The sensitivity improvement will be achieved by 10 times larger statistic amount of data, and the detector resolutions improved by a factor of two.

The schematic view of the upgraded experiment is illustrated in Fig. 9.1. Here the items in upgrades are explained for each component.

9.1.1 Beam and target

MEG II continues to be conducted in the πE5 area in PSI, which is capable of providing muon intensity up to 1×10^8 /s. The expected muon stopping rate in MEG II is 7×10^7 /s. The target will be replaced with thinner one for less disturbance to positron, and the slant angle is also changed to keep the effective thickness. As we learned in MEG experiment, the stability of the target is crucial. Therefore, the study of the target material is underway. We are also studying the possibility of the active target which is composed of scintillating fiber and SiPM sensor.

9.1.2 LXe detector

As seen in Sec. 5.2, the performance of LXe detector is limited by the size of the PMT. We overcome it by replacing PMTs in the inner face with smaller sensor, MPPC[1]. The size of the

[1] Multi-Pixel Photon Counter, by Hamamatsu Photonics.

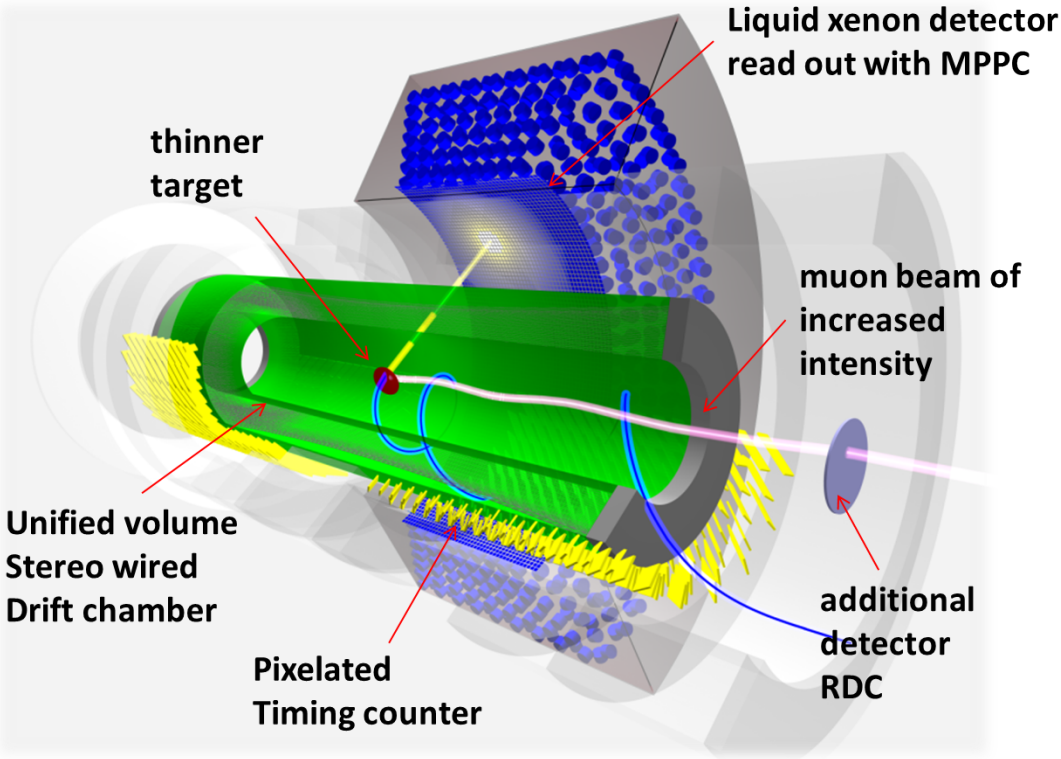

Figure 9.1: CG image of the MEG II detectors.

sensor is 12×12 mm^2, considering the performance and the number of readout channels, and they will be arranged in 44×93 array.

The θ angle acceptance will not be extended, but the entrance width is widened, by means of improvement of energy, position resolutions near lateral edge. The PMTs on lateral face are shifted outward as well, and their attached direction is modified to parallel to the lateral wall.

MPPCs operational in the LXe was not commercially available when MEG II was planned. There were mainly two issues to adopt MPPC in our LXe detector, (a) sensitivity to 175 nm wavelength (VUV) light and (b) large sensor capacitance with size of 12×12 mm^2. We successfully developed a new type of MPPC in collaboration with Hamamatsu Photonics. The design of the new MPPC is shown in Fig. 9.2.

9.1.3 Magnetic field

The COBRA magnet remains in the MEG II experiment. However, the magnetic field map will be upgraded according to the measurement with a new measurement with an improved precision.

9.1.4 Drift chamber

The drift chamber in MEG I is totally replaced with a new one. The new drift chamber has cylindrical shape and stereo-wire geometry. In MEG I drift chamber, some of the positrons hit the support structure and readout electronics at the end of module, and it caused an efficiency decrease. The drawback is solved by making drift chamber longer. Schematic images with

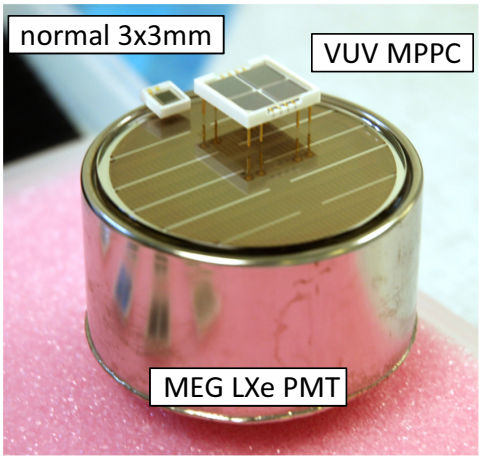

(a) VUV MPPC is put on 2-inch PMT together normal 3×3 mm^2 MPPC.

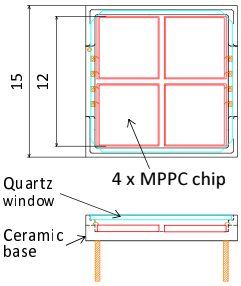

(b) Drawing of VUV MPPC. Four 6×6 mm^2 chips are mounted on ceramic base, not to block VUV light; the cover is made of artificial quartz.

Figure 9.2: VUV MPPC for MEG II

MEG I and MEG II are compared in Fig. 9.3. The tracking performance will be improved with more hit points due to finer segmented drift cell.

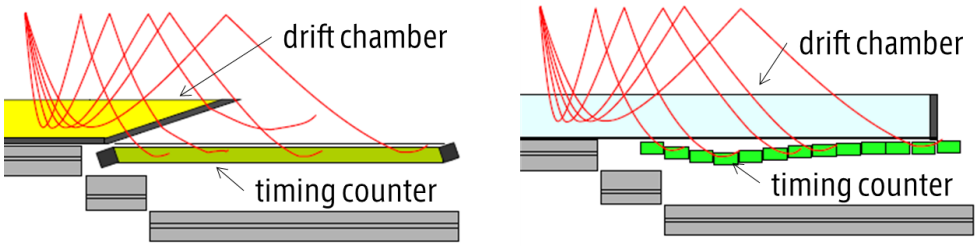

(a) Case of MEG I

(b) Case of MEG II

Figure 9.3: Drift chamber is replaced with longer one. The ratio of positrons which is scattered by the support structure will be reduced.

9.1.5 Timing counter

The timing counter system is also replaced with a new one. The concept of the new timing counter is to use multiple hits. The new system is composed of many (256 pcs both in US and DS side) small counters, and the timing is reconstructed using multiple-hits.

The single counter is based on a fast plastic scintillator ($120 \times 40(50) \times 5$ mm^3). Two circuit boards with 6 series connected SiPMs are attached on both ends. The counters are mounted on backplane readout PCBs as shown in Fig. 9.4.

9.1.6 Radiative decay counter

The radiative decay counter (RDC) is a brand new component in MEG II. It is designed to reduce accidental background whose γ-ray is originated from radiative muon decay. When

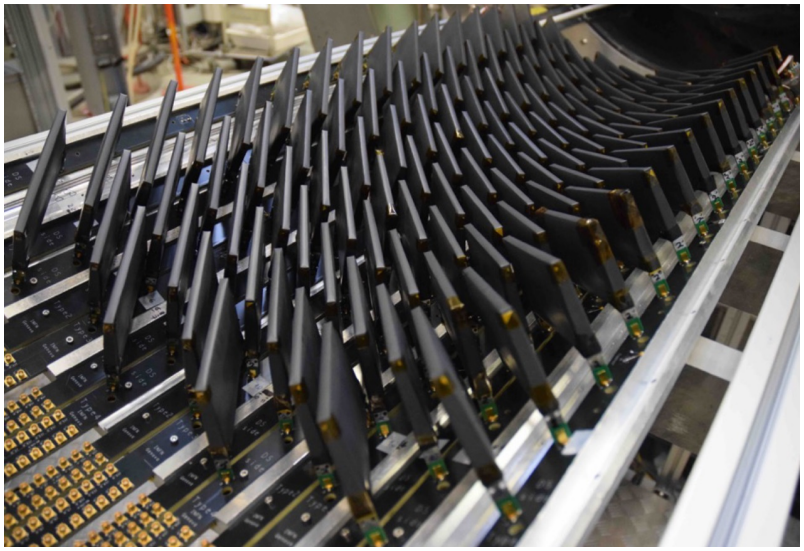

Figure 9.4: Assembled prototype of the new timing counter.

γ-ray energy is near signal energy, the momentum of the associated positron is likely to be low, and results in a small radius of the positron trajectory. The RDC is placed on the beam axis near beam axis of up-stream and down-stream side of target.

The DS side detector is composed of LYSO crystal and plastic scintillator which are both read by MPPC. The US side detector is a thin layer of scintillating fibers. A careful study about the effect on the beam property is needed as for US side detector.

9.1.7 Projected sensitivity

The expected performance of the upgraded detector is summarized in Table 9.1 [93]. With 3 years of data tracking, the expected branching ratio sensitivity is 4×10^{-14}.

Table 9.1: performance of MEG II and MEG I detector

Item	MEG II	MEG I
Beam intensity	7×10^7	3×10^7
Resolution		
γ energy (%) (w<2/w>2)	1.1 / 1.0	2.4 / 1.7
γ position (mm) ($u/v/w$)	2.6/2.2/5	5/5/6
e^+ energy (keV)	130	306 (core)
$\gamma - e^+$ angle (mrad) (θ/ϕ)	5.3/3.7	9.4/8.7
$\gamma - e^+$ timing (ps)	84	122
Efficiency (%)		
trigger	>99	>99
γ	69	63
e^+	88	40

9.2 Future projects

In order to search $\mu \to e\gamma$ with further improved sensitivity, a significantly improved detector technologies and muon sources with a much higher intensity will be needed. There are several projects which can provide more intense muon beam near future.

PSI is planning an new muon source "High-intensity Muon Beam" (HiMB) [94] with a novel concept. MEG I and MEG II use beam line πE5 where the secondary beam is produced with 4 cm thick graphite target and only about 10% of the beam interact at the target. The most of beam is sent to SINQ (neutron study facility) target (Fig. 2.2). The idea of HiMB is to produce surface muon beam at the SINQ target. According to a MC simulation, available muon intensity will be $O(10^{10})$ μ^+/s.

At Fermilab, a project "Proton Improvement Plan-II" (PIP-II)[2] is proposed. It is a plan for the accelerator complex for intensity-frontier. It is designed to be used for various experiments such as long-base line neutrino oscillation experiment or $\mu -$ e conversion search experiment.

A new muon beam facility in RCNP[3], Osaka univ. started operation with a characteristic pion capture solenoid. It has very efficient muon collection for primary beam power, 10^8 μ^+/s by 400W beam. If the injector accelerator in RCNP is upgraded by one order of the magnitude (for example $1 \to 10$ μA), it can produce more intense DC muon beam of 10^9 μ^+/s.

Although the new beam facilities are projected in the following decades, new concepts for the $\mu \to e\gamma$ search have not been established. There are two difficulties to utilize those beams. One is the accidental pile-up. As seen in Eq. (1.10), the rate of accidental background increases in proportional to beam intensity. The other one is beam quality. Above mentioned muon beams are expected to have larger emittance, comparing with beam in PSI πE5, the detector arrangement as MEG experiment may not work well. It is impossible to efficiently reach the $O(10^{-15})$ sensitivity, unless the issues about the detector are solved.

[2] previously called project-X

[3] Research Center for Nuclear Physics

Chapter 10

Conclusion

The $\mu^+ \to e^+\gamma$ search is an excellent probe to look for the physics beyond the standard model. The MEG experiment has been searching for $\mu^+ \to e^+\gamma$ with unprecedentedly high sensitivity. The final result of the MEG experiment was obtained with all the data which were taken from year 2009 to year 2013. We analysed the full dataset with improved analysis algorithms, and thereby accomplished a sensitivity of 5.3×10^{-13}. No excess of the signal was found, and the most stringent upper limit is set as

$$\mathcal{B}(\mu^+ \to e^+\gamma) < 4.2 \times 10^{-13} \text{ (90\% confidence level).} \tag{10.1}$$

It is 30 times more stringent result than the bound set by the previous experiment. The history of the $\mu^+ \to e^+\gamma$ search with the MEG experiment is summarized in Fig. 10.1. The preparation of the MEG II experiment is underway and will start physics data taking in year 2017. The expected sensitivity is one order of the magnitude higher, 4×10^{-14}.

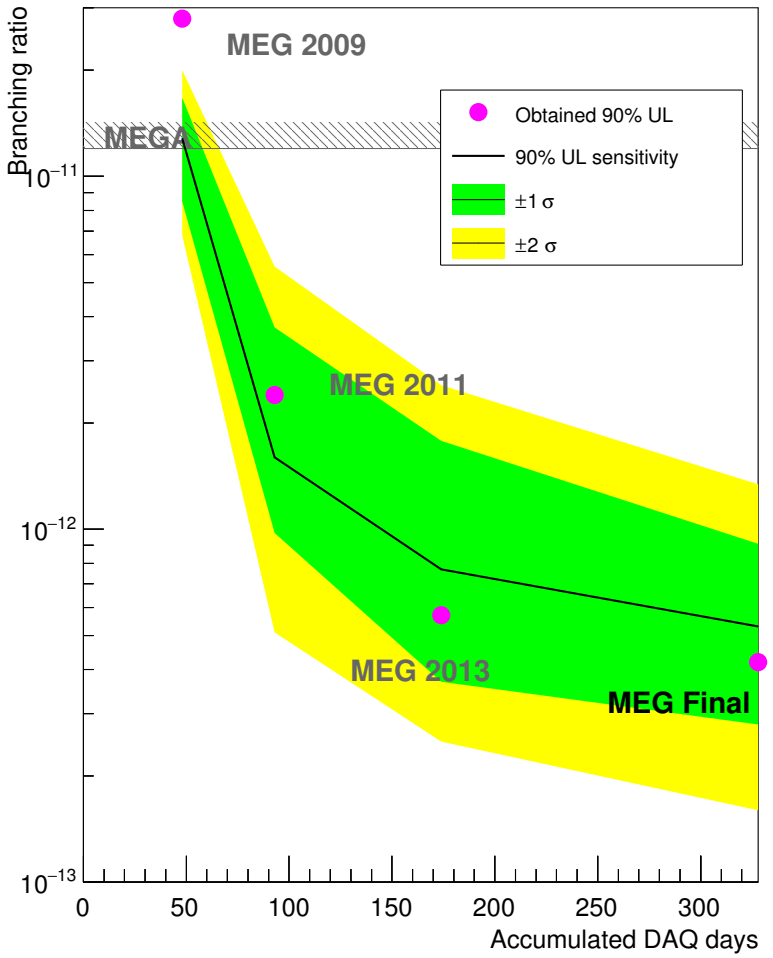

Figure 10.1: Improvement of search sensitivity of MEG experiment.

Appendix A

Performance of BGO detector

As mentioned in Sec. 4.1.2.3, we replaced the NaI detector for the π^0 calibration for the LXe detector with the BGO detector in 2011. The fundamental specifications of these detectors are summarized in Table A.1.

Table A.1: Specifications of tagging detectors

Item	unit	NaI	BGO
Material			
Density	g/cm^3	3.67	7.13
Radiation length	mm	25.9	11.2
Molière radius	mm	41.3	22.3
Relative light	%	100	21
Wavelength	nm	415	480
Design			
Size(x, y)	mm	62.5	46.0
Size(z)	mm	305	200
Arrangement		3×3	4×4
Readout		APD	PMT
Catalog No.		Hamamatsu H8664-1010	Hamamatsu H8409-70

Due to the higher density, BGO has a shorter radiation length and a smaller Molière radius than NaI. The shorter radiation length allows us to shorten the detector length and hence to switch the photo-sensor from APD to PMT with a larger coverage and a higher QE. The high QE of PMT can compensate the lower light yield of BGO. The fine-mesh-type PMT is chosen, since the BGO detector is operated in the magnetic field by COBRA. ($\sim$ 50 Gauss) The smaller Molière radius reduces shower escape from the side of the detector. The previous detector was based on 3x3 array of NaI crystals of $62.5 \times 62.5 \times 305$ mm^3 each, and only events where the central crystal detect maximum light was triggered. The new detector is more segmented with 4x4 array of BGO crystals ($46 \times 46 \times 200$ mm^3 each), while the total size is kept. The new trigger condition is any hit in the central four crystals. The detector acceptance was, therefore, increased by the factor of $9/4$.

Figure A.1(a) is a picture to compare the size of the crystals of NaI and BGO. Each BGO crystal is wrapped by a film of aluminized Mylar. Figure A.1(b) shows a CAD drawing for the

housing of the BGO detector. The housing is designed to be interchangeable with that for the NaI detector, hence the replacement of the detector is completed just by replacing the housings.

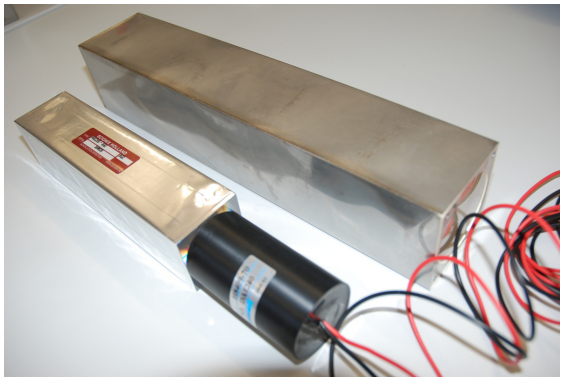

(a) (bottom) BGO crystal attached with H8409-70 PMT, (top) NaI crystal.

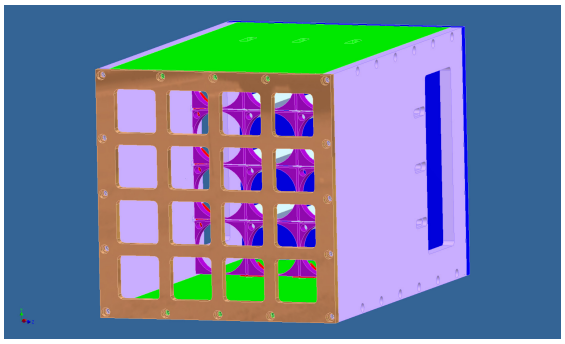

(b) Design of the housing to store BGO crystals.

Figure A.1: BGO detector.

A.1 Calibration

Each-crystal is calibrated with cosmic ray events. The high voltages for PMTs are determined so as events when a 129 MeV γ-ray (Eq. (4.5)) deposits all energy in one crystal, the pulse height to be the full dynamic-range of DRS.

The detector is mounted on a moving stage to scan all the acceptance of the LXe detector. Since the COBRA stray field around the detector is suppressed by the compensation coils as for the LXe detector, the operation of the PMT is not affected at any position. We tested the dependence of the output on the detector position by checking the spectrum of the 17.6 MeV γ in CW run of Li target (See Sec. 4.1.2.1). It turned out that the position dependence is very small, 0.4% toward the ϕ direction and 0.3% toward the z direction. The temperature dependence of the BGO light yield is known, we measured the temperature dependence by monitoring the 54.9 MeV γ-ray peak and the temperature. The coefficient is -0.97 %/K, while the temperature coefficient shown in the catalogue[1] is -1.2 %/K.

In order to minimize the effect of the position and temperature dependence, we decided to calibrate the absolute energy scale for each patch data. By using the 54.9 MeV γ-ray peak, the energy scale is calibrated. The formula to reconstruct energy is,

$$E_{\mathrm{BGO}} = C_1 \sum_{\mathrm{inner}} q_i g_i a_i + C_2 \sum_{\mathrm{outer}} q_i g_i, \tag{A.1}$$

where q_i is the observed charge and g_i is the gain measured by the cosmic ray calibration. a_i is an additional correction for the gain of inner 4 crystals, which is fixed by fitting the spectrum of each crystal. The value is determined for each patch. It is possible because the peak is clear for central crystals. C_1 and C_2 are the parameters to adjust the balance of the inner and outer contribution from the correction by a_i.

[1] SAINT-GOBAIN

A.2 Position resolution

The position resolution can affect the performance of the π^0 calibration, because in the energy resolution evaluation of LXe detector, the correlation between the opening angle and energy is corrected using the reconstructed positions of two γ-rays. We introduced a position reconstruction by the weighted sum of the detected number of the photo-electrons. The position resolution is estimated with the MC simulation (Fig. A.2) to be 1.0 cm (RMS).

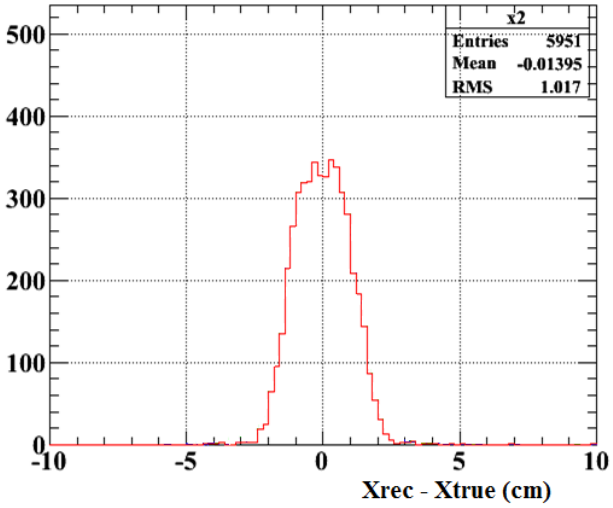

Figure A.2: Error distribution between the reconstructed position and MC truth.

A.3 Energy resolution

The energy resolution of the BGO detector is estimated by fitting 54.9 MeV peak with a function where a Gaussian function and a exponential functions are smoothly connected. Figure A.3 shows the observed spectrum in a π^0 run in year 2011. In the events, a cut is applied where the energy deposit in the central 4 crystal is more than the half of total deposit. The fitted σ for 54.9 MeV peak is 2.4%, while that of the NaI detector was 3.9%.

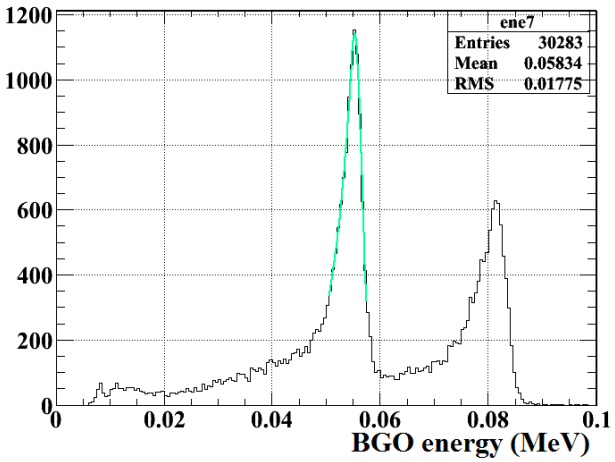

Figure A.3: Energy distribution by the BGO detector in year 2011 π^0 run.

Appendix B

AIF cut efficiency in signal/RMD event

The selection efficiency for the signal (item (c) of $\varepsilon_{\rm sel}$ in Sec. 7.7) is estimated with simulated distribution of AIF observables for the signal event. The way to estimate the efficiency is described herein.

B.1 Accidental background and signal/RMD events

The simulation used the timing sideband data with the same trigger as physics data, since we want to use the same position and timing distribution and the correlation of γ-ray and positron as data. In the timing sideband, only the accidental backgrounds are included. The accidental background can be categorized by the source of the γ-ray. In cases an AIF occurs in the detector, and the γ-ray is detected by the LXe detector (we call it "real AIF"), the AIF observables make a peak. In cases the γ-ray is not due to AIF or is due to AIF but the original positron is not found, the AIF observables do not make a peak (base events in Fig. 3.13). On the other hand in signal and RMD event, γ-ray and positron must be correlated (from one μ^+). Figure B.1 shows possible types of the events. What we want to know is the observable distribution of the (s-2) category and the fraction of (s-1) and (s-2).

B.2 Event scrambling

The distribution of (s-2) is thought to be equivalent to that of (a-2), however, it is impossible to extract only (a-2) from all mixed events. We simulate the distribution where the γ and positron are uncorrelated, by scrambling information of γ-ray and positron. However, if the trigger condition of the direction match (about ϕ direction) is not maintained, the output AIF observable is biased. Therefore, we developed a method of trigger simulation to scramble the data with keeping the trigger condition. The scrambling is done before Sec. 3.5.2, and the procedure in Sec. 3.5.2 is processed with the scrambled data. It is proceeded with following algorithm.

- The trigger table is prepared. The table is a 2D map of V position of γ-ray and id number of TIC bar. It shows the probability to find TIC hit at j-th bar, when the γ is found in i-th segment. The table is normalized as $\sum_j P_i(j) = 1$ for each i.
- The events are listed, according to which TIC bar has a hit. The lists are 15-fold (number of TICP bar) array of event numbers.

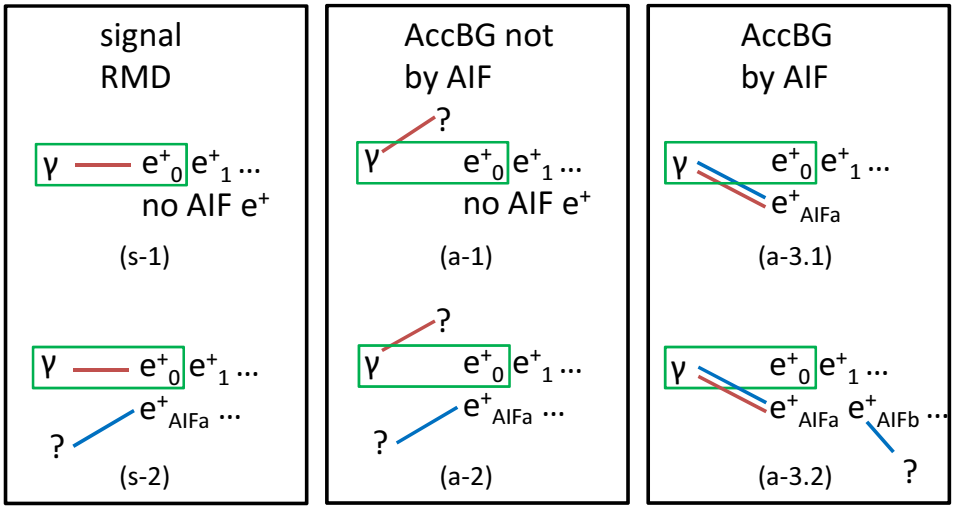

Figure B.1: Types of the events, categorized by the AIF positron. The red line shows the γ-ray and its source, the blue line shows the found AIF and the γ-ray, and the green box shows the triggered gamma positron pair.

- For every event, the V position of γ (in region a, for instance) is checked, and the a-th row in trigger table is picked up.
- An id of TIC bar is randomly selected, the probability to select b-th column is $P_a(b)$
- A positron data in the b-th list is randomly selected. If the selected number of event is the same as that of γ, select again.

Figure B.2(a) shows the trigger table and v_γ-TIC bar distribution of simulated data. The effect of the scrambling is demonstrated in Fig. B.2(b), the shape of the base agrees better with the trigger simulation. The effect of the direction matching is obvious in ϕ-direction, but the effect cannot be seen in θ-direction. So the trigger simulation only considers ϕ. Figure B.3 shows the result of the estimation of AIF observables in signal/RMD events. The distance from the peak is calculated with the same parameter $\boldsymbol{c}$ and S the same as for accidental background which were introduced in Sec. 7.6.1.

B.3 Probability to find no AIF candidate

The purpose of this section is to estimate not to find AIF candidate in the Signal/RMD events. The relation of γ and e^+ in category (a-1) and (a-2) are thought to be equivalent with that in Signal and RD events. Therefore an estimation can be written as,

$$S_{\mathrm{NOAIF},1} = \frac{P(\text{a-1})}{P(\text{a-1}) + P(\text{a-2})}. \tag{B.1}$$

On the other hand, the category (a-3) should not be found in the Signal/RMD events. The (a-3) can be further separated into (a-3.1): True AIF and no other AIF candidates and (a-3.2): True AIF with other AIF candidate(s). The Signal or RD events do not contain true AIF events. However, if the most probable AIF candidate track is removed, relation of (a-3.1) and (a-3.2)

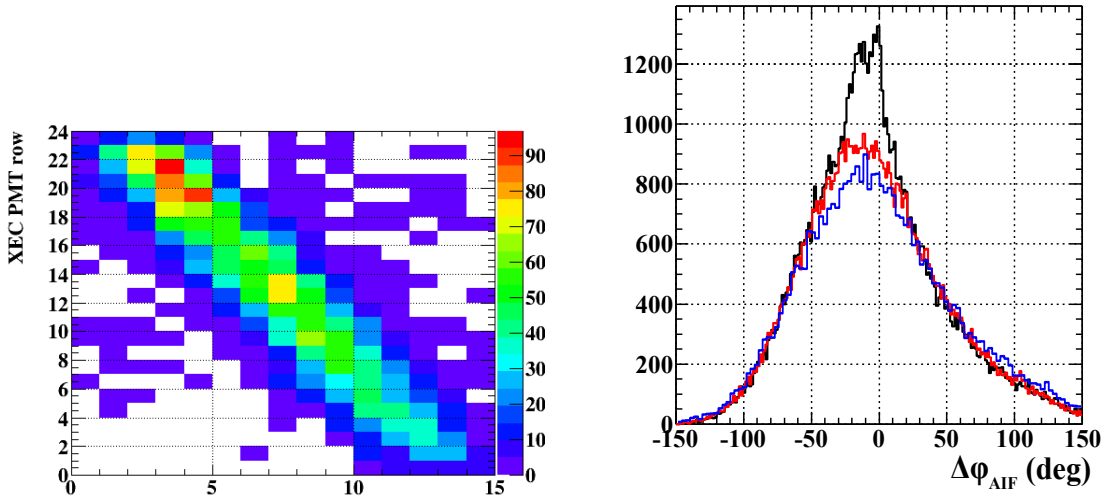

(a) A trigger table made from the sideband data in year 2013.

(b) The $\Delta\phi_{\mathrm{AIF}}$ distributions with (black) data, (red) scramble with trigger simulation, (blue) random scramble.

Figure B.2: Trigger simulation

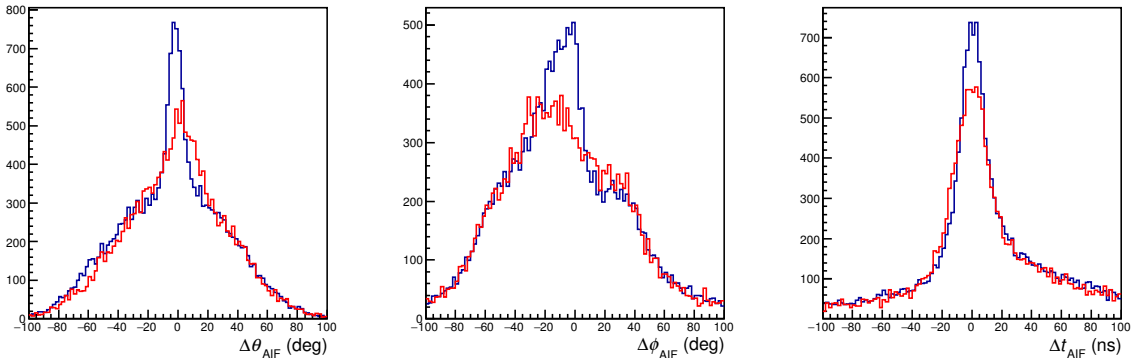

Figure B.3: The AIF observables of, (red) estimation for signal/RMD events, and (blue) data of the accidental background. $\phi_{e\gamma}$ selection is applied.

corresponds to that of (s-1) and (s-2). In this assumption, no-AIF probability of signal/RMD can be written as,

$$S_{\mathrm{NOAIF,2}} = \frac{P(\text{a-1}) + P(\text{a-3.1})}{P(\text{a-1}) + P(\text{a-2}) + P(\text{a-3.1}) + P(\text{a-3.2})}. \tag{B.2}$$

The no-AIF probability for each year is listed in Table B.1.

B.4 Error of inefficiency

The error in not finding AIF depends on the method, but the difference in the $S_{\mathrm{NOAIF,1}}$ and $S_{\mathrm{NOAIF,2}}$ are negligibly small (< 0.2%). The method to estimate the observable distribution is complex, and contains assumptions. As one example of the mistake in the calculation, is wrong positron data. When we use positron data not from MEG trigger data, but positron triggered

Table B.1: Probability to find no AIF candidate in an event. A_{NOAIF} is the probability for accidental background.

Year	A_{NOAIF}	$S_{\mathrm{NOAIF,1}}$	$S_{\mathrm{NOAIF,2}}$
2009	0.163	0.185	0.183
2010	0.170	0.187	0.186
2011	0.180	0.198	0.199
2012	0.154	0.172	0.171
2013	0.126	0.143	0.141

without LXe coincidence, or pedestal trigger data, the number of the AIF candidate around peak varies in several tens of percents. Although the error at this level can remain in the estimation, the uncertainty in the normalization factor is only 1.1%, even if the 100% error is assumed for AIF cut inefficiency. It is enough less than 3.5%: estimated systematic uncertainty for normalization factor. The additional systematic error in the normalization by the AIF reduction can be neglected.

Appendix C

List of abbreviations

ACC ACCidental (background)

AIF Annihilation In Flight (of positron)

APD Avalanche PhotoDiode

BGO Bismuth Germanium Oxide, $Bi_4Ge_3O_{12}$

BTS Beam Transport Solenoid

CEX Charge EXchange (reaction), $\pi^- + p \rightarrow \pi^0 + n$

COBRA COnstant Bending RAdius (magnet)

CW Cockcroft-Walton (accelerator)

DCH Drift CHamber

DRS Domino Ring Sampler

LFV Lepton Flavor Violation

LXe Liquid Xenon

PDF Probability Density Function

PMT PhotoMultiplier Tube

PSI Paul Scherrer Institute

RMD Radiative Muon Decay

TIC TIming Counter

Acknowledgment

I would like to express my thanks to everyone in the MEG collaboration, primarily to my academic adviser, Prof. Toshinori Mori who serves the spokesperson of the MEG experiment with Prof. Alessandro Baldini. He supervised all my study in the doctoral course and gave me an opportunity to participate in the concluding work of the MEG experiment.

I also offer my gratitude to Assoc. Prof. Wataru Ootani, who managed analysis project and lead us in the MEG upgrade studies. He gave me advises for this thesis in detail. I am obligated to Dr. Toshiyuki Iwamoto for supports not only in experiment but also in whole sojourn in PSI. To Dr. Ryu Sawada and Dr. Yusuke Uchiyama, I feel appreciation about giving me a lot of advices always when I met difficulties in our research.

In order to accomplish our tasks in final analysis studies, the discussion with Dr. Fabrizio Cei, Dr. Francesco Renga and Dr. Gordon Lim was meaningful and was enjoyable at the same time. The collaborators from KEK, Prof. Satoshi Mihara, Dr. Hajime Nishiguchi, the period to work together was not so long but gave me valuable suggestions in meetings and in PSI.

I learned much technical knowledge and skills to live in Switzerland from Dr. Hiroaki Natori, Dr. Yasuhiro Nishimura, Dr. Xue Bai, Dr. Kei Ieki and Dr. Yuki Fujii. Ms. Miki Nishimura, Mr. Shinji Ogawa, Mr. Naoya Shibata, Mr. Shota Nakaura, Mr. Kohei Yoshida, Mr. Ryoto Iwai, Mr. Mitsutaka Nakao and all students come to PSI from Kyushu univ. supported me about works in the university and gave me pleasant life as a student.

I want to present my thanks to all the staffs in international center for elementary particle physics, especially secretaries who helped me from clerical sides. I am deeply grateful to the staffs in PSI too, for accepting us in PSI and for supporting about accommodation, exports, and so on.

I would like to show special thanks to the members of Hamamatsu Photonics, it was an exciting experience to collaborating with a leading company and develop advancing products.

I owe gratitude to my former colleagues in Hitachi Ltd. to send me off the academia. I learned precious things not only as an engineer but also a member in the society.

Finally, I gratefully acknowledge my family to supporting my unproductive days.

May 2016, Tokyo
Daisuke Kaneko

Bibliography

[1] G. Aad et al. (ATLAS Collaboration), Observation of a new particle in the search for the standard model higgs boson with the atlas detector at the lhc. Physics Letters B **716**(1), 1 – 29 (2012). doi:http://dx.doi.org/10.1016/j.physletb.2012.08.020

[2] S. Chatrchyan et al. (CMS Collaboration), Observation of a new boson at a mass of 125 gev with the cms experiment at the lhc. Physics Letters B **716**(1), 30 – 61 (2012). doi:http://dx.doi.org/10.1016/j.physletb.2012.08.021

[3] Y. Fukuda et al. (Super-Kamiokande Collaboration), Evidence for oscillation of atmospheric neutrinos. Phys. Rev. Lett. **81**, 1562–1567 (1998). doi:10.1103/PhysRevLett.81.1562

[4] Ziro Maki, Masami Nakagawa, Shoichi Sakata, Remarks on the unified model of elementary particles. Progress of Theoretical Physics **28**(5), 870–880 (1962). doi:10.1143/PTP.28.870, arXiv:http://ptp.oxfordjournals.org/content/28/5/870.full.pdf+html

[5] F.P. An et al., Observation of electron-antineutrino disappearance at daya bay. Phys. Rev. Lett. **108**, 171803 (2012). doi:10.1103/PhysRevLett.108.171803

[6] J.K. Ahn et al. (RENO), Observation of Reactor Electron Antineutrino Disappearance in the RENO Experiment. Phys. Rev. Lett. **108**, 191802 (2012). doi:10.1103/PhysRevLett.108.191802, arXiv:1204.0626

[7] Y. Abe et al. (Double Chooz), Reactor electron antineutrino disappearance in the Double Chooz experiment. Phys. Rev. **D86**, 052008 (2012). doi:10.1103/PhysRevD.86.052008, arXiv:1207.6632

[8] J.C. Street, E.C. Stevenson, New evidence for the existence of a particle of mass intermediate between the proton and electron. Phys. Rev. **52**, 1003–1004 (1937). doi:10.1103/PhysRev.52.1003

[9] Y. Kuno, Y. Okada, Muon decay and physics beyond the standard model. Rev. Mod. Phys. **73**(1), 151–202 (2001). doi:10.1103/RevModPhys.73.151, arXiv:hep-ph/9909265

[10] StephenP. Martin, A Supersymmetry primer (1997). doi:10.1142/9789812839657_0001,10.1142/9789814307505_0001, arXiv:hep-ph/9709356. [Adv. Ser. Direct. High Energy Phys.18,1(1998)]

[11] R. Barbieri, L. Hall, A. Strumia, Violations of lepton flavour and CP in supersymmetric unified theories. Nucl. Phys. B **445**(2–3), 219–251 (1995). doi:10.1016/0550-3213(95)00208-A

[12] Stefan Antusch et al., Impact of θ_{13} on lepton flavour violating processes within susy seesaw. Journal of High Energy Physics **2006**(11), 090 (2006)

[13] J. Adam et al. (MEG Collaboration), New constraint on the existence of the $\mu^+ \to e^+\gamma$ decay. Phys. Rev. Lett. **110**, 201801 (2013). doi:10.1103/PhysRevLett.110.201801, arXiv:1303.0754

[14] K. Hayasaka et al., New search for $\tau \to \mu\gamma$ and $\tau \to e\gamma$ decays at belle. Physics Letters B **666**(1), 16 – 22 (2008). doi:http://dx.doi.org/10.1016/j.physletb.2008.06.056

[15] B. Aubert et al. (BABAR Collaboration), Searches for lepton flavor violation in the decays $\tau^\pm \to e^\pm\gamma$ and $\tau^\pm \to \mu^\pm\gamma$. Phys. Rev. Lett. **104**, 021802 (2010). doi:10.1103/PhysRevLett.104.021802

[16] J. Hisano et al., Exact event rates of lepton flavor violating processes in supersymmetric su(5) model. Physics Letters B **391**(3–4), 341 – 350 (1997). doi:http://dx.doi.org/10.1016/S0370-2693(96)01473-6

[17] L. Calibbi et al., Lepton flavor violation from supersymmetric grand unified theories: Where do we stand for meg, prism/prime, and a super flavor factory. Phys. Rev. D **74**, 116002 (2006). doi:10.1103/PhysRevD.74.116002

[18] R. Barbier et al., R-parity-violating supersymmetry. Physics Reports **420**(1–6), 1 – 195 (2005). doi:http://dx.doi.org/10.1016/j.physrep.2005.08.006

[19] AndrzejJ. Buras et al., Lepton Flavour Violation in the Presence of a Fourth Generation of Quarks and Leptons. JHEP **09**, 104 (2010). doi:10.1007/JHEP09(2010)104, arXiv:1006.5356

[20] Monika Blanke et al., Charged Lepton Flavour Violation and $(g-2)_\mu$ in the Littlest Higgs Model with T-Parity: A Clear Distinction from Supersymmetry. JHEP **05**, 013 (2007). doi:10.1088/1126-6708/2007/05/013, arXiv:hep-ph/0702136

[21] Kaustubh Agashe, AndrewE. Blechman, Frank Petriello, Probing the Randall-Sundrum geometric origin of flavor with lepton flavor violation. Phys. Rev. **D74**, 053011 (2006). doi:10.1103/PhysRevD.74.053011, arXiv:hep-ph/0606021

[22] E.P. Hincks, B. Pontecorvo, Search for gamma-radiation in the 2.2-microsecond meson decay process. Phys. Rev. **73**, 257–258 (1948). doi:10.1103/PhysRev.73.257

[23] S.Lokanathan, J.Steinberger, Minutes of the 1954 thanksgiving meeting held at chicago, illinois, november 26-27, 1954. Phys. Rev. **98**, 240 (1955). doi:10.1103/PhysRev.98.220

[24] David Berley, Juliet Lee, Marcel Bardon, Upper limit for the decay mode $\mu \to e + \gamma$. Phys. Rev. Lett. **2**, 357–359 (1959). doi:10.1103/PhysRevLett.2.357

[25] G. Feinberg, Decays of the μ meson in the intermediate-meson theory. Phys. Rev. **110**, 1482–1483 (1958). doi:10.1103/PhysRev.110.1482

[26] W.W. Kinnison et al., Search for $\mu^+ \to e^+\gamma$. Phys. Rev. D **25**(11), 2846–2868 (1982). doi:10.1103/PhysRevD.25.2846

[27] R.D. Bolton et al., Search for rare muon decays with the crystal box detector. Phys. Rev. D **38**(7), 2077–2101 (1988). doi:10.1103/PhysRevD.38.2077

[28] M.L. Brooks et al. (MEGA Collaboration), New limit for the lepton-family-number nonconserving decay $\mu^+ \to e^+\gamma$. Phys. Rev. Lett. **83**(8), 1521–1524 (1999). doi:10.1103/PhysRevLett.83.1521

[29] RobertH. Bernstein, PeterS. Cooper, Charged Lepton Flavor Violation: An Experimenter's Guide. Phys. Rept. **532**, 27–64 (2013). doi:10.1016/j.physrep.2013.07.002, arXiv:1307.5787

[30] K.A. Olive et al. (Particle Data Group), Review of particle physics. Chin. Phys. C **38**, 090001 (2014). doi:10.1088/1674-1137/38/9/090001

[31] Y. Kuno, Y. Okada, Proposed $\mu \to e\gamma$ Search with Polarized Muons. Phys. Rev. Lett. **77**(3), 434–437 (1996). doi:10.1103/PhysRevLett.77.434

[32] C. Fronsdal, H. Überall, μ-meson decay with inner bremsstrahlung. Phys. Rev. **113**(2), 654–657 (1959). doi:10.1103/PhysRev.113.654

[33] S.G. Eckstein, R.H. Pratt, Radiative muon decay. Ann. Phys. **8**, 297–309 (1959). doi:10.1016/0003-4916(59)90024-7

[34] A. de Gouvea, N. Saoulidou, Fermilab's Intensity Frontier. Annu. Rev. Nucl. Part. Sci. **60**, 513–38 (2010)

[35] Andrzej Czarnecki, Xavier Garcia i Tormo, WilliamJ. Marciano, Muon decay in orbit: spectrum of high-energy electrons. Phys. Rev. **D84**, 013006 (2011). doi:10.1103/PhysRevD.84.013006, arXiv:1106.4756

[36] W. Bertl et al., A search for $\mu \to e$ conversion in muonic gold. Eur. Phys. J. C **47**(2), 337–346 (2006). doi:10.1140/epjc/s2006-02582-x

[37] M. Aoki et al. (DeeMe), Proposal of an Experimental Search for μ-e Conversion in Nuclear Field at Sensitivity of 10^{-14} with Pulsed Proton Beam from RCS (2010)

[38] Y.G. Cui et al. (COMET), Conceptual design report for experimental search for lepton flavor violating $\mu^- - e^-$ conversion at sensitivity of 10^{-16} with a slow-extracted bunched proton beam (COMET) (2009)

[39] R.J. Abrams et al. (Mu2e), Mu2e Conceptual Design Report (2012). arXiv:1211.7019

[40] A. Blondel et al., Research Proposal for an Experiment to Search for the Decay $\mu \to eee$ (2013). arXiv:1301.6113

[41] Tatsumi Aoyama et al., Complete tenth-order qed contribution to the muon $g-2$. Phys. Rev. Lett. **109**, 111808 (2012). doi:10.1103/PhysRevLett.109.111808

[42] G.W. Bennett et al., Final report of the E821 muon anomalous magnetic moment measurement at BNL. Phys. Rev. D **73**(7) (2006). doi:{10.1103/PhysRevD.73.072003}

[43] G. Isidori et al., Flavor physics at large tan β with a binolike lightest supersymmetric particle. Phys. Rev. D **75**, 115019 (2007). doi:10.1103/PhysRevD.75.115019

[44] Kaoru Hagiwara et al., $(g-2)_\mu$ and $\alpha(m_z^2)$ re-eveluated using new precise data. Journal of Physics G: Nuclear and Particle Physics **38**(8), 085003 (2011)

[45] Youngjoon Kwon, Search for τ lfv decays at belle

[46] J. Adam et al. (MEG Collaboration), The MEG detector for $\mu^+ \to e^+\gamma$ decay search. Eur. Phys. J. C **73**, 2365 (2013). doi:10.1140/epjc/s10052-013-2365-2, arXiv:1303.2348

[47] Psi, high intensity proton accelerators

[48] A.E. Pifer, T. Bowen, K.R. Kendall, A high stopping density μ^+ beam. Nuclear Instruments and Methods **135**(1), 39 – 46 (1976). doi:http://dx.doi.org/10.1016/0029-554X(76)90823-5

[49] A.M. Baldini et al. (MEG Collaboration), Muon polarization in the MEG experiment: predictions and measurements. To be published in Eur. Phys. J. C (In print). arXiv:1510.04743[hep-ex]

[50] M Barakat et al., Construction of the mega photon detector. Nuclear Instruments and Methods in Physics Research Section A: Accelerators, Spectrometers, Detectors and Associated Equipment **349**(1), 118–137 (1994)

[51] R. Sawada, Performance of liquid xenon gamma ray detector for MEG. Nucl. Instrm. and Meth. A **623**(1), 258–260 (2010). doi:10.1016/j.nima.2010.02.214

[52] R. Sawada, *A Liquid Xenon Scintillation Detector to Search for the Lepton Flavor Violating Muon Decay with a Sensitivity of* 10^{-13}. PhD thesis, the Univerisity of Tokyo, 2008

[53] E. Aprile, T. Doke, Liquid Xenon Detectors for Particle Physics and Astrophysics. Rev. Mod. Phys. **82**, 2053–2097 (2010). doi:10.1103/RevModPhys.82.2053, arXiv:0910.4956

[54] E. Aprile et al., The xenon100 dark matter experiment. Astroparticle Physics **35**(9), 573 – 590 (2012). doi:http://dx.doi.org/10.1016/j.astropartphys.2012.01.003

[55] K. Abe et al., Xmass detector. Nuclear Instruments and Methods in Physics Research, Section A: Accelerators, Spectrometers, Detectors and Associated Equipment **716**, 78–85 (2013). doi:10.1016/j.nima.2013.03.059

[56] M Auger et al., The exo-200 detector, part i: detector design and construction. Journal of Instrumentation **7**(05), P05010 (2012)

[57] K. Fujii, *High-accuracy measurement of the emission spectrum of liquid xenon scintillator*. PhD thesis, Yokohama National University, 2015

[58] M.J. Berger et al., Xcom: Photon cross sections database

[59] Akira Hitachi et al., Effect of ionization density on the time dependence of luminescence from liquid argon and xenon. Phys. Rev. B **27**, 5279–5285 (1983). doi:10.1103/PhysRevB.27.5279

[60] Y. Hisamatsu. The performance test of photomultiplier for meg liquid xenon calorimeter. Master's thesis, the University of Tokyo (2005)

[61] Satoshi Mihara, MEG liquid xenon detector. J.Phys.Conf.Ser. **308**, 012009 (2011). doi:10.1088/1742-6596/308/1/012009

[62] T. Haruyama et al., Development of a high-power coaxial pulse tube refrigerator for a liquid xenon calorimeter. CEC **710**(1), 1459–1466 (2004). doi:10.1063/1.1774839

[63] A. Baldini et al., Absorption of scintillation light in a 100 l liquid xenon γ-ray detector and expected detector performance. Nucl. Instrm. and Meth. A **545**(3), 753–764 (2005). doi:10.1016/j.nima.2005.02.029, arXiv:0407033

[64] S. Mihara et al., Development of a method for liquid xenon purification using a cryogenic centrifugal pump. Cryogenics **46**(9), 688–693 (2006)

[65] W. Ootani et al., Development of a thin-wall superconducting magnet for the positron spectrometer in the MEG experiment. IEEE Trans. Appl. Supercond. **14**(2), 568–571 (2004). doi:10.1109/TASC.2004.829721

[66] Y. Fujii, W. Ootani, M. Schneebeli. Magnetic field map of meg cobra magnet. Technical Report 76, MEG (2011)

[67] C. de Boor. *A Practical Guide to Splines*. Springer (1978)

[68] M. Hildebrandt, The drift chamber system of the MEG experiment. Nucl. Instrm. and Meth. A **623**(1), 111–113 (2010). doi:10.1016/j.nima.2010.02.165

[69] H. Nishiguchi, *An Innovative Positron Spectrometer to Search for the Lepton Flavour Violating Muon Decay with a Sensitivity of* 10^{-13}. PhD thesis, University of Tokyo, 2008

[70] S. Dussoni et al., The Timing Counter of the MEG experiment: design and commissioning. Nucl. Instrm. and Meth. A **617**(1-3), 387–390 (2010). doi:10.1016/j.nima.2009.08.089

[71] M.De Gerone et al., Development and commissioning of the timing counter for the meg experiment. IEEE Transactions on Nuclear Science **59**(2), 379–388 (2012). doi:10.1109/TNS.2012.2187311

[72] *MIDAS : midas.psi.ch*

[73] L. Galli et al., An FPGA-based trigger system for the search of $\mu^+ \to e^+\gamma$ decay in the MEG experiment. J. Instrum. **8**, P01008 (2013). doi:10.1088/1748-0221/8/01/P01008

[74] L. Galli, *A real time glance at the Lepton Flavor Violating decay $\mu \to e\gamma$ in the MEG experiment*. PhD thesis, Pisa University, 2010

[75] S. Ritt, R. Dinapoli, U. Hartmann, Application of the DRS chip for fast waveform digitizing. Nucl. Instrm. and Meth. A **623**(1), 486–488 (2010). doi:10.1016/j.nima.2010.03.045

[76] Y Uchiyama et al. Analysis of gamma-ray energy for 2009 & 2010 data. Technical Report 72, MEG (2011)

[77] Y. Fujii, *Search for the Lepton Flavor Violating Muon Decay $\mu^+ \to e^+\gamma$ with a Sensitivity below 10^{-12} in the MEG Experiment*. PhD thesis, University of Tokyo, 2013. https://meg.web.psi.ch/docs/theses/fujii_phd.pdf

[78] P. Billoir, Track fitting with multiple scattering: A new method. Nucl. Instrm. and Meth. A **225**, 352–366 (1984). doi:10.1016/0167-5087(84)90274-6

[79] R. Frühwirth, Application of Kalman filtering to track and vertex fitting. Nucl. Instrm. and Meth. A **262**, 444–450 (1987). doi:10.1016/0168-9002(87)90887-4

[80] A. Fontana et al., Use of GEANE for tracking in virtual Monte Carlo. J. Phys. Conf. Ser. **119**, 032018 (2008). doi:10.1088/1742-6596/119/3/032018

[81] Francesco Renga. A new kalman filter for tracking in the meg spectrometer. Technical Report 81, MEG (2012)

[82] X. Bai, *Search for the Lepton Flavor Violating Decay $\mu^+ \to e^+\gamma$ With A Sensitivity of 10^{-12}*. PhD thesis, the University of Tokyo, 2012

[83] A. Baldini et al., A radioactive point-source lattice for calibrating and monitoring the liquid xenon calorimeter of the MEG experiment. Nucl. Instrm. and Meth. A **565**(2), 589–598 (2006). doi:10.1016/j.nima.2006.06.055

[84] Y. Nishimura, *A Search for the $\mu^+ \to e^+\gamma$ Using a High-Resolution Liquid Xenon Gamma-Ray Detector*. PhD thesis, the University of Tokyo, 2010

[85] V. Blobel, Software alignment for tracking detectors. Nucl. Instrm. and Meth. A **566**, 5–14 (2006). doi:10.1016/j.nima.2006.05.157

[86] G. Rutar et al., A dedicated calibration tool for the meg and meg ii positron spectrometer. Nuclear Instruments and Methods in Physics Research Section A: Accelerators, Spectrometers, Detectors and Associated Equipment pp. – (2015). doi:http://dx.doi.org/10.1016/j.nima.2015.11.121

[87] Robert Hofstadter, Electron scattering and nuclear structure. Rev. Mod. Phys. **28**, 214–254 (1956). doi:10.1103/RevModPhys.28.214

[88] J. Adam et al. (MEG Collaboration), A limit for the $\mu \to e\gamma$ decay from the MEG experiment. Nucl. Phys. **B834**, 1–12 (2010). doi:10.1016/j.nuclphysb.2010.03.030, arXiv:0908.2594

[89] J. Adam et al. (MEG Collaboration), New limit on the lepton-flavor violating decay $\mu^+ \to e^+\gamma$. Phys. Rev. Lett. **107**, 171801 (2011). doi:10.1103/PhysRevLett.107.171801, arXiv:1107.5547

[90] A.M. Baldini et al. (MEG Collaboration), Measurement of the radiative decay of polarized muons in the MEG experiment. Eur. Phys. J. C **76**, 108 (2016). doi:10.1140/epjc/s10052-016-3947-6, arXiv:1312.3217

[91] Roger Barlow, Extended maximum likelihood. Nuclear Instruments and Methods in Physics Research Section A: Accelerators, Spectrometers, Detectors and Associated Equipment **297**(3), 496 – 506 (1990). doi:http://dx.doi.org/10.1016/0168-9002(90)91334-8

[92] G.J. Feldman, R.D. Cousins, Unified approach to the classical statistical analysis of small signals. Phys. Rev. D **57**(7), 3873–3889 (1998). doi:10.1103/PhysRevD.57.3873

[93] A.M. Baldini et al. (MEG II Collaboration), MEG upgrade proposal (R-99-05.2) (2013), arXiv:1301.7225

[94] F. Berg et al., Himb – a possible "next generation" high-intensity muon beam facility for particle physics & materials science